University of Strathclyde
Department of Electronics and Electrical Engineering

Comparison between Three- and Five-phase Permanent Magnet Generators Connected to a diode Bridge Rectifier

by

Nagm Eldeen Abdo Mustafa Hassanain

B.Sc, M.Sc

A thesis presented in fulfilment of the requirements for the degree of
Doctor of Philosophy

2009

Acknowledgements

I would like to express my gratitude and appreciation to my supervisor, Dr. John Fletcher for his continuing guidance and help during my PhD study. Also thanks and appreciation is extended to Prof. B. W. Williams.

In addition, I would like to thank those who had helped me in this work, Mr. Charles Croser and Dr. Lim.

Also deep thanks to University of Strathclyde and my University, Sudan University for science and technology, for granting me this scholarship.

Dedication

I dedicated this work to my family, my teachers and my friends

TABLE OF CONTENTS

Chapter 5 Evaluation of the performance of the prototype five- and three-phase generators using FEA and experimental tests ... 107

Abstract:

This thesis compares the performance of 5- and 3-phase PM generators connected to a diode bridge rectifier under normal and open-circuit failure conditions. Also it describes the design of 5- and 3-phase prototype PM generators with the same volume and rated speed. The permanent magnet generator has advantages such as: simple construction, no excitation field winding, low maintenance cost. The advantages of using diode bridge rectifiers are simplicity and cost.

A simulation model is developed for 5- and 3-phase systems that includes the generator self- and mutual-inductance and phase resistance. The developed model demonstrates the effect that both self- and mutual-inductance have on the 5-phase system including an important reduction in the shaft torque ripple. The 5-phase system displays considerably lower peak-to-peak shaft torque ripple compared to three-phase system. Also it is shown that the five-phase system can use a lower value of capacitance for the same output voltage ripple. In addition, the 5-phase system requires diodes with lower current ratings compared to the 3-phase system. The operation and performance of the 5- and 3-phase systems under open-circuit phase failure is assessed and discussed. It is shown that in terms of shaft torque ripple the 5-phase system has a performance superior to the 3-phase system. With two open-circuit phase failures, the 5-phase system has adjacent and non-adjacent open-circuit failure modes. Non-adjacent failures are shown to produce a less extreme operating condition compared to adjacent phase failures in terms of torque ripple and dc output voltage ripple.

The rms current in the dc link capacitor is discussed for the 5-phase and 3-phase systems under normal and failure conditions. If, under normal conditions, the capacitor is specified to give the same output voltage ripple in the 5- and 3-phase system, then during open-circuit failure, the 5-phase system displays a larger per-unit increase in rms current in the dc link capacitor compared to the 3-phase system. For systems making use of the fault tolerance of the 5-phase generator, the specification of the dc link capacitor becomes driven by the rms current during the fault.

Simulation and FEA results are verified by experiments on practical 5- and 3-phase prototype generators. Good agreement is observed.

List of Abbreviations

AC	Alternating current
DC	Direct current
EMF	Electro-motive force
FEA	Finite Element Analysis
mmf	Magneto-motive force
MLT	Mean Length of a Turn
PM	Permanent magnet
PMG	Permanent magnet generator
rpm	Revolutions per minute
RMS	Root-mean-square
TSR	Tip-speed ratio

List of Symbol

A	the specific electrical loading (AC/m)
A_g	air-gap area (mm^2)
A_m	magnet area (mm^2)
A_s	cross section area of the conductor (mm^2)
A_{slot}	slot area (mm^2)
A_w	cross section area of the wire used in the coils (mm^2)
B	specific magnetic loading (T)
B_m	flux density (T)
B_t	rotor yoke flux density (T)
B_{th}	tooth flux density (T)
C_o	concentration factor
D_o	outer diameter (mm)
D_r	rotor diameter (mm)
d_{sh}	slot depth including the shoe depth, (mm)
D_w	conductor diameter (mm)
F_{slot}	slot fill factor
i_a, i_b, i_c, ,i_d, i_e	phase-*a* ,-*b* ,-*c*,-*d* and-*e* winding current (A)
J	current density (A/mm^2)
K_d	winding distribution factor
K	output coefficient
k_e	phase back *emf* constant (V/rads^{-1})
L_m	magnet width (mm)

L_{stk}	rotor length (mm)
L_w	total length of conductor per phase include the end winding, (mm)
N_{ph}	number of turns per phase (turn)
N_{coil}	number of conductors per slot
p	pole pairs
P_c	permanence coefficient
q	number of coil per group
R_{ESR}	equivalent series resistance of the capacitor (Ω)
T	shaft torque (Nm)
w_t	tooth width (mm)
ρ	conductor specific resistance (Ω.m)
λ_a	flux linking phase-*a*
g''	equivalent air-gap distance including the radial thickness of the magnet and the air-gap length including the stator slotting effect

Chapter 1

Introduction

1.1 Introduction

Generation of electricity causes substantial pollution. It is responsible for about one-third of all carbon-dioxide emissions and is a major source of nitrogen oxide and sulphur dioxide. Wind energy, used to generate electricity, can contribute to a reduction in emissions and has been topic of research for more than 80 years [1.1]. Wind turbines are used to convert the wind energy to electrical energy through an electromechanical energy conversion process. Wind turbines are generally grouped into two basic types: horizontal axis wind turbines and vertical axis wind turbines [1.2], figure 1.1. The horizontal-axis turbine is the most common as it is aerodynamically more efficient. However, there are many problems that researchers continue to work on, for example, reducing the construction costs and optimizing the operating costs, improving the performance of electrical equipment (generators, rectifiers, inverters controller) and aerodynamic efficiency.

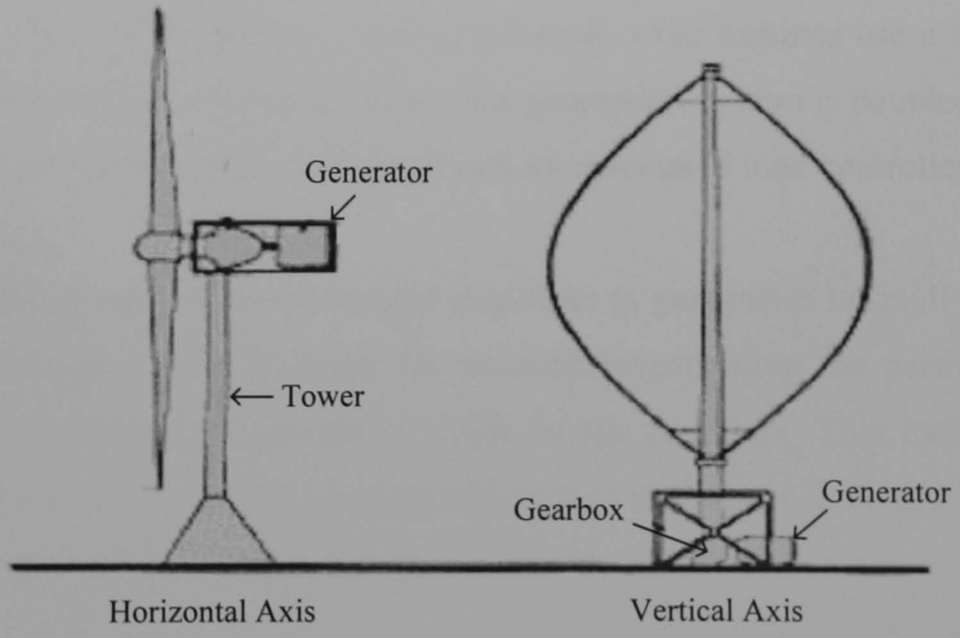

Figure 1.1. Wind turbine types (from American Wind Energy association website 1998).

Wind energy is converted to electrical energy using an electrical generator connected either directly, or via a gearbox, to the wind turbine's aerodynamic system as shown in figure 1.1. Energy generation depends on the electromechanical energy conversion process. There are inherent maintenance requirements associated with the power take-off from the aerodynamic system and some of these requirements are associated with the electrical generator.

Electrical generators, used with wind turbines, are varied: direct current generators, induction generators, synchronous generators, reluctance generators and permanent magnet generators have all been proposed. Direct current generators and synchronous generators require brush maintenance especially in applications at high altitude or where dusts and high wind can damage the brushes. Permanent magnet generators are the machine of choice in small wind turbines offering simple construction, low maintenance costs and self-exciting ability [1.3]-[1.6]

Diode bridge rectifiers are used in conjunction with permanent magnet generators to produce DC power from the generator's AC output. Diode rectifiers have the advantage of low cost and simplicity. However, diode rectifiers cause torque ripple and output voltage ripple and these reduce the performance of the generation system (blade system, generator and rectifier). Nonetheless, most small-scale wind turbines use a three-phase PM generator connected to a diode rectifier. The generation system is coupled to a grid-connect inverter or is connected to a dc load with an associated load controller.

The study of multi-phase permanent magnet machines as generators in small-scale wind turbines is a new topic. There is need for research investigating the performance of multi-phase PM generators connected to diode bridge rectifiers. This includes basic analysis of the performance of the system compared to traditional three-phase systems. This is one objective of the research reported in this thesis.

1.2 Wind turbine characteristics

The aerodynamic power generated by a wind turbine is [1.7]-[1.9]:

$$P = 0.5\rho A_{sw} C_p V^3 \qquad (1.1)$$

where

ρ = density of air (kg/m^3)

A_{sw} = swept area of the blade system (m^2)

C_p = performance coefficient

V = wind speed (ms^{-1})

The torque generated by the turbine is:

$$T = \frac{P}{\omega_s} \quad (Nm) \qquad (1.2)$$

where ω_s is the mechanical rotor speed of the wind turbine. (rad s^{-1})

The performance coefficient, C_p, is a function of tip-speed ratio (TSR) where

$$TSR = \frac{\omega_s R}{V} \qquad (1.3)$$

and R is the radius of the wind turbine rotor (m). Figure 1.2 shows a typical C_p versus TSR curve for a small-scale wind turbine assessed in a wind-tunnel. The C_p characteristic has a peak value and the wind turbine should operate at the peak C_p for a given wind speed in order to generate maximum power.

During start-up, when the rotor speed is low, the TSR is small thus the aerodynamic torque is small. For this reason, in the case of direct connection of the permanent magnet generator to the aerodynamic system, the generator must have low cogging torque to allow the turbine to start.

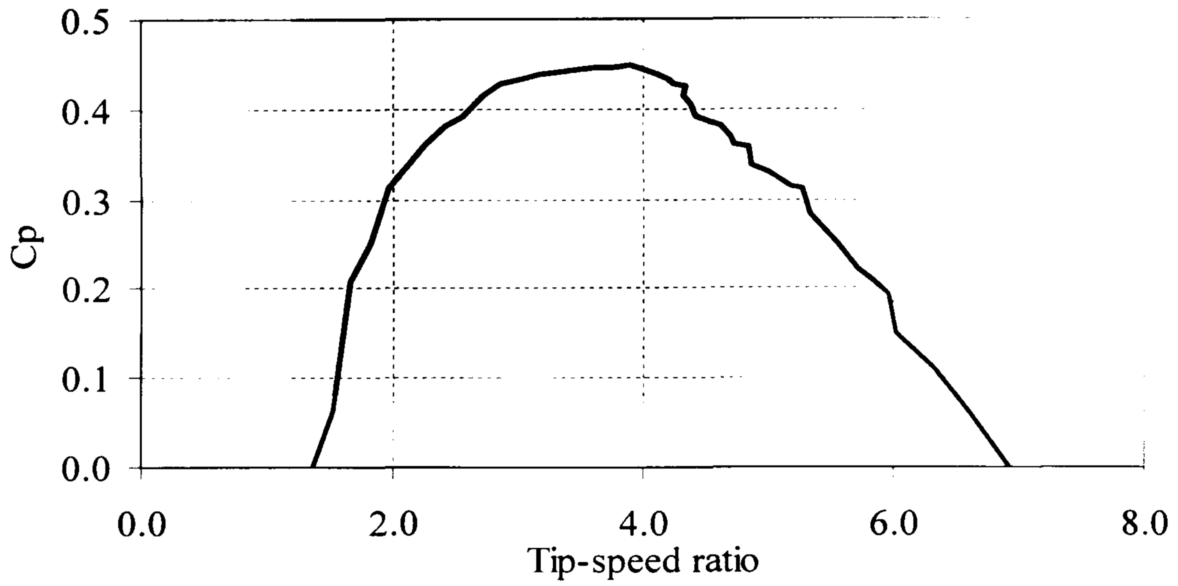

Figure 1.2. Cp versus tip speed ratio curve for the Rutland 913 wind turbine at an incident wind speed of 13.9ms^{-1}

Figure 1.3 shows a measured wind turbine power curve for a Rutland 913 turbine with an incident wind speed of 13.9ms^{-1}. The system should operate at a shaft speed that gives the maximum power, point A (475W at a speed of 125rpm). If the load power is reduced, for example, as a result of an open circuit failure in the generator, the speed of the turbine blade will increase to compensate the reduction in the output power. For example, if the power is reduced from 475W at the maximum power, point A, to 325W at point B, the rotational speed of the blade system will increase from 125rpm to 200rpm. If the maximum point tracker is in use, the control system will track the maximum point and return the system to point A by increasing output power. The response of the tracker depends on many factors, for example, the inertia of the drive train and blade system. In this research, the response of the aerodynamic system to the change output power is assumed to be slow and the speed of the shaft at the time of failure is assumed to remain constant during the fault.

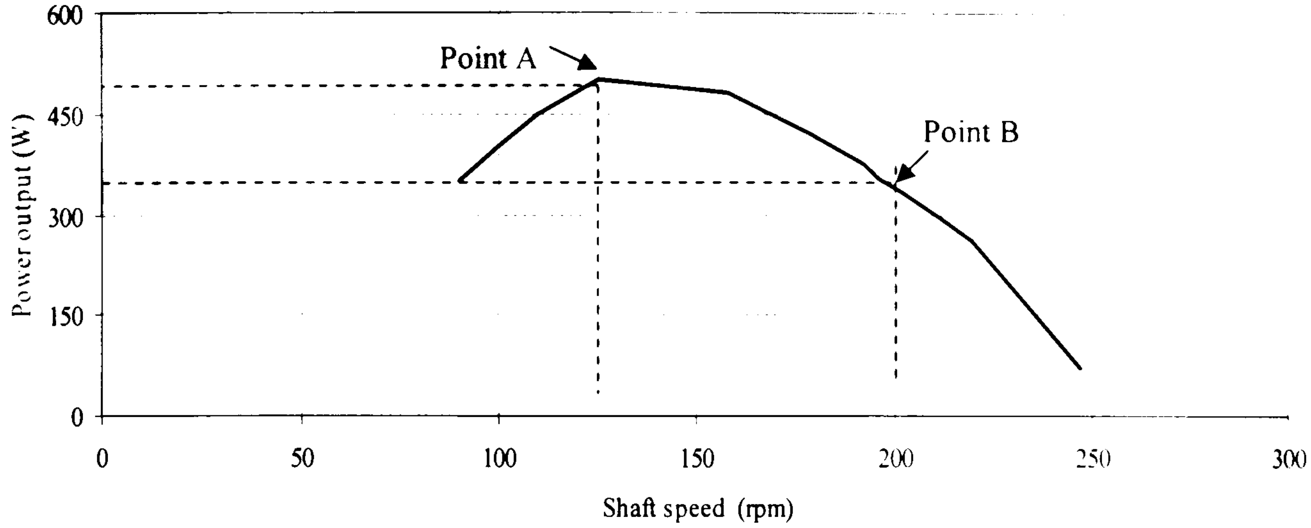

Figure 1.3. Measured wind turbine power curve for the Rutland 913 wind turbine at an incident wind speed of 13.9ms^{-1}

1.3 Permanent Magnet machines:

The term 'permanent magnet machine' is used to include all electromagnetic energy conversion devices in which the magnetic excitation is supplied by permanent magnets. Energy converters using permanent magnets come in a variety of configurations.

Today, most small-scale wind turbines are permanent magnet generators. The permanent magnet generators are usually either axial- or radial- flux machines. Radial-flux permanent-magnet generators may be divided into two types according to the magnet location; surface mount PM machines and interior PM machines [1.10, 1.11]. The subject of this thesis is radial-flux machines with surface-mounted magnets.

1.4 Multi-phase generators

Most wind generators generate three phase electrical power. Three-phase generators have been extensively researched however multi-phase generators are relatively new. Multi-phase generators have some potential advantages compared to three-phase such as; low phase current, higher output power density and low torque ripple. Disadvantages are higher space harmonics, an increase in the number of the connections to the machine and their poor commercial availability. In this research five-phase and three-phase PM generators are compared and their advantages and disadvantages identified.

1.5 Multi-phase PM generators with diode bridge-rectifiers

Analysis of multi-phase permanent magnet generators connected to diode bridge rectifiers is new. The advantages of using diode bridge rectifiers are simplicity and cost. There are no existing mathematical models presented for multi-phase permanent magnet generators connected to diode bridge rectifiers. Fundamental research is presented investigating the operation of five-phase generators with associated full-bridge, diode rectifier circuits.

1.6 Motivation for the research

The permanent magnet machine is the machine of choice in small wind turbines, offering a simple generating mechanism and excellent power density. Typically the output from the PM generator is rectified and the dc link voltage processed using power electronics-based converters and inverters to provide the desired output. The advantages of using a diode bridge rectifier rather than full or partial-field-oriented control are simplicity and cost.

Using a three phase PM generator with a rectifier is common in small-scale systems, but has some disadvantages, such as high torque ripple and output voltage ripple which affects the performance of the generator system. Using a generator which has more than three-phases may improve the generator performance. One objective of this research is to assess the improvement in performance of the generation system that uses a diode rectifier connected to multi-phase PM generator.

Another objective of this research is to design and model a five-phase generator connected to a diode bridge rectifier with dc link capacitor and resistive load. In addition, this research investigates the impact the five-phase system has on system losses including copper loss, rectifier diode losses and iron losses. Other aims of this research are to study the behaviour of the systems under open-circuit failure of one or more phases of the generator and to assess the impact this has on system performance.

It is important to present a fair comparison between 3- and 5-phase generators. In this thesis, each generator has been constructed using the same stator lamination design (which has 30 slots) and the same 4-pole rotor. Both machines will generate the same rectified output voltage at full load with the same prime-mover speed.

1.7 Scope of the thesis

Multi-phase PM generators feeding electrical power through diode rectifiers has not attracted significant research. This thesis concentrates on performance analysis of an isolated three and five-phase permanent magnet generator with bridge rectifier and constant load.

This thesis covers:

- the design of the prototype five-and three- phase PM generators,
- the modelling of the five-phase permanent magnet generator with a diode bridge rectifier,
- the effect of the self- and mutual-inductance of the generator phase windings on the performance of the system,
- the operation of the five-phase and three-phase generators with single and two-phase open-circuit phase failures, and
- the requirements and specification of the DC-link capacitor.

Chapter two reviews relative literature associated with the research.

Chapter three develops a model of three- and five-phase permanent magnet generators connected to diode bridge rectifiers. The developed model uses pulse functions. Also the effect of the phase inductance of the generator on the performance of the system is studied. The model is verified using PSpice.

In chapter four the design of both generators is presented analytically and using FEA software.

Chapter five details the experimental performance of the five- and three-phase systems with diode bridge rectifiers under full load and compares this to FEA simulation.

In chapter six, open-circuit phase failures are considered for both systems. Simulation and experimental test results demonstrate the advantages of the five-phase system over its three-phase counterpart.

In chapter seven an assessment is made of the required DC-link capacitor current. This demonstrates the rms dc link capacitor current under normal conditions and with open-circuit phase failures.

Conclusions and future directions are presented in chapter eight.

References:

[1.1] T. Ackermann, “Wind Power in Power System,” John Wiley and Sons, 2005.

[1.2] G. L. Johnson, “Wind energy systems``, Prentice Hall, January 1985.

[1.3] M. Comanescu, A. Keyhani, and M. Dai, “Design and analysis of 42-V permanent-magnet generator for automotive applications,” IEEE Trans. on Energy Conversion, Vol. 18, No. 1, March 2003. pp. 107-112.

[1.4] M. Chinchilla, S. Arnaltes, and J.C. Burgos, ``Control of Permanent-Magnet Generators Applied to Variable-Speed Wind-Energy Systems Connected to the Grid,” IEEE Trans. on Energy Conversion, Vol. 21, No.1, March 2006, pp. 130-135.

[1.5] N. Yamamura, M. Ishida, and T. Hori, ``A Simple Wind Power Generation System With Permanent Magnet Type Synchronous Generator,`` IEEE International Conference on Power Electronics and Drive Systems, PEDS’99, Vol. 2, July 1999, Hong Kong, pp. 849-854.

[1.6] A. S. McDonald, M. A. Mueller, and H. Polinder, “Structural mass in direct-drive permanent magnet electrical generators,'' IET Renewable Power Generation, Vol. 2, No.1, 2008, pp. 3-15.

[1.7] J. Zhang, M. Cheng, and Z. Chen, “Nonlinear Control for Variable-Speed Wind Turbines with Permanent Magnet Generators,`` International Conference on Electrical Machines and Systems, Oct. 8-11, 2007, Seoul, Korea, pp. 324-329.

[1.8] R. Esmaili, L. Xu, and D. K. Nichols, “A New Control Method of Permanent Magnet Generator for Maximum Power Tracking in Wind Turbine Application,'' IEEE Power Eng. Society general Meeting, June 12-16, 2005, pp. 2090-2095.

[1.9] E. Muljadi, S. Drouilhet, R. Holz, and V. Gevorgian ``Analysis of Permanent Magnet Generator for Wind Power Battery Charging,'' Industry Applications Conference, 31th IAS Annual Meeting, Vol. 1, Oct. 6-10, 1996, pp.541-548.

[1.10] J.R. Hendershot and T.J.E.Miller, “Design of brushless permanent magnet motors,” Magna Physics Pub., 1994.

[1.11] T.J.E.Miller, “Brushless permanent-magnet and reluctance motor derives,`` Clarendon Press, Oxford, 1989.

Chapter 2

Literature review

2.1 Introduction

The scope of this thesis covers the design of a five-phase permanent magnet generator, and the operation of the generator with a diode bridge rectifier with DC link storage. It is focussed on wind turbine applications of the system and particularly under normal and generator open-circuit failure conditions. In this chapter, existing relevant literature is introduced, which is classified into:

1. Theory and analysis of the diode bridge rectifier.
2. Operation, analysis and design of permanent magnet machines.

2.2 Theory and analysis of the diode bridge rectifier

Diodes perform various functions in power circuits, including switching in rectifiers, anti-parallel 'freewheel' diodes to protect semiconductor switches in switched-mode circuits, or to avoid charge reversal of capacitors [2.1].

The diode is widely used in rectifier circuits to convert ac to dc power. Figure (2.1) shows types of diode rectifier circuits.

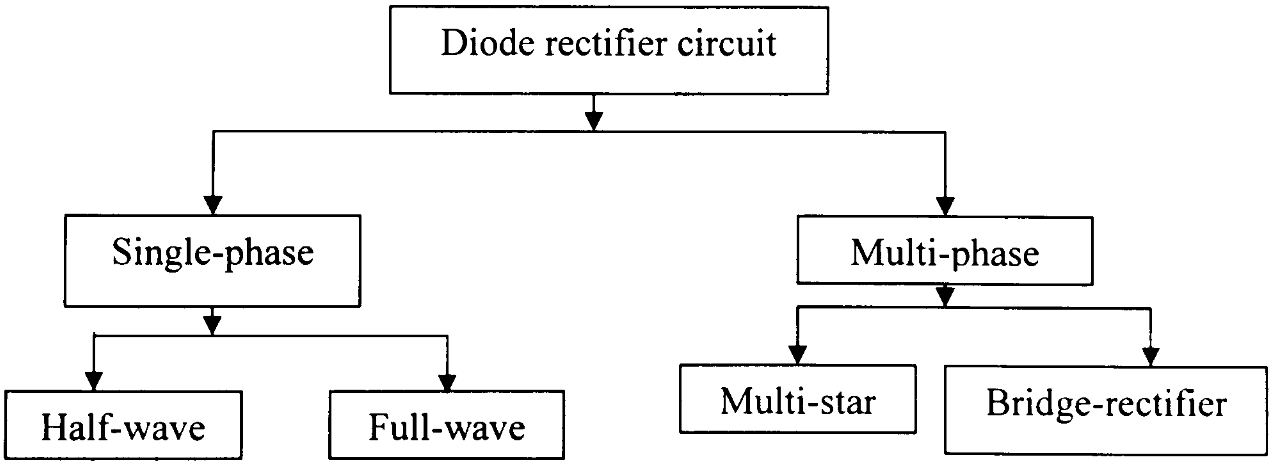

Figure 2.1. Type of diode rectifier circuits, showing single- and multi-phase types.

The single-phase, half-wave rectifier has only one diode as shown in figure 2.2(a). and single phase full-wave rectifier has four diodes as shown in figure 2.2(b). The single-phase, full-wave rectifier has advantages compared to single-phase half-wave rectifier, such as low ripple factor, higher efficiency and no dc component which can contribute to dc saturation in transformer cores [2.1]. In the multi-star rectifier circuit each phase has one diode as shown in figure 2.3(a). Each phase conducts for $(2\pi/q)$ radians, where q is the number of phases and the fundamental output frequency is $q \times f$ Hz. Figure 2.3(b) shows multi-phase diode bridge rectifier, each phase has two diodes and the output frequency is $2q \times f$ Hz, where f is the source frequency and q is the number of phases. In a similar fashion to single-phase circuits, the multi-phase diode bridge-rectifier has advantages compared to the multi-star configuration.

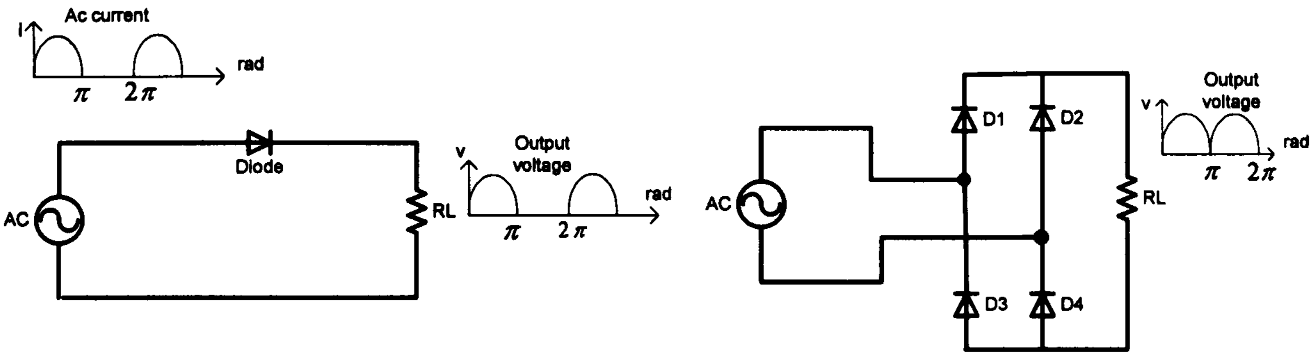

(a) (b)

Figure 2.2. Single phase diode rectifier circuits, showing (a) half wave (b) full wave rectifier (diode-bridge).

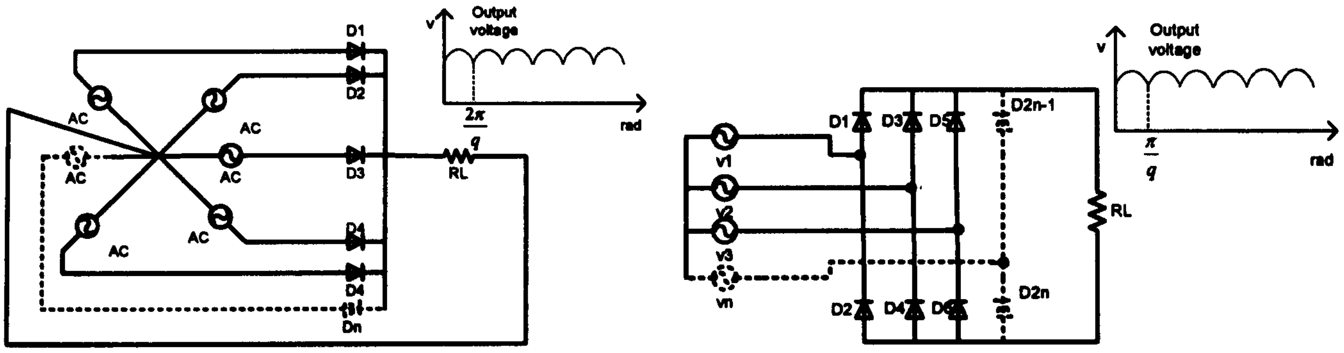

(a) (b)

Figure 2.3. Multi-phase rectifier circuits, showing (a) multi-star *n*-phase rectifier and (b) *n*-phase bridge rectifier.

In this thesis literature on multi-phase diode bridge rectifiers is reviewed. Most literature focuses on three-phase bridge rectifiers. The three-phase diode bridge rectifier is a six-plus rectifier and the fundamental frequency of the dc voltage is six times the input frequency.

Line current harmonics are an issue in diode rectifiers as they affect the efficiency of the rectifier and increase the rms ac supply current for the same load. Researchers have studied and improved methods of reducing the current harmonics.

M. Sakui and M. Shiya [2.2] presented a new method to calculate the ac current harmonics. The method is based on the frequency domain and rectifier switching function. The Fourier series is used to analyse the switching function. The method assumes the source voltage is balanced and there is a dc filter. Calculating the ac line current harmonics, when the power supply is unbalanced, is presented by M. Sakui and H. Fujita [2.3]. They used the frequency domain and switching functions. The unbalanced power supply is taken into account when the switching function is created by changing the angle of 'continuing' period when the diode is forward biased.

An analytical method to calculate the ac current harmonics with the effect of the phase impedance with both continuous and discontinuous ac current is proposed in [2.4]. The main conclusion is that larger values of phase impedance produce more continuous ac current. The paper is based on the frequency domain and switching function technique. It shows that the harmonic components from continuous and discontinuous modes are not the same, with the continuous modes displaying lower harmonic values compared to discontinuous modes.

There are many methods to reduce current harmonics in the three-phase rectifier. W. B. Lawrance and W. Miedyslaw [2.5] presents a novel method to reduce the harmonic currents. The method is based on injection of third harmonic currents into the neutral point of the supply transformer. They also used passive LC filters between the rectifier output and secondary neutral point to act as third harmonic current sources.

The harmonics become lower as the number of rectifier pulses increases. Increasing the number of phases smoothes the output DC voltage before filtering. Many researchers have presented and discussed rectifiers with more than three-phases. S. Choi *et al.* [2.6] presented 24-pulse diode rectifiers for high power ac motor drives. Two new 24-pulse rectifier systems were proposed. They transformed conventional 12-pulse rectifier to a 24-pulse rectifier by using a tapped interface transformer. The fifth, seventh, eleventh, thirteenth, seventeenth and nineteenth harmonic current in the input lines are eliminated.

Detecting a diode failure in the three phase alternator is presented in [2.7]. Diodes can fail in one of two ways; open circuit or short circuit. It showed that an open-circuit diode introduces a significant change in ac ripple of the output current and in the case of a diode short circuit the output is severely affected. It is also shows that the system can still operate safely with a diode failing open circuit but cannot operate safely if the diode fails short circuit. Table 2.1 shows the harmonic content of the dc output current relative to dc content. It is shows that the harmonic components of the dc output current change with the condition of the diode. The load in this case is the alternator's exciter (inductive load).

Table 2.1 Harmonic content of the dc output current relative to dc magnitude for the three-phase bridge rectifier connected to alternator's exciter.

	Bridge intact	Diode open-circuit	Diode short-open circuit
Fundamental	0.3%	17.0%	92.0%
2nd harmonic	0.1%	20.0%	33.0%
3rd harmonic	0.1%	14.0%	10.5%
4th harmonic	0.1%	5.0%	8.0%
5th harmonic	0.1%	2.6%	13.0%
6th harmonic	2.2%	4.7%	17.0%

2.3 Operation, analysis and design of permanent magnet machines

Permanent magnet machines can be classified into three categories: permanent magnet commutator dc motors (PMCDC), permanent magnet brushless dc motors (BLDCM) and permanent magnet ac synchronous motors (PMSM) [2.8]. The PMCDC motor is similar to a dc motor in construction but the excitation system is replaced by permanent magnets. The BLDC and PMSM design procedures are similar. They can be single or multi-phase. The differences between BLDC and PMSM are primarily the back-emf waveforms and the method of controlling the machine. The BLDC machine typically has a trapezoidal back-emf waveform, and PMSM machine has near sine-wave back-emf. The two machines do not need a commutator which reduces maintenance and improves reliability. P. Pillay and R. Krishana [2.9] present a comparison of PMSM and BLDC machines. They found that if the copper losses of the PMSM and BLDCM are equal, then the BLDC is capable of 15% higher power density; however it is shown that the ripple torque of the BLDC is higher than that of the PMSM.

During the last decade, permanent magnet material has been developing rapidly. According to their basic chemical composition, the permanent magnet material can be grouped into Alnicos, ceramics, and rare earth magnets [2.10]. To maximize the achievable magnetic field energy, permanent magnet materials are designed to have a wide magnetic hysteresis loop [2.11]. The hysteresis loop is divided into magnetization and demagnetization regions. The demagnetization region is used to define the basic performance of a permanent magnet material. Figure 2.4 shows the demagnetization curve of a permanent magnet material. The figure shows both the normal and the intrinsic curve. Only the normal curve is required to determine the operating point of the magnetic field system, [2.11].

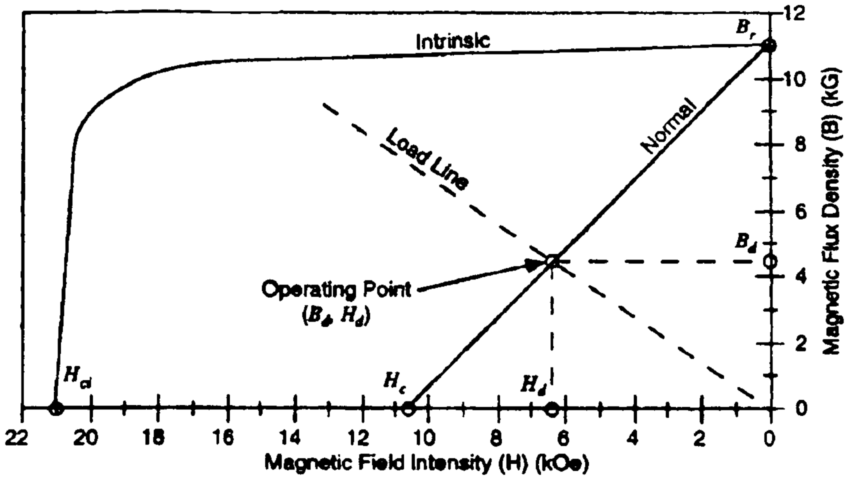

Figure 2.4. Demagnetization curve for NdFeB at 20°C, showing both intrinsic and normal curves. [Ref. [2.11], p1.5, figure 1.25].

The improvements in permanent magnet materials, energy product and high temperature operation, has led researchers to investigate how these new materials can be applied in permanent magnet machines. Research has concentrated on the design, performance and control when the permanent magnet machine is operated as a motor.

Permanent magnet machines are usually axial or radial flux machines and this refers to the orientation of the flux in the air-gap. The radial-flux permanent-magnet machine can be used for low speed as well as high speed and can have surface mounted and interior magnet rotor [2.12]. Figure 2.5 shows types of radial-flux permanent magnet rotors.

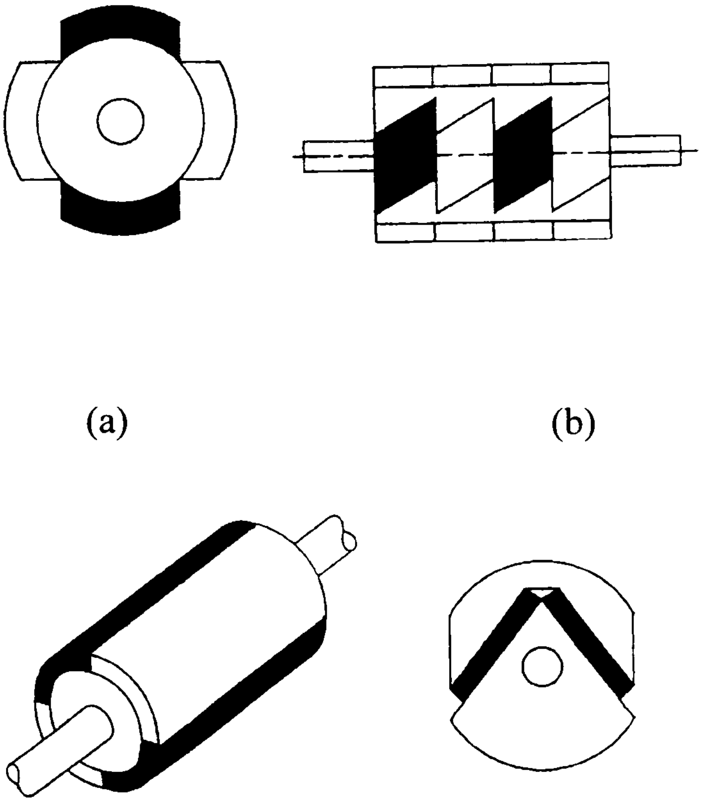

(a) (b)

(c) (d)

Figure 2.5. Type of radial-flux permanent magnet, showing four configuration (a) 4-pole surface-mount (b) skewed magnet arcs (c) ring magnet topology (d) 2-pole interior magnet design [Ref.[2.12], p3-7, figure 3.1].

In this thesis some of the relevant literature on the design of the permanent magnet machine is discussed though there are many research papers in this field. Most research work on PM machine design concentrates on improving the performance of the machine by improving the magnet design, the shape of the magnet, the analysis of the magnetic circuit and reducing the cogging torque and the losses. The permanent magnet literature in this thesis is divided into:

1. The design of magnetic circuits [2.13] to [2.22],
2. The study and reduction of cogging torque [2.23] to [2.25],
3. The modeling and analysis of the pm machine [2.26] to [2.32], and
4. Five-phase permanent magnet machine research [2.33] to [2.36].

2.3.1 Design of permanent magnet machines

The permanent magnet machine operates as a motor when it is supplied by an external electrical power supply (sinusoidal or trapezoidal waveform voltage), or a generator when driven by an external prime-mover, for example, a wind turbine. The two types of machine have a similar design procedure. First, relevant permanent magnet motor design literature is reviewed. Second, literature on the design of permanent magnet generators is discussed.

i- Permanent magnet motor design

The electromagnetic circuit and flux density distribution is described using a 2D equation by Z. Q. Zhu and D. Howe [2.13]. The equation representing the instantaneous flux density in the air-gap due to the presence of the permanent magnets is presented and improved. The instantaneous flux density in the air-gap due to armature current is presented by the same authors in a second paper [2.14]. The effects of the slots and load current on the instantaneous flux density in the air-gap are presented in [2.15] and [2.16] respectively. These papers, [2.13] to [2.16], present complete analytical equations for flux density in the air-gap which can be used in computer software to investigate the effect of the permanent magnet machine dimensions. It can also be used to predict the back-emf waveforms.

Many researchers use finite element analysis for electromagnetic systems. These techniques can help reduce design time and can assist in accurately determining and optimising performance through design. Z.Q .Zhu et al. [2.17] presented the application of finite-element analysis to both linear and rotary permanent-magnet brushless machines, with particular emphasis on the calculation of iron loss, eddy current loss in the magnets. In the motor with surface-mounted magnets, the inductance in the q-axis is slightly larger than the inductance in d-axis due to different saturation levels in d- and q-axis magnetic circuits. The results show that at low speed the iron loss on-load is higher than the no-load loss and at speeds slightly above rated speed, the iron loss on-load is lower than the no-load. It is also shown that the on-load iron loss in the surface-mount machine is lower than for the other machine topologies. The cogging torque can be reduced to less than 5% of the rated torque by optimising the width of the teeth.

M. A. Alhamadi and N. A. Demerdash [2.18] present a method of skewing a permanent magnet motor using 2D finite elements. The machine is divided into 9-sections as shown in figure 2.6 and FE solution for each section obtained. The average flux density waveform for the 9-sections is then calculated. The result shows agreement between practical and multi-section FEA model (about 3.4% difference). Using multi-section 2D FE analysis skew can be used to refine the design of permanent magnet machines with skewed magnets. However, skewing presents the manufacturers with difficulties in mass production which leads to an increase in the cost.

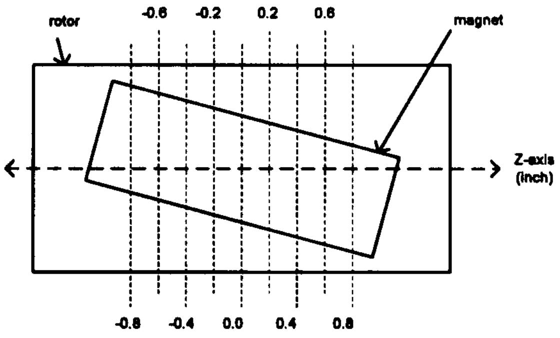

Figure 2.6. Schematic of a skew-mounted magnet on the rotor, showing 9-section used in FE analysis [2.18].

ii- Permanent magnet generator design

Permanent magnet generator design has been presented by several researchers for use in wind turbine and special purpose applications such as the aerospace field. J. Chen *et al.* [2.19] described an outer-rotor permanent-magnet generator. It is designed for multi-pole, low-speed power conversion for stand-alone applications (20kW, 170rpm). In addition, they developed design principles and equations. They used finite-element for detailed analysis and fine adjustment of the design. The result shows that a PM generator with simple construction can operate with good performance over a wide range of speeds, 70-200 rpm. In [2.20] M. Comanescu, A. Keyhani and M. Dai presented a design methodology for a three-phase permanent-magnet synchronous alternator. A three-phase 1800rpm permanent magnet synchronous alternator supplying a 2.5kW, 42 V dc load was designed to be used in an automotive electric system. An equivalent circuit model (reluctance model) of the PM machine was developed. The design was assessed using FE analysis at no-load and full load. The results show that stator currents increase the flux density and distortion of the air-gap field.

C. Zwyssig *et al.*[2.21] present the design of a high speed 100W, 500 000rpm PM generator for mesoscale gas turbines. In addition, they calculated the losses in the copper winding due to the high frequency currents and magnetic field from the permanent magnet. The total copper losses are reduced by choosing an appropriately sized wire. They compare different magnetic materials to minimise the stator core losses. The torque of 1.9mNm can be produced by either a sinusoidal current of 4.1A peak or a square-wave current with an amplitude of 3.7A. The sinusoidal current produces constant torque. The core loss of 1.2W at 10 kHz is calculated using (2.1)

$$P_{core} = C_m f^{\alpha} . B_m^{\beta} \tag{2.1}$$

where C_m, α and β are parameters taken directly from the datasheet of material, f is frequency and B_m is magnetic flux density .

H. Jussila *et al.* [2.22] produced guidelines for designing concentrated winding, fractional-slot, permanent magnet machines. If the number of slots per pole per phase, q, is not an integer the winding is called a fractional slot winding.

$$q = \frac{\text{number of slots}}{\text{number of poles} \times \text{number of phase}} \tag{2.2}$$

Fractional-slots PM synchronous machines are better suited to low speed applications as they suffer from rotor losses at high-speed. Fractional slot machines also have short end windings. In [2.22] they found that with q = 0.4 the machine has a relatively good winding factor. It is also potentially the best design for low cogging torque.

2.3.2 The study and reduction of cogging torque

Cogging torque is produced in a permanent magnet machine as a result of the change in the air-gap reluctance due to the presence of stator slots. The effect of the cogging torque is additive to the total machine torque and can impact on the ability of the machine to self-start. It also contributes to noise and mechanical vibration. Many methods to reduce the cogging torque have been reported. T. Li and G. Slemon [2.23], proposed a design method to reduce the cogging torque to an acceptable level without skewing the slot teeth. The method is based on appropriate selection of machine dimensions. The cogging torque may be reduced by appropriate choice of the magnet pitch relative to the slot pitch. Also by rotating one pair of poles relative to the other pair the cogging torque can be reduced to 0.3% of rated torque value.

A study of the influence of design parameters on cogging torque in permanent magnet machines is presented by Z. Q. Zhu and D. Howe [2.24]. They investigated the effect of the slot and pole number combination on the cogging torque. The results showed that the overlapping concentrated stator winding produced approximately twice the cogging torque compared to the non-overlapping concentrated winding.

Reduction of cogging torque in interior magnet machines is investigated by Z.Q. Zhu *et al.* [2.25]. A machine with four interior PM poles and a 6-slot, short-pitched stator and a 12-slot, full-pitched stator winding was compared. Negligible cogging torque in the surface-mounted magnet, interior rotor machine is achievable by selecting an optimum magnet pole-arc to pole-pitch ratio.

In this thesis the cogging torque is reduced by using a combination of the two methods, reported in [2.24] and [2.25], these being the use of fractional-slot windings and a 120° magnet pole-arc.

2.3.3 Modeling and analysis

Modeling and simulation of pm machines to study the performance either under steady state or transient condition is important particularly for design optimization. Modeling literature is divided here into two; modeling motors, which includes the drive control of the machine [2.26] - [2.28], and modelling generators [2.29] - [2.32].

i- Modeling and analysis as motor

The papers reviewed here introduce techniques that are adapted for use in the research reported in this thesis. There are many other papers available in this area.

P. Pillay and R. Krishana [2.26] present the modeling, simulation, and analysis of a vector-controlled brushless DC motor drive. The mathematical model of a BDCM is developed. The simulation included the state-space model of the motor and speed controller and a real-time model of the inverter switches. The paper also presents the operation of hysteresis and PWM current controllers and the structure of the drive system. C. C. Chan *et al.* [2.27] presents a novel 5-phase multi-pole square-wave PM motor drive. They described the motor configuration, the equivalent model and the design topology. The electromagnetic-field analysis of the motor was performed using FEA. Also the current ripple and torque pulsation is investigated using the state-space model of the motor as well as the real-time models of the speed controller, current controller, and inverter switches. The design and evaluation of a poly-phase brushless dc machine direct drive system suitable for high performance are presented by M. Godoy *et al.* [2.28]. A five-phase motor is designed with 60 stator slots, double-layer lap winding configuration with a 12-pole rotor.

ii- Modeling and analysis as a generator

In the eighties, researchers considered permanent magnet machines as isolated generators in wind turbines. This research studied the performance of three-phase permanent magnet generators using different methods. Only a few study the performance of five-phase permanent magnet generators.

A. A. Arkadan *et al.* [2.29] presented a computer-aided method to study the effect of stator teeth on the eddy current loss in the stator conductors, and the core losses in the lamination of a 3-phsae, 75kVA, 208V, 24000rpm, two pole, permanent magnet generator. The method is based on a magnetic field solution using radial and tangential flux density components and associated harmonics throughout the machine cross-section including the stator conductor regions. Two designs were presented; a toothless design and conventional stator design. The results show that core loss in the conventional design, with teeth, is approximately 56% higher than the toothless design. However, the toothless machine has lower power density compared to the machine with teeth. For this reason, in the research reported in this thesis the generator is designed with teeth.

A computer aided method is presented by A. A. Arkadan *et al.* [2.30] which can analyse and predict the dynamic performance of a 3-phase permanent magnet generator connected to a rectifier load system with multiple damping circuits. They used the natural *abc* frame of reference. A diode failing short-circuit followed by open circuit is simulated. The unbalanced condition resulting from diode failure causes a decrease in power output delivered to the load.

R. Krishan and G. H. Rim [2.31] described a variable-speed constant frequency (VSCF) technique applied to a permanent magnet brushless generator; the scheme is modeled in the steady-state by integrating the characteristic equation of the generator, the diode rectifier bridge, inverter, and harmonic characteristic for steady-state performance computation. The commutation overlap angle, μ, effect is also included which is calculated using (2.3).

$$\mu = \sqrt{\frac{4\pi(L-M)}{3k_p} I_{dc}} \qquad (2.3)$$

where L, M *and* I_{dc} are self inductance, mutual inductance and dc current respectively. K_p is voltage constant of the machine which equals

$$k_p = \frac{V_p}{\omega_r} \qquad (2.4)$$

where V_p and ω_r are peak phase voltage at rated speed and rated speed respectively.

Theoretical data is correlated with results from an experimental prototype. The results show that efficiency is proportional to speed. It is also shows that the reactive power decreases as speed increases.

B. Sarlioglu and T. A. Lipo [2.32] explored, by using relevant power electronic circuits, the characterization of power production capability of the doubly-salient PM synchronous generator under load conditions. The problem of deriving dc power from a double salient synchronous permanent magnet generator through a typical bridge rectifier and a boost converter with hysteresis controller is also presented. They found that more power output is obtained by using a boost converter than using a bridge rectifier.

2.3.4 Five-phase permanent magnet generators

Multi-phase permanent magnet machines are used as drive motors [2.33]. The three-phase machine is used in a wide range of generator applications, for example, most commercial wind generators use three phase generators. Three-phase generators have been researched extensively, but higher phase number generators are an emerging area. Multi-phase generators have some advantages compared to three-phase such as: lower phase current, higher output power and lower torque ripple. Disadvantages include a more complex control algorithm under vector control. However, little work is reported for five-phase permanent magnet machines operated as generators.

Analysis of a five-phase rectifier is presented by B. Zhang and S. D. Pekarek [2.34]. They investigated the steady-state behaviour of 5-phase diode rectifiers for both a voltage source with source inductance and a synchronous machine. The output dc voltage at no-load has a value calculated using (2.5).

$$V_d = \frac{10E}{\pi}\sin\left(\frac{\pi}{5}\right) \tag{2.5}$$

where E is maximum phase voltage.

The operating modes of a 5-phase diode rectifier are shown in Table 2.2. Table 2.2 shows the mode sequence and the corresponding number of conducting diodes in 36^0 (electrical degrees). Mode 1 occurs when the commutation angle is between 0^0 and 36^0 and the dc output current is less than 0.07 of the short circuit current, I_{dsh}, calculated using (2.6).

$$I_{dsh} = 1.618\frac{E}{2\pi f L_c} \tag{2.6}$$

where f and L_c are source frequency and supply inductance (phase) respectively.

If the dc current is increased, other modes are entered. The results show that the 5-phase rectifier has higher average output voltage, 13.1% higher, compared to the 3-phase system, with the same back-emf amplitude and commutating inductance when the source is an ideal voltage source and the load is light. The short circuit current in the 5-phase rectifier is approximately 61.8% higher than the 3-phase. In the case where the source is a synchronous machine the system regulation depends on the phase self- and mutual-inductance of generator. The result shows that the output voltage of the 5-phase synchronous system is lower than 3-phase system during operating modes 3 to 7.

Table 2.2. Operating modes of 5-phase rectifier system.

Operation mode	Number. of diodes conducting
1	2-3
2	3
3	3-4
4	3-4-5-4
5	4-5
6	5
7	5-6

L.A. Pereira and V. M. Canalli [2.35] have presented the design and determined the main parameters of a five-phase permanent-magnet machine operating as a generator using a rectifier bridge, and feeding a resistive load. Self and mutual inductance were calculated from the flux the stator field produced with one phase acting alone. The mutual inductance has two values, one between adjacent phases, whose values is 0.15 of the self inductance, and between non-adjacent phases, which is 0.46 of the self inductance. The main parameters were determined from static finite-element method solution. At full-load ac current the output dc voltage decreases to approximately 80% of the no-load voltage. The calculated output dc voltage ripple is 20%. The work does not consider the behaviour of the machine under failure conditions.

H. W. Lee *et al.* [2.36] presented a new technique to maximize the power density and minimize the size and weight of a multi-phase BLDC generator. The technique is based on controlling each current and induced EMF harmonics. A simple algebraic method is used to remove zero-sequence components from induced the EMF. A five-phase and a three-phase machine were selected as examples of multi-phase BLDC generators. The results show an increase of 43% in power output power using the new control method which can reduce the weight and the volume by the same percentage.

2.4 Summary

A review of diode-based rectifier circuits has been provided. A brief literature review of permanent magnet machine research, including machine design and operation, has been presented. A five-phase permanent magnet machine used as a generator is a new area and there are few publications. Most existing literature addresses three-phase systems. This thesis reports research on five-phase permanent magnet generators feeding diode rectifiers. This type of system can potentially offer low ripple torque and lower rms ac generator current and smoother output dc voltage (or lower dc link capacitance requirements).

The main objective of this work is to study the performance of a five-phase permanent magnet generator feeding a diode bridge rectifier and to compare with the conventional three-phase system. The output dc power and voltage for the two systems are designed to be the same.

The scientific contribution of the research reported in the thesis can be summarized as follows:

- A general model for the five-phase permanent magnet with diode rectifier including the effects of resistance and self- and mutual-inductances is presented.
- Design of a five-phase permanent magnet generator with fractional pitch winding arrangement is described.
- A comparison is made between the performance of five- and three-phase permanent magnet generators feeding diode rectifiers with the same dc output power and volume.
- The performance of five-phase permanent magnet generators systems under open circuit failure (one phase out and two phases out) is researched.
- The rms current in the dc link capacitor of the five- and three-phase systems under normal and open-circuit failure modes is assessed.

References

[2.1] M. H. Rashed, "Power electronics -devices, derives, and application," Prentice – Hall international, Inc. USA 1993.

[2.2] M. Sakui, and M. Shiya, "A Method for calculating harmonic currents of a three-phase-bridge uncontrolled rectifier with dc filter," IEEE Trans. on Industrial Electronics, Vol. 36, No. 3, August 1989, pp. 434-439.

[2.3] M. Sakui, and H. Fujita, "Calculation of harmonic currents in a three-phase converter with unbalance power supply conditions," IEEE Proceeding-B, Vol. 139, No. 5, Sep.1992., pp. 478-484.

[2.4] M. Sakui, and H. Fujita, "An analytical method for calculating harmonic currents of a three-phase diode-bridge rectifier with dc filter," IEEE Trans. on Power Electronics, Vol. 9, No. 6, November 1994, pp. 631-637.

[2.5] W. B. Lawrance, and W. Miedyslaw, "Harmonic currents reduction in a three-phase diode bridge rectifier," IEEE Trans. on Industrial Electronics, Vol. 39, No. 6, August 1989, pp. 571-576.

[2.6] S. Choi, B. Lee, and N. E Prasad, "New 24-pulse diode rectifier system for utility interface of high-power Ac motor drive," IEEE Trans. on Industrial Application, Vol. 33, No.2, March/April 1997, pp. 531-539.

[2.7] M. G. Mcardle, and D. J. Morrow, "Noninvasive detection of brushless exciter rotation diode failure," IEEE Tran. on Energy Conversion, Vol. 19, No. 2, June 2004, pp. 362-368.

[2.8] J. F. Gieras, and M. Wing, "Permanent Magnet Motor Technology: Design and Applications," Second Edition, CRC press, 2002

[2.9] P. Pillay and R. Krishana, "Application characteristics of permanent magnet synchronous and brushless dc motor for servo drives," IEEE Trans. on Industry Application, Vol. 27, No. 5, Sep./Oct. 1991, pp. 986-996.

[2.10] E. S. Hamdi, 'Design of small electrical machines', John Wiley and Sons, November 1994.

[2.11] W. H. Yeadon and Alan W. Yeadon, "Hand book of small electrical motors," McGraw-Hill, 2001.

[2.12] J. R. Hendershot and T. J. E. Miller, "Design of brushless permanent magnet motors," Magna Physics Pub., 1994.

[2.13] Z. Q. Zhu and D. Howe, "Instantaneous magnetic field distribution brushless permanent magnet dc motors, Parts I: open-circuit field," IEEE Trans. Magn., Vol.129, No.1, Jan.1993, pp. 124-135.

[2.14] Z. Q. Zhu and D. Howe, "Instantaneous magnetic field distribution brushless permanent magnet dc motors, Parts II: armature-reaction field," IEEE Trans. Magn. , Vol.129, No. 1, Jan.1993, pp. 136-142.

[2.15] Z. Q. Zhu and D. Howe, "Instantaneous magnetic field distribution brushless permanent magnet dc motors, Parts III: Effect of stator slotting," IEEE Trans. Magn., Vol.129, No.1, Jan.1993, pp. 143-151.

[2.16] Z. Q. Zhu, and D. Howe, "Instantaneous magnetic field distribution brushless permanent magnet dc motors, Parts I: magnetic field on load," IEEE Trans. Magn., Vol.129, No.1, Jan.1993, pp. 152-158.

[2.17] Z. Q .Zhu, G.W .Jewell, and D.Howe, "Finite element analysis in the design of permanent magnet machines," IEE Seminar on 14 Jan. 2000, pp. 1/1 -1/7.

[2.18] M. A. Alhamadi, and N. A. Demerdash , "Modeling of effects of skewing of rotor mounted permanent magnets on the performance of brushless DC motors," IEEE Trans. on Energy Conversion, Vol. 6, No. 4, Dec. 1991, pp. 721-729.

[2.19] J. Chen, V. N .Chemmangot, and X. Longya, "design of finite -element analysis of an outer- rotor permanent magnet generator for directly coupled wind turbines," IEEE Trans. on Magnetics, Vol. 36, No.5, Sep. 2000, pp. 3802-3809.

[2.20] M. Comanescu, A. Keyhani, and M. Dai, "Design and analysis of 42-V permanent-magnet generator for automotive applications," IEEE Trans. on Energy Conversion, Vol. 18, No. 1, March 2003, pp. 107-112.

[2.21] C. Zwyssig, J. W. Kolar , W. Thaler, and M. Vohrer, "Design of a 100 W, 500000 rpm permanent-magnet generator for mesoscale gas turbines," Industry Applications Conference, 40th, IAS Annual Meeting, Vol. 1, 2-6 Oct. 2005, pp. 253-260.

[2.22] H. Jussila, P. Salminen, M. Niemela, and J. Pyrhonen, "Guidelines for designing concentrated winding fractional slot permanent magnet machines," Powereng 2007, April 12-14, 2007, Setubal, Portugal, pp. 191-194.

[2.23] T. Li, and G. Slemon, "Reduction of cogging in permanent magnet motors," IEEE Trans. on Magnetics, Vol. 24, No. 6, November 1988, pp. 2901-2903.

[2.24] Z. Q. Zhu, and D. Howe, "Influence of design parameters on cogging torque in permanent magnet machines," IEEE Trans. on Energy Conversion, Vol. 15, No. 4, Decemper.2000, pp. 407-412.

[2.25] Z. Q. Zhu, S. Ruangsinchaiwanich, N. Schofield, and D. Howe, "Reduction of cogging in interior-magnet brush less machines," IEEE Trans. Magn, Vol. 39, No. 5, Sep.2003, pp. 3238-3240.

[2.26] P. Pillay, and R. Krishana, "Modelling, simulation, and analysis of permanent magnet motor drives, part II: The brushless DC motor derive," IEEE Trans. on Industry Application, Vol. 25, No. 2, March/April 1989, pp. 274-279.

[2.27] C. C. Chan, J. Z. Jiang, G. H. Chen, X. Y. Wang, and K. T. Chau, "A novel Poly multiple square-wave permanent magnet motor drive for electric vehicles," IEEE Trans. on Industry Application, Vol. 30, No.5, Sep./Oct.1991, pp.274-279.

[2.28] M. G. Simoes, N. N. Franceschetti, and P. Vieira jr. "Design and evaluation of poly-phase brushless Dc-machine direct drive system," IEEE Industry Applications Conference, Vol. 2, 30 Sept.-4 Oct. 2001, pp. 835-842.

[2.29] A. A. Arkadan, R. Vyas, J.G Vaidya, and M.J Shah., "Effect of toothless stator design and core and stator conductors eddy current losses in permanent magnet generators," IEEE Trans. on Energy Conversion, Vol. 7, Issue 1 , March 1992, pp. 231-237.

[2.30] A. A. Arkadan, T.M. Hijazi, and N.A. Demerdash, "Computer-aided modeling of a rectified DC load-permanent magnet generator system with multiple damper windings in the natural abc frame of reference," IEEE Trans. on Energy Conversion, Vol. 4, No.3, Sept. 1989, pp. 518-525.

[2.31] R. Karishan, and G. H. Rtm, "Modeling ,Simulation, and Analysis of variable-speed constant frequency power conversion scheme with a permanent magnet brushless dc generator," IEEE Trans. on Industry Application, Vol.37 , No.4, August 1990, pp. 291-296.

[2.32] B. Sarlioglu, and T. A. Lipo, "Assessment of power generation capability of doubly-salient PM generator," IEEE Electric Machines and Drives, International Conference IEMD '99, 9-12 May 1999, pp. 549-552.

[2.33] L. Parsa, and H. A. Toliyat, "Five Phase permanent motor Drives," IEEE Trans. on Industry Application, Vol. 41, No. 1, Jan./Feb. 2005. pp. 30-37.

[2.34] B. Zhang, and S. D. Pekarek, "Analysis and average value model of a source commutated 5-phase rectifier," IEEE Power electronic Specialists conference, 35th Annual, Aachen, Germany, 2004, pp. 362-368.

[2.35] L. A .Pereira, and V.M .Canalli, "Five-phase permanent magnet synchronous machine operating as generator design, parameter determination by FEM and performance," Industry Applications Conference, 37th IAS Annual Meeting. Vol. 1, 13-18 Oct. 2002, pp. 398-405.

[2.36] H.-W. Lee, T.-H. Kim, and M. Ehsani, "Maximum power throughput in multiphase brushless Dc generator," IEE Proc. Elect. Power Appl, Vol. 152, No. 3, May 2005, pp. 501-508.

Chapter 3

Analysis and modelling of five-phase system

3.1 Introduction

The three-phase full-wave diode bridge rectifier is extensively used due to its advantages compared to the single-phase rectifier. These advantages include lower line harmonics and lower dc output voltage ripple. On the other hand, higher phase number full-wave diode bridge rectifiers are sometimes used for example, five-phase, six-phase and nine-phase variants. The six-phase rectifier uses a transformer with two secondary windings phase displaced by 30^0 from each other and is often used in high voltage and high power applications [3.1]. The five-phase full-wave diode bridge rectifier is attracting research; it represents a middle ground between the three-phase and six-phase versions. The advantages of the five-phase diode bridge rectifier when compared with three-phase are lower output ripple and rms phase current [3.2]. The cost of diodes may be higher (as there are 10 compared to 6) but the dc link capacitor requirement is lower leading to a potentially cheaper and more compact system.

In this chapter the modelling of three and five-phase diode rectifier system is described. Simulation models of three- and five-phase systems are developed and include mutual inductances of the permanent magnet generator. Mutual inductance has not previously been considered in rectifier analysis but is shown here to have important consequences on the operation and performance of three- and five-phase systems. This is one contribution of this research. In the five-phase system both adjacent and non-adjacent mutual inductance is modelled.

The three-phase diode rectifier connected to an ac supply is discussed in section 3.2. Operation is considered with an ideal source model and with a source model that includes the inductances of the generator. The operation of a five-phase diode rectifier is presented in section 3.3 with an ideal ac source model and with a source model that includes the inductances of the generator. The effect of inductance on the dc output voltage and generator phase currents are considered assuming a constant load current with no dc link capacitor.

Dedicated simulation models for five- and three-phase systems are developed in section 3.4. The models help demonstrate, by analysis, the impact of self- and mutual-inductance on the performance of the systems. The models therefore include the self- and mutual inductance of the generators. In section 3.5 the developed models are validated using PSpice and also with practical data in chapter 5.

The performance of the generator is presented in section 3.6 with and without the self- and mutual-inductance. This demonstrates the impact of modelling mutual inductance during rectifier commutation.

3.2 Analysis of the three-phase diode bridge rectifier

The analysis of the three-phase rectifier is performed for two cases. In the first case the resistance and inductance of the generator are neglected (the ideal case), Section 3.2.1. In the second case the inductance of the generator are taken into account, Section 3.2.2.

3.2.1 The ideal case

Reported research analyses the three-phase system under ideal conditions, for example [3.3]-[3.5], as the rectifier is supplied by a transformer which has low phase inductance. This is not the case when a diode rectifier is coupled to a generator system that has significant phase inductance, for example, a small-scale wind generator. In the ideal case there are three assumptions made:

1. The source is a balanced sine wave,
2. diode losses are neglected, and
3. the dc load is replaced by a constant dc current sink.

The supply phase voltages are assumed as

$$\begin{aligned} E_a &= V_m \sin(\omega t) \\ E_b &= V_m \sin(\omega t - \frac{2\pi}{3}) \\ E_c &= V_m \sin(\omega t - \frac{4\pi}{3}) \end{aligned} \tag{3.1}$$

where V_m is the amplitude of the phase voltage and represents the phase back emf.

In diode bridge rectifier circuits, the two phases displaying the largest line-to-line voltage conduct [3.1]. The line voltages are

$$\begin{aligned} E_{ab} &= E_a - E_c = \sqrt{3}V_m \sin(\omega t + \frac{\pi}{6}) \\ E_{bc} &= E_b - E_a = \sqrt{3}V_m \sin(\omega t - \frac{\pi}{2}) \\ E_{ca} &= E_c - E_b = \sqrt{3}V_m \sin(\omega t - \frac{7\pi}{6}) \end{aligned} \tag{3.2}$$

Figure 3.1 shows the line voltages which have a peak value of $\sqrt{3}\ V_m$.

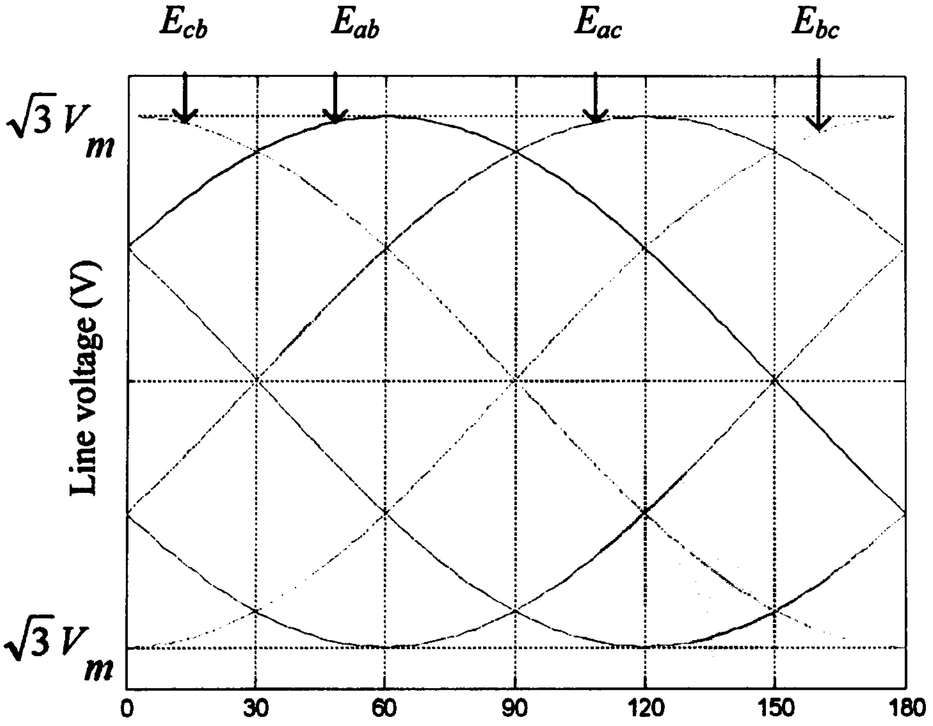

Figure 3.1. Line voltage waveforms for a three-phase system over 180° (electrical).

After full-wave rectification by the diode rectifier, the output voltage has a fundamental frequency component equal to six times the input frequency. Figure 3.2 shows the output voltage waveform.

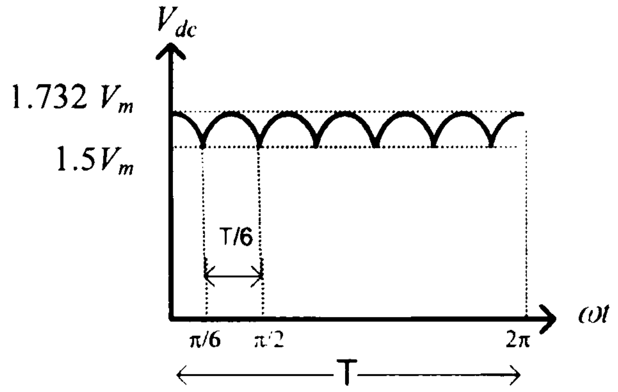

Figure 3.2. The output voltage of the three-phase full-bridge rectifier.

The average dc output voltage V_{dc} for three-phase system is calculated using one π/3 period as shown in figure 3.3.

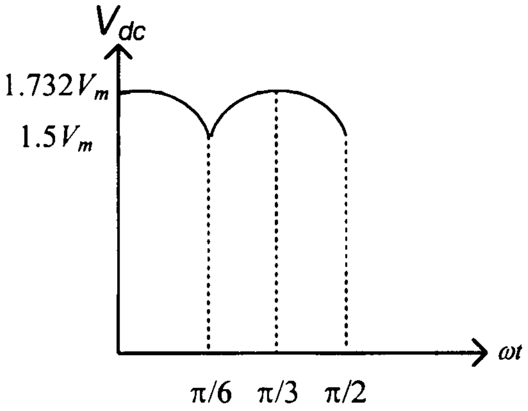

Figure 3.3. Output dc voltage showing the period between π/6 and π/2.

Using the period between 30° (π/6 rad) and 90° (π/2 rad) the average value of the output dc voltage is [3.2].

$$V_{dc} = \frac{3}{\pi}\int_{\pi/6}^{\pi/2} \sqrt{3}V_m \cos\omega t\, d\omega t = 1.654V_m \tag{3.3}$$

During the period between 30° and 90°, the output voltage from the rectifier is E_{ac}. Hence, the output voltage at $\omega t = \pi/6$ is

$$E_{ac} = 1.732V_m \sin\left(\frac{\pi}{3}\right) = 1.5V_m \tag{3.4}$$

and at $\omega t = \pi/3$ (the maximum line voltage)

$$E_{ac} = 1.732V_m \sin\left(\frac{\pi}{2}\right) = 1.732V_m \tag{3.5}$$

From (3.4) and (3.5) the output voltage varies from a minimum of $1.5V_m$ to maximum of $1.732V_m$. The peak-to-peak ripple in this case is

$$V_{dcripple} = 1.732V_m - 1.5V_m = 0.232V_m \tag{3.6}$$

From (3.6) the peak-to-peak ripple is approximately 14% of the average dc output voltage

3.2.2 Analysis including phase inductance

There is an important change in the performance of the diode rectifier when the inductance of each supply phase is included. Due to the inductance of the phases, the current commutation between phases cannot be instantaneous. Therefore, during commutation all three phases conduct at the same time. This period is called the commutation period and has an associated commutation (or overlap) angle, μ.

The commutation angle affects the output voltage of the rectifier and the supply phase currents. Figure 3.4 shows the effect of the overlap angle on the output voltage. The average output voltage is reduced from the ideal case. The average output voltage is reduced by V_{red} [3.2] where

$$V_{red} = 6f\ L\ I_{dc} \tag{3.7}$$

where f, L and I_{dc} are source frequency, phase inductance (includes self- and mutual-inductance) and average output dc current respectively.

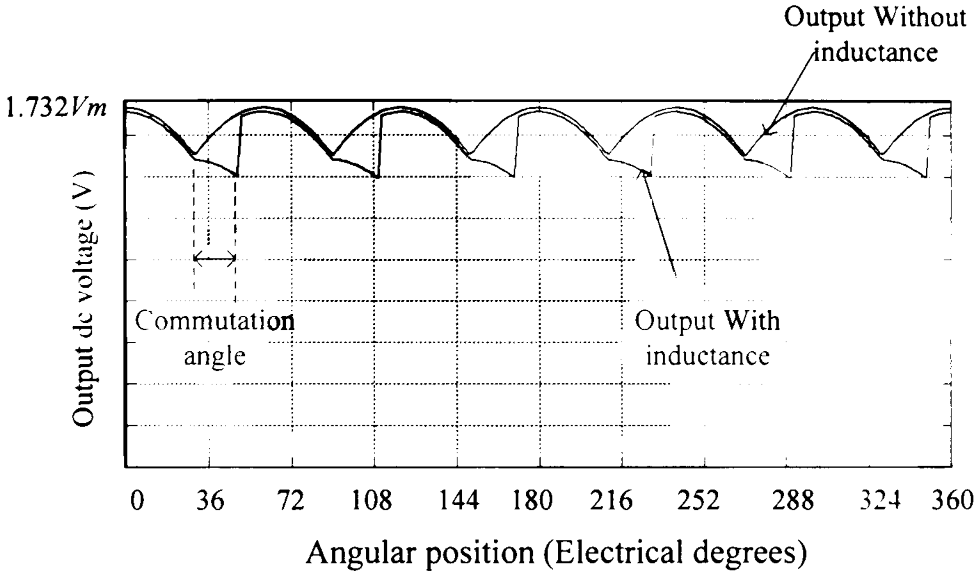

Figure 3.4. Output dc voltage without phase inductance and with phase inductance.

Using (3.3) and (3.7) the average output dc voltage is:

$$V_{dc} = 1.654V_m - 6fL_{ph}I_{dc} \tag{3.8}$$

The inductance affects the rate of rise and fall of the supply phase currents during commutation. Figure 3.5 shows simulation results and identifies the commutation angle, μ.

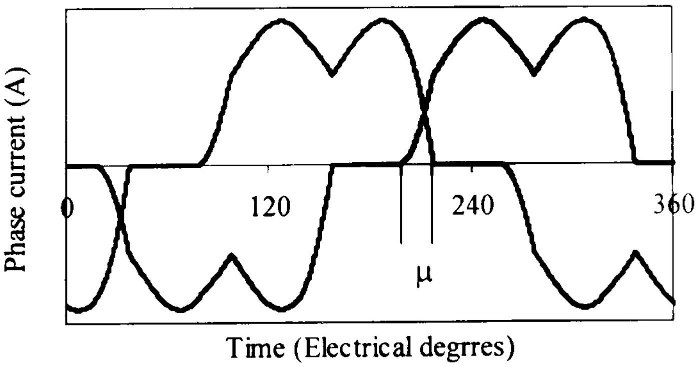

Figure 3.5. Effect of supply phase inductance on the phase current, showing the commutation angle, μ.

The commutation angle is calculated using (3.9) [3.2]. If the supply voltage and inductance are known the commutation angle depends on the load current, I_{dc}.

$$\mu = \cos^{-1}\left(1 - \frac{2\omega L I_{dc}}{V_L}\right) \tag{3.9}$$

where

L = phase inductance (H)

$\omega = 2\pi f$ rotational frequency of supply (electrical rad/s)

V_L = peak line voltage (V)

The inductance, L, in this case includes self- and mutual-inductances for the generator. In the three-phase system the mutual inductance, M, between phases is the same, and has a value equal to 1/3 of the self inductance for a concentrated winding, Section 4.6. Using (3.9) the commutation angle, including self-and mutual inductances, is

$$\mu = \cos^{-1}\left(1 - \frac{2\omega (L-M) I_{dc}}{V_L}\right) \tag{3.10}$$

Figure 3.6 shows the relationship between the commutation angle and output voltage when the commutation angle is less than 60°, and when three diodes conduct simultaneously. The output dc voltage is approximately 75% of the no-load dc voltage when the commutation angle is 60°. If the load current were to be further increased, the commutation angle would exceed 60°. The phase current becomes continuous when the commutation angle reaches 60°. However, this condition is not experienced nor analysed for the system under study.

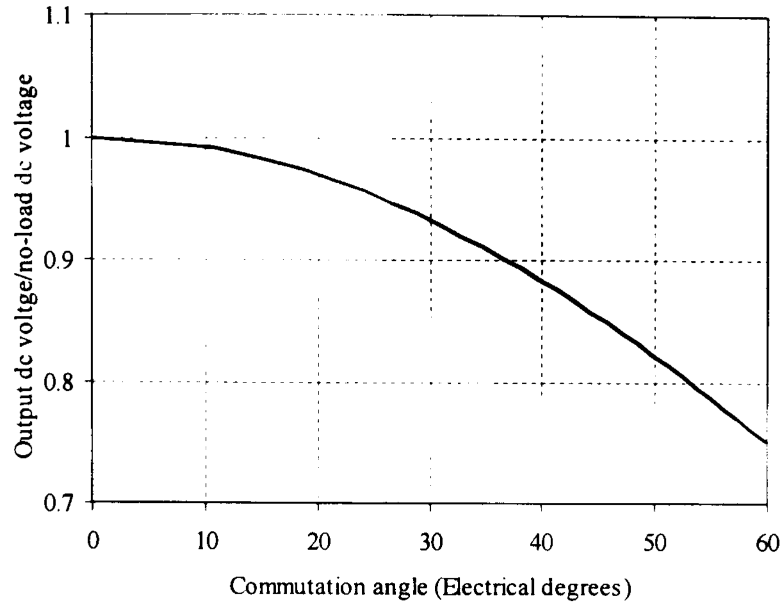

Figure 3.6. Ratio of output dc voltage to no-load dc voltage with respect to commutation angle.

3.3 Analysis of the five-phase diode rectifier

A five-phase diode bridge rectifier circuit is used in this research. The five-phase source generates a set of five phase voltages, each phase shifted by 72^0 with respect to its adjacent phase, and phase shifted by 144^0 from its non-adjacent phases. The phase voltages are

$$\begin{aligned} E_a &= V_m \sin(\omega t) \\ E_b &= V_m \sin(\omega t - \frac{2\pi}{5}) \\ E_c &= V_m \sin(\omega t - \frac{4\pi}{5}) \\ E_d &= V_m \sin(\omega t - \frac{6\pi}{5}) \\ E_e &= V_m \sin(\omega t - \frac{8\pi}{5}) \end{aligned} \tag{3.11}$$

The phasor diagram of the 5-phase system is shown in Figure 3.7.

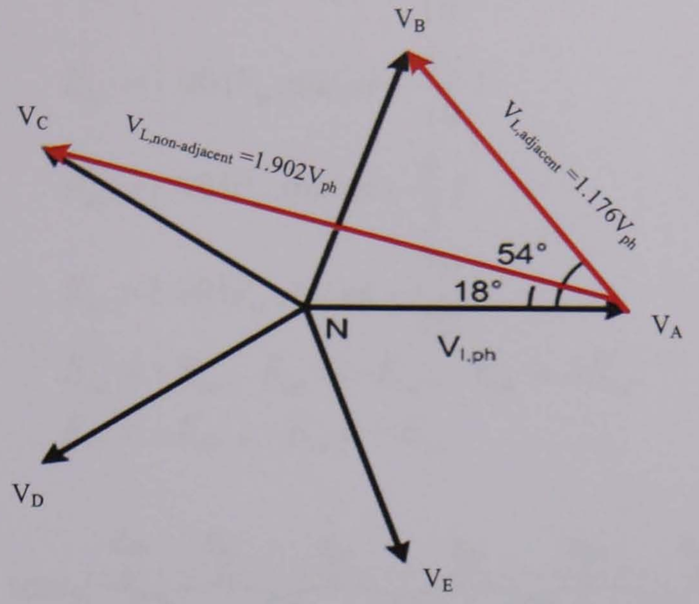

Figure 3.7. Phasor diagram of the five-phase voltages showing the adjacent and non-adjacent line voltages.

In a five-phase system there are two line-to-line voltages. The adjacent line voltage is the voltage between adjacent phases. For example, the voltage between phase-*a* and phase-*b*. The non-adjacent voltage is the line voltage between non-adjacent phases, for example, the voltage between phase-*a* and phase-*c* (V_{ac}). The two voltage magnitudes are

$$\begin{aligned} V_{l,adjacent} &= 2V_{ph}\,cos(54^o) = 1.176 \times V_{ph} \\ V_{l,non-adjacent} &= 2V_{ph}\,cos(18^o) = 1.902 \times V_{ph} \end{aligned} \tag{3.12}$$

and

$$V_{l,non-adjacent} = 1.618 V_{l,adjacent} \tag{3.13}$$

If a five-phase generator feeds a five-phase full-wave bridge rectifier, each diode conducts the load current for 72° in the ideal case. In the diode bridge rectifier the largest magnitude line voltage conducts hence the non-adjacent line voltage provides energy to the dc-side. Figure (3.8) shows the non-adjacent line voltages which are described by

$$
\begin{aligned}
E_{ac} &= 1.901V_m \, sin(\omega t + \frac{\pi}{10}) \\
E_{ad} &= 1.901V_m \, sin(\omega t - \frac{\pi}{10}) \\
E_{bd} &= 1.901V_m \, sin(\omega t - \frac{3\pi}{10}) \\
E_{be} &= 1.901V_m \, sin(\omega t - \frac{\pi}{2}) \\
E_{ce} &= 1.901V_m \, sin(\omega t - \frac{7\pi}{10}) \\
E_{ca} &= -E_{ac}, \quad E_{da} = -E_{ad}, \quad E_{db} = -E_{bd} \\
E_{eb} &= -E_{be}, \quad E_{ec} = -E_{ce}
\end{aligned}
\qquad (3.14)
$$

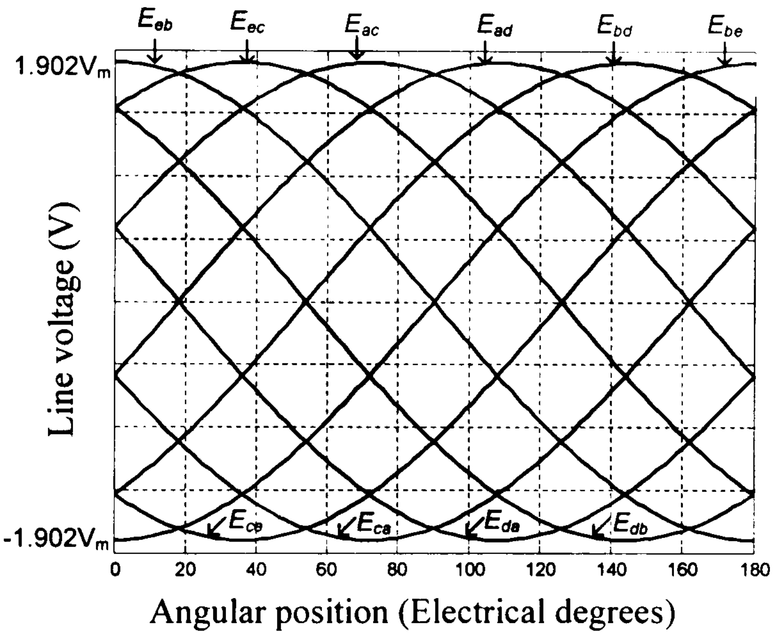

Figure 3.8. Five-phase non-adjacent line voltages for one half cycle.

As with the three-phase case, two analyses for the five-phase diode rectifier are performed: the ideal case and the case with phase inductance.

3.3.1 Ideal five phase rectifier system.

In this case the generator phase inductance is neglected. The same assumptions are made to that in the three-phase case.

The output dc voltage has a fundamental frequency of ten times the input frequency and peak value of $1.902V_m$. Figure (3.9) shows the output voltage.

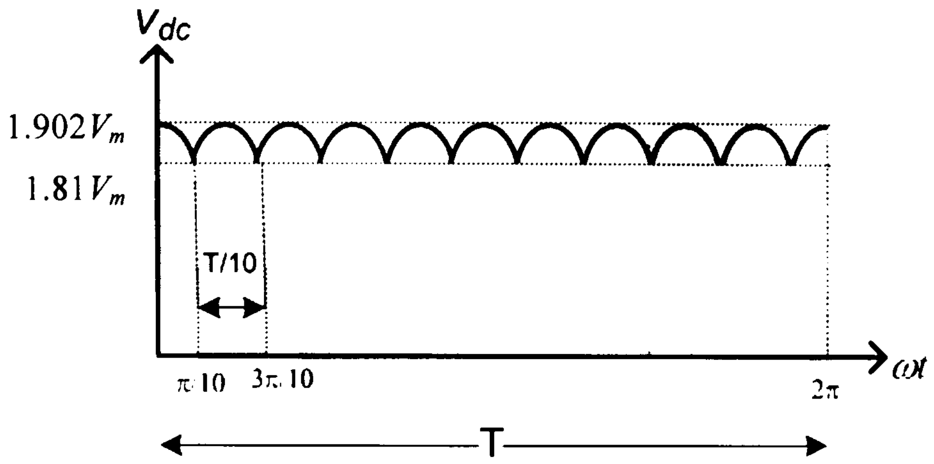

Figure 3.9. Output voltage from the five-phase rectifier

The period between 54° (3π/10 rad) and 72° (2π/5 rad) can be used to calculate the average output voltage and the peak-to-peak ripple, Figure 3.10.

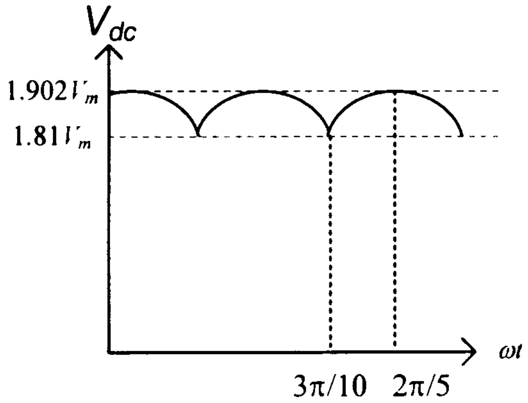

Figure 3.10. Output dc voltage showing the period between 3π/10 and 2π/5.

The average dc output voltage V_{dc} for a five-phase diode rectifier is

$$V_{dc} = \frac{5}{\pi} \int_{\frac{3\pi}{10}}^{\frac{2\pi}{5}} 1.902V_m \cos \omega t \, d\omega t = 1.85V_m \tag{3.15}$$

The minimum output voltage occurs at $\omega t = 54^{\circ}$

$$E_{ac} = 1.902V_m \sin\left(\frac{2\pi}{5}\right) = 1.81V_m \tag{3.16}$$

and maximum value occurs at $\omega t = 72^{\circ}$.

$$E_{ac} = 1.902V_m \sin\left(\frac{\pi}{2}\right) = 1.902V_m \tag{3.17}$$

hence the peak-to-peak ripple is

$$V_{dcripple} = 1.902V_m - 1.81V_m = 0.092V_m \tag{3.18}$$

From (3.16) and (3.18) the peak-to-peak ripple is 5% of the average output voltage. This is significantly better than the three-phase case (14%).

3.3.2 Analysis of the five-phase system including phase inductance

As discussed in section 3.2.1, inductance affects phase current commutation and consequently there is a commutation period between phases. In the five-phase system the commutation angle is typically less than 36° electrical degrees. Otherwise, there are more than three phases conducting at one time and the output dc voltage rapidly falls away.

The commutation angle, when three phases conduct simultaneously, for example, phase-*a*, phase-*e* and phase-*c*, as shown in figure 3.11, is calculated. Phase-*e* is commutating off and phase-*a* is turning on.

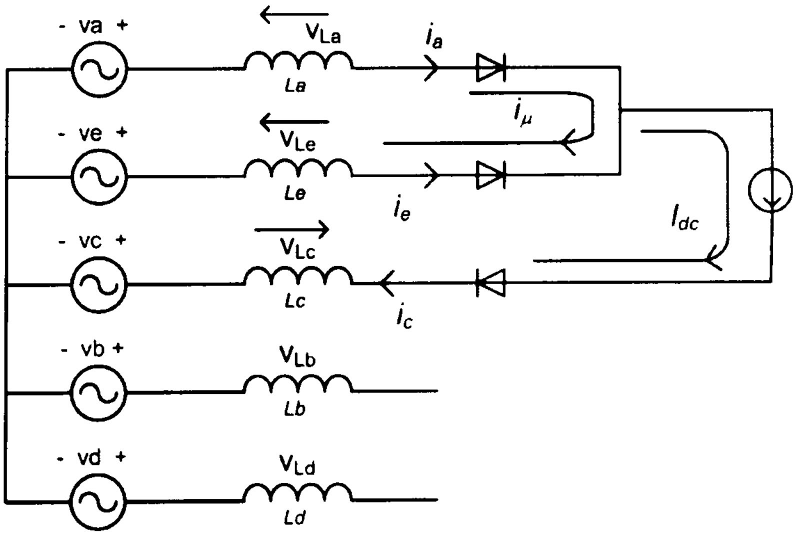

Figure 3.11. Shows the current direction during the commutation period, when phase-*a*, phase-*e* and phase-*c* conduct simultaneously

The commutation current i_μ, due to the short-circuit between phase-a and phase-e, is equal to phase-a current, i_a. This current builds up from zero to a final value equal to the dc output current, I_{dc}, at the end of commutation period, $\omega t = \mu$. In the circuit of figure 3.11,

$$v_{La} = L_a \frac{di_a}{dt} = L_a \frac{di_\mu}{dt} \tag{3.19}$$

and

$$v_{Le} = L_e \frac{di_e}{dt} = -L_e \frac{di_\mu}{dt} \tag{3.20}$$

The i_μ mesh equation is

$$v_a - v_e = L_a \frac{di_\mu}{dt} - (-L_e \frac{di_\mu}{dt}) \tag{3.21}$$

As all phase inductances are assumed equal, $L_a=L_e=L$, and $v_a - v_e$ is the line voltage, v_{ae}, (3.21) becomes

$$v_{ae} = 2L \frac{di_\mu}{dt} \tag{3.22}$$

multiplying both sides of (3.22) by ω, which equals $2\pi f$, and integrating gives

$$\frac{1}{2}\int_0^{\mu} v_{ae} d\omega t = \omega L \int_0^{I_{dc}} di_u \tag{3.23}$$

The line voltage in this case is the non-adjacent line voltage, $v_{L,non\text{-}adjacent}$, (3.12), substituting in (3.23) gives

$$\frac{v_{l,non-adjacent}(1 - cos\,\mu)}{2} = \omega L i_{dc} \tag{3.24}$$

From (3.24) the commutation angle in the five-phase rectifier is

$$\mu = cos^{-1}\left(1 - \frac{2\omega L i_{dc}}{V_L}\right) \tag{3.25}$$

where V_L = non-adjacent line voltage peak value (V)

The inductance, L, in this case includes self- and mutual-inductances. In the five-phase system there are two mutual inductances, Section 4.6. Using self- and both mutual-inductances the commutation angle become

$$\mu = cos^{-1}\left(1 - \frac{2\omega(L - M_1 + M_2)i_{dc}}{V_L}\right) \tag{3.26}$$

where M_1 and M_2 are mutual inductance between adjacent and non-adjacent phases respectively.

M_1 equal 1/5 of the self inductance, L, and has negative value, and M_2 equal 3/5 of L with a positive value, Section 4.6.

The effect of commutation angle is to reduce the average dc output voltage. Figure 3.12 shows the output voltages with and without inductance. The average output voltage with inductance is reduced by the area ($A\mu$) which represents the voltage drop across the inductance during commutation.

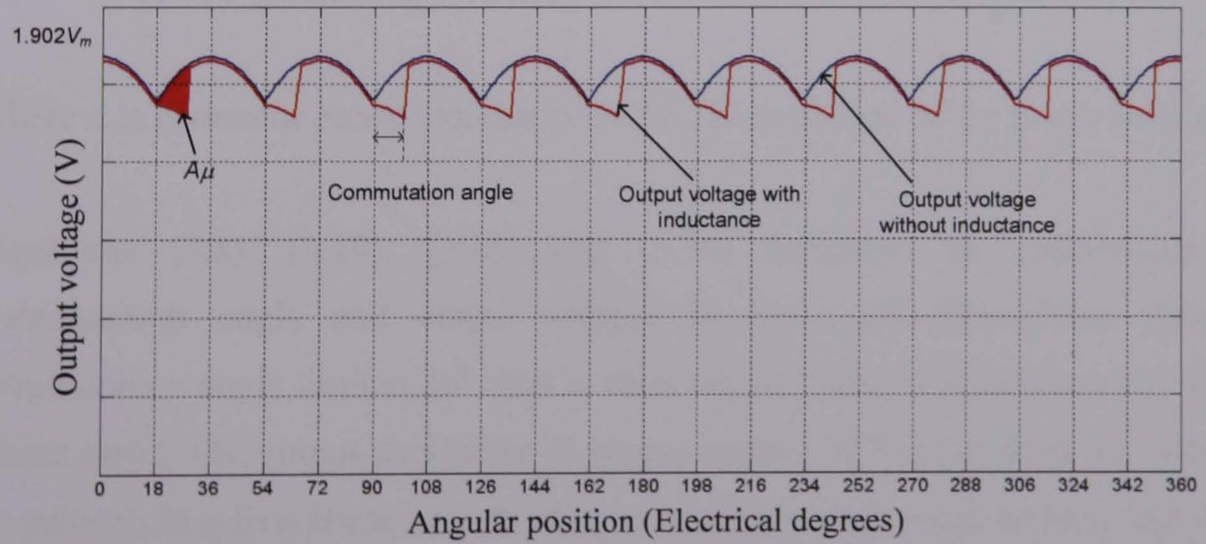

Figure 3.12. Output dc voltage with and without phase inductance.

The voltage across the inductance, L, due to the commutation current, i_μ, is

$$V_L = L\frac{di_\mu}{dt} \tag{3.27}$$

The integral of this voltage is the area A_μ in figure 3.12, which is

$$A_\mu = \omega L i_d \tag{3.28}$$

This area is repeated every ten times in one complete period. Using (3.28) the average voltage reduction due to the commutation angle, V_{red}, is

$$V_{red} = \frac{10\times(2\pi f)}{2\pi} L i_{dc} = 10 f L i_{dc} \tag{3.29}$$

where f is source frequency.

Comparing (3.7) with (3.29), the dc output voltage in the five-phase system falls faster as the load current increases compared with the three phase case, assuming all other parameters are the same.

Using (3.14) and (3.29) the average output dc voltage from the 5-phase system is

$$V_{dc} = 1.854 V_m - 10 f L\, i_{dc} \tag{3.30}$$

where L is generator phase inductance and V_m is amplitude of the phase voltage.

Equations (3.8), (3.10), (3.26) and (3.30) represent the relationship between commutation angle and output voltage in five- and three-phase systems. The commutation angle limit is 36° (that is three diodes conduct simultaneously in the five-phase case). The output dc voltage is approximately 91% of no-load dc voltage at 36°. In general, in a five-phase system, the commutation angle must be kept less than 36° to avoid rapid reduction in the dc output voltage.

In the practical system, with the same output dc voltage for five- and three-phase systems at full load, the generator self- and mutual-inductances are different in both generators (section 4.7) and the peak phase voltage is higher in the three-phase system (54V) compared to the five-phase system (48V). Figure (3.13) shows the change of dc output voltage with output dc load power. The two systems have the same output dc voltage at full load (610W). It is clear from figure 3.13 that increasing the load increases the voltage reduction in the five-phase system faster than the three-phase system. It can be seen that there is a period in which the five-phase output voltage is lower than the three-phase system. This due to the output dc voltage reduction which depends on the self- and mutual-inductance and the output load current as discussed previously.

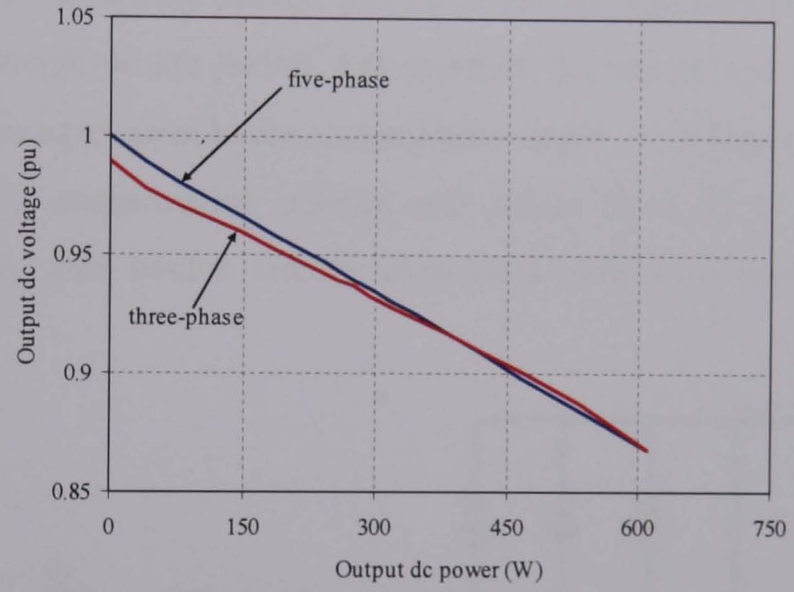

Figure 3.13. Voltage regulation vs. Power, showing the comparison between five- and three-phase system with the same output dc voltage

3.4 Simulation model

In this section, equations that represent the diode bridge rectifier and permanent magnet generator are developed using a pulse function description. The permanent magnet generator model includes phase resistance, inductance and mutual inductance. The simulation models of both three- and five-phase generators are developed. The models are easily programmed using Matlab/Simulink. This model demonstrates the effect of generator parameters during commutation and the conduction period and helps observe the effect of each generator parameter on the performance of the systems.

3.4.1 Simulation model of the three-phase PM generator with diode rectifier

In order to determine the equations representing a three-phase permanent magnet generator with diode bridge rectifier, figure 3.14 is used which shows the back EMF and generator parameters (resistance, inductance and mutual inductance) and the rectifier. Dc link capacitor, *C*, and resistive load, R_L. The mutual inductance between the phases, M_l, is equal to 1/3 of the self inductance, Section 4.6. In this thesis there are two cases examined: two diodes conducting simultaneously and three diodes conducting simultaneously. Figure 3.15 shows phase voltage for one cycle which can be divided into twelve periods: six periods when only two diodes conduct and six periods where three diodes conduct. The periods where two diodes conduct are termed the conduction periods and the periods when three diodes conduct are called commutation periods, μ. The periods are represented by pulses. The pulse has per-unit amplitude for each period and duration dependent on the period. For example, for the period of commutation the pulse has a duration equivalent to the commutation angle, μ. In figure 3.15 the pulses S1 to S6 represent the commutation periods and pulses from S7 to S12 represent the conduction periods. The twelve circuits associated with each period are detailed in Appendix A.

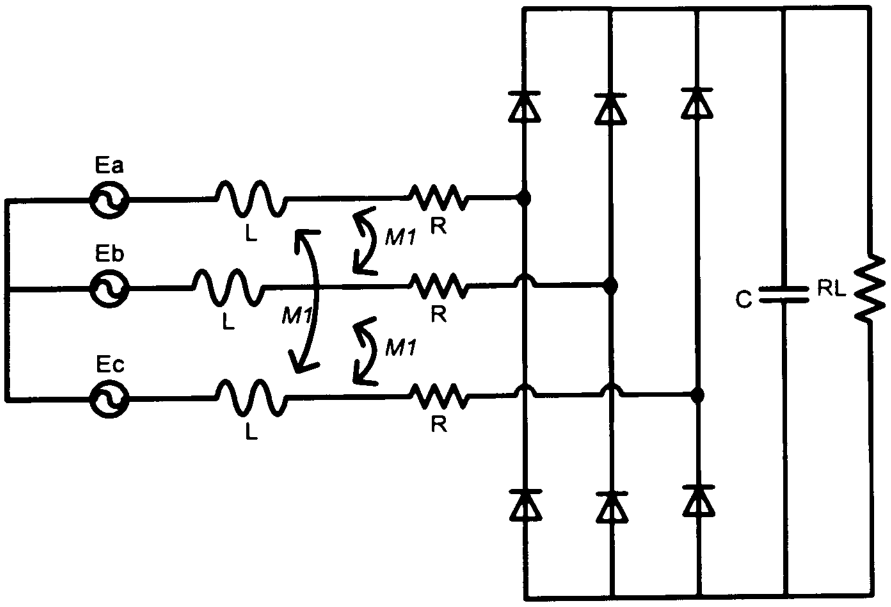

Figure 3.14. Three-phase diode bridge rectifier with permanent magnet generator showing the PM generator back emf and the generator resistance and inductance.

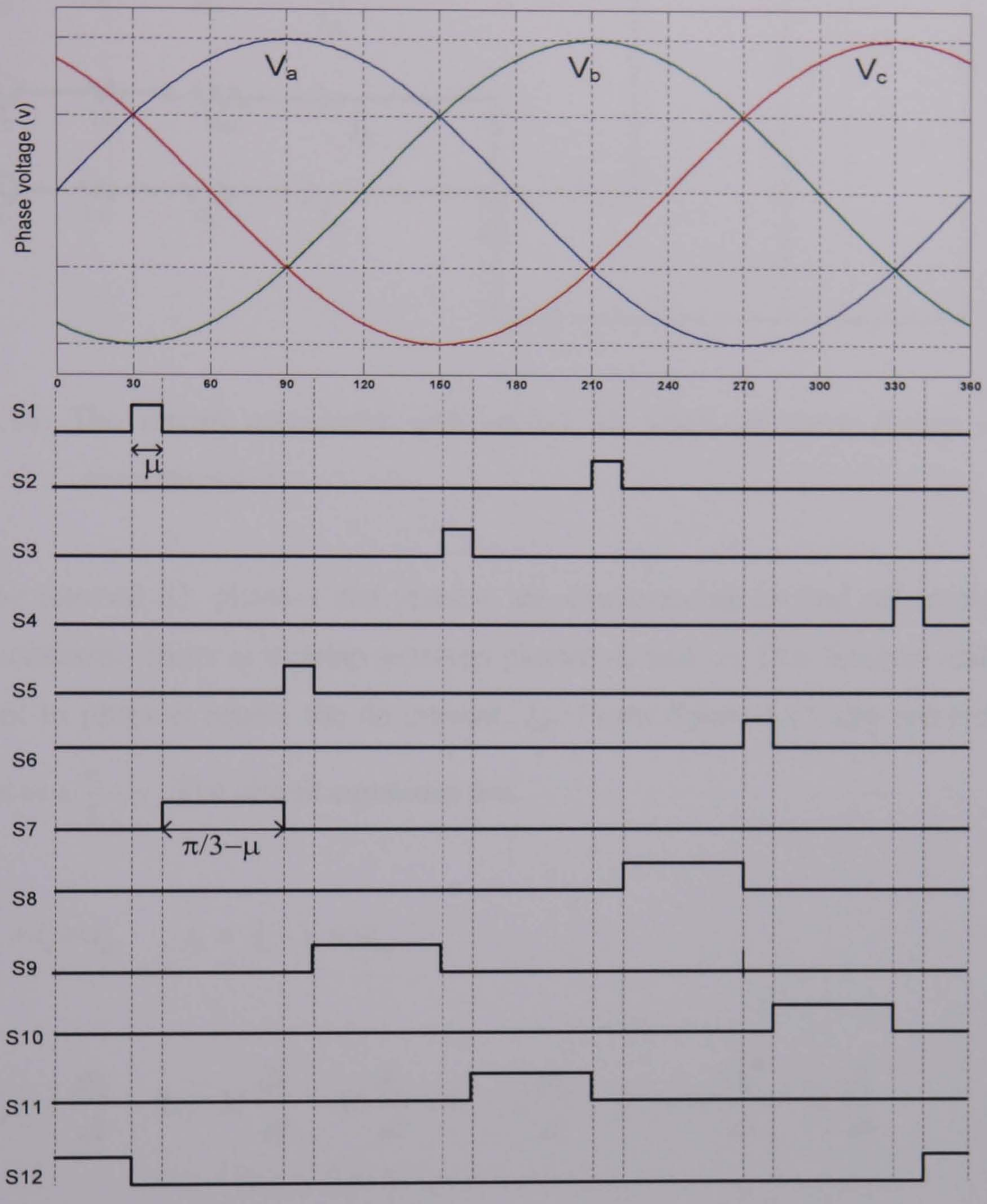

Figure 3.15. Phase back emf voltages of the three-phase generator and the twelve pulses used to define each conduction and commutation period.

Differential equations are developed for each interval shown in figure 3.15. Two examples of how the equations are derived are described here for two intervals. One interval represents a commutation period (interval S1) and the other interval represents conduction period (interval S7).

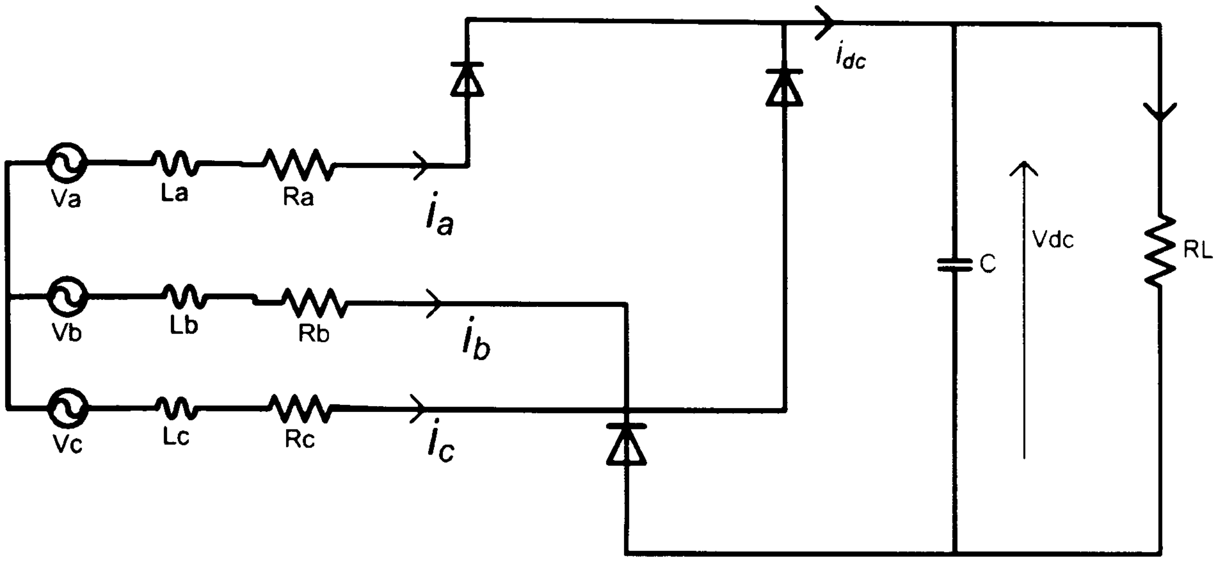

Figure 3.16. The circuit associated with period S1 when all three phases conduct simultaneously .

During the interval S1, phase-*a* and phase-*c* are commutating on and off respectively. Phase-*b* conducts. There is overlap between phases -*a* and -*c*. This interval ends when the current in phase-*a* equals the dc current, I_{dc}. From figure 3.15 this interval has a period $\frac{\pi}{6} \leq wt \leq \frac{\pi}{6} + \mu$. The circuit equations are:

$$i_a + i_c = i_{dc} \quad ; \; i_b = -i_c - i_a = -i_{dc} \tag{3.31}$$

$$V_a - L\frac{di_a}{dt} - Ri_a - M\frac{di_c}{dt} - M\frac{di_b}{dt} = V_c - L\frac{di_c}{dt} - Ri_c - M\frac{di_a}{dt} - M\frac{di_b}{dt} \tag{3.32}$$

$$V_c - L\frac{di_c}{dt} - Ri_c - M\frac{di_a}{dt} - M\frac{di_b}{dt} - V_{dc} = V_b - L\frac{di_b}{dt} - Ri_b - M\frac{di_a}{dt} - M\frac{di_c}{dt} \tag{3.33}$$

by manipulation of (3.31), (3.32) and (3.33) the differential equation representing i_a during S1 is

$$\frac{di_a}{dt} = \frac{\left(2V_a - Vc - V_b - 3Ri_a - V_{dc}\right)}{3(L - M)} \tag{3.34}$$

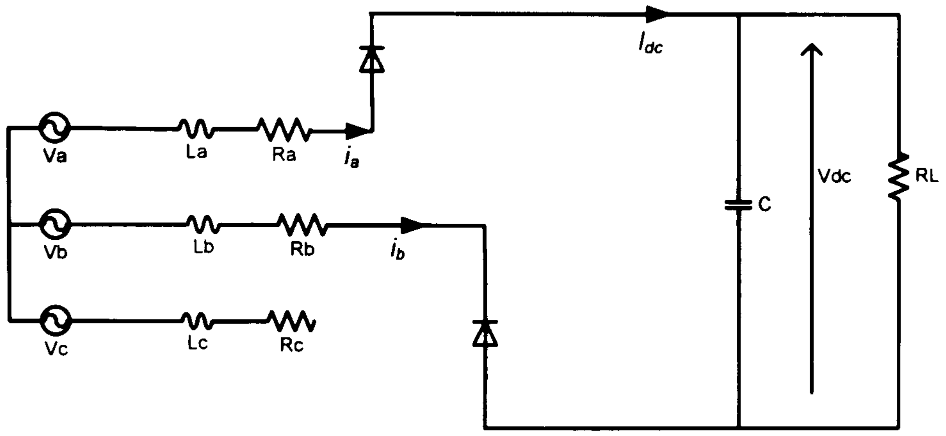

Figure 3.17. The circuit associated with period S7 when phases *a* and *b* conduct

During interval S7, the current in phase-*c* is zero, and two phases conduct, phase-*a* and-*b*. This interval is defined by $\frac{\pi}{6} + \mu \le wt \le \frac{\pi}{2}$. From figure 3.17 the circuit equations for this interval are

$$i_a = -i_b = i_{dc} \quad ; \; i_c = 0 \tag{3.35}$$

$$V_a - L\frac{di_a}{dt} - Ri_a - M\frac{di_b}{dt} - V_{dc} = V_b - L\frac{di_b}{dt} - Ri_b - M\frac{di_a}{dt} \tag{3.36}$$

$$V_a - V_b - 2(L-M)\frac{di_a}{dt} - 2Ri_a - V_{dc} = 0 \tag{3.37}$$

by manipulation of (3.35), (3.36) and (3.37) the differential equation representing i_a during S7 is

$$\frac{di_a}{dt} = \frac{(V_a - V_b - 2Ri_a - V_{dc})}{2(L-M)} \tag{3.38}$$

Other intervals are calculated using a similar procedure and are derived in Appendix A. Tables 3.1 to 3.3 summarise the intervals and associated differential equations for phase-*a*, phase-*b* and phase-*c* respectively for each period, S1-S12.

Table 3.1. Differential equations for phase-*a* current

Interval (S)	$(L-M)\frac{di_a}{dt}=$
S1 and S3	$\frac{(2v_a - v_c - v_b - 3Ri_a - V_{dc})}{3}$
S2 and S4	$\frac{(2v_a - v_c - v_b - 3Ri_a + V_{dc})}{3}$
S5	$\frac{(2v_a - v_c - v_b - 3Ri_a - 2V_{dc})}{3}$
S6	$\frac{(2v_a - v_c - v_b - 3Ri_a + 2V_{dc})}{3}$
S7	$\frac{(v_a - v_b - 2Ri_a - V_{dc})}{2}$
S9	$\frac{(v_a - v_c - 2Ri_a - V_{dc})}{2}$
S8	$\frac{(v_a - v_b - 2Ri_a + V_{dc})}{2}$
S10	$\frac{(v_a - v_c - 2Ri_a + V_{dc})}{2}$
S11 and S12	0

Table 3.2. Differential equations for phase-*b* current

Interval (S)	$(L-M)\dfrac{di_b}{dt}=$
S3 and S6	$\dfrac{(2v_b-v_a-v_c-3Ri_b-V_{dc})}{3}$
S4 and S5	$\dfrac{(2v_b-v_a-v_c-3Ri_b+V_{dc})}{3}$
S2	$\dfrac{(2v_b-v_a-v_c-3Ri_b-2V_{dc})}{3}$
S1	$\dfrac{(2v_b-v_a-v_c-3Ri_b+2V_{dc})}{3}$
S7	$\dfrac{(v_b-v_a-2Ri_b+V_{dc})}{2}$
S8	$\dfrac{(v_b-v_a-2Ri_b-V_{dc})}{2}$
S11	$\dfrac{(v_b-v_c-2Ri_b-V_{dc})}{2}$
S12	$\dfrac{(v_b-v_c-2Ri_b+V_{dc})}{2}$
S9	0
S10	0

Table 3.3. Differential equations for phase-*c* current

Interval (S)	$(L-M)\frac{di_c}{dt}=$
S1 and S6	$\frac{(2v_c-v_a-v_b-3Ri_c-V_{dc})}{3}$
S4	$\frac{(2v_c-v_a-v_b-3Ri_c-2V_{dc})}{3}$
S2 and S5	$\frac{(2v_c-v_a-v_b-3Ri_c+V_{dc})}{3}$
S3	$\frac{(2v_c-v_a-v_b-3Ri_c+2V_{dc})}{3}$
S10	$\frac{(v_c-v_a-2Ri_c-V_{dc})}{2}$
S9	$\frac{(v_c-v_a-2Ri_c+V_{dc})}{2}$
S11	$\frac{(v_c-v_b-2Ri_c+V_{dc})}{2}$
S12	$\frac{(v_c-v_b-2Ri_c-V_{dc})}{2}$
S7	0
S8	0

The differential equation for the output dc voltage is calculated from the total output dc current, I_{dc}, which is the sum of the capacitor current, I_c, and load current, I_L as shown in figure 3.18.

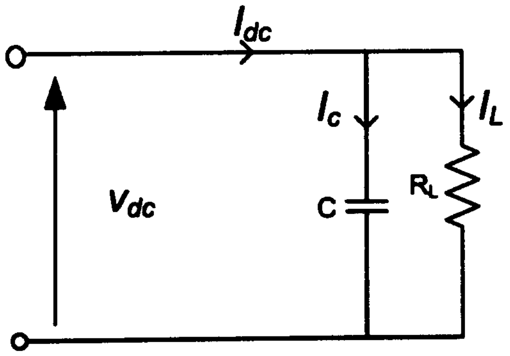

Figure 3.18 The output section showing the dc output current, I_{dc}, dc link capacitor current, I_c, and load current, I_L.

$$I_{dc} = I_c + I_L \tag{3.39}$$

The capacitor current is $$I_c = C\frac{dV_{dc}}{dt} \tag{3.40}$$

and load current $$I_L = \frac{V_{dc}}{R_L} \tag{3.41}$$

where V_{dc} and R_L are the output dc voltage and load resistance respectively.

Substitute (3.39) and (3.40) into (3.38) and rearranging gives

$$\frac{dV_{dc}}{dt} = \frac{I_{dc}}{C} - \frac{V_{dc}}{CR_L} \tag{3.42}$$

Using the pulse function and the phase currents the dc current, i_{dc}, is calculated as:

$$i_{dc} = i_a(S5 + S9 - S6 - S10) + i_b(S2 + S8 - S1 - S7) + i_c(S4 + S12 - S3 - S11) \tag{3.43}$$

Equation (3.44) represents the differential equations for phase-*a* and the output dc voltage during S1.

$$\frac{d}{dt}\begin{bmatrix} i_a \\ i_b \\ i_c \\ v_{dc} \end{bmatrix} = \begin{bmatrix} \frac{-R}{L-m} & 0 & 0 & \frac{-1}{3(L-m)} \\ 0 & \frac{-R}{L-m} & 0 & \frac{2}{3(L-m)} \\ 0 & 0 & \frac{-R}{L-m} & \frac{-1}{3(L-m)} \\ 0 & \frac{-1}{C} & 0 & \frac{-1}{R_L C} \end{bmatrix} \begin{bmatrix} i_a \\ i_b \\ i_c \\ v_{dc} \end{bmatrix} + \begin{bmatrix} \frac{2}{3(L-m)} & \frac{-1}{3(L-m)} & \frac{-1}{3(L-m)} & 0 \\ \frac{-1}{3(L-m)} & \frac{2}{3(L-m)} & \frac{-1}{3(L-m)} & 0 \\ \frac{-1}{3(L-m)} & \frac{-1}{3(L-m)} & \frac{2}{3(L-m)} & 0 \\ 0 & 0 & 0 & 0 \end{bmatrix} \begin{bmatrix} v_a \\ v_b \\ v_c \\ 0 \end{bmatrix} \tag{3.44}$$

The other differential equations for the three-phase currents and output dc voltage are presented by matrices A1 to A12 in Appendix A for the twelve intervals. The commutation period is calculated using an iteration process which depends on the phase current value. The calculation is started with initial value for commutation period using (3.9). If the calculated value of phase-*a* current is less than zero at the end of its commutation period then the commutation period is increased by a small amount and the calculation repeated until it equals zero, and vice-versa. In this way, the commutation period converges to its final value. This pulse function description, with iteration, produces faster simulation times compared with PSpice or SIMULINK-based simulation and can easily from part of a complete analysis package for multi-phase generators connected to diode bridge rectifiers.

3.4.2 Simulation model of the five-phase PM generator with diode rectifier

In order to determine the equations required to represent the five-phase permanent magnet generator with a diode bridge rectifier, a similar procedure is used. Figure 3.19 shows the circuit with back EMF and generator parameters (resistance, self- and mutual-inductances) and also shows the rectifier, Dc link capacitor, *C*, and resistive load, R_L. The five-phase generator has two mutual inductances (Section 4.6); mutual inductance between adjacent phases, M_1, and mutual inductance between non adjacent phases, M_2. As for the three-phase generator, two cases are examined: when two diodes conduct and when three diodes conduct simultaneously. Figure 3.20 shows phase back emf voltages for one period which can be divided into twenty sub-periods: ten periods when only two diodes conduct and ten periods when three diodes conduct. The periods are represented by pulses (in a similar way to that described in the previous section for the three-phase generator).

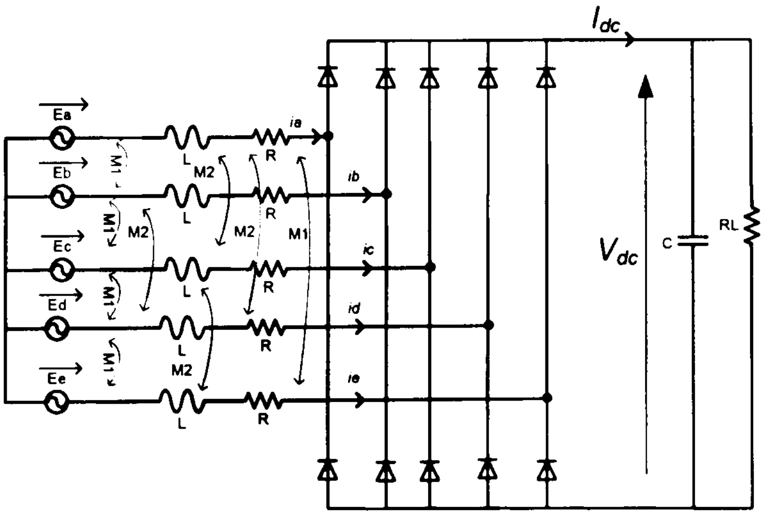

Figure 3.19. Five-phase diode bridge rectifier with permanent magnet generator showing the PM generator back emf, the resistance and self- and mutual-inductances (L, M_1, M_2)

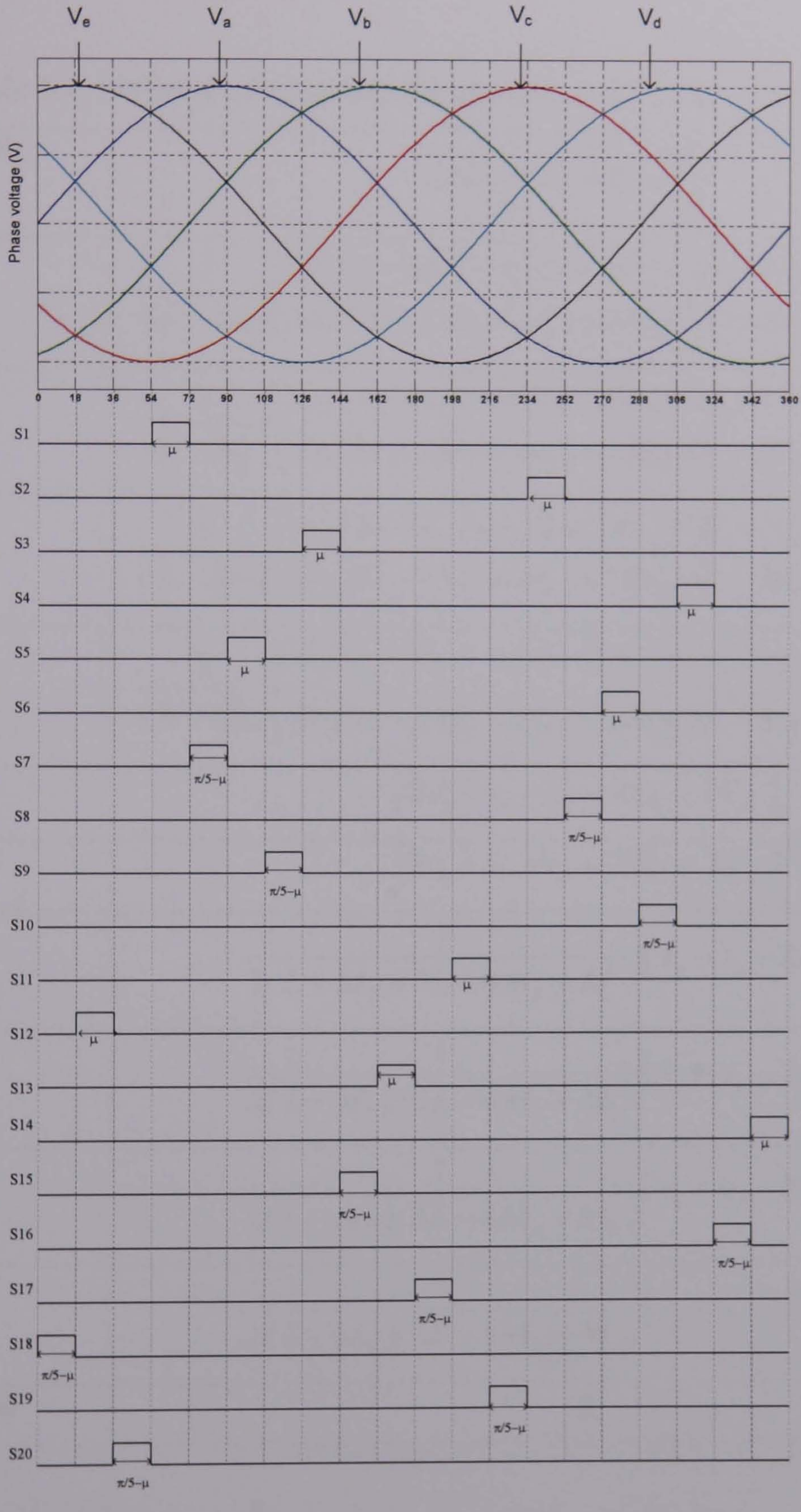

Figure 3.20. Phase back emf voltages of the five-phase system and the twenty pulses used to define each fundamental period

The complete set of twenty circuits associated with each interval is shown in Appendix A. From these circuits the differential equations representing each phase current are shown in tables 3.4 to 3.8.

Table 3.4. Differential equations for phase-*a* current for all intervals

Interval (S)	$(3L-4M_2+M_1)\frac{di_a}{dt}=$
S1	$\frac{1}{(L-M_1)}\begin{bmatrix}2v_a(L-M_2)-v_e(L-2M_2+M_1)-v_c(L-M_1)- \\ Ri_a(3L-2M_2+M_1)+2Ri_e(M_1-M_2)-V_{dc}(L-M_1)\end{bmatrix}$
S2	$\frac{1}{(L-M_1)}\begin{bmatrix}2v_a(L-M_2)-v_e(L-2M_2+M_1)-v_c(L-M_1)- \\ Ri_a(3L-2M_2+M_1)+2Ri_e(M_1-M_2)+V_{dc}(L-M_1)\end{bmatrix}$
S3	$\frac{1}{(L-M_1)}\begin{bmatrix}2v_a(L-M_2)-v_b(L-2M_2+M_1)-v_d(L-M_1)- \\ Ri_a(3L-2M_2+M_1)+2Ri_b(M_1-M_2)-V_{dc}(L-M_1)\end{bmatrix}$
S4	$\frac{1}{(L-M_1)}\begin{bmatrix}2v_a(L-M_2)-v_b(L-2M_2+M_1)-v_d(L-M_1)- \\ Ri_a(3L-2M_2+M_1)+2Ri_b(M_1-M_2)+V_{dc}(L-M_1)\end{bmatrix}$
S5	$\left[2v_a-v_c-v_d-3Ri_a-2V_{dc}\right]$
S6	$\left[2v_a-v_c-v_d-3Ri_a+.2V_{dc}\right]$
S7	$\frac{1}{2(L-M_2)(3L-4M_2+M_1)}\left[v_a-v_c-2Ri_a-V_{dc}\right]$
S8	$\frac{1}{2(L-M_2)(3L-4M_2+M_1)}\left[v_a-v_c-2Ri_a+V_{dc}\right]$
S9	$\frac{1}{2(L-M_2)(3L-4M_2+M_1)}\left[v_a-v_d-2Ri_a-V_{dc}\right]$
S10	$\frac{1}{2(L-M_2)(3L-4M_2+M_1)}\left[v_a-v_d-2Ri_a+V_{dc}\right]$
S11 to S20	0

Table 3.5. Differential equations for phase-*b* current for all intervals

Interval (S)	$(3L-4M_2+M_2)\frac{di_b}{dt}=$
S3	$\frac{1}{(L-M_1)}\begin{bmatrix}2v_b(L-M_2)-v_a(L-2M_2+M_1)-v_d(L-M_1)-\\Ri_b(3L-2M_2+M_1)+2Ri_a(M_1-M_2)-V_{dc}(L-M_1)\end{bmatrix}$
S4	$\frac{1}{(L-M_1)}\begin{bmatrix}2v_b(L-M_2)-v_a(L-2M_2+M_1)-v_d(L-M_1)-\\Ri_b(3L-2M_2+M_1)+2Ri_a(M_1-M_2)+V_{dc}(L-M_1)\end{bmatrix}$
S11	$\frac{1}{(L-M_1)}\begin{bmatrix}2v_b(L-M_2)-v_c(L-2M_2+M_1)-v_e(L-M_1)-\\Ri_b(3L-2M_2+M_1)+2Ri_c(M_1-M_2)-V_{dc}(L-M_1)\end{bmatrix}$
S12	$\frac{1}{(L-M_1)}\begin{bmatrix}2v_b(L-M_2)-v_c(L-2M_2+M_1)-v_e(L-M_1)-\\Ri_b(3L-2M_2+M_1)+2Ri_c(M_1-M_2)+V_{dc}(L-M_1)\end{bmatrix}$
S13	$\left[2v_b-v_d-v_e-3Ri_b-2V_{dc}\right]$
S14	$\left[2v_b-v_d-v_e-3Ri_b+.2V_{dc}\right]$
S15	$\frac{1}{2(L-M_2)(3L-4M_2+M_1)}\left[v_b-v_d-2Ri_b-V_{dc}\right]$
S16	$\frac{1}{2(L-M_2)(3L-4M_2+M_1)}\left[v_b-v_d-2Ri_b+V_{dc}\right]$
S17	$\frac{1}{2(L-M_2)(3L-4M_2+M_1)}\left[v_b-v_e-2Ri_b-V_{dc}\right]$
S18	$\frac{1}{2(L-M_2)(3L-4M_2+M_1)}\left[v_b-v_e-2Ri_b+V_{dc}\right]$
S1, S2, S5, S6, S7, S8, S9, S10, S19, and S20	0

Table 3.6. Differential equations for phase-*c* current for all intervals

Interval (S)	$(3L-4M_2+M_1)\frac{di_c}{dt}=$
S11	$\frac{1}{(L-M_1)}\begin{bmatrix}2v_c(L-M_2)-v_b(L-2M_2+M_1)-v_e(L-M_1)- \\ Ri_c(3L-2M_2+M_1)+2Ri_b(M_1-M_2)-V_{dc}(L-M_1)\end{bmatrix}$
S12	$\frac{1}{(L-M_1)}\begin{bmatrix}2v_c(L-M_2)-v_b(L-2M_2+M_1)-v_e(L-M_1)- \\ Ri_c(3L-2M_2+M_1)+2Ri_b(M_1-M_2)+V_{dc}(L-M_1)\end{bmatrix}$
S6	$\frac{1}{(L-M_1)}\begin{bmatrix}2v_c(L-M_2)-v_d(L-2M_2+M_1)-v_a(L-M_1)- \\ Ri_c(3L-2M_2+M_1)+2Ri_d(M_1-M_2)-V_{dc}(L-M_1)\end{bmatrix}$
S5	$\frac{1}{(L-M_1)}\begin{bmatrix}2v_c(L-M_2)-v_d(L-2M_2+M_1)-v_a(L-M_1)- \\ Ri_c(3L-2M_2+M_1)+2Ri_d(M_1-M_2)+V_{dc}(L-M_1)\end{bmatrix}$
S2	$[2v_c-v_e-v_a-3Ri_c-2V_{dc}]$
S1	$[2v_c-v_e-v_a-3Ri_c+2V_{dc}]$
S19	$\frac{1}{2(L-M_2)(3L-4M_2+M_1)}[v_c-v_e-2Ri_c-V_{dc}]$
S20	$\frac{1}{2(L-M_2)(3L-4M_2+M_1)}[v_c-v_e-2Ri_c+V_{dC}]$
S8	$\frac{1}{2(L-M_2)(3L-4M_2+M_1)}[v_c-v_a-2Ri_c-V_{dc}]$
S9	$\frac{1}{2(L-M_2)(3L-4M_2+M_1)}[v_c-v_a-2Ri_c+V_{dc}]$
S3, S4, S7, S10, S13, S14, S15, S16, S17, and S18	0

Table 3.7. Differential equations for phase-*d* current for all intervals

Interval (S)	$(3L-4M_2+M_1)\frac{di_d}{dt}=$
S6	$\frac{1}{(L-M_1)}\begin{bmatrix}2v_d(L-M_2)-v_c(L-2M_2+M_1)-v_a(L-M_1)- \\ Ri_d(3L-2M_2+M_1)+2Ri_c(M_1-M_2)-V_{dc}(L-M_1)\end{bmatrix}$
S5	$\frac{1}{(L-M_1)}\begin{bmatrix}2v_d(L-M_2)-v_c(L-2M_2+M_1)-v_a(L-M_1)- \\ Ri_d(3L-2M_2+M_1)+2Ri_c(M_1-M_2)+V_{dc}(L-M_1)\end{bmatrix}$
S14	$\frac{1}{(L-M_1)}\begin{bmatrix}2v_d(L-M_2)-v_e(L-2M_2+M_1)-v_b(L-M_1)- \\ Ri_d(3L-2M_2+M_1)+2Ri_e(M_1-M_2)-V_{dc}(L-M_1)\end{bmatrix}$
S13	$\frac{1}{(L-M_1)}\begin{bmatrix}2v_d(L-M_2)-v_e(L-2M_2+M_1)-v_b(L-M_1)- \\ Ri_d(3L-2M_2+M_1)+2Ri_e(M_1-M_2)+V_{dc}(L-M_1)\end{bmatrix}$
S4	$\left[2v_d-v_a-v_b-3Ri_d-2V_{dc}\right]$
S3	$\left[2v_d-v_a-v_b-3Ri_d+2V_{dc}\right]$
S10	$\frac{1}{2(L-M_2)(3L-4M_2+M_1)}\left[v_d-v_a-2Ri_d-V_{dc}\right]$
S9	$\frac{1}{2(L-M_2)(3L-4M_2+M_1)}\left[v_d-v_a-2Ri_d+V_{dc}\right]$
S16	$\frac{1}{2(L-M_2)(3L-4M_2+M_1)}\left[v_d-v_b-2Ri_d-V_{dc}\right]$
S15	$\frac{1}{2(L-M_2)(3L-4M_2+M_1)}\left[v_d-v_b-2Ri_d+V_{dc}\right]$
S1, S2, S7, S8, S11, S12, S17, S18, S19, and S20	0

Table 3.8. Differential equations for phase-*e* current for all intervals

Interval (S)	$(3L-4M_2+M_1)\frac{di_e}{dt}=$
S14	$\frac{1}{(L-M_1)}\left[\begin{array}{l}2v_e(L-M_2)-v_d(L-2M_2+M_1)-v_b(L-M_1)-\\ Ri_e(3L-2M_2+M_1)+2Ri_d(M_1-M_2)-V_{dc}(L-M_1)\end{array}\right]$
S13	$\frac{1}{(L-M_1)}\left[\begin{array}{l}2v_e(L-M_2)-v_d(L-2M_2+M_1)-v_b(L-M_1)-\\ Ri_e(3L-2M_2+M_1)+2Ri_d(M_1-M_2)+V_{dc}(L-M_1)\end{array}\right]$
S1	$\frac{1}{(L-M_1)}\left[\begin{array}{l}2v_e(L-M_2)-v_a(L-2M_2+M_1)-v_c(L-M_1)-\\ Ri_e(3L-2M_2+M_1)+2Ri_a(M_1-M_2)-V_{dc}(L-M_1)\end{array}\right]$
S2	$\frac{1}{(L-M_1)}\left[\begin{array}{l}2v_e(L-M_2)-v_a(L-2M_2+M_1)-v_c(L-M_1)-\\ Ri_e(3L-2M_2+M_1)+2Ri_a(M_1-M_2)+V_{dc}(L-M_1)\end{array}\right]$
S12	$[2v_e-v_b-v_c-3Ri_e-2V_{dc}]$
S11	$[2v_e-v_b-v_c-3Ri_e+2V_{dc}]$
S18	$\frac{1}{2(L-M_2)(3L-4M_2+M_1)}[v_e-v_b-2Ri_e-V_{dc}]$
S17	$\frac{1}{2(L-M_2)(3L-4M_2+M_1)}[v_e-v_b-2Ri_e+V_{dc}]$
S20	$\frac{1}{2(L-M_2)(3L-4M_2+M_1)}[v_e-v_c-2Ri_e-V_{dc}]$
S19	$\frac{1}{2(L-M_2)(3L-4M_2+M_1)}[v_e-v_c-2Ri_e+V_{dc}]$
S3, S4, S5, S6, S7, S8, S9, S10, S15, and S16	0

The differential equation for the dc link voltage, V_{dc}, is the same as in three-phase case. The output is then determined by the differential equation

$$\frac{dV_{dc}}{dt}=\frac{I_{dc}}{C}-\frac{V_{dc}}{CR_L} \qquad (3.45)$$

Using the pulse function and the phase current equations the dc current, i_{dc}, is calculated from:

$$\begin{aligned} i_{dc} = {} & i_a(S5+S9-S6-S10)+i_b(S13+S17-S14-S18)+i_c(S2+S8-S1-S7)+ \\ & i_d(S4+S16-S3-S15)+i_e(S12+S20-S11-S19) \end{aligned} \tag{3.46}$$

Equation (3.47) represents the differential equations for phase-*a*, -*c* and -*e* and the output dc voltage during S1.

$$\frac{d}{dt}\begin{bmatrix} i_a \\ i_c \\ i_e \\ v_{dc} \end{bmatrix} = [\mathrm{A}]\begin{bmatrix} i_a \\ i_c \\ i_e \\ v_{dc} \end{bmatrix} + [\mathrm{B}]\begin{bmatrix} v_a \\ v_c \\ v_e \\ 0 \end{bmatrix} \tag{3.47}$$

where [A] =

$$\begin{bmatrix} \dfrac{-R(3L-2M_2-M_1)}{(L-M_1)(3L-4M_2+M_1)} & 0 & \dfrac{2R(M_1-M_2)}{(L-M_1)(3L-4M_2+M_1)} & \dfrac{-(L-M_1)}{(L-M_1)(3L-4M_2+M_1)} \\ 0 & \dfrac{-3R}{(3L-4M_2+M_1)} & 0 & \dfrac{2}{(3L-4M_2+M_1)} \\ 0 & 0 & \dfrac{-R(3L-2M_2-M_1)}{(L-M_1)(3L-4M_2+M_1)} & \dfrac{-(L-M_1)}{(L-M_1)(3L-4M_2+M_1)} \\ 0 & \dfrac{-1}{C} & 0 & \dfrac{-1}{R_L C} \end{bmatrix}$$

and [B] =

$$\begin{bmatrix} \dfrac{2(L-M_2)}{(L-M_1)(3L-4M_2+M_1)} & \dfrac{-(L-M_1)}{(L-M_1)(3L-4M_2+M_1)} & \dfrac{-(L-2M_2+M_1)}{(L-M_1)(3L-4M_2+M_1)} & 0 \\ \dfrac{-1}{(3L-4M_2+M_1)} & \dfrac{2}{(3L-4M_2+M_1)} & \dfrac{-1}{(3L-4M_2+M_1)} & 0 \\ \dfrac{-(L-2M_2+M_1)}{(L-M_1)(3L-4M_2+M_1)} & \dfrac{-(L-M_1)}{(L-M_1)(3L-4M_2+M_1)} & \dfrac{2(L-M_2)}{(L-M_1)(3L-4M_2+M_1)} & 0 \\ 0 & 0 & 0 & 0 \end{bmatrix}$$

The other differential equations for the five-phase currents and output dc voltage are presented by matrices A13 to A33 in Appendix A for the twenty intervals. The commutation period is calculated using an iterative procedure similar to the three-phase case.

3.5 Evaluation of the developed models

The developed models for the three- and the five-phase systems are implemented in MATLAB/Simulink. Data from the practical permanent magnet generators described in Chapter 5 are used. The simulation results from the developed models are compared with PSpice results to validate the models. Table 3.9 shows the system parameters. The phase voltages in these simulations are sine wave (in the practical case they are distorted sine waves). The generator parameters yield the same average dc output voltage in both systems at full-load and the Dc link capacitors in each case are selected to give the same output peak-to-peak ripple for both systems at full load, R_L=10Ω.

Table 3.9. The three-phase and five-phase systems parameters used in the simulation

Parameters	Three-phase	Five-phase
Phase voltage amplitude (V_m), V	54	48
Frequency, Hz	46.67	46.67
Phase resistance (R), Ω	0.56	0.65
Phase Inductance (L), mH	1.2	1.3
Mutual inductance (M_1), mH	0.36	0.62
Mutual inductance (M_2), mH		0.24
Dc link capacitor (C), μF	2200	470
Resistive load (R_L), Ω	10	10

The simulation results of the five-phase system using the developed model and PSpice model are shown in figure 3.21 and 3.22. Figure 3.21 shows the comparison of the dc output voltage for both models. The average output voltage is 78.1V, and has peak-to-peak ripple approximately 0.7% of average voltage. It can be seen that the developed model closely matches the PSpice waveform.

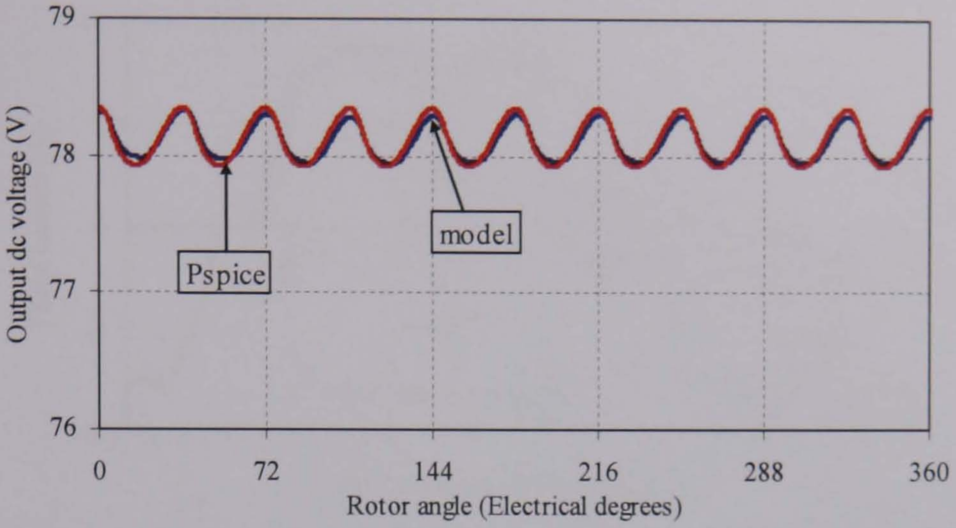

Figure 3.21. Five-phase rectifier output dc voltage showing the waveforms generated by the developed model and the PSpice model.

Figure 3.22 shows phase-*a* current for both models. The current has rms value equal 4.6A (which is the permanent magnet generator's rated current).

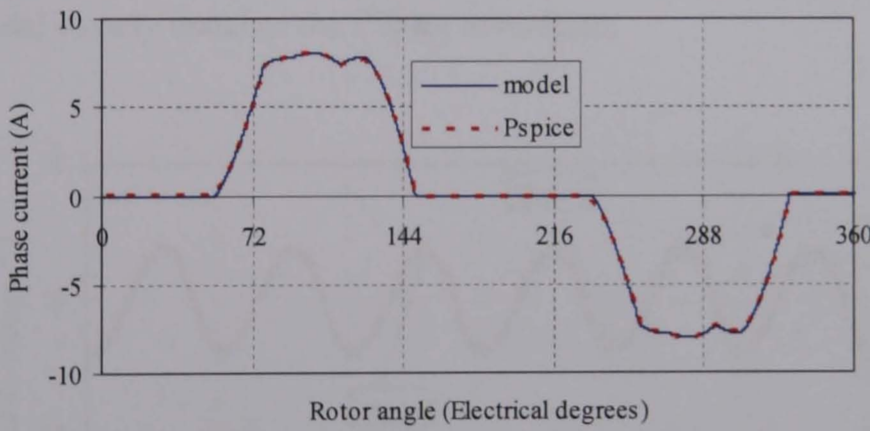

Figure 3.22. Phase-*a* current in the five-phase generator showing the waveforms generated by the developed model and the PSpice model.

Figure 3.23 shows that the commutation angle is 23.3°, between phase-*a* and phase-*b* currents using the developed model. This commutation angle is due to the self- and mutual-inductances of the phase winding as discussed in section 3.2.

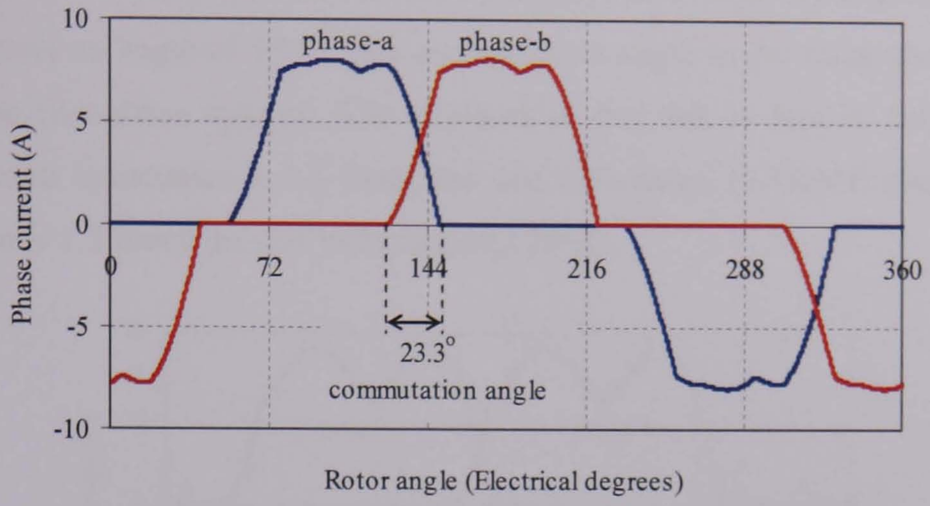

Figure 3.23. Phase-*a* and phase-*b* currents showing the commutation angle, 23.3° for the five-phase generator.

The results for the three-phase system are shown in figures 3.24 and 3.25. Figure 3.24 shows the three-phase dc output voltage from the developed model and the PSpice model. The average voltage is, 78.1V, which is the same as the five-phase system as is the peak-to-peak voltage ripple. Also it can be seen that the waveform from the developed model closely matches the PSpice waveform.

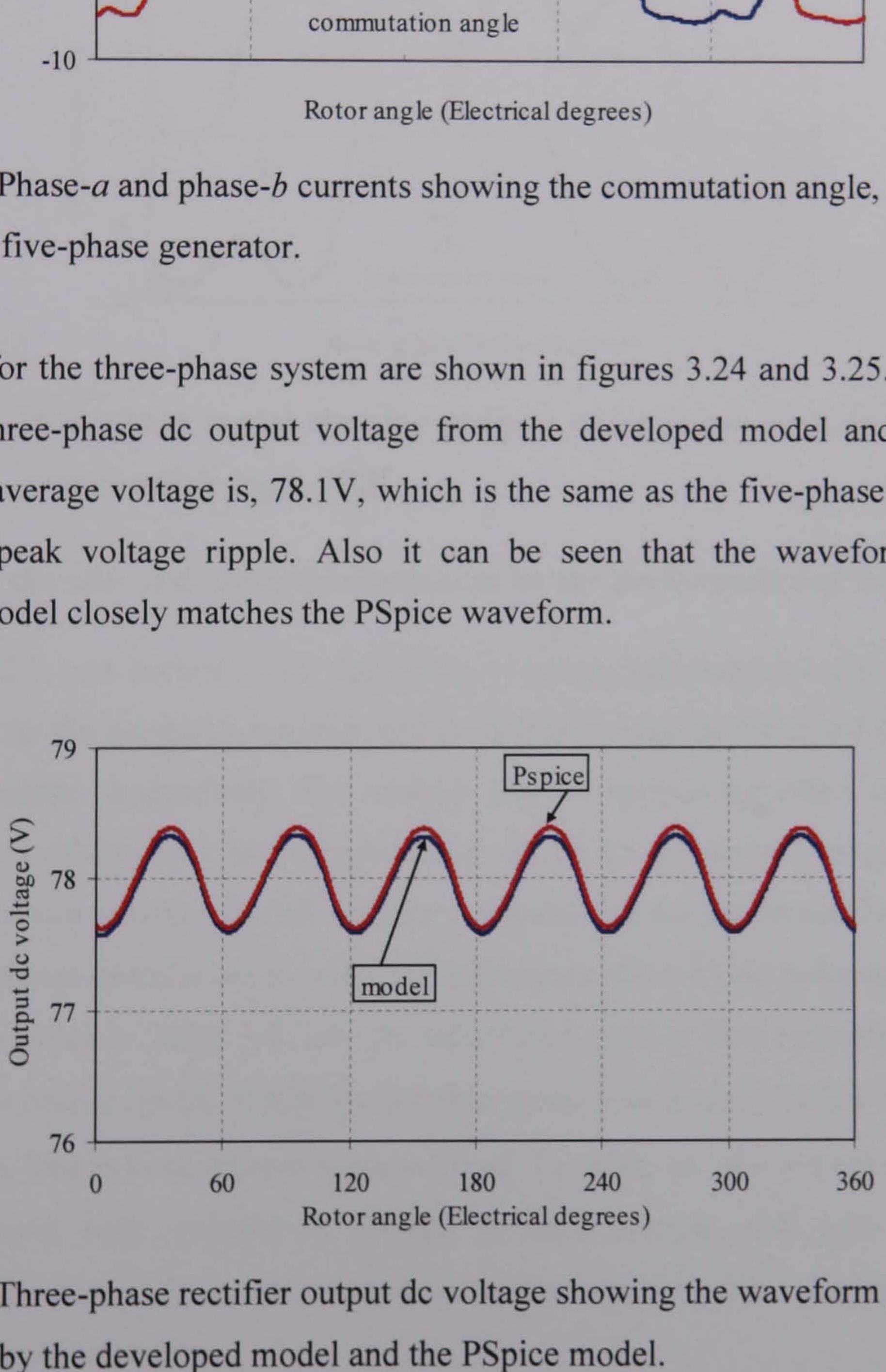

Figure 3.24. Three-phase rectifier output dc voltage showing the waveform generated by the developed model and the PSpice model.

Figure 3.25 shows the results from the three-phase system. Phase-*a* and phase-*b* currents commutate over an angle of 19.8°. The commutation angle in the three-phase system is less than the five-phase system. The explanation for this is that in the three-phase system the total inductance is 1.3 times the self inductance (1.56mH) and in the five-phase system is 1.7 times the self inductance (2.2mH).

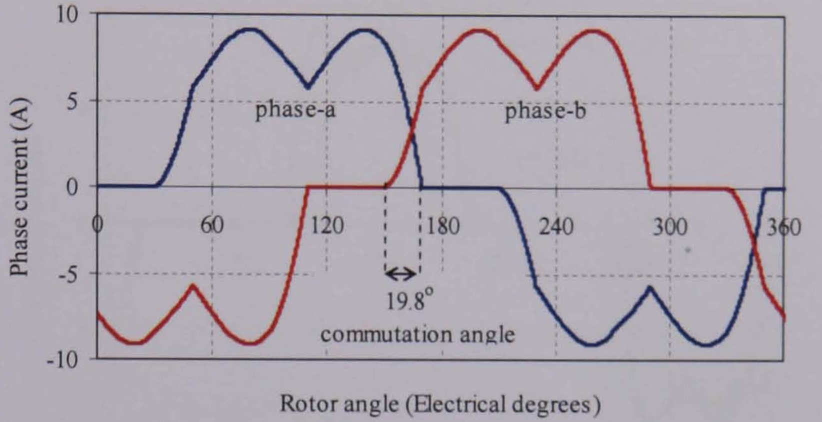

Figure 3.25. Three-phase model showing phase-*a* and phase-*b* currents showing the commutation angle, 19.8°.

3.6 Effect of the self- and mutual-inductances on the performance of the generators

In section 3.2.2 and section 3.3.2 the effect of phase inductances (self- and mutual-inductances) on the generator currents and dc output voltage is discussed for three- and five-phase systems respectively. The analysis did not include the effect of the dc link capacitor. To evaluate how phase inductances affect the permanent magnet generator systems performance with a dc link capacitor, simulations are performed for three cases: with self- and mutual-inductance, with self-inductance and with no inductance using the practical data given in Table 3.9. The dc capacitance used in both systems is chosen to give the same output ripple: 470μF for the five-phase system and 2200μF for the three-phase system. The load resistance value is fixed, R_L=10Ω, in all simulation cases. This resistance forces both systems to operate at rated current with self- and mutual inductance. The term inductance is used here to represent the total inductance including self- and mutual-inductance.

Figures 3.26 to 3.28 show phase-*a* current, output dc voltage and generator power respectively for the simulation results of the five-phase system. It can be seen that without phase inductance the current has higher distortion and a higher rms value compared to other the cases. However, the mutual inductance has a minor effect on the current waveform when compared to the impact that the self-inductance has on the current waveform. In all cases, there is distortion in the current waveform which will manifest itself as the generator power ripple (hence shaft torque ripple).

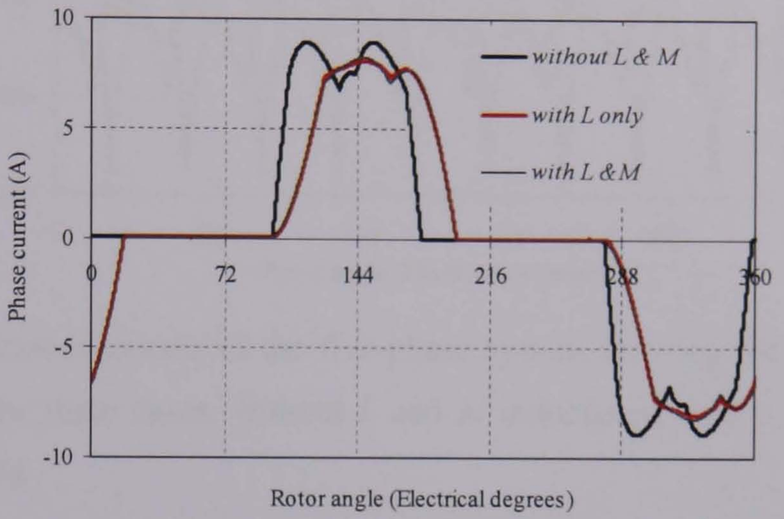

Figure 3.26. Simulation results of the five-phase system showing the generator phase-*a* current for the three cases, without *L* and *M* inductance, with *L* only and with *L* and *M*.

The electrical power delivered by the generator when connected to the diode rectifier is important in order to assess and to study the shaft torque ripple. Electrical power, P_e, from the five-phase generator is given by

$$P_e = i_a v_a + i_b v_b + i_c v_c + i_d v_d + i_e v_e \tag{3.48}$$

where all values are instantaneous and the voltages are the back emfs of each phase.

By neglecting the generator mechanical losses, P_e represents the shaft power. Using (3.48) the shaft torque, T_e,

$$T_e = \frac{P_e}{\omega_e} \tag{3.49}$$

where ω_e is the shaft angular velocity (rads^{-1}).

Figure 3.27 shows the simulation results of the five-phase permanent magnet power for the three cases, with *L* and *M*, with *L* only and without *L* and *M*.

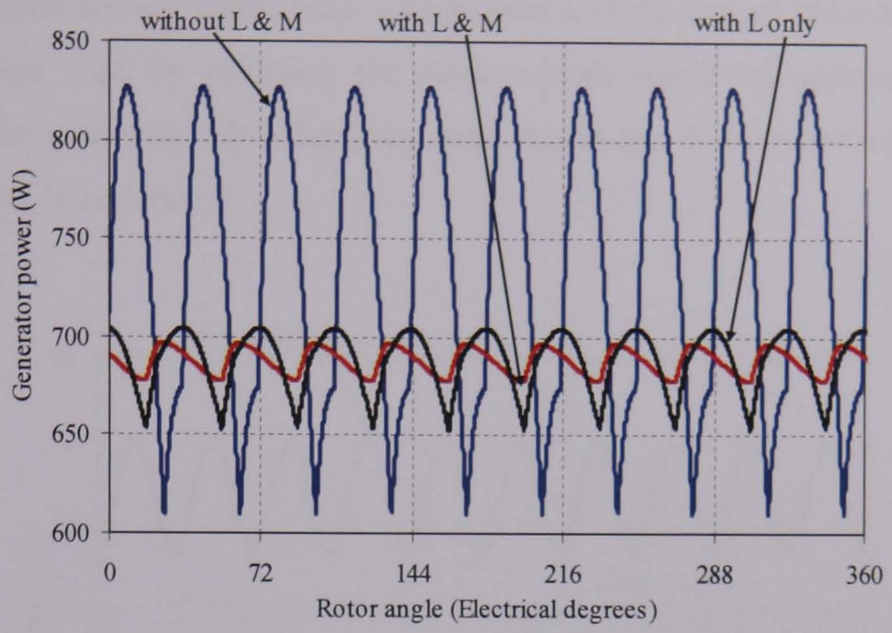

Figure 3.27. Simulation results of the five-phase system showing the generator power for the three cases, without L and M inductance, with L only and with L and M.

Several remarks can be made regarding the waveforms shown in figure 3.27 and Table 3.10. In the case without inductance the generator is predicted to deliver more power but with a peak-to-peak ripple of 29.5% of average power. The ripple in the shaft power is reflected in the shaft torque and leads to mechanical vibration and noise. Including the self- and mutual-inductance reduces the ripple by a factor of 12. Without mutual inductance the predicted ripple is approximately three times that when mutual inductance is included. These results show the significant effect that mutual inductance has on generator power and shaft torque ripple. Although the phase currents are not appreciably different, the mutual-inductance significantly affects the shaft torque ripple and demonstrates a clear need to include the mutual inductance in the model of the generator.

Figure 3.28 shows the dc output voltage for the three cases. In the case without self and mutual inductance the average dc voltage, 80V, is less than no-load voltage, 91.5V. This is due to the voltage drop across the diodes and phase resistance. In the other cases the reduction of the dc output voltage includes a contribution due to phase inductance in addition to the phase resistance and diode drop. It is seen from figure 3.28 that the peak-to-peak ripple in the case with self and mutual inductance is reduced by approximately

59% from the case without inductance. The influence of the mutual inductance is clearly shown in figure 3.28 by reducing the peak-to-peak ripple by approximately 22% compared to the case with self inductance only. Again this demonstrates the clear need to model mutual inductance.

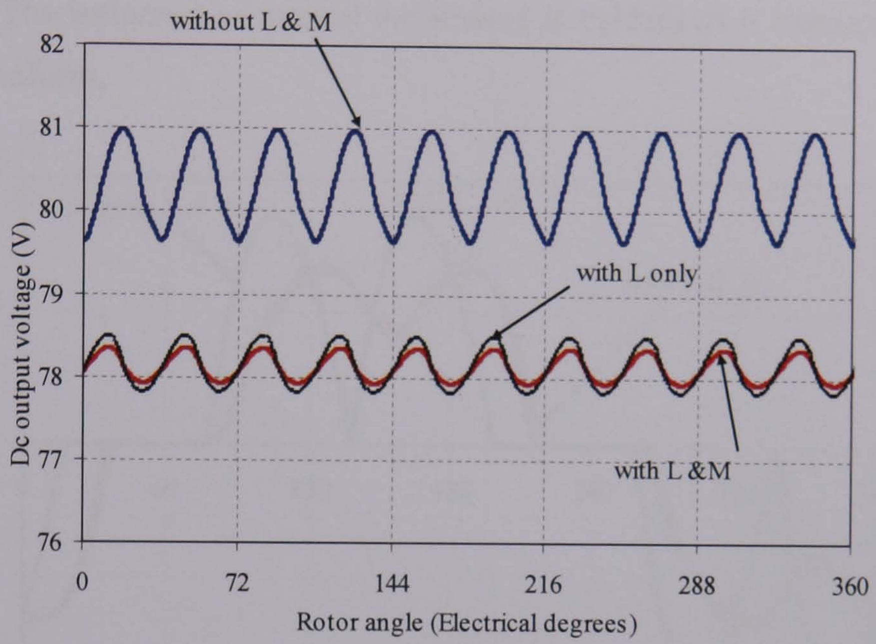

Figure 3.28. Simulation results of the five-phase system showing the dc output voltage for the three cases.

Table 3.10 summarises the results of the five-phase system for the three cases. The percentages of the peak-to-peak ripple are calculated relative to the average value.

Table 3.10. Summary of simulation results of the five-phase system for the three cases.

	Without self and mutual inductance		With self inductance only		With self and mutual inductance	
	rms/ average	Peak-peak ripple	rms/ average	Peak-peak ripple	rms/ average	Peak-peak ripple
Generator power	733.4W	29.6%	708W	7.5%	687.7W	2.7%
Output dc voltage	80.3V	1.7%	78.7V	0.9%	78.12V	0.7%
Output dc power	645W	3%	615W	1.7%	610W	1.1%
Phase current	5A		4.6A		4.65A	

The results of the three-phase system simulation are shown in figures 3.29 to 3.31. As in the five-phase system, three cases are simulated. The ac phase current is illustrated in figure 3.29. It is clear that in the case without inductance the current is highly distortion when compared to the five-phase system. With self inductance only and with self and mutual inductance, the current distortion is reduced, but is still higher than for the five-phase system. The influence of mutual inductance is evident as it changes the shape of the current waveform.

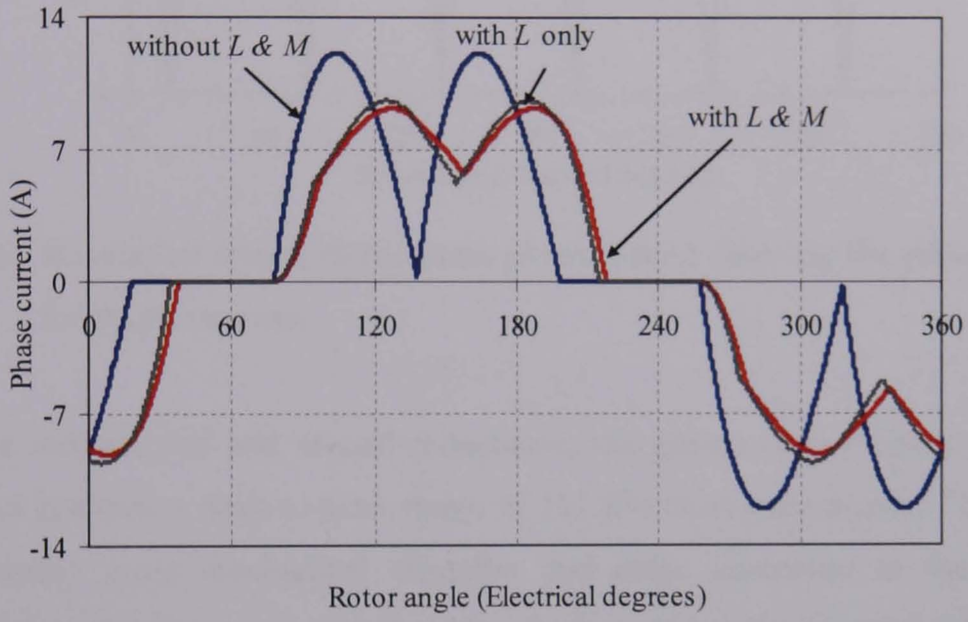

Figure 3.29. Simulation results of the three-phase system showing the generator phase-*a* current for the three cases.

The three-phase generator shaft power, P_e, is given by

$$P_e = i_a v_a + i_b v_b + i_c v_c \tag{3.50}$$

where all values are instantaneous.

Figure 3.27 shows the simulated shaft power of the three-phase generator for the three cases, with self-and mutual-inductance, without self-and mutual-inductance and with self-inductance only.

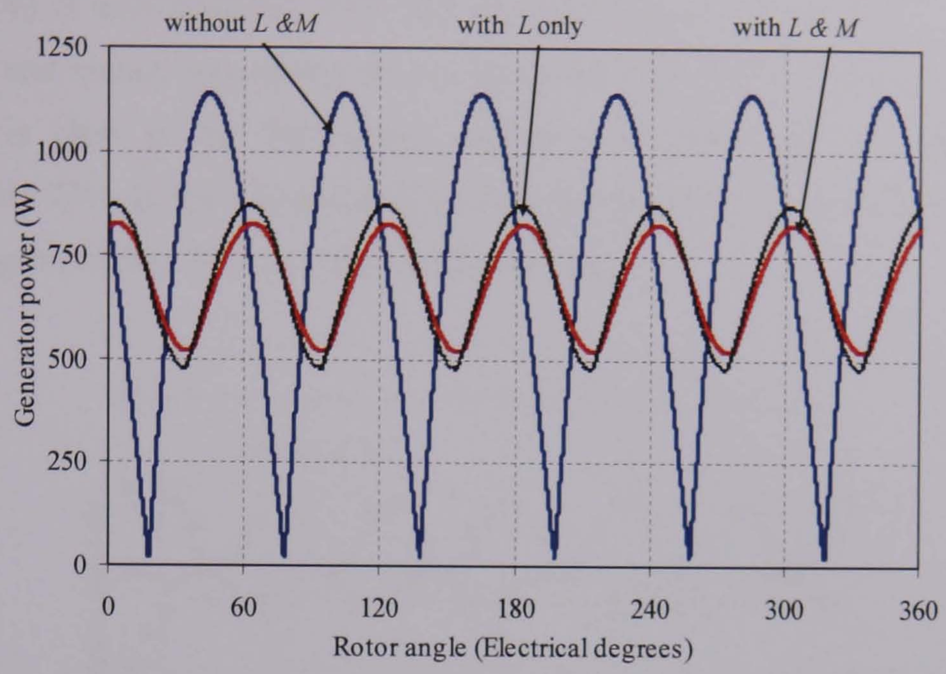

Figure 3.30. Simulation results of the three-phase system showing the generator power for the three cases.

In the case without self and mutual inductance, the generator is estimated to deliver more power but with a peak-to-peak ripple of 151.8% of average power. This will lead to considerably more mechanical vibration and noise compared to the five-phase system. With self inductance modelled, the ripple is reduced approximately 2.7 times compared to the case without self inductance. Including the phase self- and mutual-inductance estimates a reduction in ripple in the shaft power of approximately 3.4 times compared to without self- and mutual-inductance. It is clear from waveforms shown in figures 3.27 and 3.30 and Tables 3.10 and 3.11 that the mutual inductance has an impact on the five-phase simulation, the shaft torque ripple is reduced by 2.8 times from the case where self-inductance is modelled only. This reduction is more significant than that demonstrated by the three-phase generator, where the ripple is reduced by 1.3 times if mutual-inductance is included. This is clear evidence of need to include all mutual inductances in the simulation.

Figure 3.31 shows the dc output voltage for the three cases. In the case without inductance the average dc voltage is 80.4V. In the other cases the additional reduction of the dc output voltage is due to the phase inductance voltage drop. It is observed from the five- and three-phase results that the peak-to-peak voltage ripple in the five-phase system (1.3V) is approximately 45% less than three-phase system (2.4V) in the case where self- and mutual-inductance are not modelled. The effect of the self and mutual inductance is clear in the three-phase system and reduces the voltage ripple by approximately 71%. In the five-phase system the self and mutual inductance reduces the ripple by approximately 59% as discussed previously.

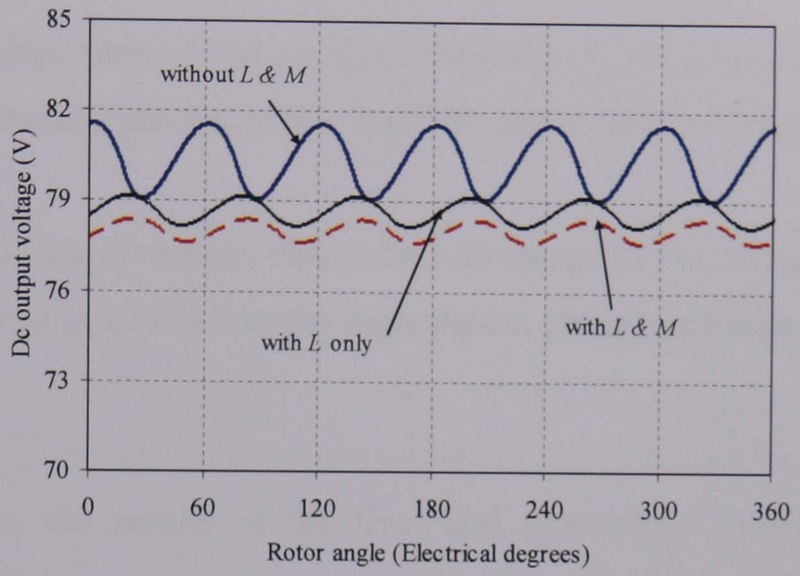

Figure 3.31. Simulation results of the three-phase system, showing the dc output voltage for the three cases.

Table 3.11 summarises the results of the three-phase system for the three cases. The percentages of peak-to-peak ripple are calculated relative to the average value.

Table 3.11. Summary of simulation results of the three-phase systems for the three cases

Cases	Without self and mutual inductance		With self inductance only		With self and mutual inductance	
	Average/rms	p-p ripple	average/rms	p-p ripple	average/rms	p-p ripple
Generator power	737.6W	151.8%	694.8W	57%	682W	45%
Output dc voltage	80.4V	3.1%	78.7V	1.3%	78.0V	0.9%
Output dc power	646	6.2%	618W	2.5%	609W	2%
Phase current	7.18A		6.4A		6.32A	

Ignoring phase inductance the dc capacitor charges through the series combination of two phase resistances with a time constant,τ, equal to

$$\tau = RC \tag{3.51}$$

where R is twice the phase resistance.

The capacitor discharges through load resistance, R_L, with time constant equal

$$\tau = R_L C \tag{3.52}$$

Therefore, the charge time of the capacitor depends on the capacitance and the phase resistance. The capacitor discharge rate depends on the load resistance and capacitance.

With phase inductance, however, charge and discharge of the dc capacitor depends on the phase inductance in addition to the capacitance, phase resistance and load resistance values.

It is evident from the results of the five- and three-phase systems that there is a considerable difference between the three cases. It is also evident that inductance has a positive impact on the permanent magnet generator's torque ripple, however, large phase inductance leads to increase commutation angles and reduces the output voltage, as discussed in sections 3.2.1 and 3.2.2. As the power output is an issue it is recommended to keep the commutation angle in the five phase system less than 36° and in the three-phase system less than 60°.

The comparison results of the dc output voltage and generator power respectively for the five- and the three-phase systems are shown in Figure 3.32 to 3.35. The comparison is for two cases: with self and mutual inductance and without inductance. From the figures, it can bee seen that the peak-to-peak ripple of dc voltage in the three-phase system without self and mutual inductance is a factor of 1.8 greater than the five-phase system. With self and mutual inductance the peak-to-peak ripple is almost equal in both systems (the capacitor is selected to give the same output ripple in the practical case).

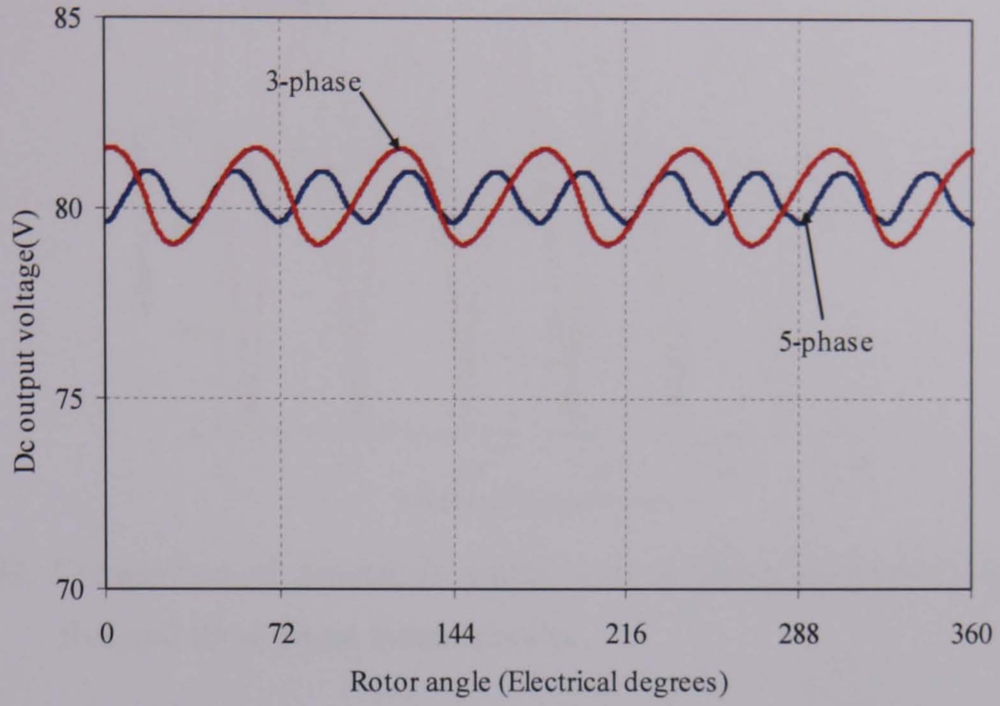

Figure 3.32. Comparison of dc output voltage without phase inductance showing the five-and three-phase system results.

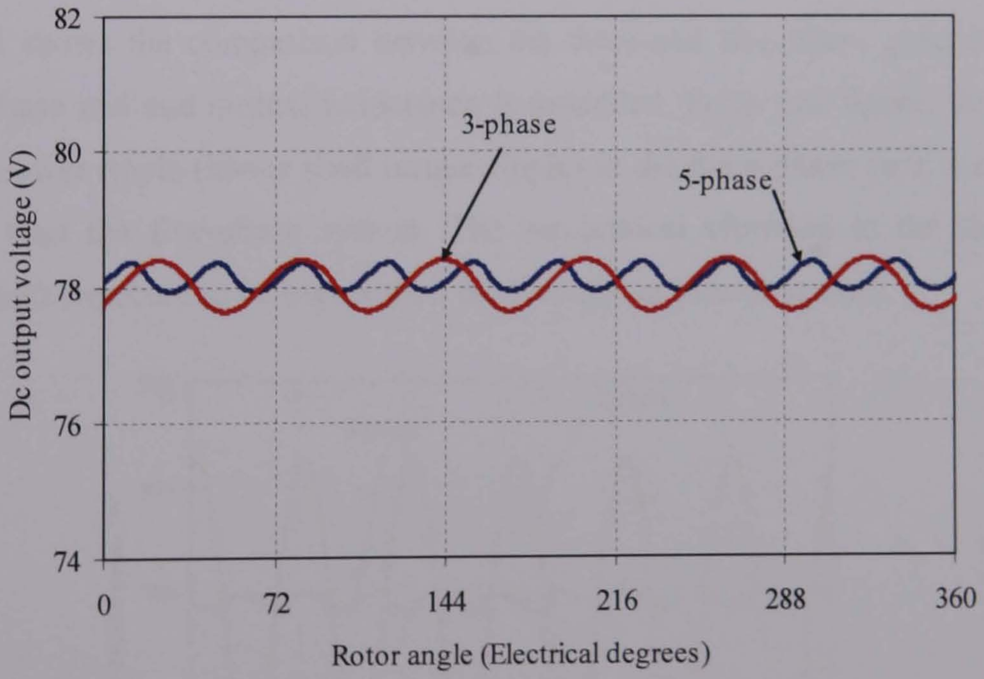

Figure 3.33. Comparison of dc output voltage with phase inductance showing the five- and three-phase system results.

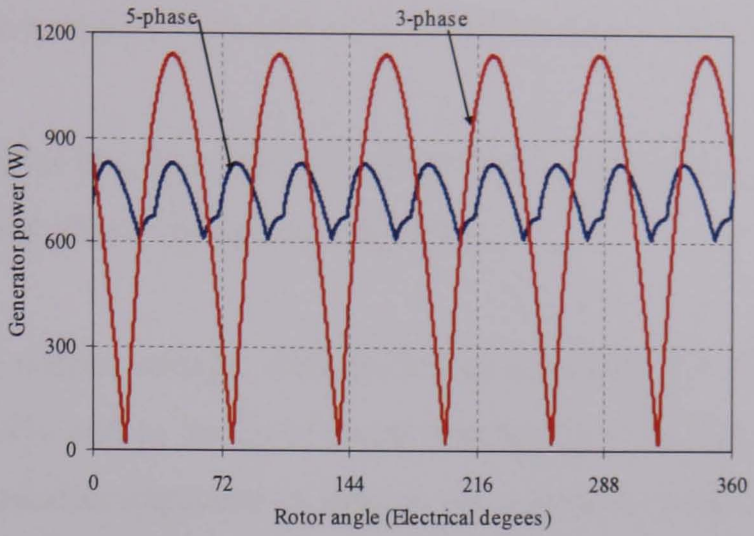

Figure 3.34. Comparison of generators power without phase inductance showing the five-and three-phase system results.

Figure 3.34 shows the generator power for the five- and three-phase systems without inductance. The peak-to-peak ripple in three-phase system is a factor of 5.1 greater than in the five-phase system.

Figure 3.35 shows the comparison between the three-and five-phase generator power when the phase self and mutual inductance is modelled. From this figure, the peak-to-peak shaft power ripple (hence shaft torque ripple) in the three-phase case is a factor of 16 greater than the five-phase system. The mechanical vibration in the three-phase generator shaft expected to be higher than the five-phase generator shaft.

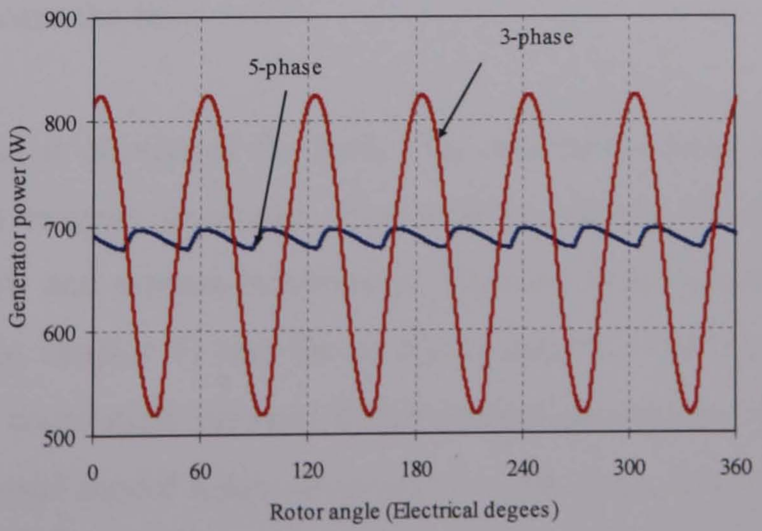

Figure 3.35. Comparison of generators power with phase inductance showing the five- and three-phase system results.

3.7 Summary

In this chapter the principle of three-phase and five-phase diode rectifiers are discussed. The analysis of both rectifiers with and without inductance is studied.

The five-phase rectifier has an output dc voltage that is 12% higher than the three-phase rectifier if the no-load phase voltages are the same.

The ripple in the dc output voltage, with no dc link capacitor, for the five-phase rectifier is approximately 4.8% and in the three-phase rectifier is 13%. This means a five-phase rectifier requires a smaller capacitor to smooth the output dc voltage to a specified level compared to a three-phase system. The capacitor rms current is discussed in chapter 7.

The effect of the phase inductance in reducing the output voltage is higher in the five-phase case than in the three-phase case (if the inductance and average output dc current are the same in both rectifiers). This is because the commutation periods in the five-phase case occupy a larger proportion of the fundamental cycle when compared to the three-phase case.

The commutation angle in both rectifiers depends on the self and mutual inductance, the supply frequency, and the average output dc current. The maximum value of commutation angle for a five-phase rectifier is 36° otherwise there are more than three phases conducting simultaneously which has serious effects on the voltage regulation. In the three-phase case the limit is 60°.

A simulation model is developed for both five- and three-phase rectifier systems feed from a permanent magnet generator. The models include the generator parameters specifically the self- and mutual-inductances. The developed models are verified using practical data (from chapter 5) and the results compared with PSpice simulation. The results show good correlation between the developed model and the PSpice simulation model. The developed model helps describe how the generator performs with a diode bridge rectifier and also shows the importance of generator parameters and the effect that mutual inductance has on the five-phase system.

Practical data for three- and five-phase pm generators (from chapter 5) is used to simulate the five- and three-phase systems for three-cases, without self- and mutual inductance, with self inductance only and with self and mutual inductance. This demonstrates the effect of phase inductance on the performance of the permanent magnet generator. The results show that the five-phase system displays considerably lower peak-to-peak shaft power and torque ripple compared to three-phase system. This is a significant advantage of the five-phase system.

The dc link capacitor in the three-phase system is 4.7 times larger than the five-phase system for the same dc output peak-to-peak ripple. This is another significant advantage of the five-phase system compared to the three-phase system.

References

[3.1] S. Choi, B. Lee, and N. E Prasad, "New 24-pulse diode rectifier system for utility interface of high-power Ac motor drive," IEEE Trans. on Industrial Applications, Vol. 33, No.2, March/April 1997. pp. 531-539.

[3.2] B. Zhang, and S. D. Pekarek, "Analysis and average value model of a source commutated 5-phase rectifier," IEEE, Power electronic Specialists conference, 35th Annual, Aachen, Germany, 2004. pp. 362-368.

[3.3] M. H. Rashed, "Power electronics -devices, derives, and application." Prentice - Hall International, Inc. USA 1993.

[3.4] N. Mohan, T. M. Undeland, W. P. Robbins, "Power Electronics: Converters, Applications, and Design," Second edition. Wiley, 1995

[3.5] P. Pejović, "Three-Phase Diode Rectifiers With Low Harmonics," Springer US, 2007

Chapter 4

Design of the Prototype Five-phase Permanent Magnet Generator

4.1 Introduction

In this chapter, the stator and rotor of a 4-pole permanent magnet generator is designed for operation both in a 3-phase and 5-phase configuration as a permanent magnet generator. Both generators are designed to have a rated speed of 1400rpm and feed six-pulse and ten-pulse diode bridge rectifiers.

The initial phase of the design is to define the type of rotor (an interior or external rotor, radial or axial-gap generator), the number of poles and the number of stator slots. In section 4.2 these aspects are chosen.

The design procedure for the rotor is described in section 4.3. The rotor diameter is determined based on the availability of magnet size and shape to make fabrication quicker and easier. The stator topology and outline design is described in section 4.4. The stator slot dimensions are chosen in section 4.5. The flux density is designed to be less than the iron saturation flux density in order to reduce the rotor and stator iron losses.

The stator windings are designed based on current density, generator rating, slot area and air-gap flux density. The design choices include winding configuration, conductor size and number of conductors per slot. This process is discussed in section 4.6. The phase resistance, self- and mutual-inductances are estimated in section 4.7.

The initial design uses linear equations and the demagnetisation curve of the chosen magnet. Finite element analysis (FEA) is used to validate this model. Sections 4.8 and 4.9 of this chapter discuss the FEA software and the results of the analysis. In sections 4.10 and 4.11 the cogging torque and back EMF are estimated and discussed using results from the FEA program.

4.2 Initial design choices

If a low speed, PM generator is required, it would be wise to consider an axial rotor design. This is particularly true if zero cogging torque is desired. However, this type of machine is expensive when low cost is an objective. Also the axial permanent magnet machine has a large outside diameter which does not always suit wind turbines. If a high-torque, low speed machine is required, then an interior-rotor design would be appropriate. In addition, it has a smaller diameter, is more compact and can be easily connected directly to wind turbines or through a gear-box. In this research an interior-rotor is selected as it is easier to manufacture using the traditional machine manufacturing processes that were available for this research.

The selection of the number of magnet poles depends upon many factors [4.1], for example:

a. the magnet material and grade,
b. the rotor type (interior-rotor, exterior-rotor, axial rotor),
c. the mechanical assembly of the rotor and magnet,
d. the speed of rotation, and
e. the inertia requirements.

The number of poles is generally inversely proportional to the desired rated speed of the machine. If smooth torque is required at low speed, such as in a DC torque motor, a large number of poles should be selected. Also, as the number of poles is doubled, the required thickness of the stator and rotor back-iron is reduced by one half [4.1-4.2]. Therefore, for a given magnetic and electrical loading and given rotor diameter, the overall machine diameter can be reduced by increasing the number of poles. However, there are some disadvantages such as an increase in fabrication cost and finding appropriate methods of fixing many magnets to the rotor.

Until recently, certain ratios of pole to slot numbers have been more popular. However, there are many combinations of slot- and pole-numbers that can be used effectively [4.1]. Table B.1 and B.2 in Appendix B list all the possible pole-numbers which will operate with stator laminations having slot-numbers from 3 to 48 for 3- and 5-phase machines respectively. In this research the number of rotor poles and stator slots are selected to be 4 and 30 respectively. This reduces the cogging torque as will be discussed in section 4.9.

4.3 Rotor design

In this research, the design of the rotor is driven by the availability of the permanent magnets for the rotor, which in this case is a bread-loaf shape that is made from *NdFeB N38H* magnetic material with dimensions shown in figure 4.1. Four poles are selected, which suites the approximate diameter of the rotor and also the dimensions of available magnets. The stack length is defined by the magnet length of 50mm. The rotor radius is determined by the radius of the magnet which is 35.65mm. This results in a pole arc of 120^0 (electrical) (a coverage factor of 0.67) which is acceptable, and reduces the volume of PM material.

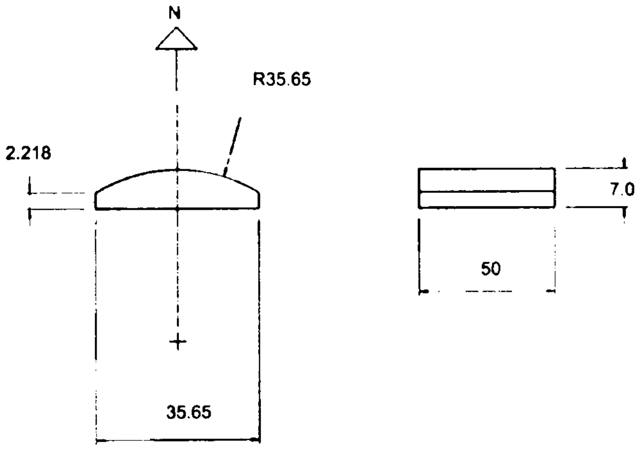

Figure 4.1. The *NdFeB* permanent magnet shape. Magnet material is grade *N38H*. The outside radius is 35.65mm.

In this research a direct and simple method of calculating the flux density in the air-gap is used. This direct method depends on demagnetisation curve of the PM material and the magnet dimensions. The permanence coefficient P_c is [4.1]

$$P_c = \frac{L_m}{gC_o} \tag{4.1}$$

where L_m is magnet width, g is air gap length (1 mm) and C_o is concentration factor which is defined as

$$C_o = \frac{A_m}{A_g} = 0.6667 \tag{4.2}$$

where A_m is the air-gap surface area of the magnet and A_g is the total air-gap surface area. Using (4.1) with a magnet useful thickness L_{um} =5.1mm, and the value of concentration factor C_o =0.67, the permanence coefficient, P_c, is 7.6

Using the demagnetisation curve of the *N38H* grade material at a temperature of 120°C, and plotting the 'load line' value of P_c calculated by (4.1), the maximum flux density is 0.95T and magnetisation force equal 143 kA/m as shown by the dotted lines in figure 4.2. The total useful magnet area, A_{um}, is calculated at a radius, R_{rr}, of 33.74mm [4.2] and is:

$$A_{um} = 2 \times \pi \times C_o \times R_{rr} \times L_{stk} = 7067\ mm^2 \qquad (4.3)$$

The air gap area, A_g, is 11200mm^2 calculated at a radius of 35.65mm.

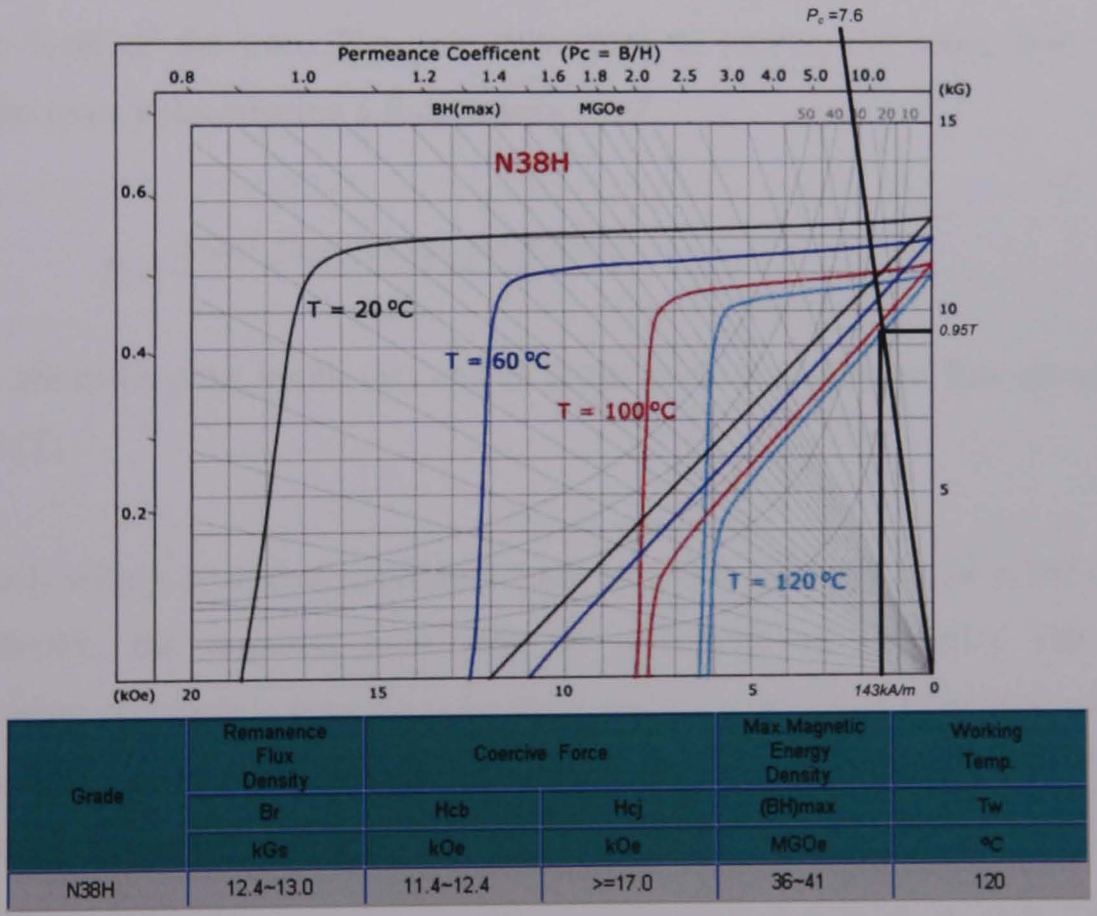

Grade	Remanence Flux Density	Coercive Force		Max Magnetic Energy Density	Working Temp.
	Br	Hcb	Hcj	(BH)max	Tw
	kGs	kOe	kOe	MGOe	°C
N38H	12.4~13.0	11.4~12.4	>=17.0	36~41	120

Figure 4.2. Demagnetisation curve of *N38H NdFeB* magnet material showing the operating point which is the intersection of the 120°C demagnetisation curve and the line representing the permanence coefficient of 7.6.

(KO_e =79.6 kA/m, KG = 0.1 T)

Since the useful magnet area and flux density are known, the useful flux per pole is calculated as:

$$\phi = B_m \frac{A_{um}}{4} = 0.95 \times \frac{7067 \times 10^{-6}}{4} = 1.68\, mWb \qquad (4.4)$$

The specific magnetic loading (*B*), which represents the average flux density over the rotor surface, is

$$B = \frac{flux\ linkage\ per\ pole \times no\ of\ poles}{\pi D_r L_{stk}} = \frac{1.68 \times 10^{-3} \times 4}{\pi \times 0.0713 \times .05} \approx 0.6T \quad (4.5)$$

where D_r is rotor diameter and L_{stk} is rotor length.

Rotor back iron (rotor yoke) width is chosen to keep the flux density below the saturation level of the iron. The pole flux splits in half in the rotor, and circulates through the rotor yoke creating a flux density B_t of:

$$B_t = \frac{Total\ flux\ \text{linkage per pole}/2}{w_r L_{stk}} \qquad (4.6)$$

where w_r are rotor yoke width (m) and B_t is the desired maximum flux density in the rotor iron (T).

Using (4.6), with a specified maximum back iron flux density, B_t, of 1.55T and total flux 1.68m*Wb*, the required rotor yoke is calculated as 10.83mm. For ease of manufacturing, the shaft is selected to be 9mm and the rotor yoke 10.65mm, resulting in maximum flux density of 1.58T in the rotor yoke. The final dimension of the rotor lamination is shown in figure 4.3.

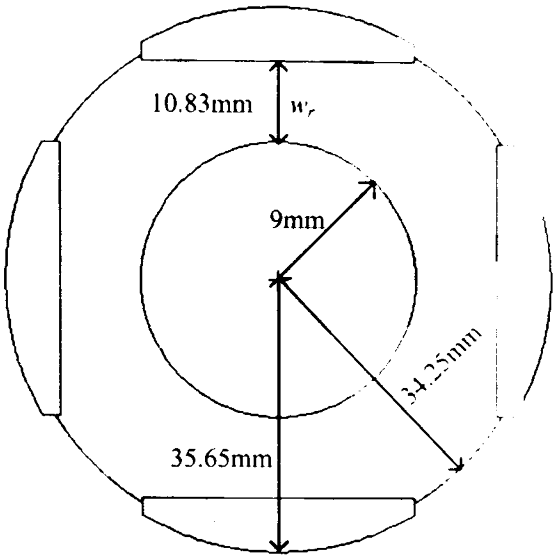

Figure 4.3. Finalised rotor lamination design.

4.4 Basic stator dimensions

This section determines the stator topology based on the calculated rotor parameters. From section 4.3 the rotor radius is 35.65mm. The chosen air-gap is 1mm, thus the inner radius of stator bore is 36.65mm. This results in a stator bore circumference of 230.28mm. The number of stator slots is chosen to be 30 slots so that the stator can use either a three-phase or five-phase winding configuration.

The stator tooth width is calculated based on the total flux crossing the air-gap and the air-gap flux density. The tooth flux density is adjusted to keep the flux density below saturation. The flux in each tooth is the total air-gap flux divided by the number of teeth. If the required tooth flux density is B_{th} then

$$w_t = \frac{\textit{Total air - gap flux/ number of teeth}}{B_{th} L_{stk}} \tag{4.7}$$

where w_t is the tooth width and B_{th} is tooth flux density.

The total air-gap flux is 27.2mWb, the number of teeth is 30 and maximum flux density in the tooth is chosen as 1.75T. Therefore the tooth width, w_t, is 3.8mm.

The stator back iron, w_y, is calculated to be 9.66mm using similar methods to calculate rotor yoke.

4.5 Stator slot design

A larger slot opening is desired to make winding insertion easier. However, a large slot opening can decrease the machine efficiency and increase cogging torque hence noise. The slot opening is selected to be 2.21mm which provides an opening adequate for winding insertion. This results in a total slot opening of 66.3mm around the stator bore circumference. The slot opening provides a tooth shoe of 5.57mm.

The shape of the back of the slot is generally either a square bottom or a round bottom. The round bottom is a preferred shape for manufacture by automatic winding machines. In this research a round bottom is selected with radius 3.1mm. The slot depth, d_{sh}, is 13.91mm. This is determined by the stator back iron, w_y, stator outer diameter, D_o, and stator inner diameter, D_i. The dimensions are shown in figure 4.3 with the outer diameter (121.2mm) chosen to suit a standard 48 range frame from LEMAC who fabricated the test machine and experimental rig. The slot area is 79.13 mm^2 per slot given the dimensions in figure 4.4.

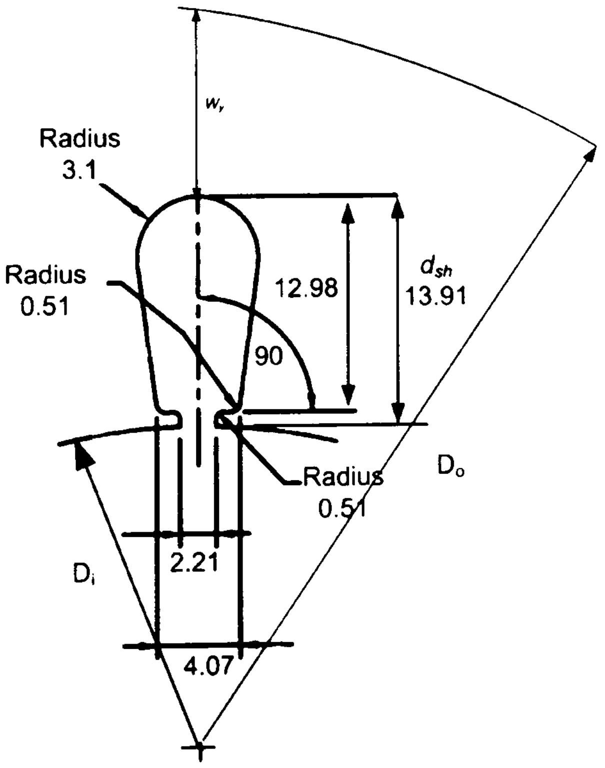

Figure 4.4. The round bottom slot dimensions shows the shape of slot end, depth and slots opening (all dimensions in *mm*)

The proposed design has no mounting holes in the stator. But due to manufacturing constraints, four bolt holes are located in the stator back iron to locate the machine end-caps. Steel screws are used in the holes in an attempt to reduce the effect of the holes on the magnetic field distribution. However, the holes have a significant effect on the flux density distribution in the lamination. The final dimension of the stator lamination is shown in figure 4.5.

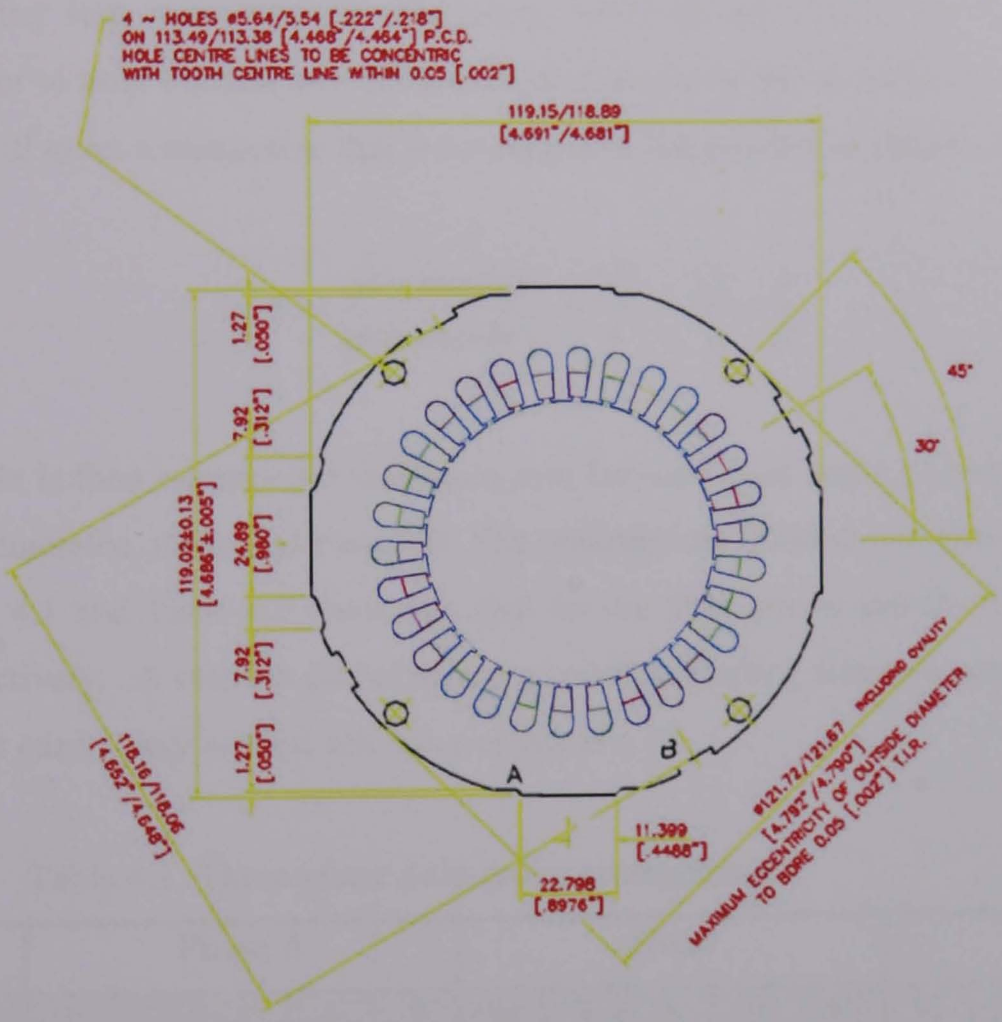

Figure 4.5. Finalised stator lamination design.

4.6 Winding configuration

The prototype generator has 30 stator slots and 4 rotor poles. The number of slots per pole is non-integral and is 7.5. This type of machine called "*a fractional-slot machine*", [4.1]. Each slot has two coils in a double-layer winding configuration in the fractional-slot machine. There are many methods to design a fractional-slot winding. A procedure that gives general results for double-layer windings, which tends to minimize the build-up of phase displacement is presented in [4.1]. A pole-group arrangement is described in [4.3] for double-layer winding of the two sets of pole groups around the fractional-slot. The distribution factor is determined and depends on the pole-group arrangement.

In this thesis, the winding configuration is developed by combining the procedure in [4.1] and pole group arrangement of [4.3]. This method eases the winding configuration, and also gives good results for a double-layer winding. The procedure is now described. The first step is to arrange pole-groups [4.3] by calculating the fraction, F, of slot number to pole number and reducing this fraction to the lowest pair of whole numbers that still gives a numerator that is a multiple of the number of phases. In this case

$$F = \frac{slot\ number}{pole\ number} = \frac{30}{4} \Rightarrow \frac{15}{2} = \frac{y}{x} \tag{4.8}$$

A table is then constructed that has a row for each pole and a column number equal to the numerator, y, (in this case 15). The columns are divided into the number of phases. Table 4.1 and Table 4.2 show this step for the three-phase and the five-phase machine respectively. A cross is placed every x column (starting from the top left of the table). In this case, every second cell has a cross, as x =2.

Table 4.1. Three-phase pole-group arrangement.

poles	Phase A					Phase					Phase C				
	1	2	3	4	5	6	7	8	9	10	11	12	13	14	15
1	×		×		×		×		×		×		×		×
2		×		×		×		×		×		×		×	
3	×		×		×		×		×		×		×		×
4		×		×		×		×		×		×		×	

Table 4.2. Five-phase pole-group arrangement.

Poles	Phase A			Phase B			Phase C			Phase D			Phase E		
	1	2	3	4	5	6	7	8	9	10	11	12	13	14	15
1	×		×		×		×		×		×		×		×
2		×		×		×		×		×		×		×	
3	×		×		×		×		×		×		×		×
4		×		×		×		×		×		×		×	

The two tables demonstrate that both the three-phase and five-phase machine can be split into two identical sections (poles section 1 and 2, poles section 3 and 4). Each pole section occupies 15 slots.

The number of slots per phase for each pole group moving from left to right and row-by-row from upper left to lower right of table 4.1 and 4.2 are

For the three-phase stator

Pole-1			Pole-2			Pole-3			Pole-4		
a-	b-	c-	a-	b-	c-	a-	b-	c-	a-	b-	c-
3	2	3	2	3	2	3	2	3	2	3	2

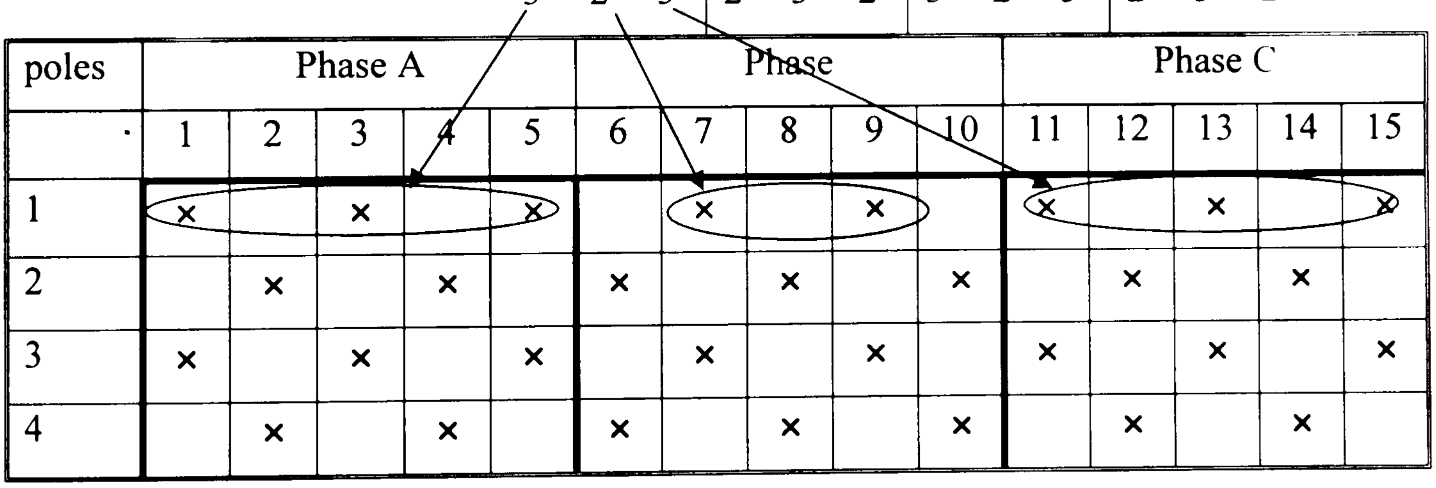

poles	Phase A					Phase					Phase C				
·	1	2	3	4	5	6	7	8	9	10	11	12	13	14	15
1	×		×		×		×		×		×		×		×
2		×		×		×		×		×		×		×	
3	×		×		×		×		×		×		×		×
4		×		×		×		×		×		×		×	

For the five-phase stator

Pole-1					Pole-2					Pole-3					Pole-4				
a-	b-	c-	d-	e-	a-	b-	c-	d-	e-	a-	b-	c-	d-	e-	a-	b-	c-	d-	e-
2	1	2	1	2	1	2	1	2	1	2	1	2	1	2	1	2	1	2	1

This means for the three-phase case, there are three coils for phase-*a*, two coils for phase-*b* and three coils for phase-*c* in pole 1. But in pole 2, there are two coils for phase-*a*, three for phase-*b* and two for phase-*c*. And for the five-phase case, for pole-1 there are two coils for phase-*a* and one for phase-*b*, two for phase-*c*, one for phase-*d* and two for phase-*e* . A similar process yields coil numbers for pole 2, 3 and 4.
The second step determines the winding configuration by using the method described in [4.1]. The number of slots per pole is calculated, (4.9), which is an integer, S, plus fractional number, f_r.

$$Cs = \frac{number\ of\ slots}{number\ of\ poles} = \frac{\mathrm{N_s}}{2p} \Rightarrow \frac{30}{4} = S + f_r = 7 + 0.5 \qquad (4.9)$$

S represents the maximum slot-pitch of each coil, which can be less than or equal to S. For the generators designed it equals 6 slots. If f_r is less than or equal to 0.5 the number of slots forward from the return coil-side of the previous phase coil to the go-side of the next coil in the phase winding is equal to maximum coil span plus one, and if it is more than 0.5, the number of slots forward equals the number of slots per section minus the maximum coil span. The number of slots per section is equal to the highest common factor of the number of coils per phase and pole-pairs. These rules are applied and all phase coils are located.

To locate the other phase coil sides the term *offset* is used which is defined as the number of slot-pitches in 2/3 of a pole pitch for the three-phase case and 2/5 of a pole-pitch for the five phase case. (In the three-phase case the phase windings are displaced from one another by 120° (electrical) and in the five phase case they are displaced by 72° (electrical)).

These rules and restrictions are programmed using Microsoft Excel allowing many configurations to be investigated using different coil spans. Three configurations are checked using FEA. The first configuration has a coil span of 7 slots, in the second configuration the coil span is 6 slots, and the third configuration has a coil span of 5 slots. On the basis of this investigation the coil span with 6 slots is selected as it displayed fewer harmonics in the back emf compared to the other two configurations. Tables 4.3 and 4.4 show the winding configuration of the three-phase and five-phase machines respectively.

Table 4.3. Three-phase winding configuration. The number in the 'go' and 'return' columns indicate slot number.

	Phase a		Phase b		Phase c	
coil	go	return	go	return	go	return
1	1	7	6	12	11	17
2	14	8	19	13	24	18
3	15	21	20	26	25	1
4	28	22	3	27	8	2
5	29	5	4	10	9	15
6	16	22	21	27	26	2
7	29	23	4	28	9	3
8	30	6	5	11	10	16
9	13	7	18	12	23	17
10	14	20	19	25	24	30

Table 4.4. Five-phase winding configuration. The number in the 'go' and 'return' columns indicate slot number.

	Phase a		Phase b		Phase c		Phase d		Phase e	
coil	go	return	go	return	go	return	go	return	go	return
1	1	7	4	10	7	13	10	16	13	19
2	14	8	17	11	20	14	23	17	26	20
3	15	21	18	24	21	27	24	30	27	3
4	16	22	19	25	22	28	25	1	28	4
5	29	23	2	26	5	29	8	2	11	5
6	30	6	3	9	6	12	9	15	12	18

The diagrams B3 and B4 in Appendix B show the distribution of coils in the stator slots. The figures show the coil span and the upper and lower coil sides in the stator slots. The winding distribution factor is calculated for the winding configuration using Tables 4.1 and 4.2 by replacing the cross by slots number from left to right. Only the first section is shown in tables 4.5 and 4.6 below to demonstrate.

Table 4.5. Two pole sections of table 4.1 for the three-phase machine. The cross is replaced by slot number.

	Phase A					Phase B					Phase C				
poles	1	2	3	4	5	6	7	8	9	10	11	12	13	14	15
1	1		2		3		4		5		6		7		8
2		9		10		11		12		13		14		15	

Table 4.6. Two pole sections of table 4.2 for the five-phase machine. The cross is replaced by slot number.

	Phase A			Phase B			Phase C			Phase D			Phase E		
poles	1	2	3	4	5	6	7	8	9	10	11	12	13	14	15
1	1		2		3		4		5		6		7		8
2		9		10		11		12		13		14		15	

The electrical span of adjacent slots is

$$\frac{360^{\circ}}{30/2} = 24^{o} \qquad (4.10)$$

From tables 4.5 and 4.6, the span between slot 1 and 9 is then

$$8 \times 24^{o} = 192^{o} \qquad (4.11)$$

This is equivalent to phase displacement between adjacent coils of

$$d = 192^{o} - 180^{o} = 12^{o}$$

The winding distribution factor is then calculated using

$$K_d = \frac{sinn(q \times d/2)}{q\, sinn(d/2)} \qquad (4.12)$$

where q is number of coils per group (3) and n is the harmonic number and d is phase displacement between adjacent coils (12°). Using (4.11), for the first harmonic the distribution factor is 0.98. This value is used to calculate the output coefficient of the generator in section 4.6.3.

4.6.1 Winding specification: number of turns per phase

Two stators were to be built: a three-phase and a five-phase stator both with winding configurations that give the same rectified output voltage at rated current and rated speed. Both these generators are connected to diode bridge rectifiers which have an average output dc voltage, neglecting diode voltage drop, as shown in Chapter 3, of

For the three-phase case $$V_{dc} = 1.63V_S \tag{4.13}$$

For the five-phase case $$V_{dc} = 1.87V_S \tag{4.14}$$

where V_s is the peak phase voltage.

In order to achieve equal average dc output voltages in both the three-phase and five-phase systems, the phase back *emf* in the three-phase generator has to be higher than the five-phase generator by factor of 1.15 (in the ideal case), ignoring stator impedance and voltage drop. However, in the practical system this factor depends on the generator's phase inductance and resistance. In this research, the factor is 1.125 and this was determined by a set of finite-element simulations that included estimated values of phase resistance, phase inductance and diode voltage drop. The five-phase machine was to have an output phase voltage of 48V peak, therefore the required three-phase generator phase voltage is 54V peak. The required no-load line back *emf* for the three-phase and for the five-phase generator is then

Back *emf* for three-phase, $$V_L = \sqrt{3} \times 54 = 93.5V \tag{4.15}$$

Back *emf* for five-phase, $$V_L = 1.902 \times 48 = 91.3V \tag{4.16}$$

The phase back *emf* constant k_e at a speed, ω_{NL}, of 1400rpm (146 rads^{-1}), is calculated for three and five phase systems,

$$K_e = \frac{V_L}{\omega_{NL}} \tag{4.17}$$

Three-phase back emf constant, $$K_e = \frac{93.5}{146.6} = 0.638 \quad Vs\, rad^{-1} \tag{4.18}$$

Five-phase back emf constant, $$K_e = \frac{91.3}{146.6} = 0.623 \quad Vs\, rad^{-1} \tag{4.19}$$

The number of turns per phase is calculated using

$$N_{ph} = \frac{EMF_{per-phase}}{\omega_{NL} \times D_r \times L_{stk} \times B_m} \tag{4.20}$$

where D_r=73.3mm, L_{stk}=50mm and B_m=0.95T.

Hence for the three-phase case, $N_{ph} \approx 110\, turns$

and for the five-phase case, $N_{ph} \approx 96\, turns$

The three-phase generator has 10 coils per phase; hence the number of turns per coil is 11 turns. The five-phase generator has 6 coils per phase; hence the number of turns per coil is 16 turns. These values generate a peak phase back emf of 48V for the five-phase generator and 54V for the three-phase generator.

4.6.2 Winding specification: Conductor diameter

The conductor diameter must be chosen to allow easy forming and insertion of each coil by hand. The required conductor diameter, D_w, can be calculated using

$$D_w \approx \sqrt{\frac{A_{slot} F_{slot}}{N_{coil}}} \tag{4.21}$$

where A_{slot}, F_{slot} and N_{coil} are slot area, slot fill factor and the number of conductors per slot respectively.

An achievable fill factor of 50% of the slot area (79.13 mm^2) is assumed, and the total number of conductors in a slot is double the coil number, as each slot has two layers.

Using these parameters the wire diameters are calculated as

$D_w \approx 1.34mm$ for the three-phase generator, and

$D_w \approx 1.11mm$ for the five-phase generator.

From the *AWG* table the wire gauge selected is *AWG 18* for five-phase with diameter 1.02mm and cross sectional area 0.82mm^2, and for three-phase is *AWG 16* with diameter 1.29mm and cross sectional area 1.31mm^2.

4.6.3 Winding specification: Generator current

The machine's rms rated current is defined as

$$I_{rms} = J \times A_w \tag{4.22}$$

where J is the achievable current density (A$_{rms}$ mm^{-2}), and A_w is the cross-sectional area of the conductor used in the coils.

The maximum current density of the conductor is assumed to be 5A$_{rms}$/mm^2; because the ventilation condition is poor (the stator is cooled by natural convection only).

The maximum *rms* current is then

$I_{rms} = J \times A_w = 5 \times 1.31 = 6.55 A_{rms}$ for the three-phase case

$I_{rms} = J \times A_w = 5 \times 0.823 = 4.5 A_{rms}$ for the five-phase case

The *specific electrical loading*, is 19299A/m for the three-phase and 19286 A/m for the five-phase, as shown in (4.23) and (4.24)

Three-phase specific electrical loading, $A = \dfrac{2 \times 3 \times N_{ph} I_{rms}}{\pi D_r} = 19299 A/m$ (4.23)

Five-phase specific electrical loading, $A = \dfrac{2 \times 5 \times N_{ph} I_{rms}}{\pi D_r} = 19286 A/m$ (4.24)

The specific electrical loading; *A*, and specific magnetic loading, *B*=0.6T, are known and equal. The output coefficient

$$\begin{aligned} K &= 1.74 K_w BA \\ &= 19746 \quad \text{for the three-phase case} \\ &= 19732 \quad \text{for the five-phase case} \end{aligned}$$

where K_w is the first harmonic winding factor (in this case, 0.98). That is both machines are designed to have same magnetic and electrical loading making the comparison between performance of three-and five-phase machines fair.

The shaft torque, *T*, can be calculated for both machines from

$$T = K D_r^2 L_{stk}$$

For the three-phase generator, $T = 19745.7 \times 0.0713^2 \times 0.05 = 5Nm$ (4.25)

For the five-phase generator, $T = 19732 \times 0.0713^2 \times 0.05 = 5Nm$ (4.26)

4.7 Generator Parameters

The parameters of the machine, such as winding resistance, self inductance and mutual inductance, need to be estimated in order to simulate the performance of the generators.

4.7.1 Winding resistance

The winding resistance depends on the length of the phase winding and conductor cross-sectional area. The Mean Length of a Turn (MLT) has four sections: two active sides (length equal to the stack length) and two end windings. The MLT is multiplied by the total number of turns per phase to define the length of a phase winding.

For the three-phase generator MLT is 32032mm and for the five-phase generator MLT is 27955mm. The cross-sectional area of the conductors is calculated in section 4.5. Using (4.27) the phase winding resistance for three-phase generator is 0.43Ω and for five-phase generator 0.6Ω.

$$R = \rho \frac{L_w}{A_s} \tag{4.27}$$

L_w is total length of conductor per phase including the end winding, ρ is conductor specific resistance (1.76×10^{-8} ohm-meter) and A_s is the cross sectional area of the conductor.

The total copper losses in the machine depend on the square of the total rms phase current, the number of phases, and the phase resistance. The phase winding copper loss in the three-phase generator is predicted to be 54.5W. For the five-phase generator it is 60.8W. The slightly higher value of copper loss for the five-phase generator is partly due to the use of a small conductor diameter (AWG 18) than ideally required.

4.7.2 Winding inductance

Each phase displays self-inductance and mutual-inductance with other phases. There are three components of self inductance [4.1], [4.2]:

1. the air gap component,
2. the slot-leakage component, and
3. the end-winding component.

i- Self inductance

The air-gap inductance can be directly calculated from the magnetic potential solution based on the flux linkage approach

$$L_a = \frac{\lambda_a}{i_a} \tag{4.28}$$

where λ_a and i_a are flux linking phase-a and the phase-a current respectively.

The flux linkage is calculated using

$$\psi_a = N_{ph}\theta_a \tag{4.29}$$

where N_{ph} is the total number of turn per phase and θ_a is the total flux linkage in the air-gap produced by winding current, i_a, which is approximated by

$$\theta_a = \frac{i_a \pi N_{ph} \mu_o L_{stk} r_1}{2p^2 g''} \tag{4.30}$$

where p is the pole pairs, g'' is the equivalent air-gap distance and includes the radial thickness of the magnet and the air-gap length with the stator slotting effect (Carter's coefficient) and equals.

$$g'' = K_c g + \frac{L_m}{\mu_r} \tag{4.31}$$

where K_c is Carter coefficient (see Appendix B), L_m magnet thickness and μ_r is recoil permeability of the magnet (and equals 1.1 from the specification of the magnet in figure (4.2)).

Using (4.30) and (4.31) the flux-linkage is

$$\psi_a = \frac{i_a \pi N_{ph}^2 \mu_o L_{stk} r_1}{2p^2 g''} \tag{4.32}$$

and the air-gap-inductance

$$L_a = \frac{\pi N_{ph}^2 \mu_o L_{stk} r_1}{2p^2 g''} \tag{4.33}$$

The end winding inductance is small compared to the self inductance and the value is approximated at 10% of the self inductance value. For the three- and five-phase machine the calculated self inductances are equal to 1.3mH and 1.2mH respectively.

ii- Mutual inductance

The electrical angle between two phases in the three phase generator is 120°(electrical). They are not in quadrature therefore there is non-zero value of mutual inductance between phases. It is important to calculate the mutual inductance as it has an impact on current commutation as the diode rectifiers commutates current from one phase to another [4.1] Due to the winding configuration, the mutual inductance in the three phase generator is

$$M = -\frac{L}{3} = M_1 \qquad (4.34)$$

where L is the total self inductance of the phase.

In a five-phase generator there are two values for the mutual inductance, a value between two adjacent phases and a value between two non-adjacent phases. As the electrical angle between adjacent phases is 72° the mutual inductance is expected to be small. It is indicated in figure 4.5 which represents phase-*b* coil sides placed in the flux generated by phase *a*. The flux-linking phase-*b*, due to phase-*a*, is shown as a shaded area in figure 4.6.

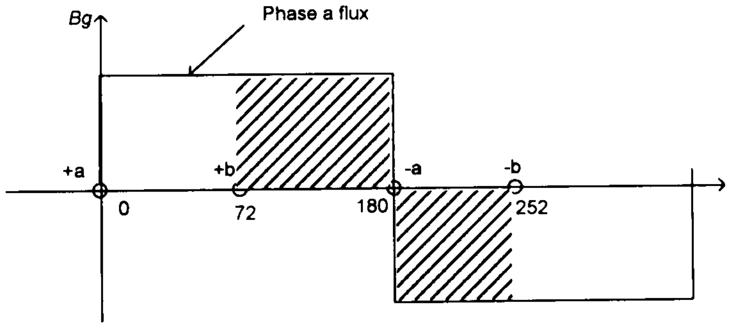

Figure 4.6. Showing the flux linking phase-*b* due to the flux generated by phase-*a*

The flux linking phase-*b* is calculated as

$$\psi_{ba} = \frac{\mu_o N_{ph}^2 L_{st} r_1}{2p^2 g''}\left[-\left(\frac{7\pi}{5} - \pi\right) + \left(\pi - \frac{2\pi}{5}\right)\right] = \frac{\mu_o i_a N_{ph}^2 L_{st} r_1}{2p^2 g''}\left[\frac{\pi}{5}\right] \qquad (4.35)$$

where N_{ph} and i_a are the number of turn per phase and phase-*a* current respectively.

The mutual inductance, M_{ba}, is then

$$M_{ba} = \frac{\psi_{ba}}{i_a} = \left[\frac{1}{5}\right] \frac{\pi \mu_o N_{ph}^2 L_{st} r_1}{2p^2 g''} = \frac{L}{5} \tag{4.36}$$

where L is the self inductance of the phase.

From this equation the mutual inductance between adjacent phases is 1/5 the self inductance and has positive value.

Using the same procedure above the mutual inductance between non-adjacent phases, for example, phase-*a* and phase-*c*, which are displaced by 144° (electrical) is approximately equal to 3/5 of the self inductance of a phase and has a negative value. Table 4.7 summarises the estimated generator parameters for the five- and three-phase generators.

Table 4.7 The five- and three-phase generators estimated parameters

	Three-phase	Five-phase
Phase resistance	0.43Ω	0.6Ω
Phase self-inductance	1.3mH	1.2mH
Adjacent phase mutual inductance	0.43mH	0.2mH
Non-adjacent mutual inductance		0.6mH

4.8 Finite Element Analysis

Finite element analysis is a commonly used method for electromagnetic field computation and analysis and allows nonlinear verification of the basic linear design carried out in the previous sections. The finite element method (FEM) is a numerical method for solving electromagnetic field problems which are too complex to be solved accurately using analytical techniques. Finite element analysis is based on dividing the heterogeneous medium into a large number of small elements. These elements are connected together at nodes. Within each element a simple polynomial is used to approximate the solution over the area of the element. The process to divide complex problems to elements is called discretisation or 'meshing'. Maxwell's partial differential equations are transformed into a large number of simultaneous nonlinear algebraic equations, which include the unknown node potentials. Iteration, such as Newton-Raphson method, is used to numerically solve the partial differential equations. In the software chosen to perform FEA the field distribution within each element follows a pre-defined function boundary. The field varies linearly between two nodes therefore the flux density is constant within each element.

Example of elements and nodes from the FEM mesh is shown in figure 4.7. The accuracy of the results from FEM is a function of the correct discretisation of the region, in particular, refining the mesh in regions where rapid spatial variation of the magnetic flux density is expected.

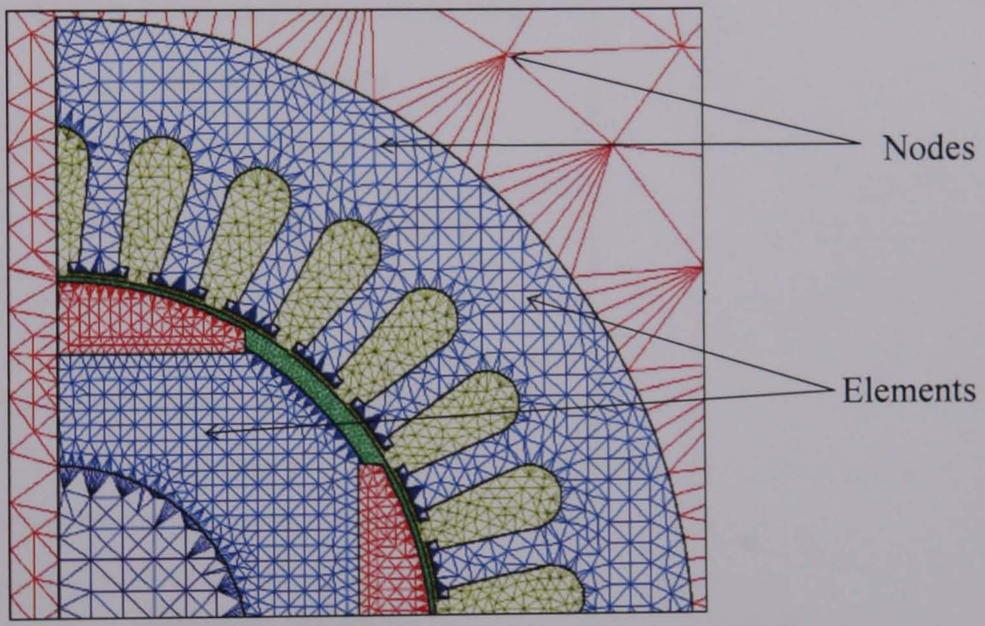

Figure 4.7. Mesh of a complex problem, showing the elements and the nodes

There are many finite element software packages available to help solve the electromagnetic problem. Most of these packages have three main components. The first one is a pre-processor in which the finite element model is created, geometric outlines are drawn, material properties are assigned, current source and boundary conditions are applied, and then the finite element mesh is created. The second component is the solver where the finite element problem is numerically solved. The final component is a post-processor where the magnetic field quantities are displayed, and quantities, such as energy, flux and force, are calculated.

4.9 Maxwell 2D Finite Element Analysis software

In this research, Maxwell 2D software is used to solve both static and transient problems. Maxwell 2D programme is divided into steps to enable the definition of the problem. These steps are summarised in figure 4.8

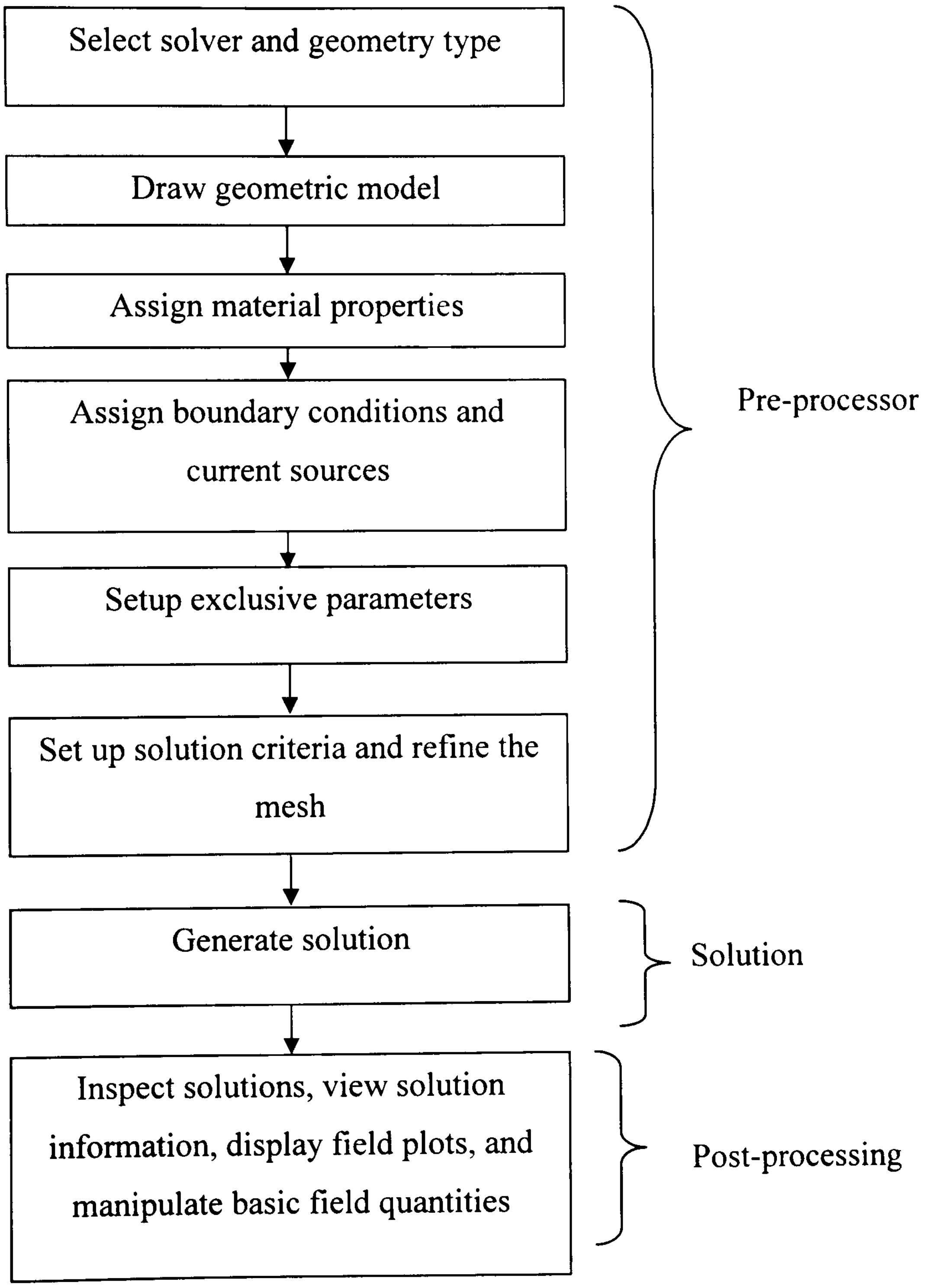

Figure 4.8. Summary of steps in Maxwell 2D software. Showing the three stages of FEA: Pre-processor, Solution, Post-processing.

4.9.1 Initial design data

The outline dimensions of the rotor and the stator dimensions determined in sections 4.3 and 4.4 is used to define the MAXWELL 2D geometric model.

The material used to define the stator and rotor lamination characteristics is *M800* and is based on the material supplied by the manufacturer. The B/H characteristic curve of this material is shown in figure 4.9.

The other materials used in object definition are:

- air,
- stainless steel for the shaft (μ_r=1),
- copper for windings, and
- the permanent magnet material, *N35H*.
-

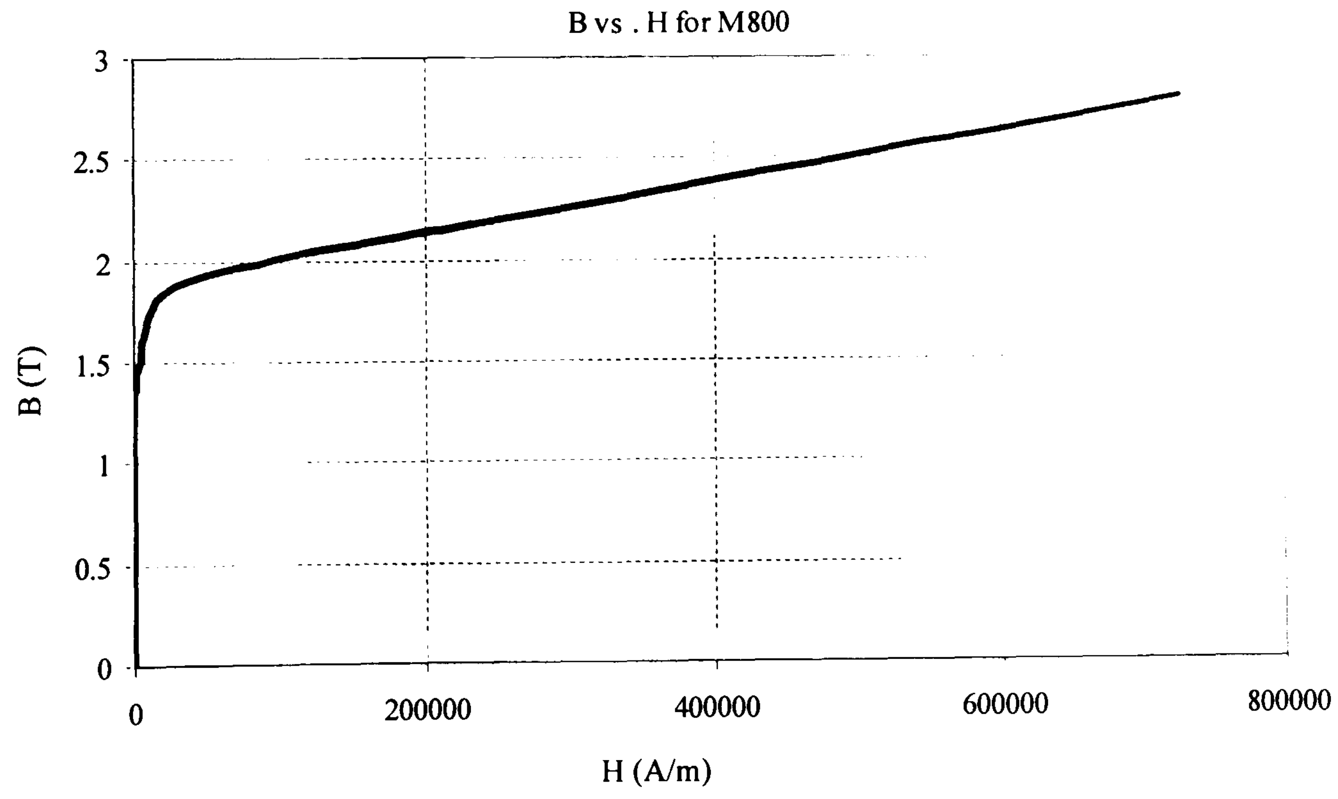

Figure 4.9 .The *B-H* characteristics of stator steel defined as *M800*

The flux density around the air-gap, through 360° electrical angle, is shown in figure 4.10. The figure shows the effect of the teeth on the shape of the flux density. The flux density has a maximum value near to 0.95 which agrees with the value calculated from linear analysis, section 4.3.

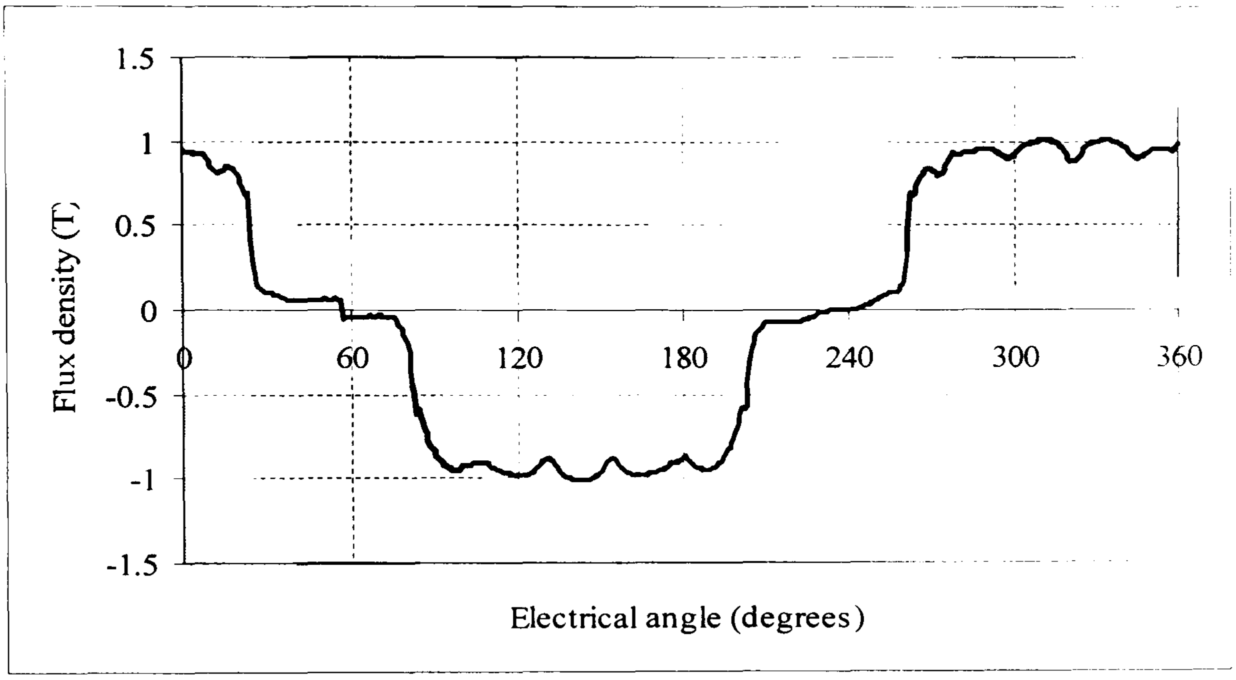

Figure 4.10. Flux density around the air-gap. The effect of stator slots and teeth on the shape of the flux density waveform is clear seen.

Figure 4.11 illustrates a flux density map of the geometry with no armature current and a fixed rotor position. As expected, the flux density in the slots is close to zero. It is clear from the figure that the flux density in the teeth agrees with the linear design, 1.75T. The figure also shows that the flux density around the stator mounting holes is around 2.5T, which is a saturated value. This then distorts the back EMF and the effect is different for each phase as will be discussed in section 4.11.

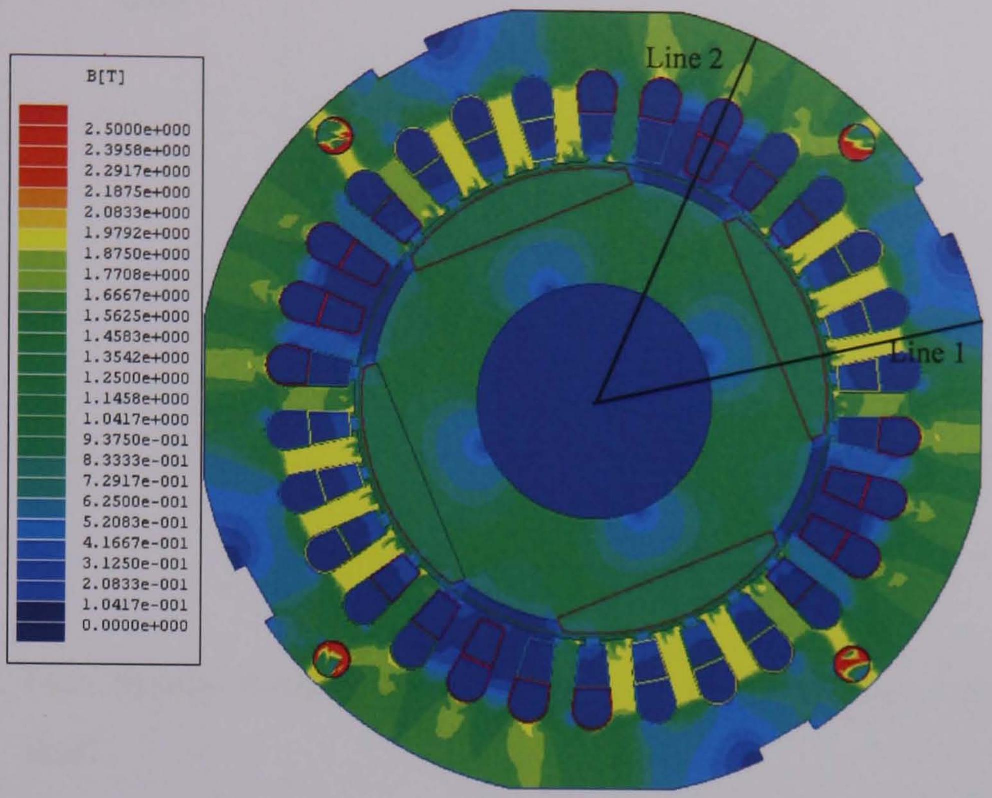

Figure 4.11. Flux density map of the machine with associated key. The maximum flux density, 2.5T. Two contour lines are shown, one through a tooth (line1) and the other through a slot (line2). These are used to plot flux density profiles in figure 4.12 and 4.13.

Figures 4.12 and 4.13 show the flux density plot along the two contour lines shown in figure 4.11. Figure 4.12 shows the flux density along line 1. The flux density has a zero value in the shaft as the shaft is non-magnetic. The maximum value of flux density in the tooth is 1.8T. This value is comparable to the linear design, 1.75T. Figure 4.13 shows the flux density along line 2 from the centre of the machine through a slot. The flux density in the slot is equal to zero. The maximum flux density occurs at the back iron, 1.75T, which agrees with the linear design value. It is clear from figure 4.10 to 4.13 that the flux density in the stator lamination does not reach a saturated value except for around the mounting holes in the stator.

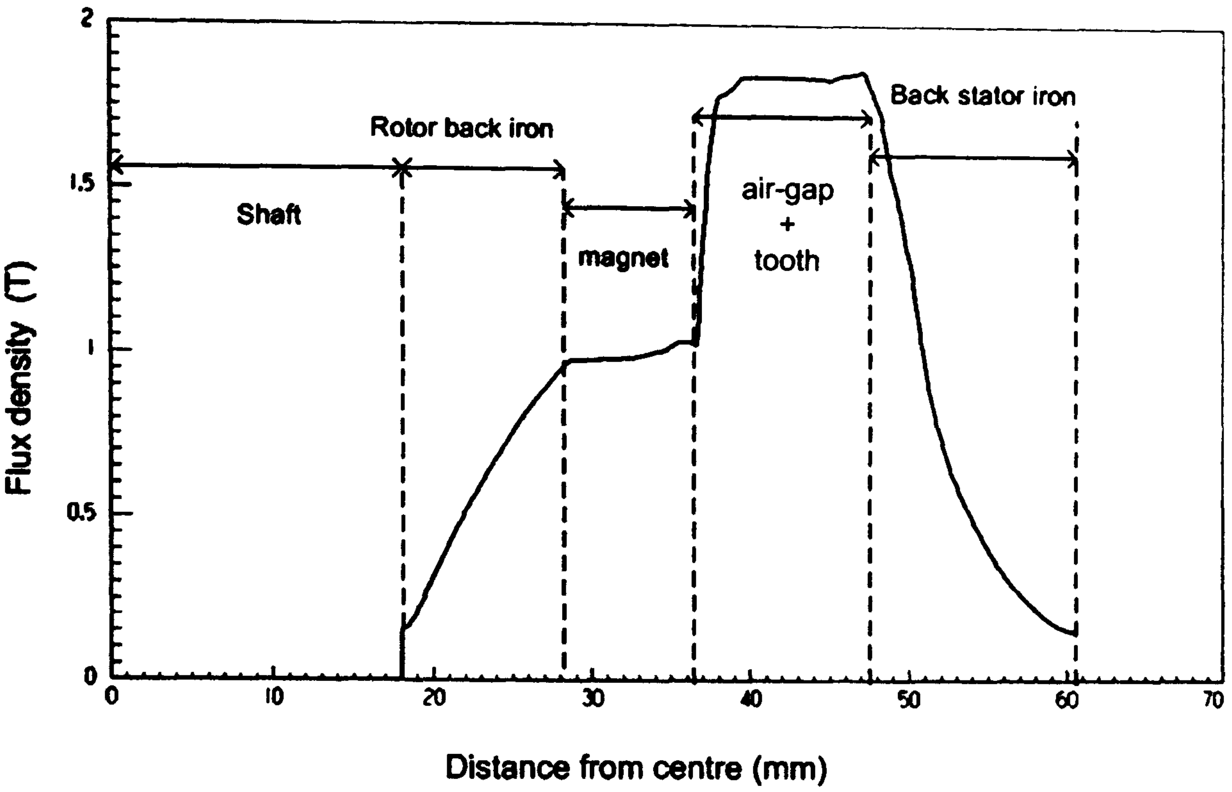

Figure 4.12. Flux density from the centre of the rotor to the outside of the stator along line1.

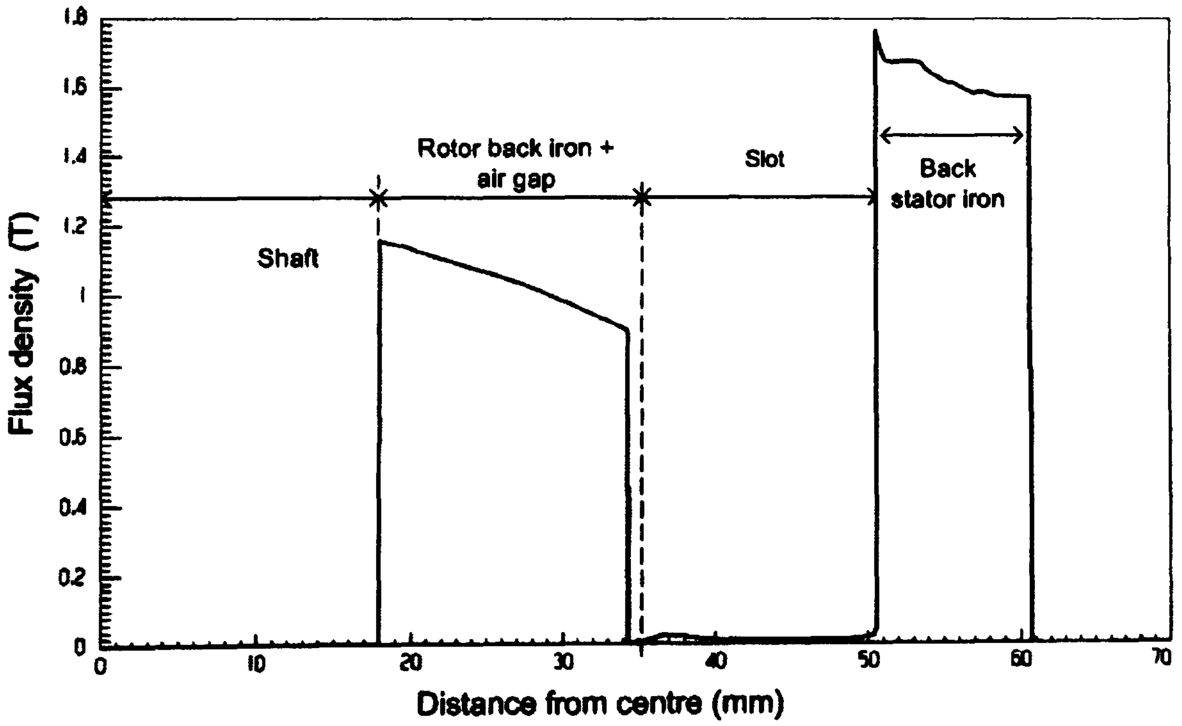

Figure 4.13. Flux density from the centre of the rotor to the outside of the stator along line2.

4.10 Cogging torque

Cogging torque is an important issue in permanent magnet machines and, as identified in Chapter 2, significant in deterring low speed start up of wind turbines [4.4]. Cogging torque is caused by the magnetic interaction between the rotor-mounted permanent magnets and the salient stator structure [4.5]. The salient stator structure changes the air-gap reluctance and results in periodic stable rotor positions. Many studies have investigated cogging torque reduction [4.6]-[4.10], such as reducing the magnet arc, skewing magnets or slots, auxiliary slots and teeth, and fractional slots. Many of these methods are expensive and reduce the flux and torque capability. The method used in this thesis combines fractional slots with a reduced magnet arc as described in section 4.1. The fractional slot is a good method to reduce the cogging torque [4.1]-[4.2], [4.10]-[4.11]. The cogging torque produced by the prototype machine is shown in figure 4.14 for one slot pitch and was estimated using FEA. This figure shows that the peak-to-peak cogging torque is 0.21Nm which represents 4.2% of maximum torque (5Nm).

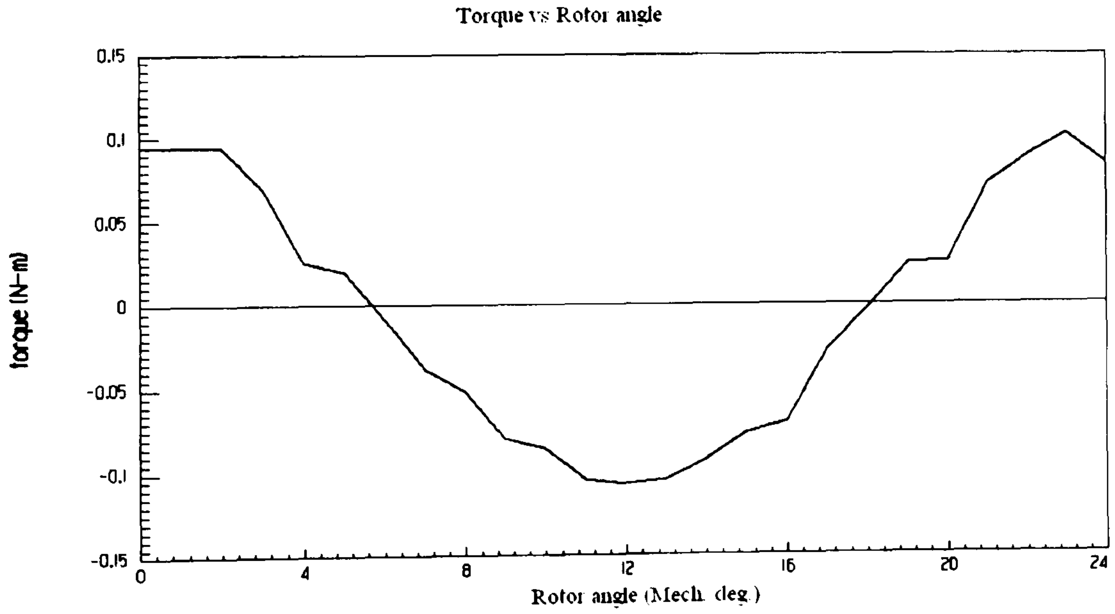

Figure 4.14. Cogging torque over one slot pitch for the unexcited 4-pole, 30-slot prototype generator.

4.11 No-load Back EMF

The no-load back EMF can be calculated from the distribution of magnetic field in the air-gap produced by the magnets. The calculation is performed on two designs: the proposed design, without mounting holes in the stator, and the practical design with mounting holes in the stator. Figure 4.15 and 4.16 show the back EMF for the three- and five-phase for the proposed design. The back EMF of the five-phase generator has a flat top equal to 45° and the three-phase generator has a flat top equal to 54°. It is clear from the figures that in the five-phase generator each phase is displaced by 72° (electrical) and in the three-phase generator each phase is displaced by 120° (electrical). This confirms the winding configuration in section 4.6. The peak phase voltage is 48V for the five-phase generator and 55V for three-phase generator. These are close to the design values in section 4.6

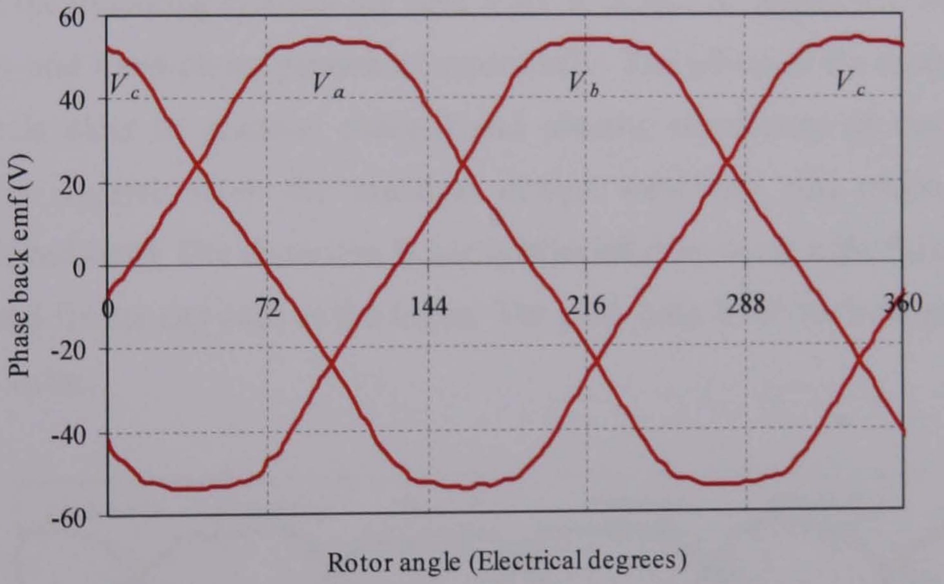

Figure 4.15. Back emf waveform of the three-phase generator at 1400rpm for the proposed design.

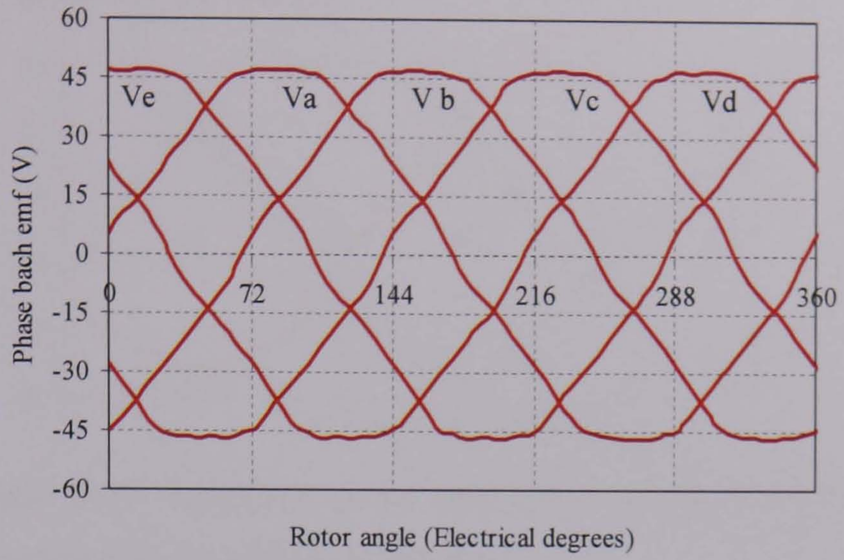

Figure 4.16. Back emf waveform of the five-phase generator at 1400rpm for the proposed design.

The effect of the mounting holes in the back EMF is shown in figures 4.17 and 4.18 for both the five- and three-phase generator respectively. The effect of the mounting holes in the stator is clear in phase-*e*, phase-*d* and phase-*c* waveforms in the five-phase generator. The figures show the practical design waveform and proposed design waveform (dotted line). The distortion is partly alleviated by using tight fitting steel rod to orientate and fix the end caps to the frame. The peak back EMF for both generators is the designed value.

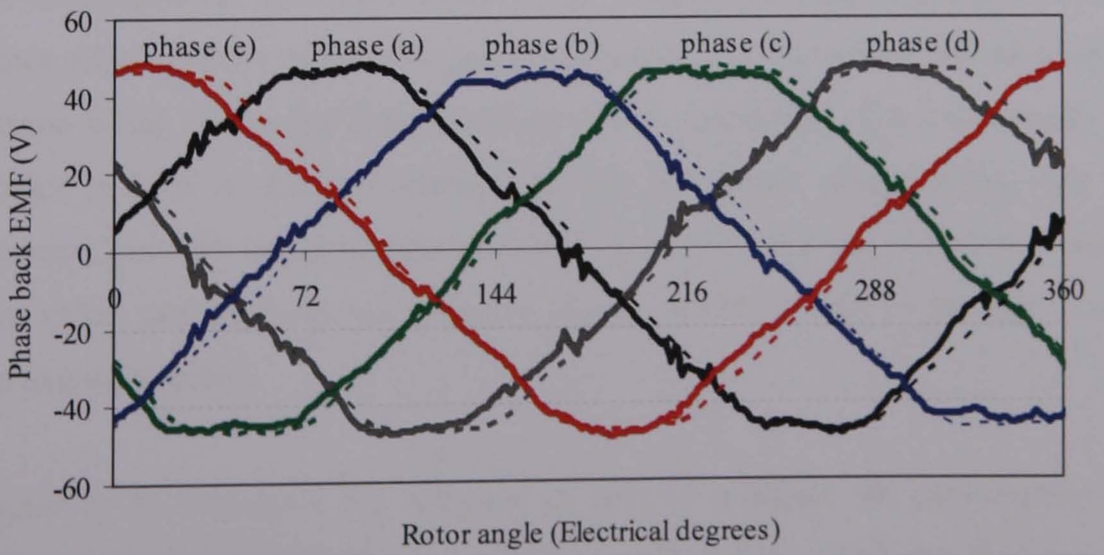

Figure 4.17. Back EMF waveform of the five-phase generator at 1400rpm for the practical design and proposed design.

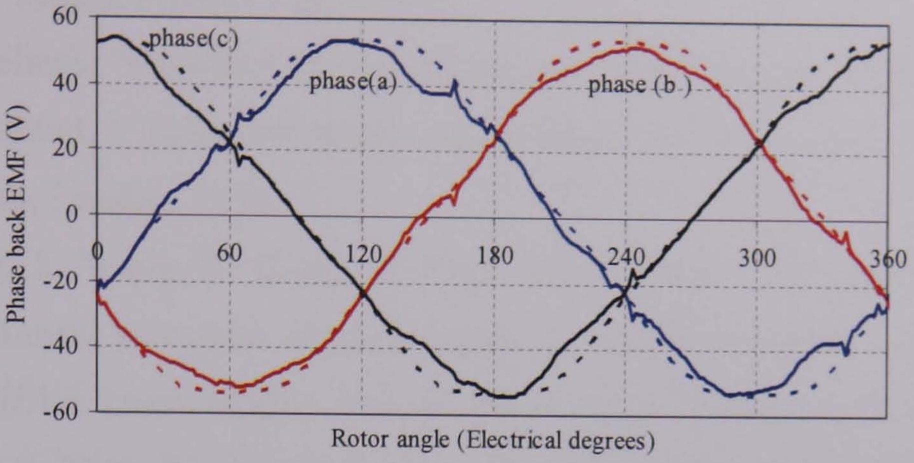

Figure 4.18. Back EMF waveform of the three-phase generator at 1400rpm for the proposed design and proposed design.

4.12 Summary

In this chapter, the three-phase and five-phase permanent magnet generators are designed. Linear design is performed first, using the PM magnetisation curve and simple analytical methods. Winding configurations for both generators are proposed to give the same rectified output dc voltage and power.

The conductor size and the number of turns per phase is calculated using the linear design technique and is checked using FEA. The phase resistance, self inductance and mutual inductance are estimated using linear design. The three-phase generator has a resistance which is 65% of the five-phase generator. The five-phase generator has a self inductance which is 8% less than the three-phase counterpart. The three-phase mutual inductance is 30% of the self inductance. The five-phase generator has two mutual inductances; between adjacent phases, which is 20% of the self inductance and has a positive value, and between non-adjacent phases, which is 60% of the self inductance (with a negative value).

In chapter 5, the Maxwell 2D software is used to evaluate the performance of the generator when connected to the diode bridge rectifier with a resistive load and dc link capacitor and uses the software's transient solver.

References

[4.1] J. R. Hendershot and T. J. E. Miller, "Design of brushless permanent magnet motors," Magna Physics Pub., 1994

[4.2] C. Hanselman, "Brushless Permanent-magnet Motor Design" McGraw-Hill. 1994

[4.3] C. S. Siskind, " Induction motor: single-phase and poly-phase." McGraw-Hill. New York, London, 1958

[4.4] Y. Yang, X. Wang, R. Zhang, T. Ding, and R. Tang, "The Optimization of pole arc coefficient to reduce cogging torque in surface mounted Permanent magnet motor," IEEE Trans. Magn., Vol. 42, No. 4, April 2006. pp.1135-1138.

[4.5] Y. Wang, J. Shen, W. fei, and Z. Fang, "Reduction of cogging torque in permanent magnet Flux-switching machines," J. Electrical Analysis and Applications, March 2009, pp 11-14.

[4.6] C. Studer, A. Keyhani, T. Sebastian, S. K. Murthy. "Study of Cogging Torque in Permanent Magnet Machines," Industry Applications Conference, 32th IAS Annual Meeting, New Orleans, Louisiana, USA. Vol. 1. Oct. 4-9, 1997, pp. 42-49.

[4.7] Z.Q.Zhu, D. Howe, "Influence of design parameter on cogging torque in permanent magnet machine," IEEE Trans. on Energy Conversion, Vol.15. No.4. December 2000, pp. 407-412.

[4.8] S.A. Saied, K. Abbaszadeh, S. Hemmati, and M. Fadaie, "A New Approach to Cogging Torque Reduction in Surface-Mounted Permanent-Magnet Motors." European Journal of Scientific Research, Vol. 26, No.4, 2009. pp. 499-509.

[4.9] S. M. Hwang, J. B. Eom, Y. H. Jung, D. W. Lee, and B. S. Kang, "Various Design Techniques to Reduce Cogging Torque by Controlling Energy Variation in Permanent Magnet Motors,'' IEEE Trans. Magn., Vol. 37, No.4. July 2001. pp. 2806-2809.

[4.10] P. Salminen, M. Niemela, J. Pyrhonen, and J. Mantere, "Performance Analysis of Fractional Slot Wound PM Motors for Low Speed Applications," Industry Applications Conference, 39th IAS Annual Meeting, Vol. 2. Oct. 3-7. pp. 1032-1037.

[4.11] A. M. El-Refie, T. M. Jahns, and D. W. Novotny. "Analysis of Surface Permanent Magnet Machines With Fractional-Slot Concentrated Windings." IEEE Trans. on Energy Conversion. Vol. 21, No.1. March 2006. pp. 34-43.

Chapter 5

Evaluation of the performance of the prototype five- and three-phase generators using FEA and experimental tests

5.1 Introduction

In this chapter, the performance of the prototype five- and three-phase PM generators, connected to diode bridge rectifiers, is evaluated using both the FEA and experimental tests. The Maxwell 2D software discussed in Chapter 4 is used for FEA.

FEA analysis is performed on two designs. One design does not have the four mounting holes in the stator lamination (the 'proposed design') and the second design includes the mounting holes (the 'practical design'). The results for both designs are discussed in sections 5.2 and 5.3. A comparison between the five- and three-phase systems is presented. Section 5.4 considers the impact of introducing the mounting holes in the stator. The mounting holes were an undesired addition made by the manufacturer during the fabrication process. Unfortunately, they have a significant impact on the performance of the two machines, particularly the 5-phase generator, which will be discussed.

The two stator stacks with windings were fabricated and could be interchanged within a common stator frame (one stator stack for the five-phase generator and the other stator stack for the three-phase generator). The 4-pole rotor designed in chapter 4 is also common to the five- and three-phase generator. A test rig was constructed to assess the performance of the permanent magnet generators connected to associated diode rectifiers and a comparison made between the five- and three-phase system.

In section 5.5 of this chapter, the generator iron losses and the generator parameter measurements are discussed. The generators are connected to diode bridge rectifiers with resistive loads and a dc link capacitor. The shaft torque and shaft power are estimated from the instantaneous phase currents and back emfs. The dc output voltage and power are measured under full load conditions. The results from the five-phase system are compared with the results from the three-phase system and are discussed in section 5.6. The significant outcome of the testing is that the five-phase system has improved performance in terms of shaft torque ripple compared to the three-phase system.

5.2 Simulation using finite element analysis

The Maxwell 2D transient solver is used to analyse the performance of the two systems and has a feature to connect external electrical circuits to the phase windings. This provides a means of coupling the electromagnetics of the generator to the electrical circuit characteristics of the diode rectifier. This allows variables such as shaft torque, phase current and rectifier output voltage to be accurately simulated and assessed. The five- and three-phase systems are analysed both for the proposed design and the practical design. The mounting holes of the practical design effect the phase back emf waveform. The FEA results from the practical design are compared with the experimental results and comparison made on both the AC side and DC side. The AC side comparison includes the generator shaft power, shaft torque and phase currents, and the DC side compares the output dc voltage, load power and capacitor current.

5.3 FEA results of proposed design

The phase back emf voltages of the five- and three-phase systems are shown in figure 5.1. The five-phase back emf has waveform with a 45° (electrical) flat top. The three-phase back emf has a 54° (electrical) flat top. The resultant non-adjacent line voltage in the five-phase system and the line voltage in the three-phase system are shown in figure 5.2(a) and (b) respectively. Figure 5.2 shows only two line voltages, the remaining line voltages have the same waveshape. From figure 5.2, the output voltage from the rectifier is expected to have a peak-to-peak ripple in the ideal case (that is, without Dc link capacitor and generator self- and mutual-inductance) of 8.7% of the peak value in the five-phase system. In the three-phase system this would be 21% of the peak value. Therefore, more capacitance is required in the three-phase system to achieve the same output voltage ripple. The FEA results confirm the findings reported in Section 3.3.1 for the developed model.

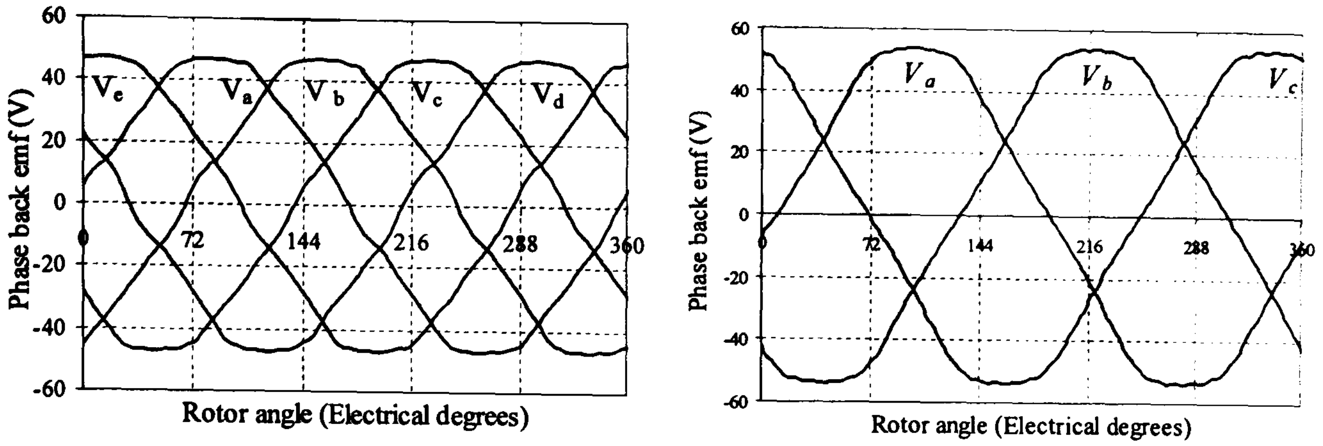

(a) (b)

Figure 5.1. FEA back emf (phase) for the five-phase and three-phase generators on no load, for the proposed design, (a) five-phase (b) three-phase.

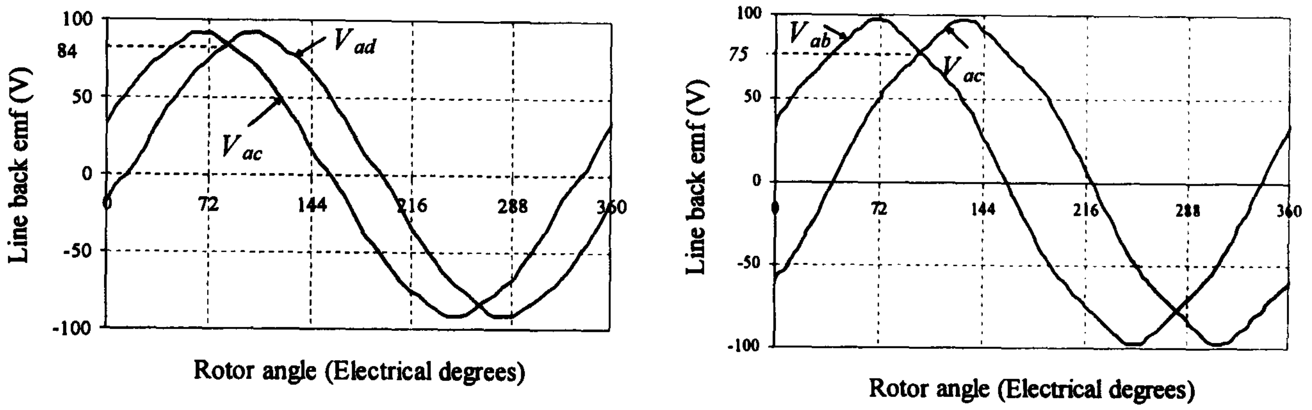

(a) (b)

Figure 5.2. FEA back emf (line) for the five-phase and three-phase systems on no load, for the proposed design, (a) five-phase (b) three-phase

5.3.1 Generator shaft torque, power, and phase current

Figure 5.3 shows the generator shaft torque for the five- and three-phase systems at full load with a dc link capacitor of 470μF for the five-phase system and 2200μF for the three-phase system. The speed of the generator shaft is 1400rpm for both generators. The peak-to-peak ripple in the five-phase system (0.7Nm) is approximately 15% of the average torque (4.7Nm). The peak-to-peak ripple for the three-phase system is 34% of the average torque (4.6Nm). It is observed from the figure that the generator torque has fundamental frequency for the five-phase system equal to ten times the generator frequency and for the three-phase system it is six times. The generator noise and vibration will be significantly greater in the three-phase system when compared with the five-phase system. Firstly, as the magnitude of the torque ripple is higher in the three-phase system. Secondly, the low pass filtering effect the mechanical system attenuates the vibration more in the five-phase case as the frequency of the torque ripple is higher.

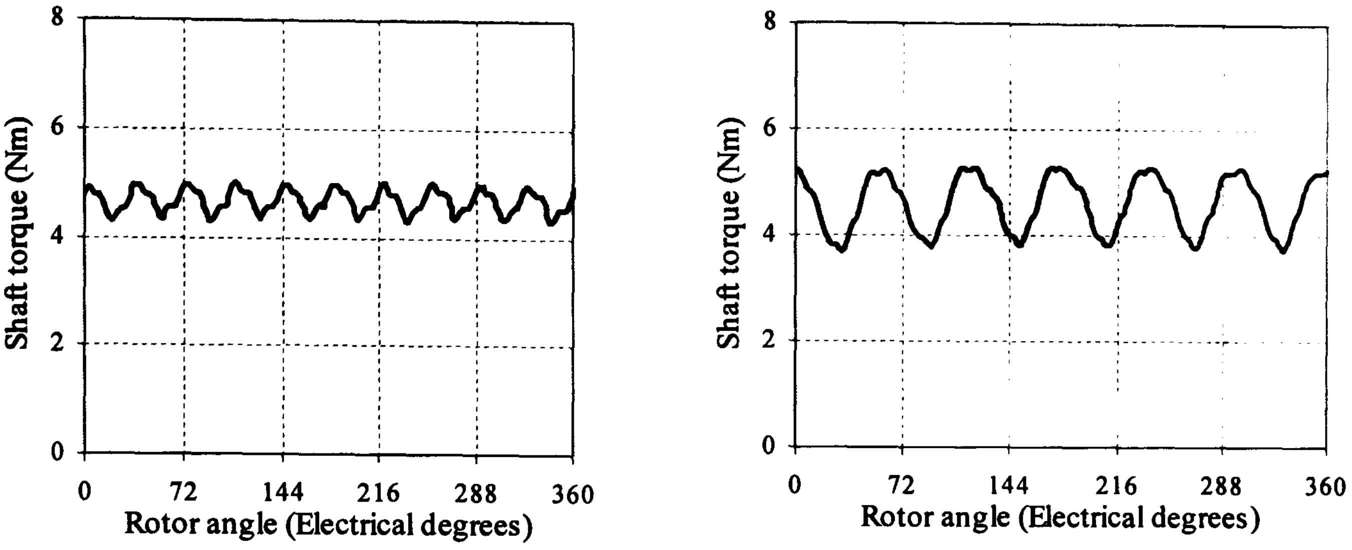

(a) (b)

Figure 5.3. Generator shaft torque for the proposed design using FEA (a) five-phase system, and (b) three-phase system.

Figure 5.4 shows the input shaft power to the generator for the five- and three-phase systems. The peak-to-peak ripple for the three-phase system (233W) is approximately 34% of average value (674W). It is clear from the figure that the five-phase system has a lower peak-to-peak ripple compared to the three-phase system (a factor 2.2 of lower). This is a significant advantage of the five-phase system over the three-phase system.

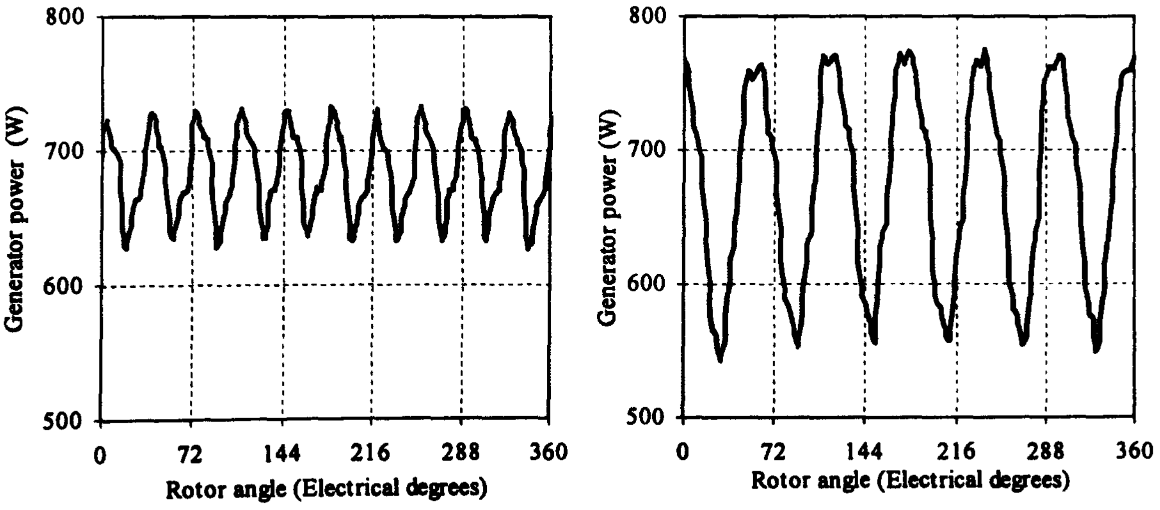

(a) (b)

Figure 5.4. Input shaft power to the generator for the proposed design using FEA (a) five-phase system, and (b) three-phase system.

Figure 5.5 shows phase-*a* current in the five- and three-phase systems. The RMS currents are 4.5A and 6.5A for the five- and three-phase generators respectively. This is the rated RMS current for both generators. As expected the RMS value of the phase current of the three-phase system is 30% higher than the five-phase system. The commutation angle in the five-phase system is equal to 19° (electrical) and for the three-phase is 18° (electrical) which are close to the simulation results (23.3° for the five-phase system and 19.8° for the three-phase system).

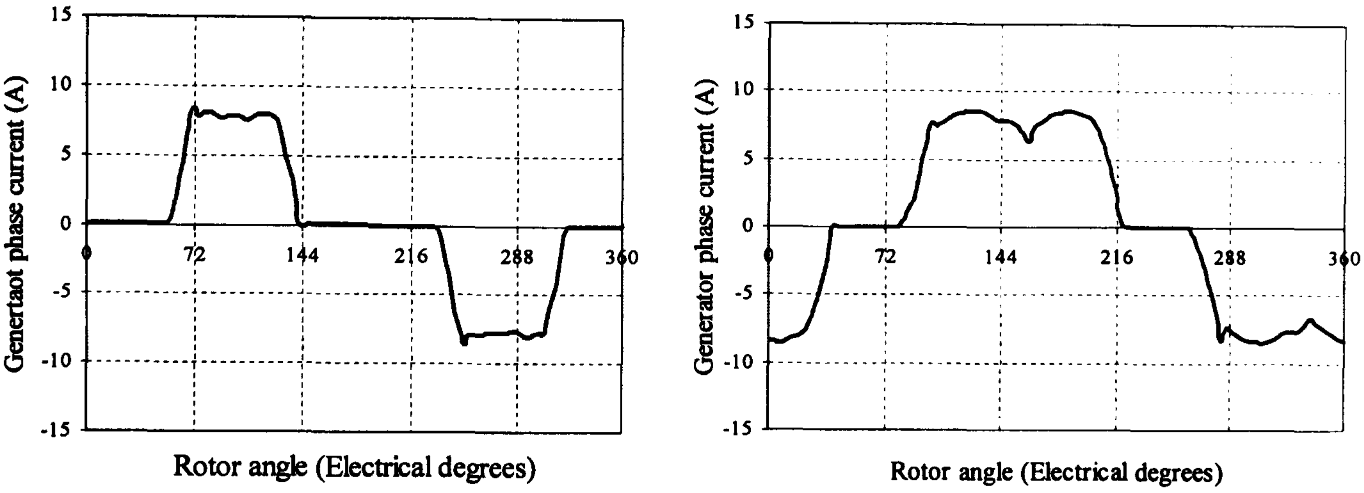

(a) (b)

Figure 5.5. Phase-*a* current in the generator for proposed design using FEA (a) five-phase system, and (b) three-phase system.

The diode current for the five- and three-phase systems is shown in figure 5.6. The diode in the five-phase system conducts for a period of 92.5° and in the three-phase conducts for 138°. The diode rms current in the five-phase system (1.6A) is 48% lower than the three-phase system (2.9A). The diode losses are calculated using

$$P_{diode\ loss} = \int_{t_1}^{t_2} V_d(t) I_d(t) dt \qquad (5.1)$$

where $V_d(t)$ and $I_d(t)$ are the instantaneous diode voltage (0.8V) and current respectively, and t_1 and t_2 are the initiation and termination times of the diode conduction period. The diode losses in the three-phase system are a factor of 1.8 greater than the five-phase system. Even though the total number of the diodes in the five-phase system is higher than the three-phase system (10 compared to 6), the total diodes losses in the five-phase system (12.8W) are still lower than the three-phase system (14W).

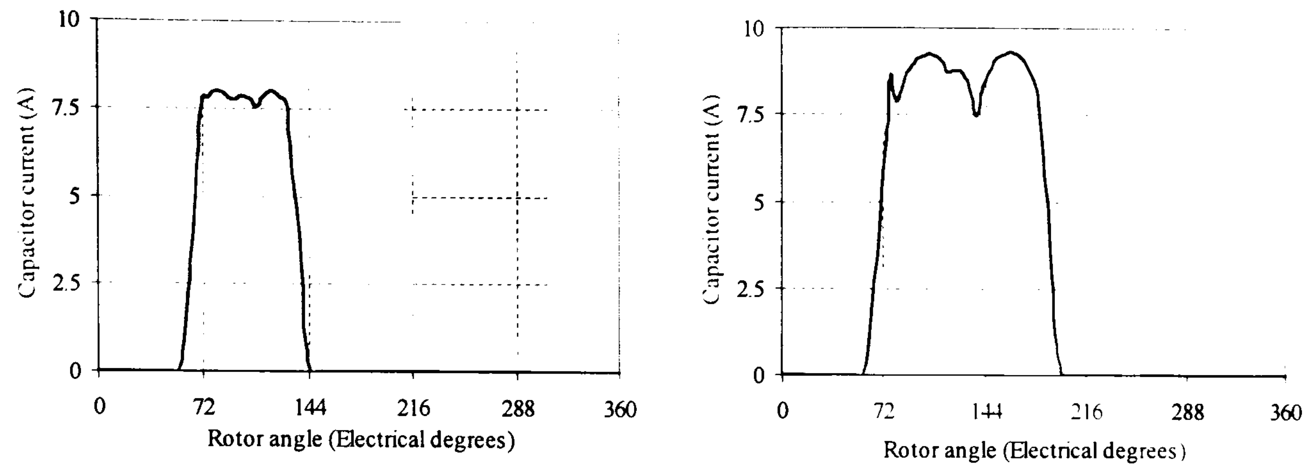

(a) (b)

Figure 5.6. Diode current for proposed design using FEA (a) five-phase system, and (b) three-phase system.

5.3.2 Dc output voltage and power

Figure 5.7 illustrates the output voltage of the diode rectifier for the five- and three-phase systems. The Dc link capacitor in the five-phase system (470μF) was chosen to give a similar voltage ripple to the three-phase system using a 2200μF dc link capacitor. The five-phase peak-to-peak voltage ripple is 0.4V at rated load. The peak-to-peak ripple in the three-phase system is only slightly higher than the five-phase system (about 16% higher). The lower voltage ripple is the five-phase case is due to the flatter top in the phase back emf of the five-phase generator as shown previously in figure 5.2. The three-phase system requires more capacitance for the same ripple voltage or a higher magnet coverage factor. This leads to higher cost. Hence the five-phase system will generate less peak-to-peak output voltage ripple compared to the three-phase system with the same magnet material.

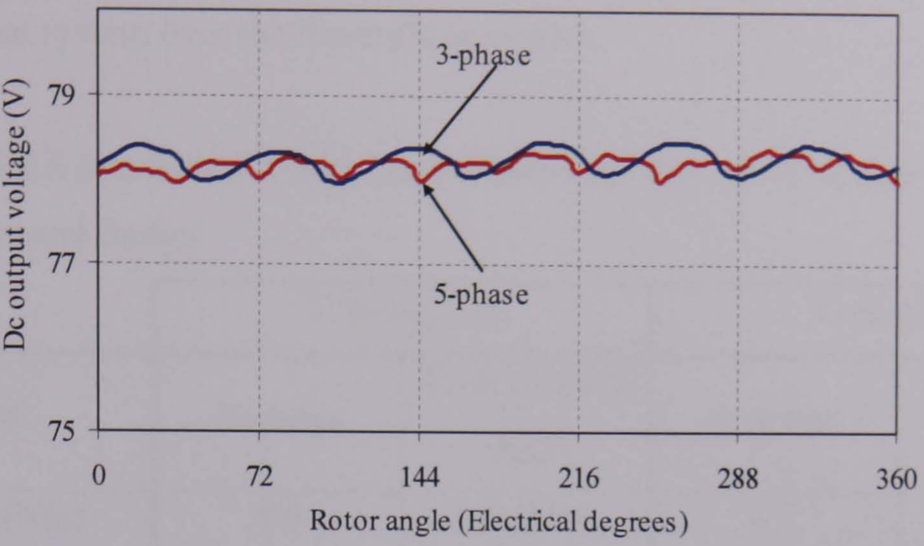

Figure 5.7. Dc output voltage from FEA without mounting holes in the stator.

Figure 5.8 shows the dc load power for the five- and three-phase systems. The average load power in both systems is nearly the same value. From these figures the peak-to-peak ripple in the dc power delivered by the five-phase system is 0.4 of the three-phase system.

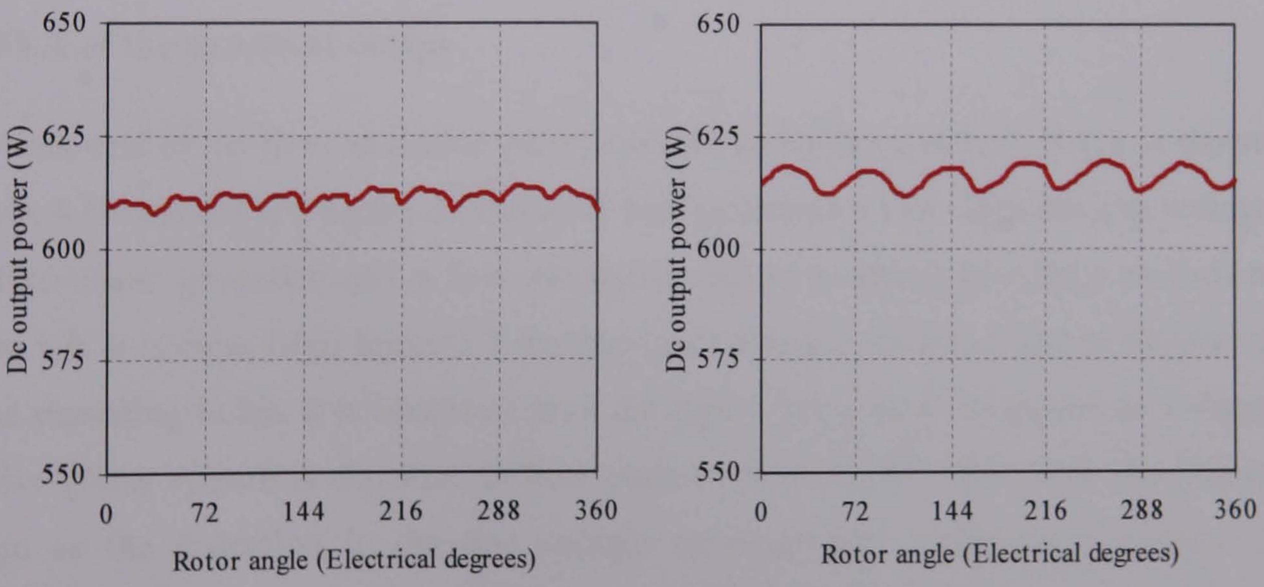

(a) (b)

Figure 5.8. Dc output power for the proposed design using FEA (a) five-phase system, and (b) three-phase system.

Table 5.1 summarises the FEA results of the two systems for the proposed design. It is clear from the table that the five-phase system has improved performance compared to the three-phase system in the case of shaft torque ripple. This is a significant advantage of the five-phase system over the three-phase system.

Table 5.1 The FEA simulation results for the three- and five-phase systems for the proposed design.

	Three-phase		Five-phase	
Ac side	Average	Peak-to-peak ripple	Average	Peak-to-peak ripple
Shaft torque (Nm)	4.6	1.6 (34%)	4.7	0.7 (15%)
Shaft Power (W)	674	233 (34%)	683	104 (15%)
Phase current (A_{rms})	6.5		4.7	
Dc side				
Dc voltage (V)	78.4	0.7 (0.9%)	78.2	0.4 (0.5%)
Dc power (W)	616	13 (2%)	611	6 (1.2%)

5.4 FEA of the practical design

The back emf of the five- and three-phase systems using the practical design is shown in figures 4.16 and 4.17, Chapter 4. The back emf generates a non-adjacent line voltage in the five-phase generator and a line voltage in the three-phase generator as shown in figure 5.9. It is clear from figure 5.9 that the line voltage is distorted due to the presence of the mounting holes. It is observed from the figure 5.9(a) that the output dc voltage in the five-phase system is expected to have peak-to-peak ripple higher than the proposed design as the distortion in the line voltage envelope has a significant impact. The performance of the practical design will be different from the proposed design. The discussion through this section of the thesis is for the five-phase system over one complete electrical period but focused on the period where the non-adjacent line voltage is similar to the waveform of the proposed design. Figure 5.9(a) identifies this period, 'A'. The effect of the mounting holes manifest themselves in the dc output voltage and power. The five-phase system still delivers a lower peak-to-peak shaft torque ripple compared to the three-phase system, Section 5.3.1. The effect of the holes in the three-phase system is the same in all phases such that the three-phase system still generates balanced line voltages as shown in figure 5.9(b). Hence, the mounting holes have a minimal effect on the three-phase generator.

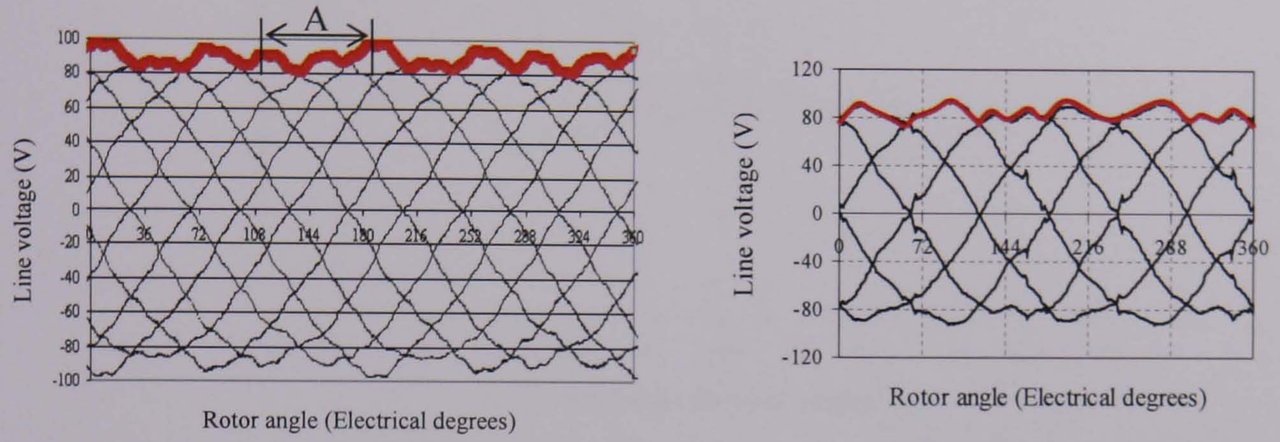

(a) (b)

Figure 5.9. FEA results for (a) five-phase non-adjacent line voltages and their inverse and (b) three-phase line voltages and their inverse, for the practical design showing the line voltage envelope. 'A' identifies the period over which the practical design and proposed design are similar.

5.4.1 Generator shaft torque, power and phase current

The five- and three-phase FEA simulation results for the practical machine (with mounting holes) is shown in Figures 5.10 to 5.12 for the generator side. Figure 5.10 shows the generator shaft torque for the five-phase system. The figure focuses on the period 'A' between 108° and 180°. From the figure the generator has a peak-to-peak torque ripple in this period equal to 0.9Nm and it is approximately 19% of the average value. This value increases to 34% if one complete cycle is analysed. It is observed from the figure that the fundamental frequency of the shaft torque is two times the generator output frequency (46.7Hz) but has a significant component at ten times the generator frequency. The torque component observed at ten times the frequency is predicted from the simulation results in Chapter 4 and with FEA simulation on the proposed design (Section 5.2).

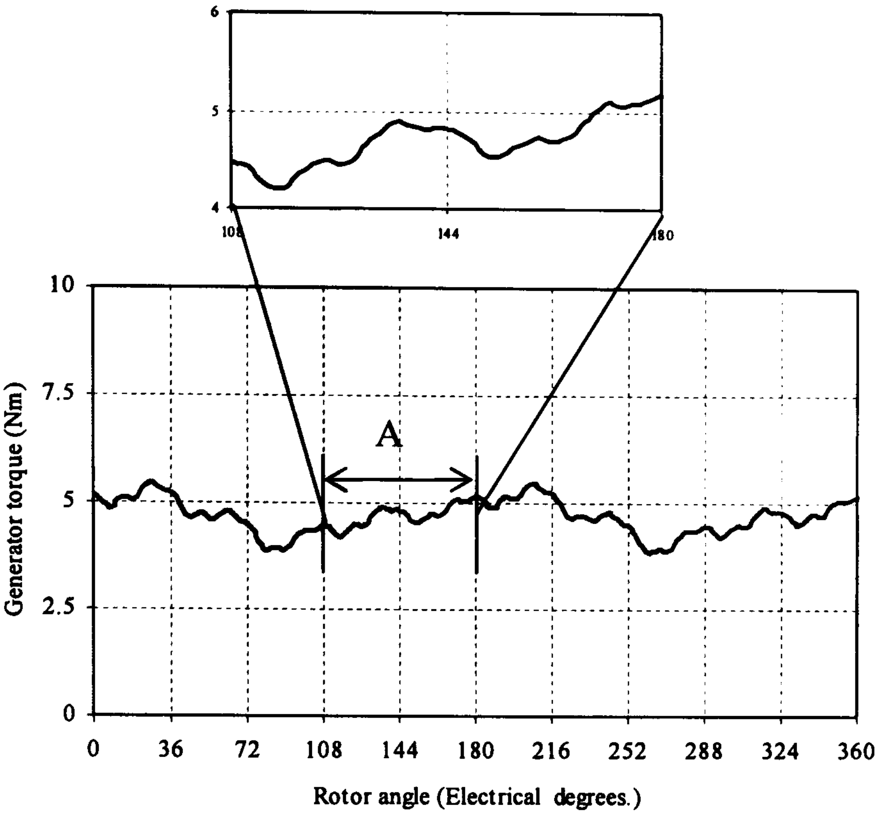

Figure 5.10. Five-phase generator shaft torque of practical design using FEA showing the period 'A' between 108° and 180° (72°).

Figure 5.11 shows the three-phase generator shaft torque for one complete electrical period. The peak-to-peak ripple (1.7Nm) is 37% of the average value (4.6Nm). The mounting holes have the effect of increasing the torque ripple in the three-phase system by around 4% compared to the proposed design.

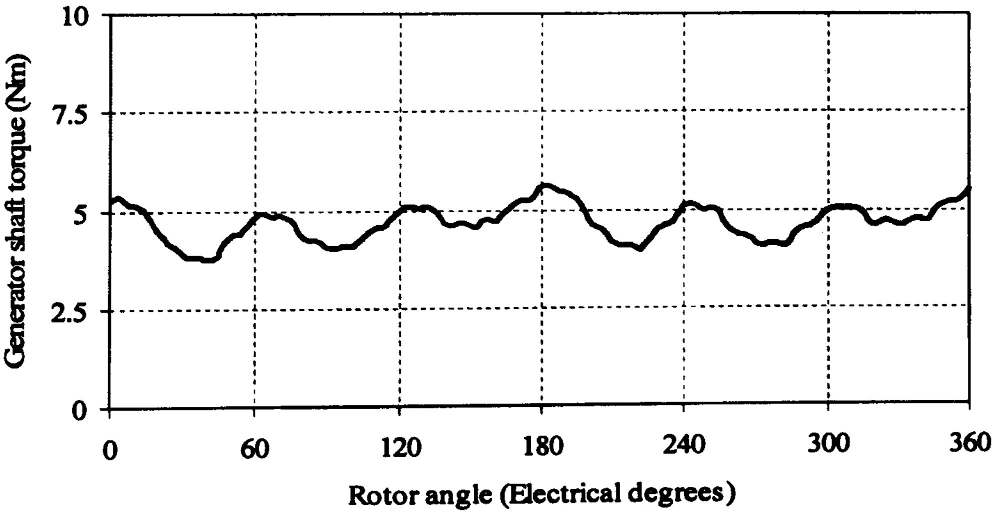

Figure 5.11. Three-phase generator shaft torque of the practical design using FEA

Figure 5.12 shows the generator shaft power for the five-phase system. If the complete electrical period is taken the peak-to-peak ripple (238W) is approximately 34% of the average value (689W). During period A, the peak-to-peak ripple (140W) is approximately 20% of the average value and this agrees with the simulation of the proposed design.

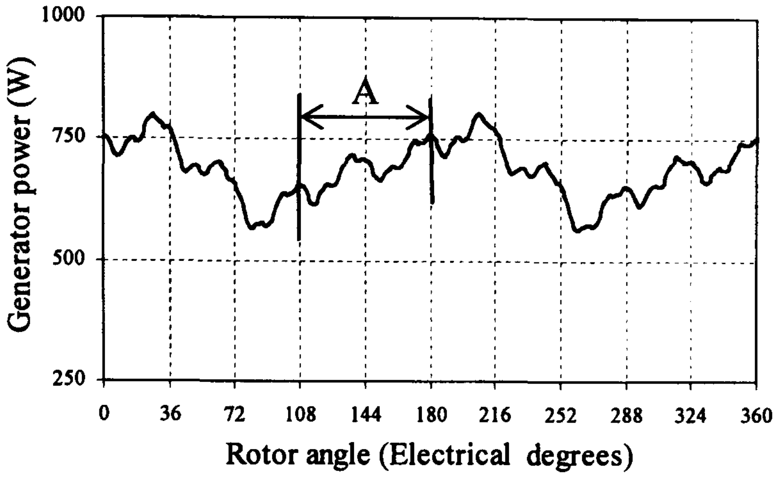

Figure 5.12. Five-phase generator shaft power of the practical design using FEA, showing the period 'A' between 108° and 180° (72°).

Figure 5.13 shows the three-phase generator shaft power over one period. The peak-to-peak ripple is approximately 38% of the average value (684W). It is clear from figures 5.12 and 5.13 that the five-phase system still generate a lower peak-to-peak ripple in the shaft power (238W) compared to the three-phase system (424W). This reduction in shaft power ripple occurs even though the mounting holes have a significant impact on the back emf waveform of the five-phase generator.

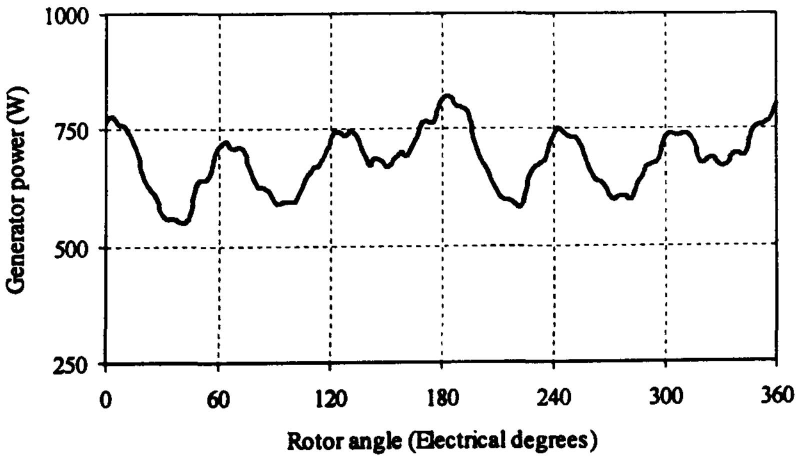

Figure 5.13. Three-phase generator shaft power of the practical design using FEA, showing the period 'A' between 108° and 180° (72°).

Each phase current in the five-phase generator has a different rms value. This difference is as high as 6% and is primarily due to the distortion in the phase back emf caused by the presence of the mounting holes in the stator.

5.4.2 Dc output voltage and power

Figures 5.14 and 5.15 show the dc output voltage and power respectively for the five- and three-phase systems. From figure 5.14(a) the dc output voltage of the five-phase system has a peak-to-peak ripple of 4.7V which is approximately 6 % of the average value (73V). The three-phase system has a lower peak-to-peak ripple (3%). However, focussing on period A, the peak-to-peak ripple for the five-phase systems is as predicted by simulation.

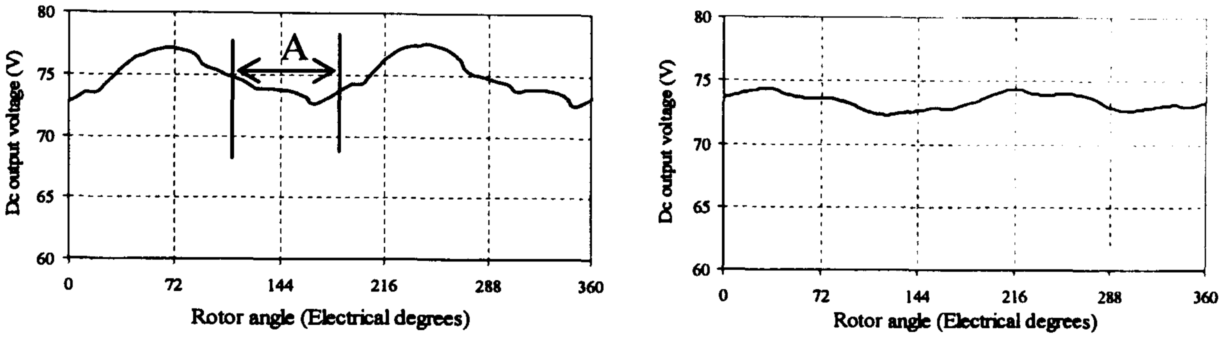

(a) (b)

Figure 5.14. Dc output voltage of the practical design using FEA (a) five-phase and (b) three-phase.

Figure 5.15 shows the output power for both the five- and three-phase systems. The five-phase system has an average value of 618W and peak-to-peak ripple of 12% of the average value. This ripple is twice the ripple in the three-phase system as observed from the figure.

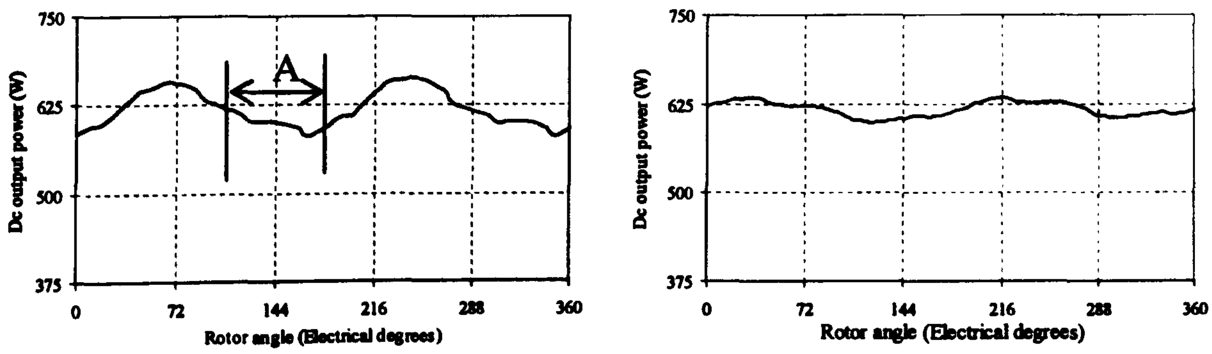

(a) (b)

Figure 5.15. Dc output power of the practical design using FEA (a) five-phase and (b) three-phase.

Table 5.2 summarises the FEA results of the two systems for the practical design. It is clear from the table that the five-phase system has better performance compared to the three-phase system in terms of generator shaft torque ripple, but the three-phase has better performance in terms of ripple in the output dc voltage and power. This primarily due to the effect of the mounting holes in the stator. By focussing on a limited period 'A' of the output and input waveforms, where the effect of the mounting holes are not significant, it has been shown that the practical design produces output and input waveforms that correlate well with simulation of the proposed design. Therefore, focussing on the this period of operation provides a mechanism of validating the design and the performance improvement by the 5-phase design compared to the 3-phase design.

Table 5.2. The FEA simulation results for the three-and five-phase systems for the practical design.

	Three-phase		Five-phase		Five-phase for period 'A' (72^{o})	
Ac side	Average	Peak-peak ripple	Average	Peak-peak ripple	Average	Peak-peak ripple
Shaft torque (Nm)	4.6	38%	4.7	34%	4.7	20%
Shaft Power (W)	684	38%	686	34%	688	20%
Dc side						
Dc voltage (V)	73	3%	73	6%	74	3%
Dc power (W)	617	6%	618	12%	605	6%

5.5 Performance analysis using experimental tests

The two stators designed in Chapter 4 were fabricated (one stator for the five-phase generator and one stator for the three-phase generator). Both stators include the mounting holes. The 4 pole rotor described in section 4.3 is common to both generators. A test rig was designed and constructed to assess the performance of the five- and three-phase permanent magnet generators operated with a diode rectifier. The results are used to compare the performance of the 3- and 5-phase system.

5.5.1 Test rig layout

The general layout of the test rig is shown in figure 5.16. The rig comprises a

1. Variable dc power supply.
2. Permanent magnet dc motor.
3. Permanent magnet generator.
4. Diode bridge rectifier.
5. Dc link capacitor.
6. Resistive load bank.

The variable dc power supply is used here in a current controlled mode and supplies the permanent magnet dc motor. The permanent magnet dc motor is used to drive the permanent magnet generator and is rated at 5Nm at 39A and 1400rpm at 36V. Appendix C provides the specification of the motor.

The diode bridge rectifier is designed to work with both five- and three-phase permanent magnet generators at full load. The diode used in this experiment is a 30A 200V (30CTH02). The output from the rectifier supplies a resistive load bank and the Dc link capacitor. The dc link capacitor is 470μF for the five-phase system and 2200μF for the three-phase system which give the same output dc voltage ripple for both the five- and three-phase system at rated load, Section 7.4.

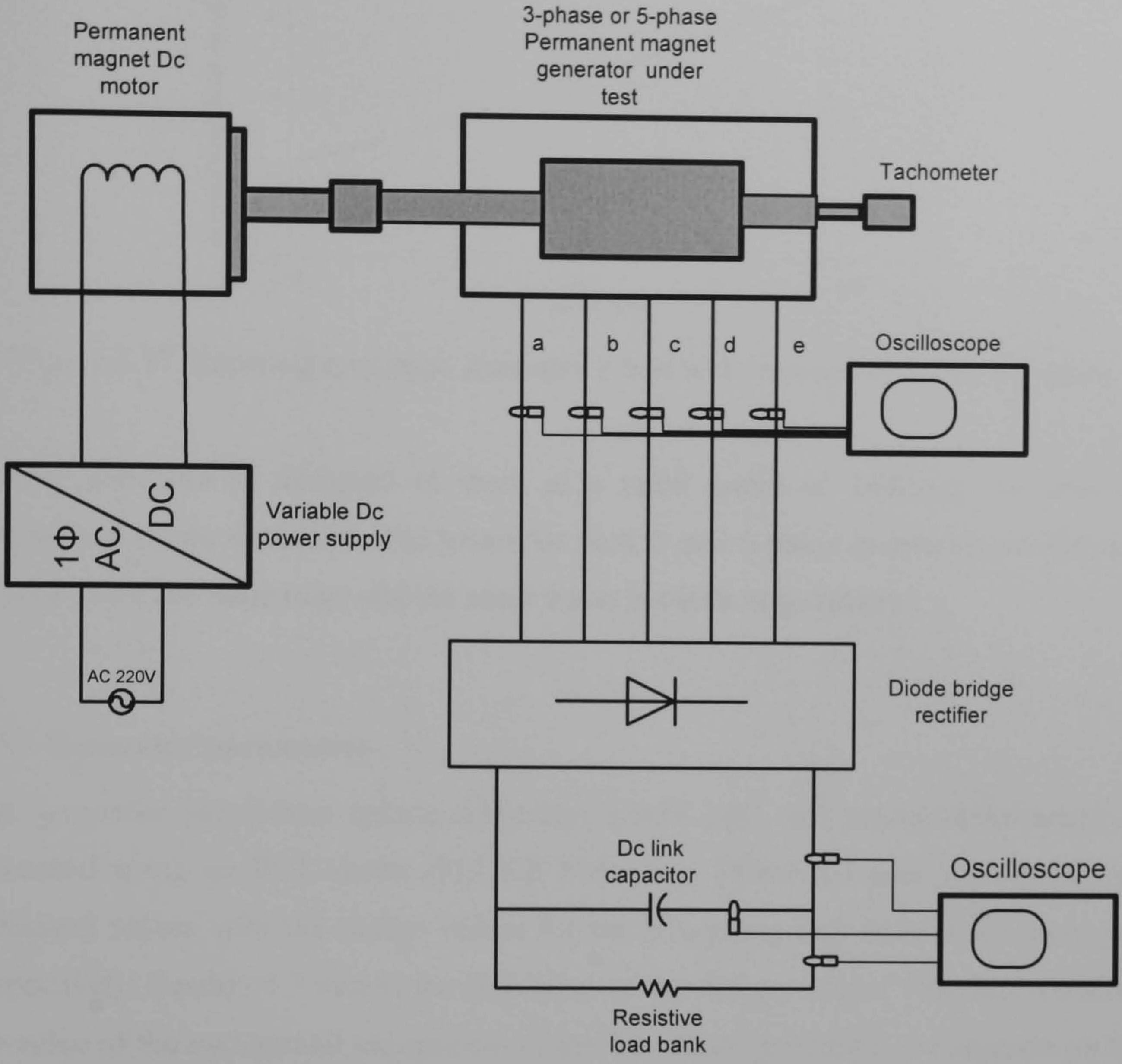

Figure 5.16. The general arrangement of the test rig showing the permanent magnet generator under test, the prime mover and diode rectifier.

5.5.2 Assessment of generator iron loss and friction and windage loss

The iron, and friction and windage loss primarily depends on the shaft speed [5.1]-[5.4]. The generator iron and friction and windage loss is calculated using standard loss separation tests where generator is driven by the prime mover. Figure 5.17 shows the variation of the losses with generator shaft speed.

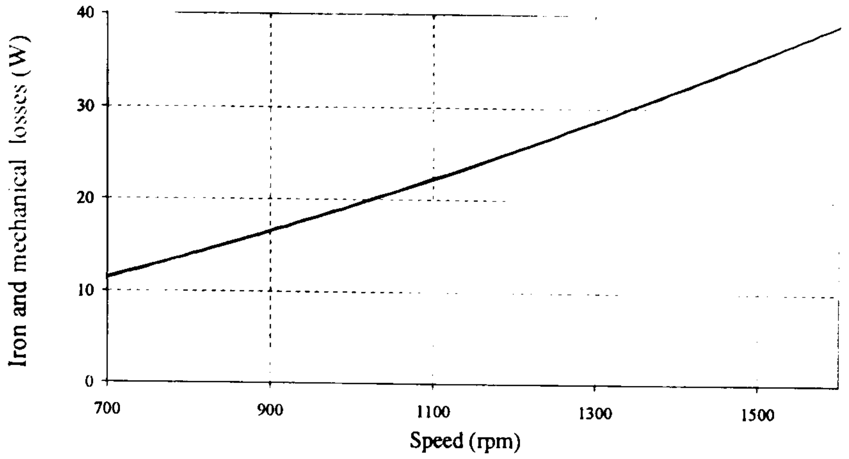

Figure 5.17. Showing prototype generator's iron and mechanical losses vs. speed.

As the generator is designed to work at a rated speed of 1400rpm the iron and mechanical losses total 32W. The losses for both 3- and 5-phase generators are the same as they share the same rotor and the same stator lamination geometry.

5.5.3 Generator parameters

The generator parameters (phase resistance, phase self- and mutual-inductance) are measured using an RCL meter (FLUKE PM6306). Tables 5.3 and 5.4 compare the measured values with the design values for the five-phase and three-phase generators respectively. Section 4.7 details the derivation of the design values. The results confirm the value of the two mutual inductances of the five-phase generator; the adjacent mutual inductance, M_1, has a value approximately equal to 1/5 of the self inductance and the non-adjacent mutual inductance, M_2, has a value approximately equal to 3/5 of the self inductance. This agrees with the theoretical values. It is also shows the mutual inductance in the three-phase generator is 1/3 of the self inductance.

Table 5.3. Five-phase generator parameters

Parameter	Practical	Analytical
Phase resistance, R	0.65Ω	0.6Ω
Phase inductance, L	1.3mH	1.2mH
Adjacent mutual inductance, M_1	0.24mH	0.2mH
Non-adjacent mutual inductance, M_2	0.62mH	0.6mH

Table 5.4. Three-phase generators parameters

Parameter	Practical	Analytical
Phase resistance, *R*	0.54Ω	0.43Ω
Phase inductance, *L*	1.1mH	1.3mH
Mutual inductance, *M*	0.36mH	0.43mH

5.5.4 Back EMF waveforms

The back EMF of the generator phases on no load, at rated speed (1400rpm), were measured. The generator is rotated using the PM dc motor. Figures 5.18 and 5.19 show the five-phase and three-phase back EMFs respectively. These figures show the distortion of the back EMF waveforms due to the presence of the mounting holes in the stator. Phase-*e* and *c* in the five-phase generator are particularly affected and have a higher peak value with a less pronounced flat top. The amplitude of phase back EMF is 48V in five-phase generator and 53V in three-phase generator, which are similar to the design values in section 4.6.

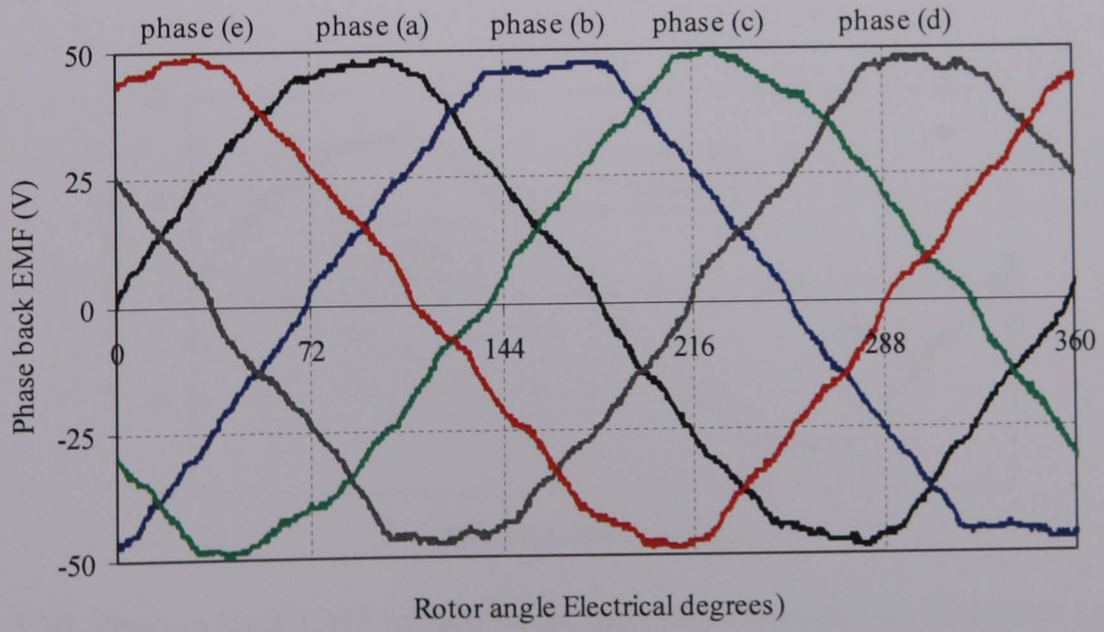

Figure 5.18. Measured phase back EMFs of the five-phase generator.

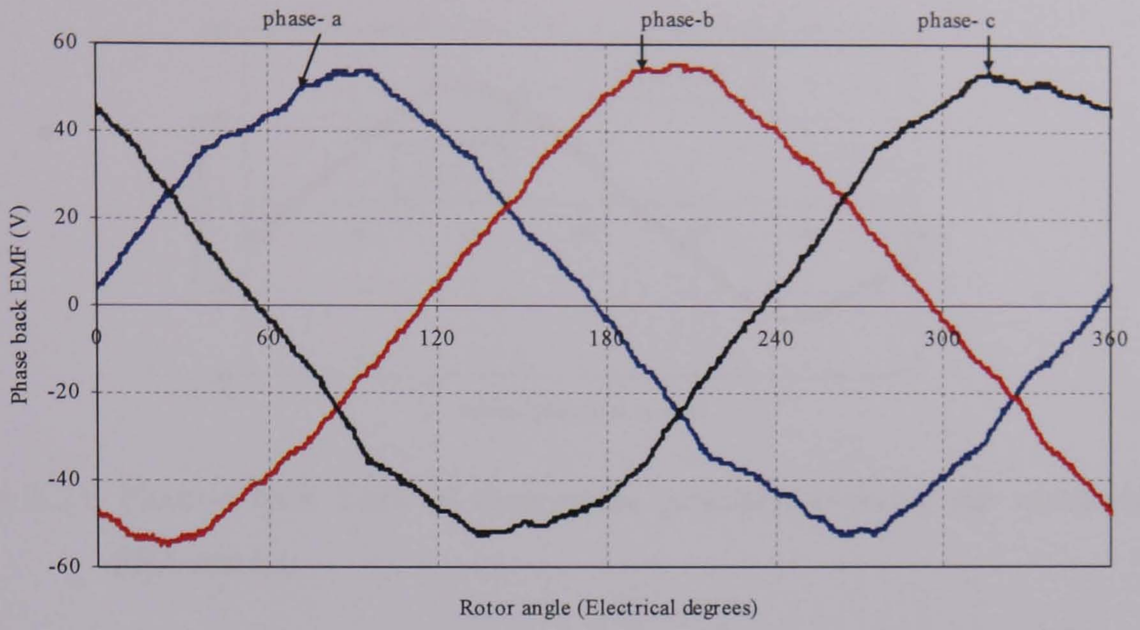

Figure 5.19 Measured phase back EMFs of the three-phase generator.

The measured phase back EMF is compared with FEA results. Figure 5.20 shows phase-*a* back EMF of the five-phase generator. Figure 5.21 shows the equivalent for the three-phase generator. It is clear from the figures that the measured results confirm the FEA results in section 4.11.

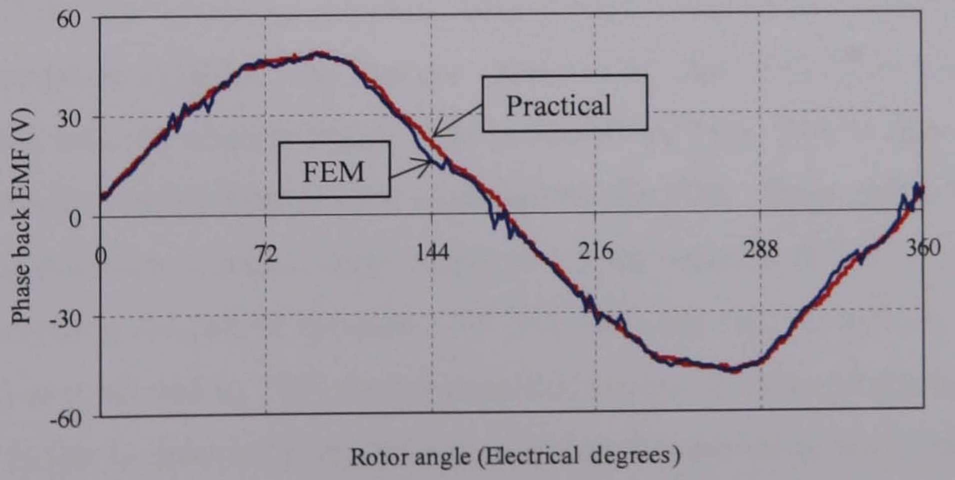

Figure 5.20. Phase-a back EMF of five-phase generator showing the measured and FEA results.

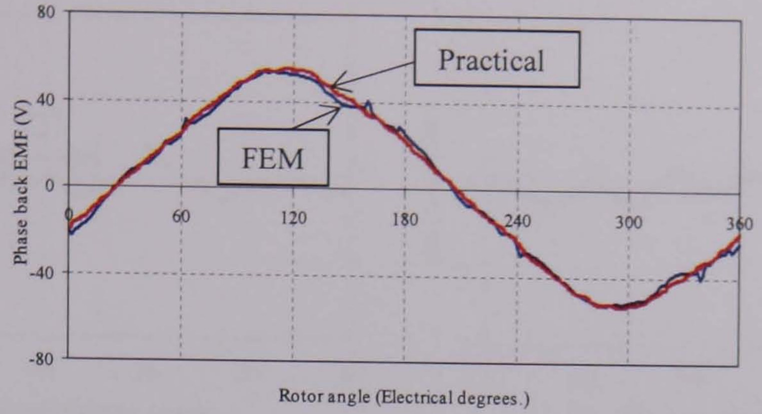

Figure 5.21. Phase-*a* back EMF of three-phase generator showing the measured and FEA results.

5.6 Experimental Results

The generator is connected to a diode bridge rectifier with a resistive load and dc link capacitor. The generator speed is set at 1400rpm with a resistive load of 10Ω. The dc link capacitor for the five-phase system is 470μF and for the three-phase system 2200μF.

5.6.1 Generator shaft torque, power and phase current

The generator shaft torque and power are estimated from the phase currents and the phase back EMF. The estimated generator shaft torque is shown in Figure 5.22 for the five- and three-phase systems. The average values of the shaft torque for both systems to deliver rated load are slightly higher than predicted by FEA. This is due to the iron loss and mechanical loss which are not modelled by the FEA. From figure 5.22(a) the five-phase generator has a peak-to-peak ripple of 1.8Nm which is 36% of the average of 4.9Nm. By selecting the period between 108° and 180°, the torque ripple is reduced to 0.9Nm (18%) as predicted by FEA for the proposed design. In terms of the performance discussion it is fair to discuss the performance during this period as being indicative of the proposed design. The three-phase generator has an average torque value of 4.9Nm with a peak-to-peak ripple of 1.5Nm (31%). Because the distortion in the three-phase back emf is the same in all phases and the line to line voltage is not distorted significantly, unlike the five-phase generator, the calculation for the three-phase system is performed over one complete electrical period.

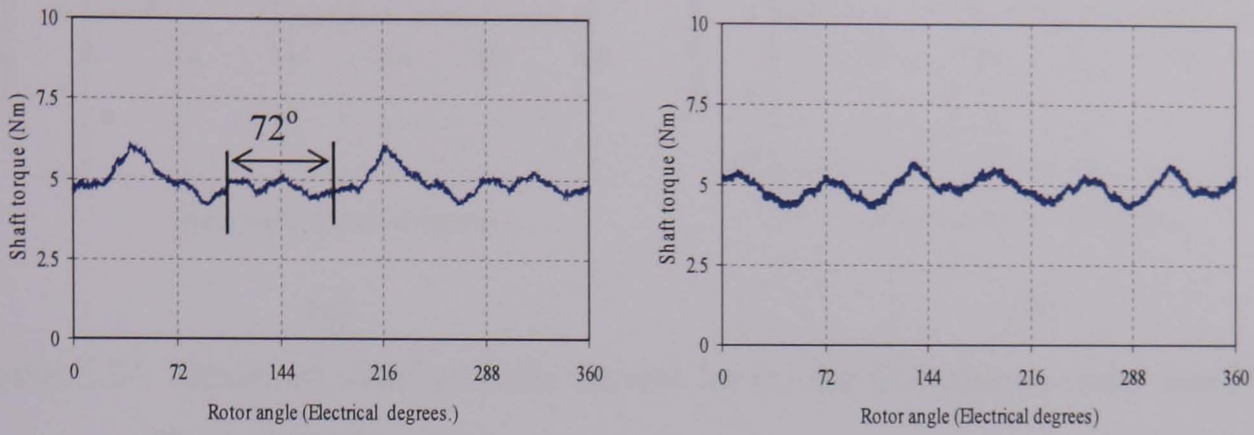

(a) (b)

Figure 5.22. Estimated shaft torque from the practical test for the (a) the five-phase generator showing the period A where the non-adjacent line voltage is not distorted (72°), and (b) the three-phase generator.

Figure 5.23 shows phase-*a* and -*b* currents in the five- and three-phase systems. The commutation angle in the five-phase system is equal to 21° (electrical) and for the three-phase is 22° (electrical) which are slightly different from the simulation.

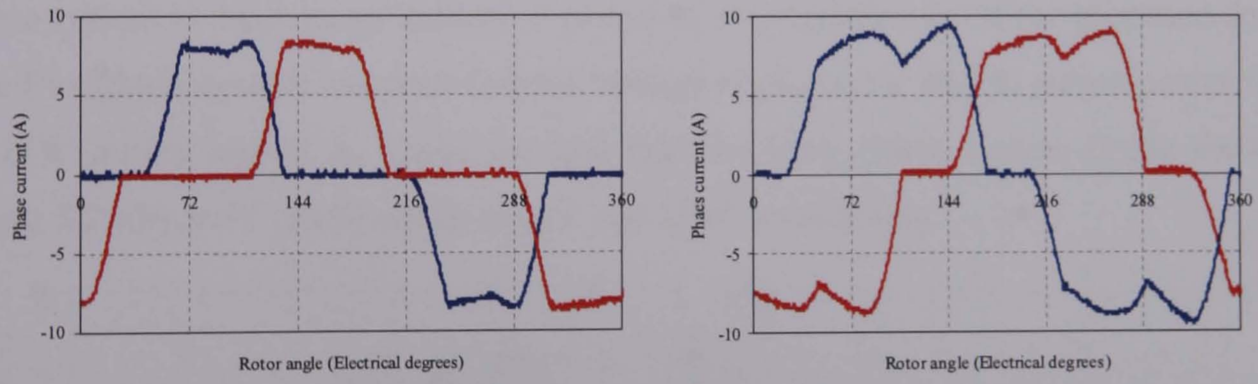

Figure 5.23. Measured phase-*a* and -*b* currents in the generator for the (a) five-phase system, and (b) the three-phase system.

Figure 5.24 shows the diode current for the five- and three-phase rectifiers. It is clear from the figure that the diode conducts for a shorter time in the five-phase system compared to the three-phase system. The rms current in the diode is 1.5A in the five-phase system and 2.9A in the three-phase system. These correlate with the FEA results reported in Section 5.3.

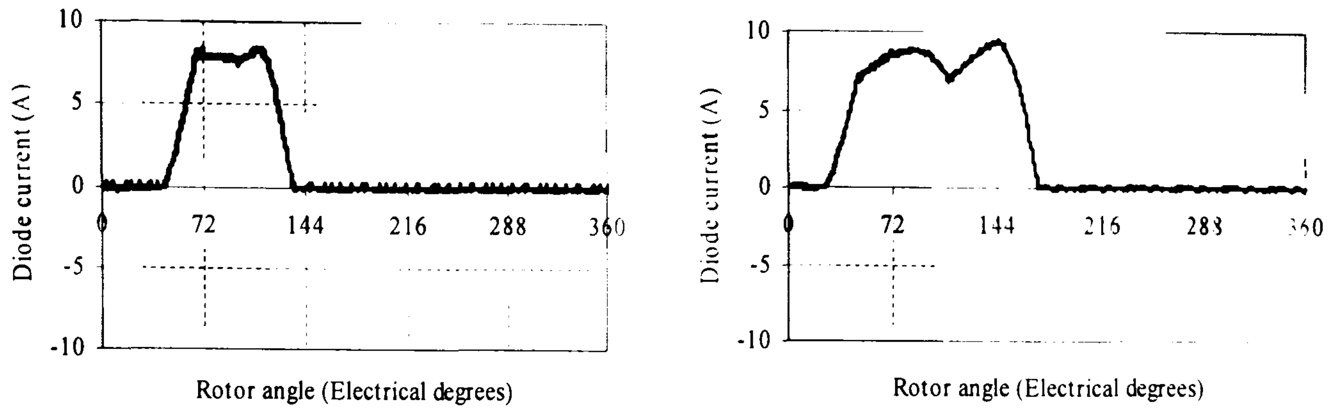

(a) (b)

Figure 5.24. Measured rectifier diode current for (a) the five-phase system and (b) the three-phase system.

5.6.2 Output dc voltage and power

Figures 5.25 and 5.26 show the output dc voltage and load power for the five- and three-phase systems respectively. It is clear from the figures that the peak-to-peak ripple in the five-phase system is greater than the three-phase system, and different from that predicted by simulation in chapter 3 and FEA in section 5.3. This is due to the distortion in the phase back emf due to the presence of the mounting holes in the stator. For a fair comparison between the two systems period A in figure 5.25(a) and 5.26(a) for the five-phase system is taken as an indicative period of the performance of the proposed design. The five-phase system has peak-to-peak voltage ripple of 1V and an output power ripple of 17W during period A. These are less than the three-phase system ripple shown in figure 5.25(b) and 5.26(b) which are 2V and 36W respectively.

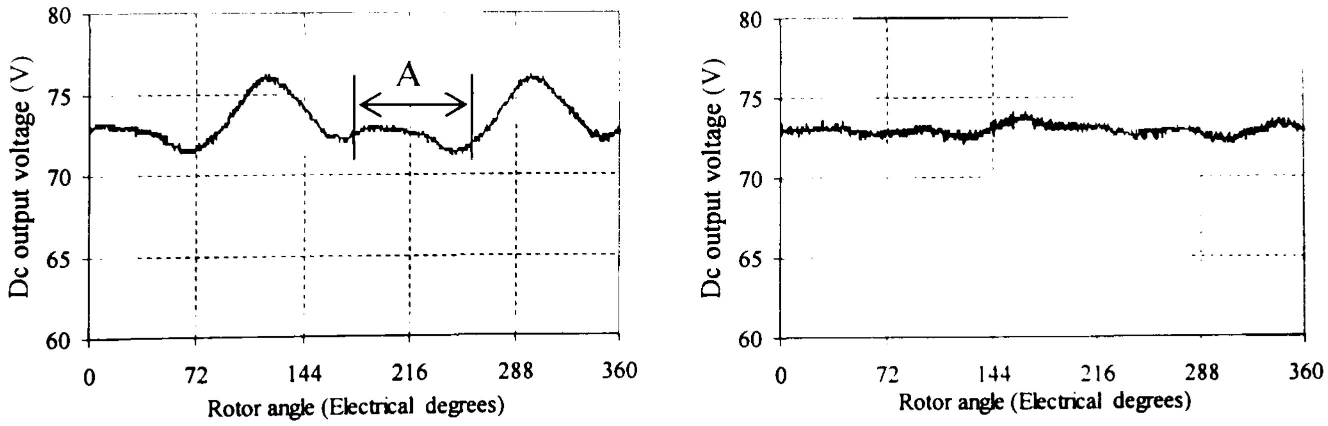

Figure 5.25. Output dc voltage from the practical test for (a) the five-phase system, showing the period 'A' where the non-adjacent line voltage is not distorted and (b) the three-phase system.

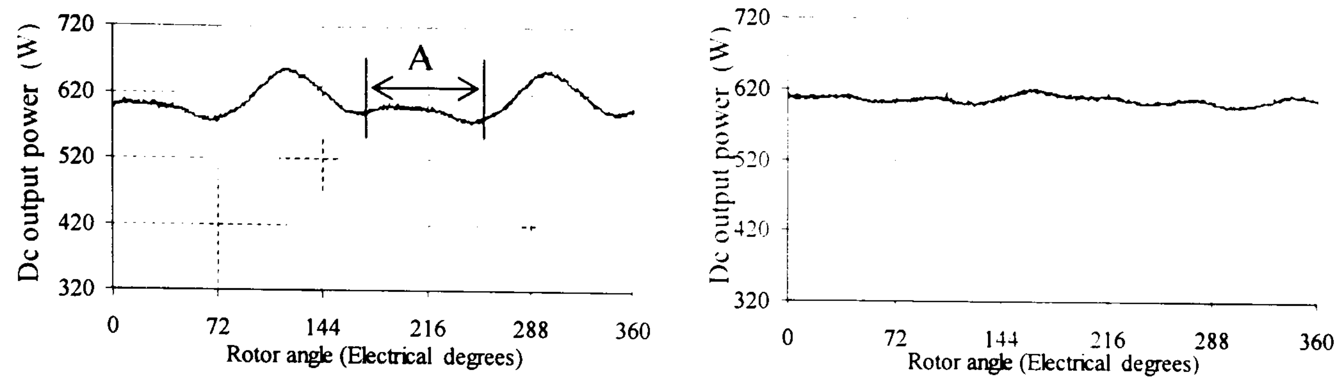

Figure 5.26. Output dc power from the practical test for (a) the five-phase system. showing the period A where the non-adjacent line voltage is not distorted and (b) the three-phase system.

The results are summarised in Table 5.5. It is clear from the results that the five-phase system has better performance than the three-phase system in the period where the non-adjacent line voltages are not distorted by the mounting holes.

Table 5.5 The experimental results for the five-and three-phase systems

	Three-phase		Five-phase for one completed period		Five- phase for period 'A'(72°)	
Ac side	Average	Peak-peak ripple	Average	Peak-peak ripple	Average	Peak-peak ripple
Shaft torque (Nm)	4.9	31%	4.88	36%	4.7	18%
Shaft Power (W)	719	31%	716	36%	692	18%
Diode current (A_{rms})	4.8		3.3		3.3	
Dc side						
Dc voltage (V)	73	3%	73	6.5%	72	1.4%
Dc power (w)	606	6%	607	13%	595	2.9%

5.7 Summary

In this chapter, the performance of a five-phase and three-phase permanent magnet generator connected to diode bridge rectifier is evaluated using FEA and practical tests.

Two designs are modelled using FEA to evaluate performance of the proposed design, (without mounting holes in the stator) and the practical design (with mounting holes). The FEA results for the proposed design show that the five-phase system has lower peak-to-peak shaft torque ripple, 0.7Nm, compared to the three-phase system, 1.6Nm. The output voltage and load power peak-to-peak ripple in the three-phase system is 16% higher than the five-phase system for the chosen values of the dc link capacitor. For the same capacitance the five-phase system can use less magnetic material and generate the same dc output peak-to-peak ripple compared to the three-phase system. Alternatively, with the same volume of magnetic material, less capacitance is required in the five-phase system to generate the same output voltage ripple as the three-phase system.

An experimental test rig is described and tests on the five- and three-phase systems at rated load are reported. A comparison between the five- and three-phase system is provided. Due to the distorted phase back EMF in the five-phase system, the comparison of the practical design do not compare well with the FEA or simulation results. Hence comparison is made over a restricted period of the electrical cycle where the non-adjacent line voltages are not significantly affected in the five-phase system.

The diode rms current in the five-phase system is a factor of 0.55 of the three-phase system and the total diode losses are lower in the five-phase rectifier. Therefore, the five-phase system requires diodes with lower current ratings compared to the three-phase system. It is also shown that the five-phase system can use a lower value of capacitance for the same output voltage ripple. In this case 470μF compared to 2200μF for the three-phase system. The performance and specification of the capacitor in both systems are discussed further in Chapter 7.

In general, if the practical machine was fabricated without the mounting holes the five-phase system would have better performance in term of shaft torque ripple compared to the three-phase system for the same output dc voltage and power.

References

[5.1] J. H. Seo, S. Y. Kwak, S. Y. Jung, C. G. Lee, T. K. Chung, and H. K. Jung, "A Research on Iron Loss of IPMSM With a Fractional Number of Slot Per Pole," IEEE Trans. Magn., Vol. 45, No.3, March 2009, pp1824-1827.

[5.2] R. Dutta, M. F. Rahman, "Design and Analysis of an Interior Permanent Magnet (IPM) Machine With Very Wide Constant Power Operation Rang," IEEE Trans. on Energy Conversion, Vol.23, No.1, March 2008, pp.25-33.

[5.3] K. Yamazaki, and Y. Seto, "Iron Loss Analysis of Interior Permanent Magnet Synchronous Motor—Variation of Main Loss Factors Due to Driving Condition," IEEE Trans. on Industrial Application, Vol. 42, No.4, Jul./Aug.2006, pp.1045-1052.

[5.4] D. M. Ionel, M. Popescu, S. J. Dellinger, T. J. E. Miller, R. J. Heideman, and M. I. McGilp, "On the Variation With Flux and Frequency of the Core Loss Coefficients in Electrical Machines," IEEE Trans. on Industrial Application, Vol. 42, No.3, May/Jun. 2006, pp. 658-667.

Chapter 6

Performance of a five-phase PM generator with diode bridge rectifier under open-circuit phase failures

6.1 Introduction

In this chapter, the performance of a five-phase permanent magnet generator connected to a diode bridge rectifier under open-circuit failure conditions is assessed through simulation and experiment. The performance of the five-phase system is compared with that of a three-phase system under open-circuit failure.

Three possible open-circuit phase failure modes in the five-phase machine are considered [6.1]-[6.2]

1. one open-circuit failure,
2. two adjacent phases failing open circuit (for example, A and B), and
3. two non-adjacent phases failing open circuit (for example, A and C).

For the three-phase machine one single phase open-circuit failure mode is assessed.

In this chapter, the estimated permanent magnet generator torque and power are presented for each of these failure modes. Also the impact of these failure modes on rectifier output dc voltage and power are discussed. In section 6.2, simulation results are used to examine the performance of the five- and three-phase generator systems under the open-circuit failures described above. To verify the simulation and demonstrate practical applicability, experiments are performed and the results presented in section 6.3

6.2 Simulation of permanent magnet generators with open-circuit phase failures

In the five-phase system two cases of open-circuit failure considered; a single-phase open-circuit and two phases open-circuit. The two phase open-circuit mode can occur in two ways; two adjacent and two non-adjacent open-circuit phase failures. The adjacent and non-adjacent failure modes have a radically different impact on the resultant performance of the generator. The simulation assumes a sine wave back emf and the generator parameters from Tables 5.3 and 5.4.

6.2.1 Single open-circuit phase failure

Figure 6.1 shows a five-phase permanent magnet generator connected to a diode bridge rectifier with phase-*a* open-circuit. The permanent magnet generator is still able to deliver power to the load through the remaining four phases.

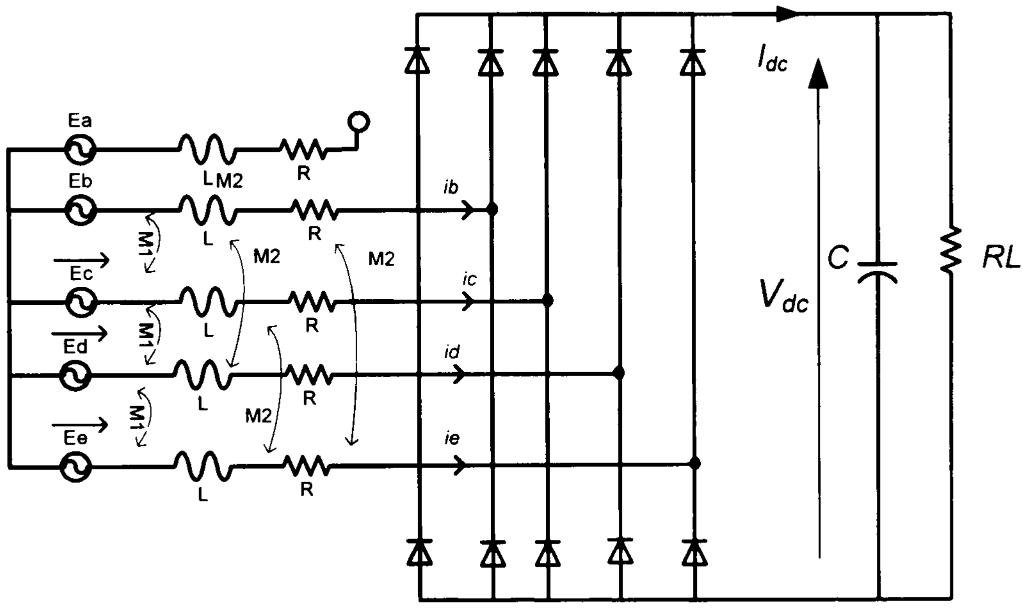

Figure 6.1. Five-phase permanent magnet generator feeding a diode bridge rectifier with single open-circuit phase failure. Phase-*a* is open-circuit.

Similar to when all phases in the five-phase generator are functioning correctly, under a single open-circuit failure, non-adjacent line voltages provide load power through their associate diodes. Figure 6.2 shows the resultant non-adjacent line voltages when phase-*a* is open-circuit. This figure clearly shows the periods where phase-*a* and its related non-adjacent line voltages, are absent. Effectively 4 out of 10 line voltages are no longer generated. This leaves 6 line voltages- still twice as may as three-phase case under normal conditions. The line voltages E_{ec} and E_{ce} now have to conduct until they fall to 42% of the peak line voltage, (neglecting phase inductance and resistance and an assumption of no dc link capacitor). The diode rectifier output voltage decreases to a minimum of $0.42V_L$. In a practical system, the dc link capacitor and phase inductance will impact on output voltage and the resultant output voltage may be more than $0.42V_L$. However, in both ideal and practical cases, the output ripple voltage is expected to be higher and the average output voltage reduced compared with all 5 phases functioning correctly.

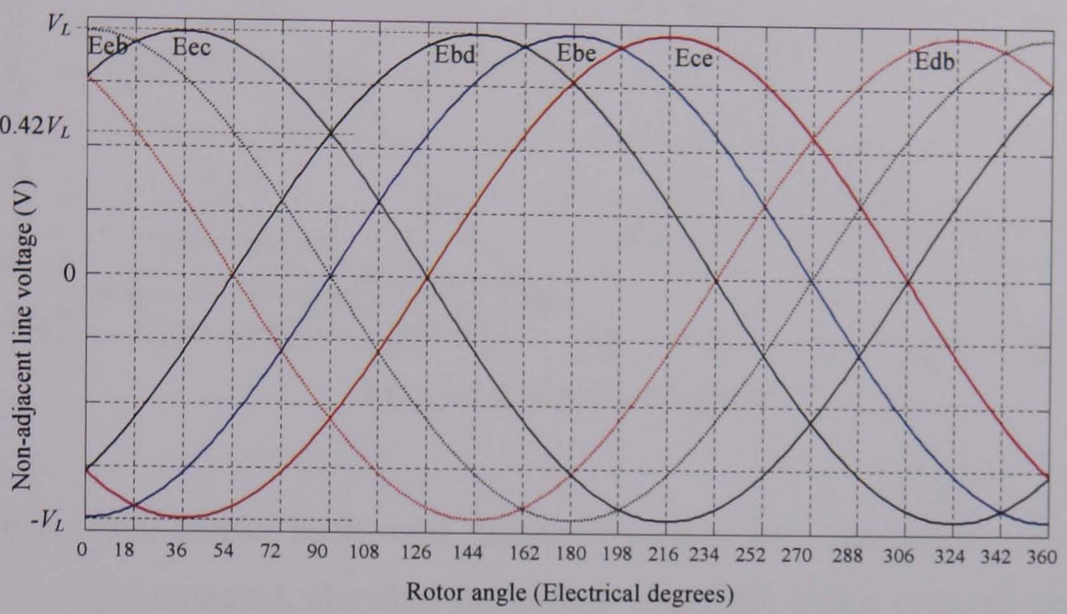

Figure 6.2. Five-phase non-adjacent line voltage for one cycle, with phase-*a* open-circuit

Figure 6.3 shows the back emf phase voltages when phase-*a* is open-circuit and identifiers the approximate conduction periods of each phase. From figure 6.3 non-adjacent phases -*c* and -*d* conduct for periods of 72° (electrical). The adjacent phases, to the open-circuit phase, phase-*e* and phase-*b*, conduct for periods of 108° (electrical). Therefore, the rms phase current is expected to be higher in the adjacent phases (e and b) compared to non-adjacent phases (c and d), and potentially, higher compared to the normal condition (under the same load conditions). The increase in rms current of phase-e and -b leads to an increase in the copper loss in phase-*e* and -*b*. Likewise the decrease in rms current in phase-*c* and -*d* leads to a decrease in copper loss. The insulation temperature of phase-*e* and -*b* will increase if the phase current is higher than rated current and potentially will exceed maximum rating. In the practical system, the resultant value of the rms phase current depends on permanent magnet generator parameters and dc link capacitor and load. The dc link capacitor has a significant effect on the rms phase currents. The phase current conduction periods are altered when a dc link capacitor is included. For example, in Figure 6.2, the capacitor will not be charged from the peak of E_{ec} at 36° until close to peak of E_{bd} at 144°. That is a 108° period during which no phase will conduct and charge the dc link capacitor. Under such circumstances, the rms phase current of phase-*b* and -*d* will be significantly higher as all the energy supplied to the load during this 108° period is replenished by phases *b* and *d* resulting in high crest factor phase current.

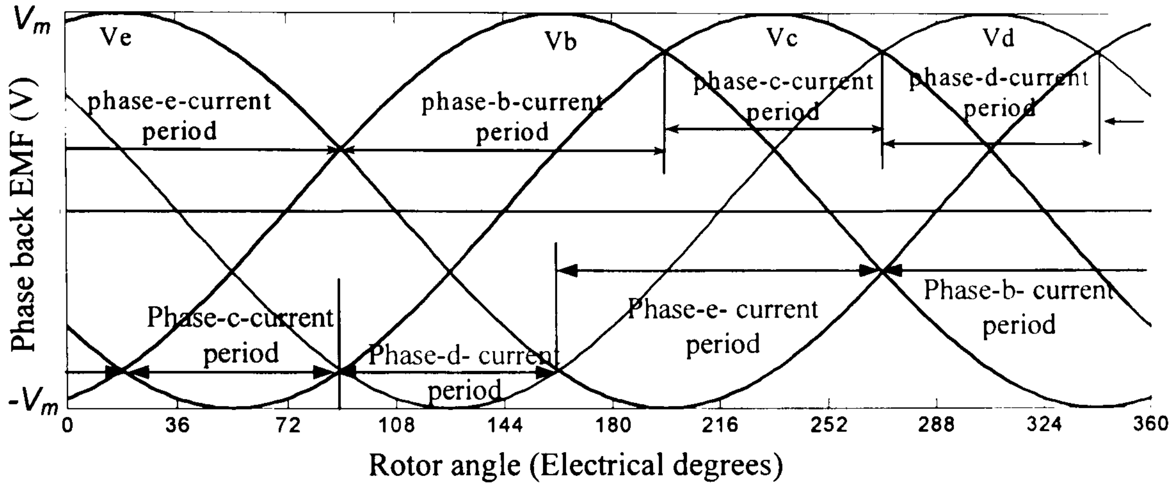

Figure 6.3. Five-phase back emf phase voltages for one cycle, when phase-*a* disconnected, showing the period where the phase currents conduct under ideal conditions with R, L,M and dc link capacitor neglected.

In the three-phase system, with one phase open-circuit failure the system effectively functions as a single-phase full-bridge rectifier. The remaining two phase currents have the same rms value.

In this section, the generator parameters used in chapter 3 to simulate the five-phase and three-phase systems are used to simulate the generator torque and power, rectifier output dc voltage, and output power with one open-circuit phase failure. The results are used to compare between the two systems in order to evaluate advantages and disadvantages of five- and three-phase systems. The generator speed is kept constant, at 1400rpm, as the system is assumed to be driven by a wind turbine's blade system, where the mechanical and aerodynamic time constant are such that for the initial period of the fault the rotor speed can be assumed constant. The results are categorised into: generator torque and shaft power, rectifier dc output voltage and power, and rms phase current.

i- Generator shaft torque and power

Figure 6.4 shows the generator torque with phase-*a* disconnected. The peak-to-peak ripple (8.5Nm) is approximately two times the average torque value (4.28Nm). The average torque is decreased by 9.9% compared to the normal condition. It is observed from the figure that the generator torque reaches a null for a short time, in this case less than 2° (electrical). The fundamental frequency of the shaft torque is 93.3Hz. The torque ripple will generate vibration and noise. The simulation results of the three-phase generator torque when phase-*a* is open-circuit are shown in figure 6.5. The peak-to-peak ripple (9.5Nm) is approximately 2.9 times the average torque value (3.28Nm). The average torque is decreased by 18.6% from the normal condition. The figure shows that the generator torque has a null period that is 72° (electrical).

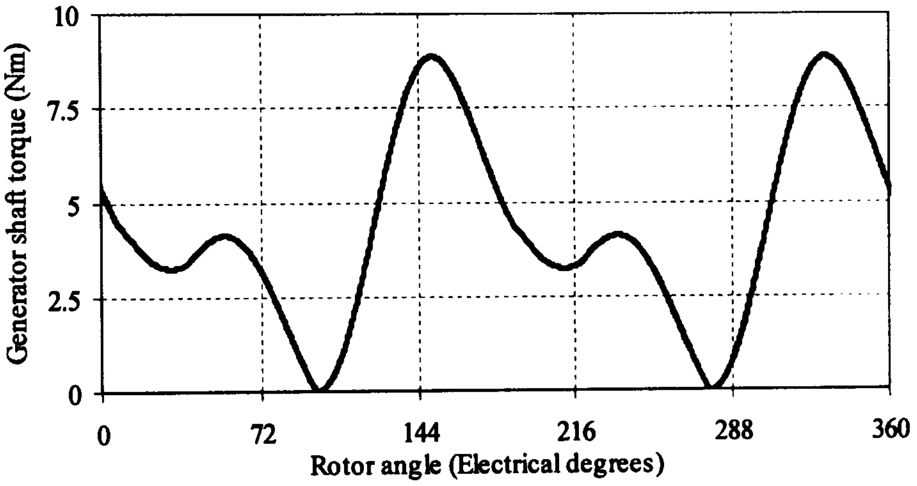

Figure 6.4. Five-phase PM generator shaft torque with phase-a open-circuit.

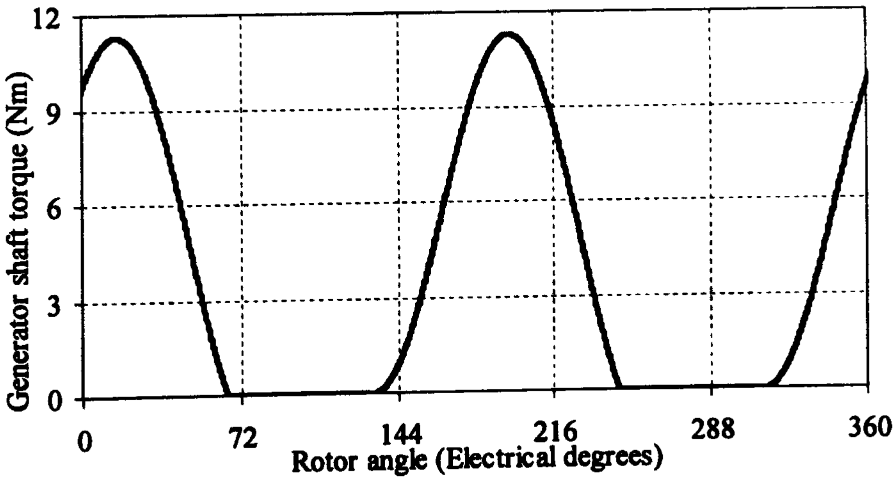

Figure 6.5. Three-phase PM generator shaft torque with phase-*a* open-circuit showing the 72° period where the torque equals zero.

From Figures 6.4 and 6.5, the torque ripple of the five-phase machine is lower in magnitude than that of the three-phase machine, and the average torque of the five-phase machine is 23% higher than the three-phase machine. The vibration and the noise from the three-phase generator would be expected to be higher than the five-phase generator as the result of the higher magnitude fundamental torque ripple component.

Figure 6.6 shows the generator power for the five- and three-phase case when phase-*a* is open-circuit. The five-phase system has an average value approximately 10.5% higher than the three-phase system. The power in the five-phase generator decreases by 8.9% and in the three-phase generator decreases by 18.2% from the normal condition. It can be seen that five-phase system captures more power from the prime-mover than the three-phase system. This is an advantage of the five-phase system over the three-phase system under single open-circuit failure conditions.

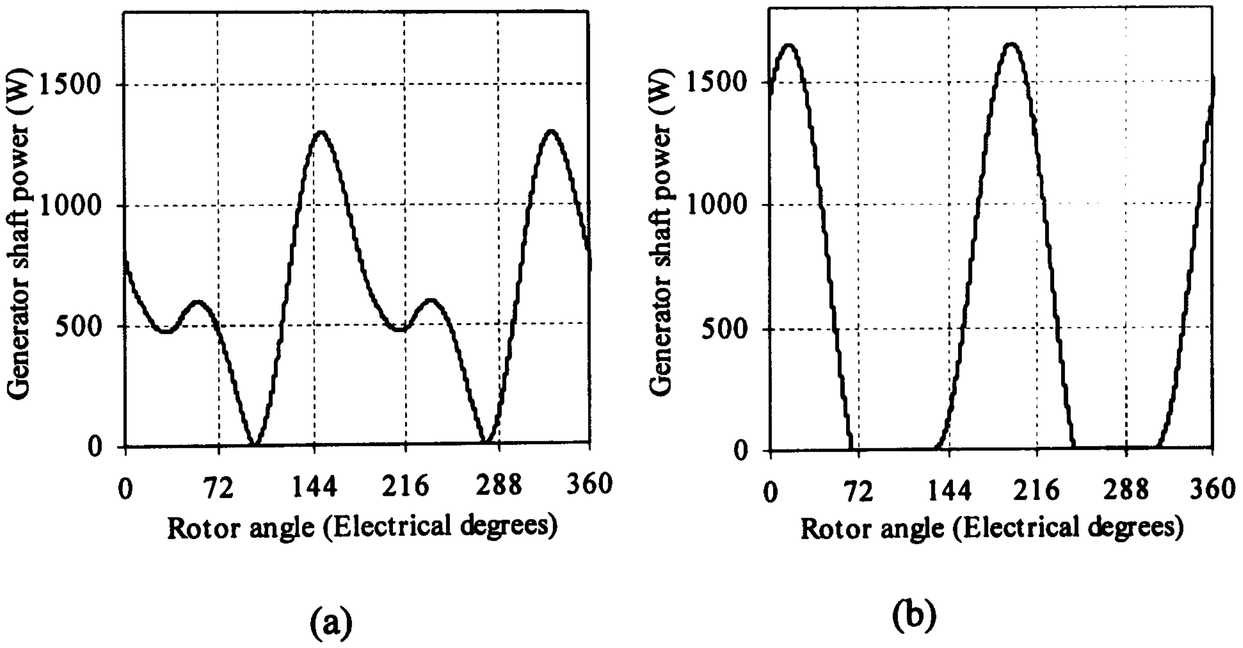

Figure 6.6. Generator shaft power with phase-*a* open-circuit for (a) the five-phase generator, and (b) the three-phase generator at 1400rpm

ii- Dc output voltage and power

Figure 6.7 demonstrates the impact that an open-circuit failure has on the output voltage of the diode rectifier for the five- and three-phase systems. The output voltage from the rectifier that is feed from the five-phase generator has an average dc output voltage that is 10% higher than the three-phase system. The influence of the phase-*a* failure in the five-phase system is clearly shown during the period between 54°and 144° in figure 6.7.

The dc voltage decreases to 53V which is 0.6 of the peak dc voltage. In the three-phase system, as a higher dc link capacitor has been chosen (such that the ripple under normal conditions is the same for the three- and five-phase cases) the peak-to-peak ripple is less (15.8V compared to 35V).

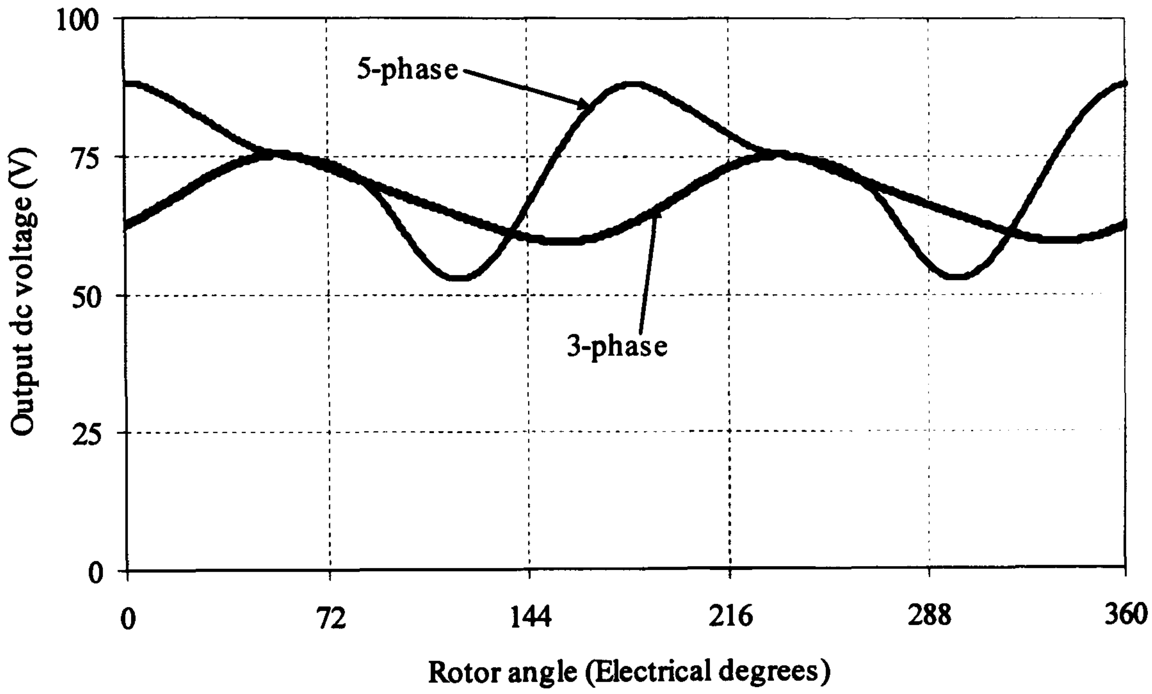

Figure 6.7. Five- and three-phase system output dc voltage with phase-*a* open-circuit. The dc link capacitor is 470 μF for the five-phase system and 2200 μF for the three-phase system.

Figure 6.8 shows the load power for the five- and three-phase system with phase-*a* open-circuit. The average load power in the five-phase system is factor of 1.2 higher than the three-phase system. From these figures the peak-to-peak ripple in the five-phase system is a factor of 2 higher than the three-phase system.

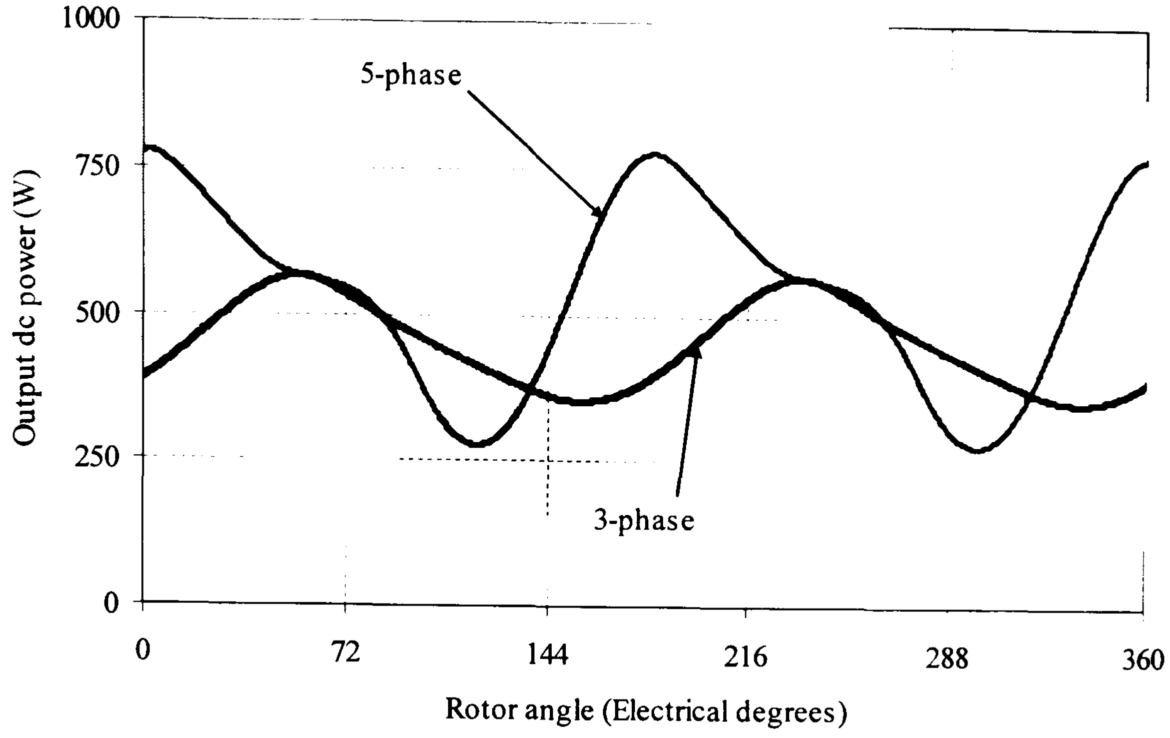

Figure 6.8 Five- and three-phase system load power with phase-*a* open-circuit. The dc link capacitor is 470 μF for the five-phase system and 2200 μF for the three-phase system.

Table 6.1 summarises the results of the two systems when phase-*a* is open-circuit. It is clear from the table that the five-phase system has improved performance compared to the three-phase system with a single open-circuit failure. The table shows that the total losses in the three-phase system are a factor of 1.2 greater than the five-phase system. The five-phase system efficiency is lowered by approximately 3.3% compared to the normal condition but is higher than the three-phase system. In this simulation, as the dc capacitor in the three-phase system is a factor of 4.7 greater than the five-phase system, the output dc voltage and power ripple in the three-phase case is lower than the five-phase case. The maximum Dc voltage is 88V in the five-phase system and 75V in the three-phase system. The key outcome is that the five-phase system can deliver 538W whilst the three-phase system can only provide 452W.

Table 6.1. The simulation results for the three- and five-phase systems under one open-circuit failure

	Three-phase		Five-phase	
Ac side	average	Peak-peak ripple	Average	Peak-peak ripple
Shaft torque (Nm)	3.28	198%	4.28	179%
Shaft Power (W)	561	198%	627	179%
Dc side	Average		Average	
Dc voltage (V)	67	23.6%	72.5	48%
Dc power (w)	452	46.6%	538	89.2%
Losses				
Total losses(w)	108		89	
Efficiency	80.7%		85.8%	

iii- Generator rms phase current

The rms phase currents in the five-phase generator are increased in the adjacent phases and decreased in non-adjacent phases. In the three-phase system phase-*b* and -*c* rms currents are increased from the normal condition. Figure 6.9 shows the phase currents for the five- and three-phase system. The figure shows the difference in the phase currents in the five-phase system. Table 6.2 shows the percentage increase and decrease of the rms phase currents for both systems relative to the normal condition. The values in the five-phase case are not the same in all phases due to the effects of phase inductance and the dc link capacitor. The total generator copper losses with a single open-circuit phase for the five-phase generator (78.8W) is higher than the loss under normal conditions (65.8W) and in the three-phase generator the copper losses (102W) significantly higher than the copper losses in normal condition (68.5W). This leads to increased heat generation in both cases with a greater change in the three-phase generator. In the five-phase system phase-*a* and -*e* have a peak value of phase current of 7A and phase-*b* and -*d* have the same peak value of 14.1A which is less than the peak value in the three-phase system (18.4A).

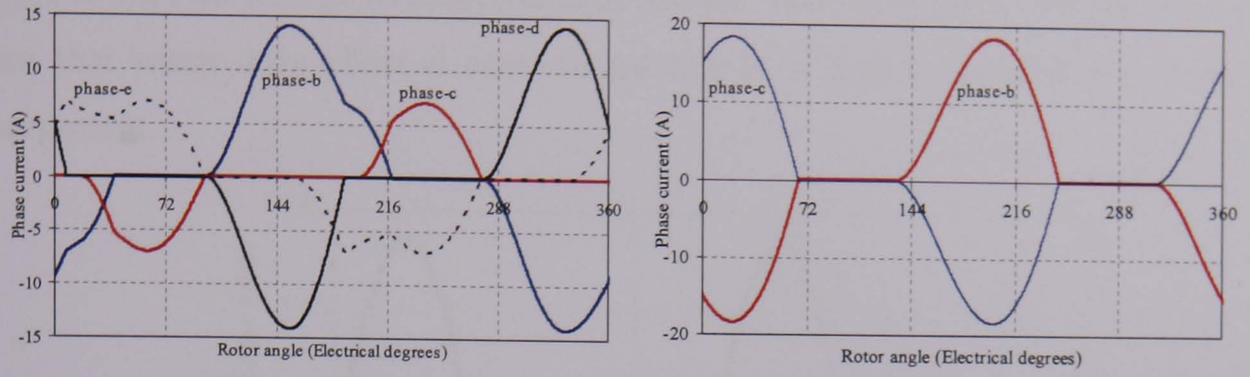

(a) (b)

Figure 6.9. Phase currents for the (a) five- and (b) three-phase generators with phase-*a* open-circuit.

Table 6.2. Percentage change in rms phase current values relative to the normal condition, and peak phase current, in the five- and three-phase systems with phase-*a* open-circuit.

	Three-phase		Five-phase	
	Percentage change in rms	Peak value (A)	Percentage change in rms	Peak value (A)
Phase-*b*	55%	18.4	62%	14.1
Phase-*c*	55%	18.4	-28.5%	7
Phase-*d*			45%	14.1
Phase-*e*			-7.5%	7

6.2.2 Adjacent open-circuit phase failures

In this case, phase-*a* and -*b* are open-circuit in the five-phase system; this is an adjacent phase open-circuit failure. The system continues to deliver power to the load, but with higher shaft torque ripple and output voltage ripple.

i- Generator shaft torque and power

The generator shaft torque depends on phase currents. In this case only phases-*c*, -*d* and -*e* conduct. Figure 6.10 shows the simulated generator shaft torque during one electrical cycle. The torque drops to zero for approximately 70° (electrical). This null period is where under normal conditions, phases-*a* and -*b* would be conducting. The peak-to-peak ripple is 9.2 Nm with an average value of 3.4Nm. The generator vibration will be higher than that when only phase-*a* open-circuit due to a higher fundamental torque ripple component.

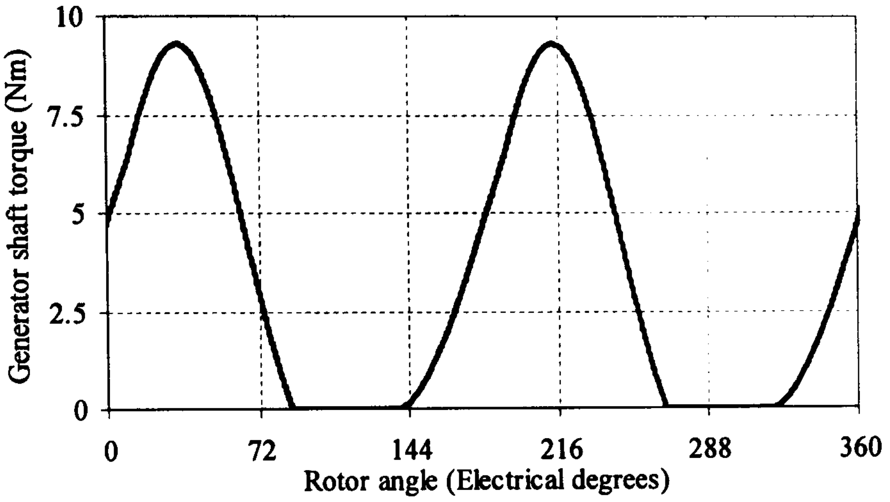

Figure 6.10. Generator shaft torque for the five-phase system with phase-*a* and-*b* open-circuit.

Figure 6.11 shows the generator shaft power. The power has average value which is 73% of the average power developed by the system under normal operation conditions, and 80% of the average power developed with one open-circuit failure. Further it is seen that the peak-to-peak power ripple is increased by approximately 7% compared to the single phase failure.

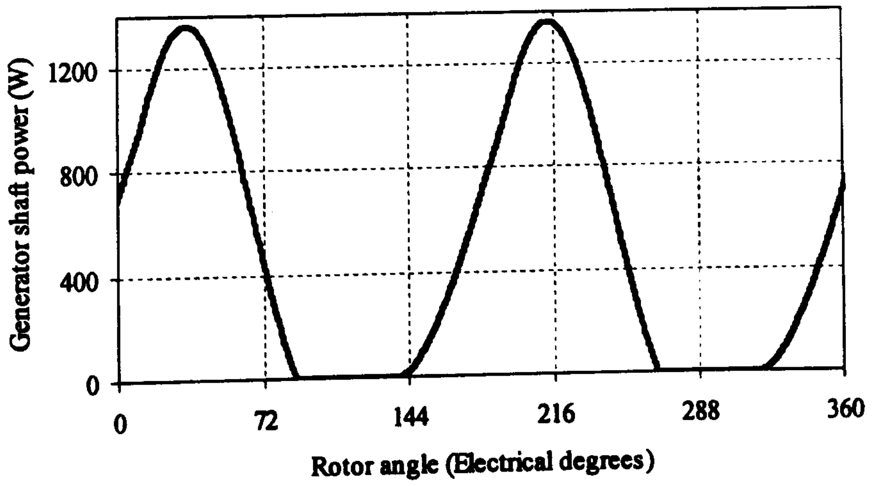

Figure 6.11. Generator shaft power for the five-phase system with phase-*a* and-*b* open-circuit.

ii- Dc output voltage and load power

The average values of dc output voltage and load power are calculated over one complete electrical period. Figures 6.12 and 6.13 show the output dc voltage and load power respectively when phase-*a* and -*b* are open-circuit. The average dc voltage and load power are reduced from normal conditions by 21.6% and 22.4% respectively and the voltage (hence power) ripple is significantly higher.

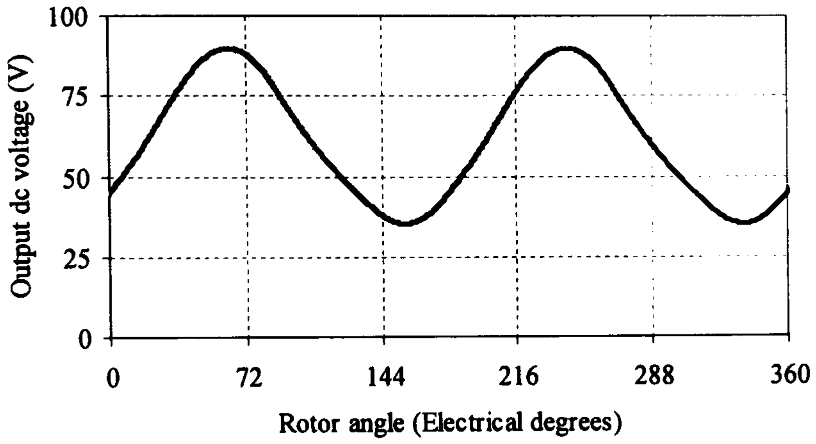

Figure 6.12. Load voltage from five-phase system with phase-*a* and-*b* open-circuit. The dc link capacitor is 470 μF.

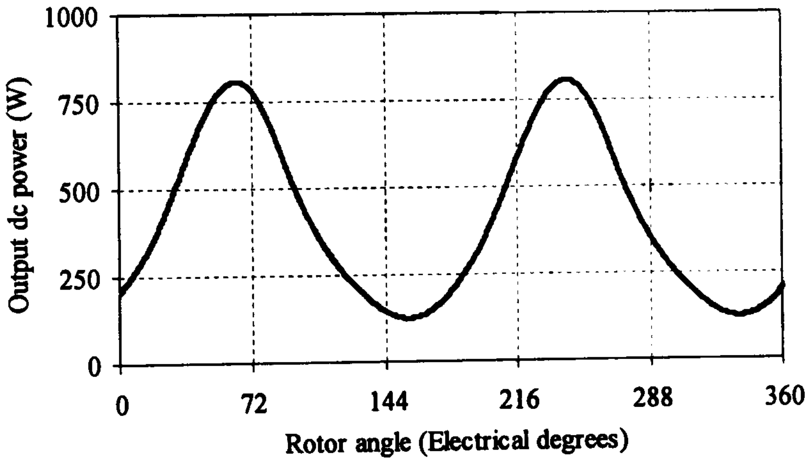

Figure 6.13. Load power from five-phase system with phase-*a* and-*b* open-circuit. The dc link capacitor is 470 μF.

Table 6.3 summarises the simulation results for the adjacent phase open-circuit failure condition. The peak-to-peak ripple is calculated with respect to the average value. The total losses are calculated by subtracting the output dc power from the generator power. With an adjacent phase failure the system efficiency is reduced by approximately 7.4% from the normal condition. This efficiency reduction is due to the increase of stator copper losses caused by the increased rms phase current in the three operational phases.

Table 6.3. Simulation results for the five-phase system with adjacent open-circuit phase failures

Ac side	Average	Peak-peak ripple
Shaft torque (Nm)	3.4	193%
Shaft Power (W)	500	193%
Dc side	Average	
Dc voltage (V)	61.3	85%
Dc power (W)	410	144%
Losses		
Total losses(W)	89.7	
Efficiency	82.1%	

iii- Generator rms phase current

The rms phase currents in the five-phase generator are increased in phase-*c* and -*e* and decreased in phase-*d* as shown in figure 6.14. This is different from the ideal case due to the presence of the dc link capacitor and generator parameters. Table 6.4 shows the percentage change in the rms phase currents for the five-phase system relative to the normal conditions. The increase of the currents in some phases leads to increase the temperature in these phases. Imbalance in the phase current value increases the vibration at the generator shaft. Table 6.4 also details the peak value of phase current.

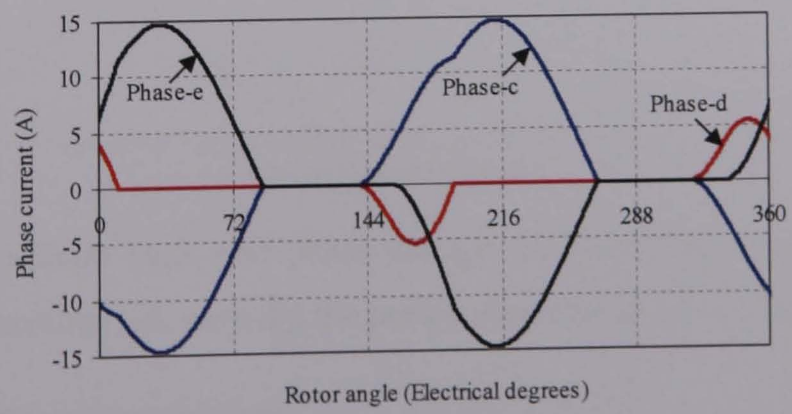

Figure 6.14. Phase currents for the five-phase system with phase-*a* and -*b* open-circuit.

Table 6.4. The percentage change in rms phase currents relative to the normal condition, and peak phase current, in the five- phase system when phase-*a* and -*b* are open-circuit.

	Percentage change in rms	Peak value (A)
Phase-*c*	80%	15
Phase-*d*	-58%	15
Phase-*e*	68%	5.4

6.2.3 Non-adjacent open-circuit phase failures

In the case of a pair of non-adjacent phase failures, for example, phase-*a* and phase-*c*, there are two phase current that conduct for 108° electrical degrees and the other conducts for 144°, as shown in figure 6.15 for the case with no dc link capacitor. The generator delivers power to the load through the remaining 6 conduction periods. The simulation uses the same data in section 6.2.

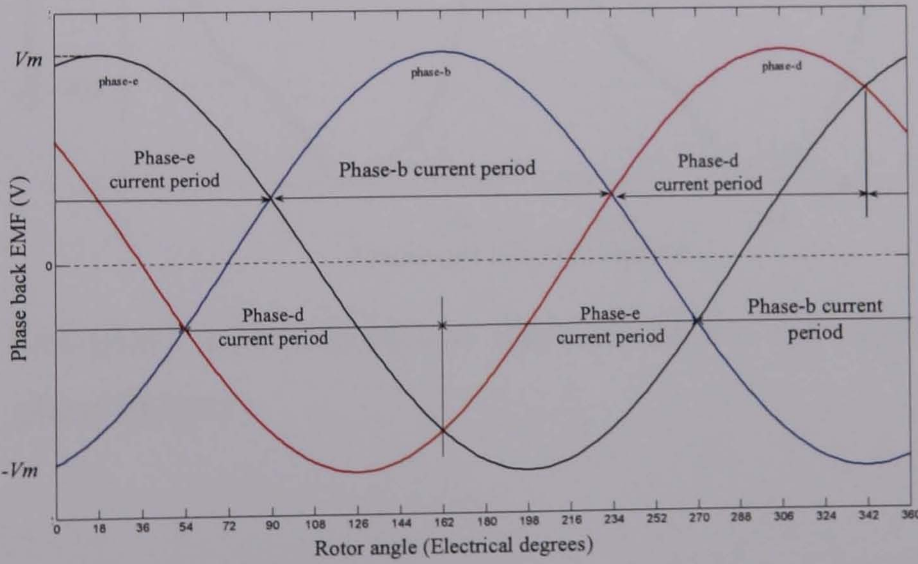

Figure 6.15. Five-phase back emf phase voltage for one cycle, when phase-*a* and-*b* disconnected, showing the period where the phase currents conduct.

i- Generator shaft torque and power

Figures 6.16 and 6.17 show the simulation results of the generator shaft torque and power respectively. From figure 6.18, the torque falls to zero for two periods in one electrical cycle. Each of these periods lasts for 18° (electrical). The total period of zero torque production is 36° compared to 144° for adjacent phase failures. The average torque output is 3.9Nm with a peak-to-peak ripple of 9.2Nm. This represents 0.83 of the average torque value under normal conditions.

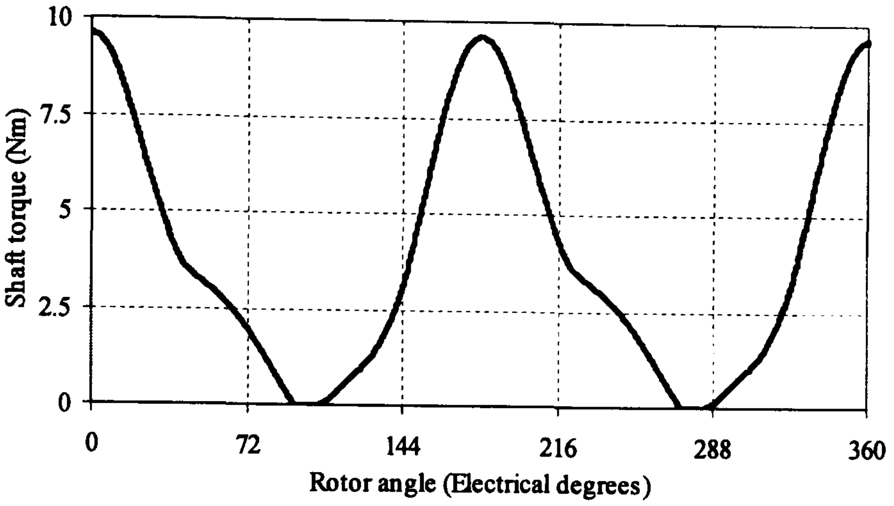

Figure 6.16. Five-phase system generator shaft power for non-adjacent open-circuit phase failures.

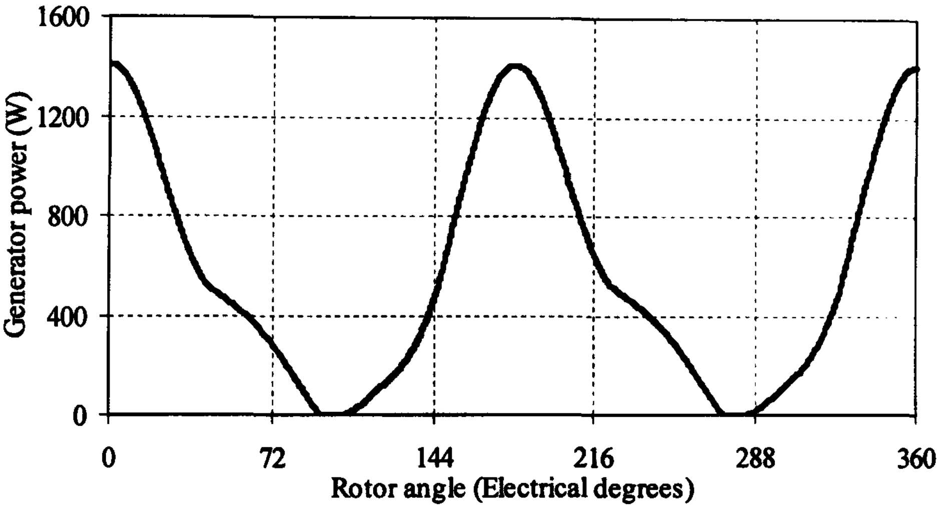

Figure 6.17. Five-phase system generator shaft power for non-adjacent open-circuit phase failures.

ii- Dc output voltage and power

Figures 6.18 and 6.19 present the rectifier output dc voltage and load power respectively when phase-*a* and -*b* are open-circuit. The average dc output voltage is 66.9V and resultant load power 475W. This is 1.1 of the voltage with adjacent phase failure, and 1.16 of the average power. It is clear that a non-adjacent phase failures captures and delivers more power compared to adjacent phase failures.

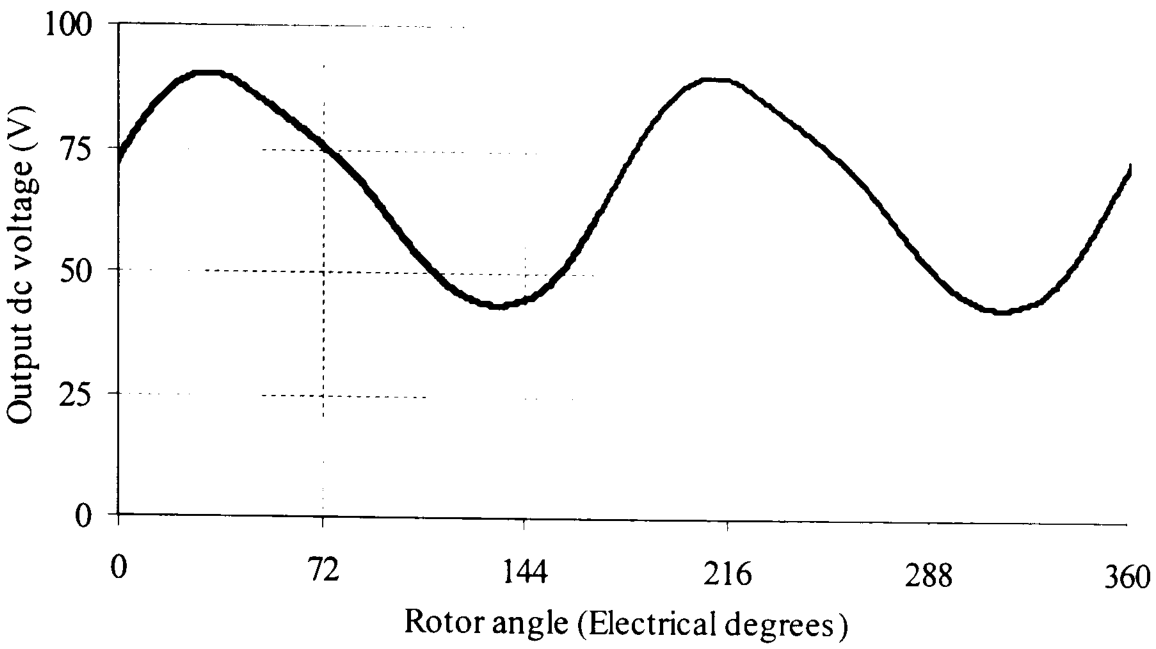

Figure 6.18. Output dc voltage of the five-phase system with non-adjacent open-circuit phase failures. The dc link capacitor is 470 μF.

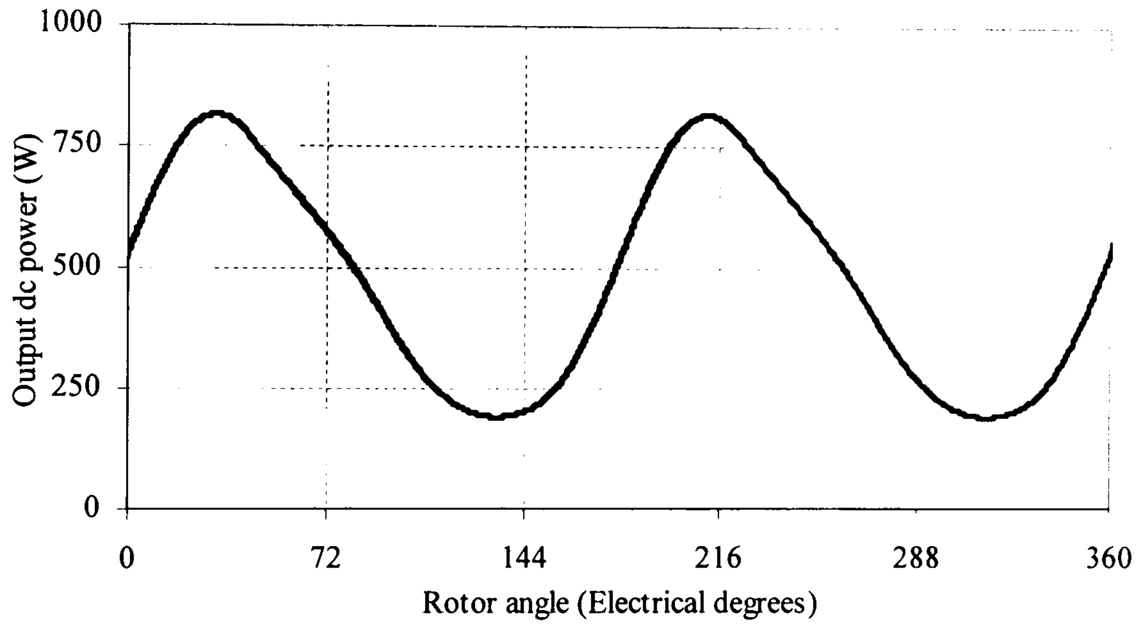

Figure 6.19. Output dc power of the five-phase system with non-adjacent open-circuit phase failures. The dc link capacitor is 470 μF.

Table 6.5 summarises the simulation results with a non-adjacent open-circuit failure. In the case of a non-adjacent failure the efficiency is increased by approximately 2% compared to the adjacent phase failure. The non-adjacent phase failure is a less extreme operating condition compared to the adjacent phase failure mode.

Table 6.5. Simulation results for the five-phase system with a pair of non-adjacent open-circuit phase failures

Ac side	Average	Peak-peak ripple
Shaft torque (Nm)	3.9	192%
Shaft Power (W)	566	192%
Dc side	Average	
Dc voltage (V)	66.9	68%
Dc power (W)	475	119%
Losses		
Total losses(W)	91.6	
Efficiency	83.8%	

iii- Generator rms phase current

The rms phase currents in the five-phase generator are increased in phase-*b* and -*d* and decreased in phase-*e* as shown in figure 6.20. Table 6.6 shows the percentage change in the rms phase currents for the five-phase system relative to the normal rms current. The rms current in phase-*b* and -*d* are not equal due to the presence of the dc capacitor in the rectifier circuit. The dc link capacitor alters the conduction period of the rectifier circuit. The total generator copper loss is a factor of 1.2 of the rated copper loss. The generator may sustain this mode of operation but there will be two phases operating at significantly higher temperature than under normal operating conditions.

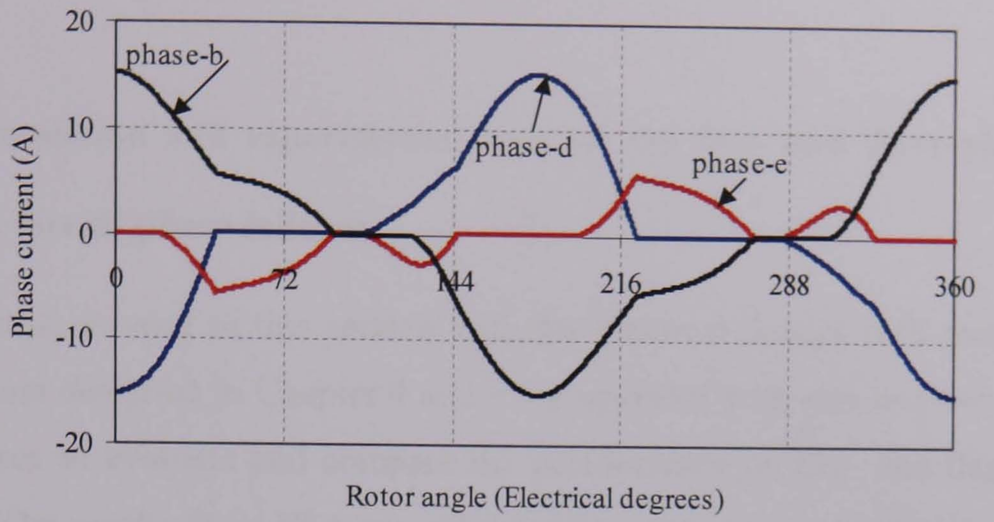

Figure 6.20. Phase currents for the five-phase system with phase-*a* and -*c* open-circuit.

Table 6.6. The percentage increase and decrease of rms phase current relative to the normal condition in the five-phase system when phase-*a* and -*c* are open-circuit.

	Percentage change in rms	Peak value (A)
Phase-*b*	78.8%	15.2
Phase-*d*	69%	15.2
Phase-*e*	-45%	5.7

It is observed from the simulation results that when a single phase open-circuit failure occurs, the five-phase system captures more power from the prime mover compared to the three-phase system, with lower peak-to-peak voltage ripple. Also the total copper loss is less in the five-phase generator compared to the three-phase generator despite imbalance in the phase currents. When two adjacent phases are open-circuit in the five-phase system the system still captures more power than the three-phase system with a single phase open-circuit failure. The generator peak-to-peak torque ripple and output dc voltage ripple are higher in the five-phase system with single phase open-circuit failure compared to the normal condition. The non-adjacent phase failure mode results in a less extreme condition compared to an adjacent phase failure in terms of torque ripple and output dc voltage and power ripple. In both cases the total copper losses are less than rated copper losses in the generator, though it is expected that sustained operation in these modes would result in higher insulation temperature in two of the three remaining phases.

6.3 FEA simulation and experimental tests on the five- and three-phase systems under open-circuit phase failures

FEA simulation is used in this section with the practical design with mounting holes. The generators designed in Chapter 4 and 5 are operated with one and two phase open-circuit failures to evaluate and compare the performance of five- and three-phase PM generators. The results from FEA are validated by comparing with the results from the experimental test. The speed is fixed at 1400rpm for all tests the dc link capacitor is 470μF for the five-phase system and 2200μF for the three-phase system.

The results differ from the simulations in section 6.2 due to back emf distortion. The distortion in the back emf is caused by back iron saturation due to the mounting holes in the stator lamination. The distorted back emf has a significant impact on the operation of both the three- and five-phase system. Nonetheless the practical results provide evidence of the advantages of the five-phase system compared to the three-phase system under open-circuit failure conditions.

6.3.1 Single open-circuit phase failure

This test is carried out for both the five- and three-phase systems. During the test phase-*a* is open-circuit. The experimental generator torque and power and FEA results for the five-and three-phase systems are shown in figures 6.21 and 6.22 respectively. The experimental results are estimated using the phase currents and the phase back emf. There is a slight difference between the results from FEA and the results from experimental primarily due to the estimation process using the experimental test results.

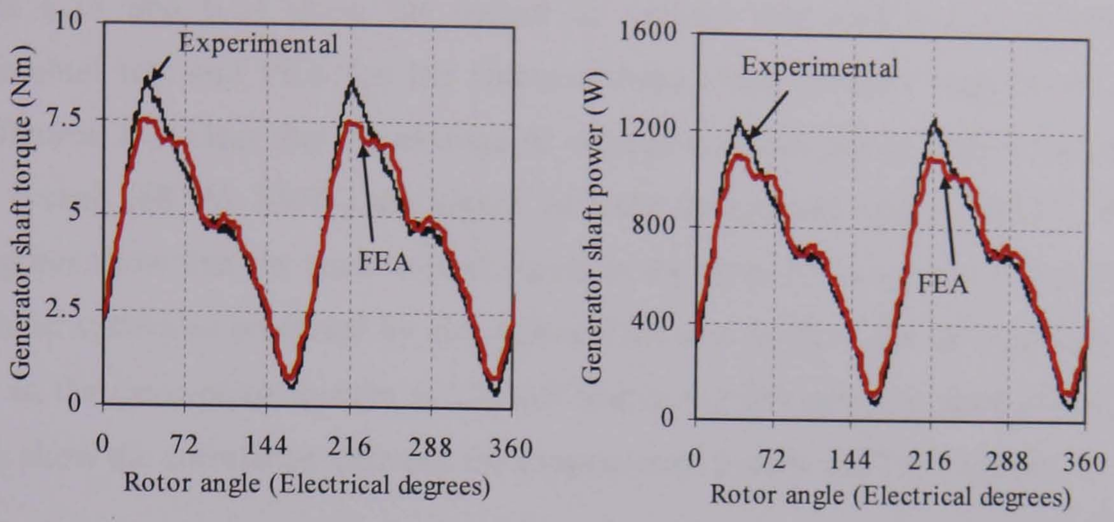

(a) (b)

Figure 6.21. Five-phase generator with phase-*a* open-circuit showing (a) estimated shaft torque, and (b) generator shaft power at 1400rpm.

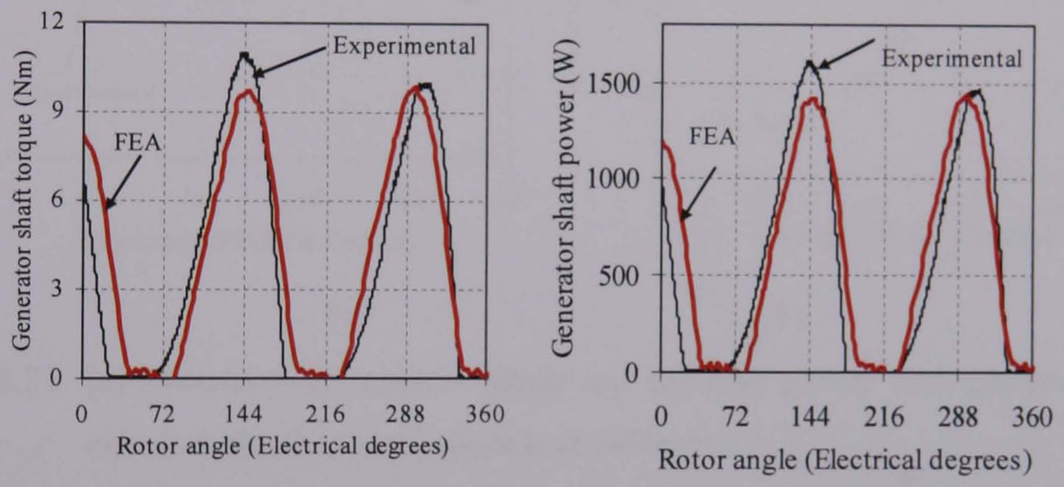

(a) (b)

Figure 6.22. Three-phase generator with phase-*a* open-circuit showing (a) estimated shaft torque, and (b) generator shaft power at 1400rpm.

It can be seen from the estimated torque waveform that the five-phase system has a lower peak-to-peak torque ripple (8.2Nm) than the three-phase system, (10Nm). The average torque is 4.5Nm for the five-phase system and 3.8Nm for the three-phase system. The audible vibration noise from the three- phase system is significantly higher than five-phase system.

Figures 6.23 and 6.24 show the output dc voltage and load power results from experimental test and FEA for the five-and three-phase systems respectively. From these figures, it is clear that the average dc voltage and load power values for the five-phase system (68.4V, 540W) are higher than the three-phase system (60.5V, 429W). The figures show that the peak-to-peak ripple in the three-phase system is less than the five-phase system as predicted by simulation. This is a result of the dc capacitor value, which in the three-phase system is 2200μF and in the five-phase system 470μF. The figures show the correlation between the experimental results and FEA results.

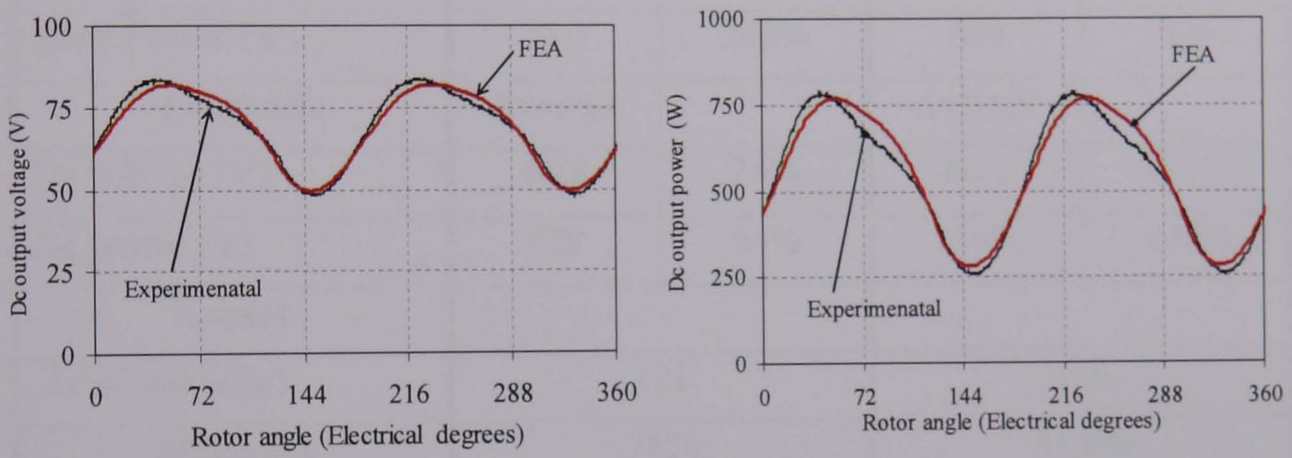

(a) (b)

Figure 6.23. (a) Measured dc output voltage and (b) load power with phase-*a* open-circuit in the five-phase system at 1400rpm.

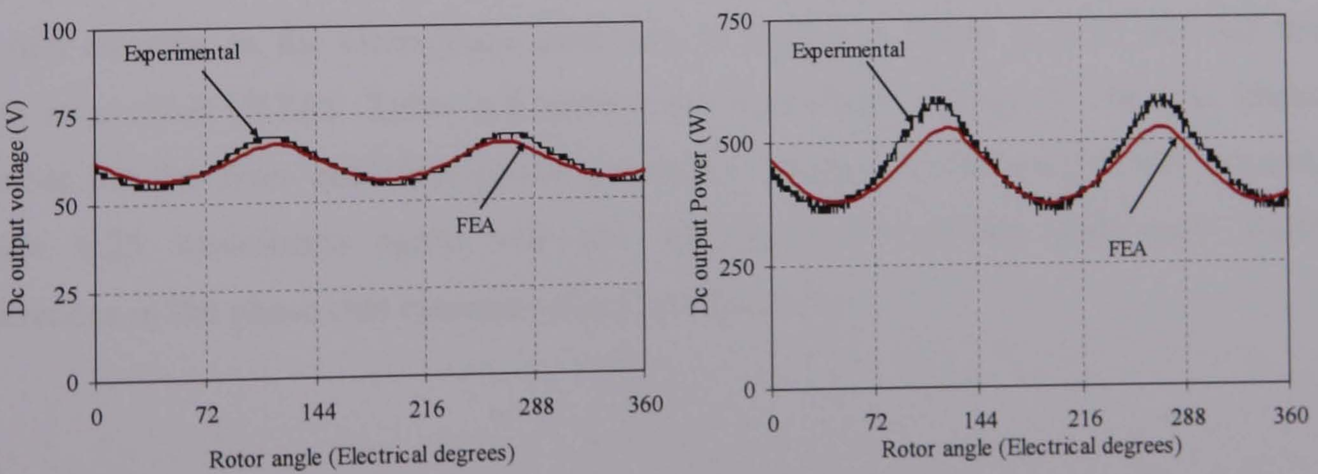

(a) (b)

Figure 6.24. (a) Measured dc output voltage and (b) load power with phase-*a* open-circuit in the three-phase system at 1400rpm.

The experimental results are summarised in Table 6.7. The efficiency of the five-phase system is 4.7% higher than the three-phase system. It is clear from the results that the five-phase system has better performance than the three-phase system under single phase open-circuit failure in terms of shaft torque ripple and power ripple (7% less).

Table 6.7 Experimental results for the three-and five-phase systems with a single open-circuit phase failure.

	Three-phase		Five-phase	
Generator side	Average	Peak-peak ripple	Average	Peak-peak ripple
Shaft torque (Nm)	3.8	263%	4.5	183%
Shaft Power (W)	550	263%	660	183%
Load side	Average		Average	
Dc voltage (V)	60.5	24%	68.4	53.9%
Dc power (w)	429	54%	540	100%
Losses				
Total losses(w)	121		120	
Efficiency	78%		81.8%	

The rms phase currents in the five-phase generator are shown in figure 6.25(a). The rms current is increased in phase-*b* and -*d* and decreased in phase-*e* and -*c*. The waveform of the rms currents in the three-phase generator is shown in figure 6.25(b) and has the same rms value (9.7A). Table 6.8 shows the percentage change in the rms phase currents for the five- and three-phase generators relative to the normal rms current. Figure 6.25 waveforms agree with the simulation waveforms with only slight differences in the phase rms currents values in Table 6.8.

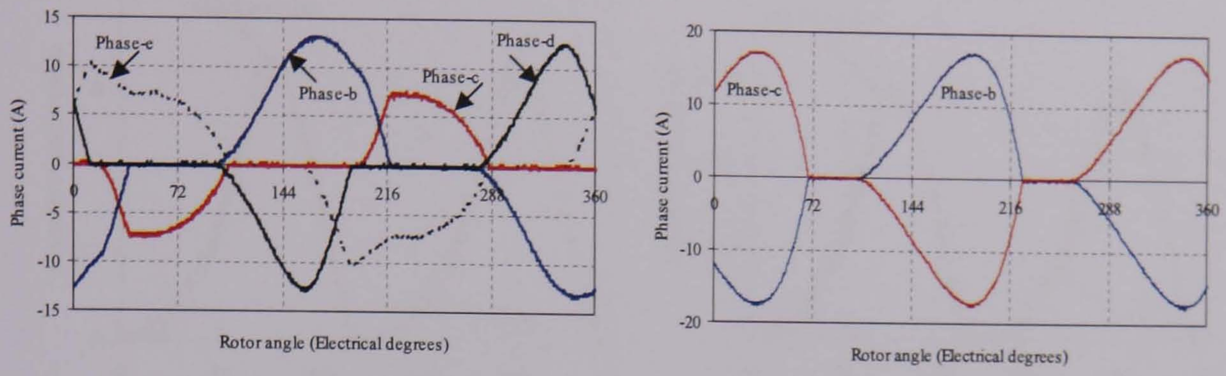

(a) (b)

Figure 6.25. Phase currents for the (a) five- and (b) three-phase generators with phase-*a* open-circuit.

Table 6.8. Percentage change in rms phase current values relative to the normal conditions in the five- and three-phase systems when phase-*a* is open-circuit

	Three-phase		Five-phase	
	Percentage change	Peak value (A)	Percentage change	Peak value (A)
Phase-*b*	51%	17.4	64%	13.2
Phase-*c*	51%	17.4	-16%	7.6
Phase-*d*			29%	13
Phase-*e*			-1%	10.1

6.3.2 Adjacent open-circuit phase failures

This test is carried-out with phase-*a* and-*b* open-circuit in the five-phase system. The vibration and noise is higher than that from the single phase failure. Figure 6.26 shows the generator estimated torque and power compared with FEA results when phase-*a* and -*b* are open-circuit. Figure 6.26 clearly shows the period where the shaft torque and power fall to zero. The peak-to-peak ripple in figure 6.26(a), 7.9Nm, generates noise and vibration.

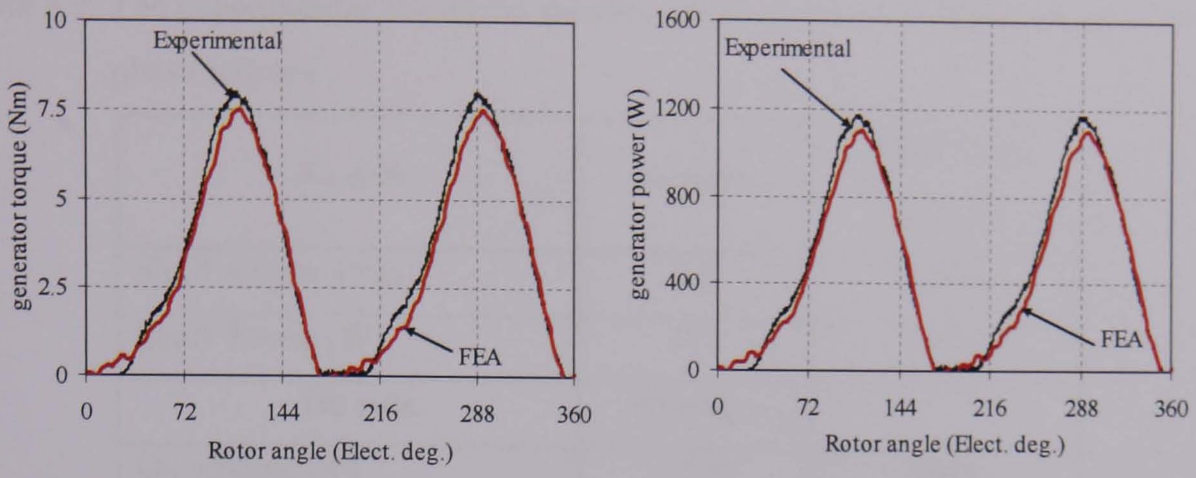

(a) (b)

Figure 6.26. Five-phase (a) estimated shaft torque and (b) shaft power with phase-*a* and-*b* open- circuit at 1400rpm.

The output dc voltage and load power are shown in figure 6.27. The FEA results show good agreement with the experimental results in term of average value and waveform shape.

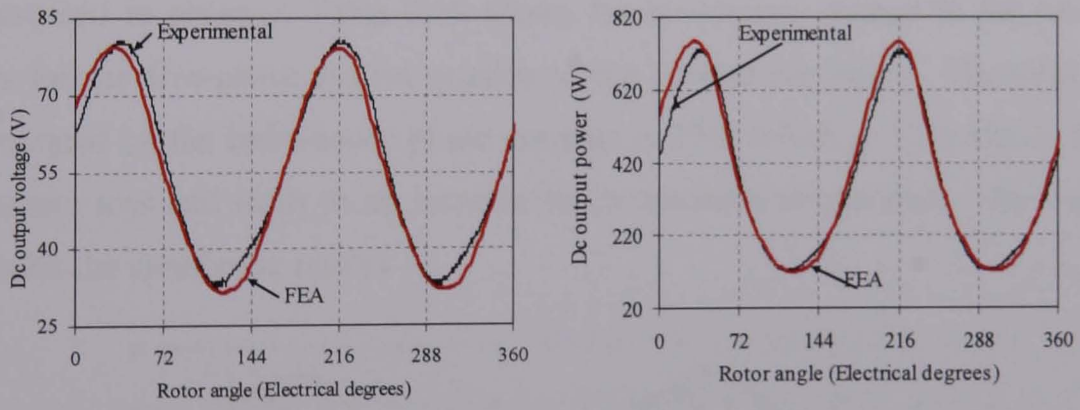

(a) (b)

Figure 6.27. Five-phase (a) measured dc output voltage and (b) load power with phase-*a* and -*b* open-circuit at 1400rpm.

Experimental results are summarised in Table 6.9. The results show that the total losses are less than when only one phase is open-circuit. Also the system efficiency decreases by approximately 4% compared to the single open-circuit failure mode which agrees with the simulation results.

Table 6.9. The experimental results for the five-phase system with adjacent open-circuit phase failures

Ac side	Average	Peak-peak ripple %
Shaft torque (Nm)	3.2	246%
Shaft Power (W)	475	246%
Dc side	Average	
Dc voltage (V)	55.4	88%
Dc power (W)	373.3	164%
Losses		
Total losses(W)	101.7	
Efficiency	78.6%	

The waveform of the phase current when phase-*a* and -*b* are open-circuit is shown in figure 6.28. Phase-*c* and -*e* rms current are increased compared to the normal condition and decreased in phase-*d*. Table 6.10 shows the percentage change in the rms phase currents for the five-phase system relative to the normal conditions. The total copper loss generated by the imbalanced phase currents is 77W which is 12% higher than the rated copper loss and leads to an increase in the machine temperature. The waveform agrees with the simulation results.

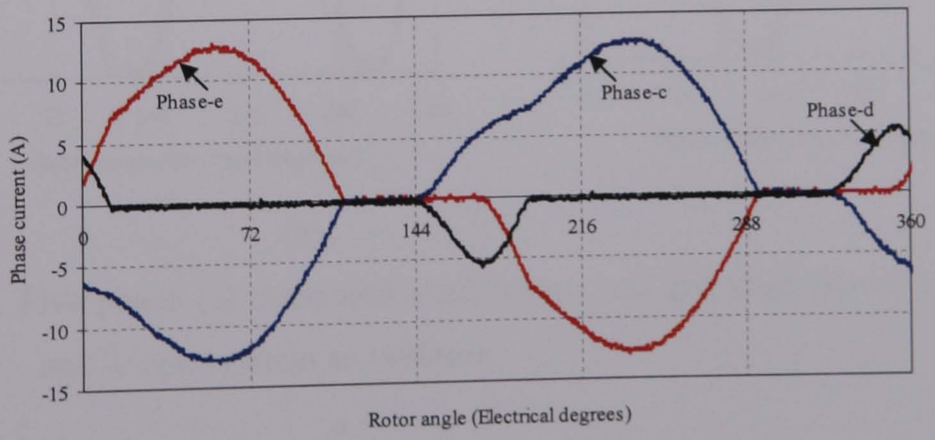

Figure 6.28. Phase currents for the five-phase system with phase-*a* and -*b* open-circuit.

Table 6.10. The percentage increase and decrease of rms phase currents relative to the normal condition, and peak phase current, in the five-phase system when phase-*a* and -*b* are open-circuit

	Percentage change	Peak value (A)
Phase-*c*	73%	13
Phase-*e*	67%	13
Phase-*d*	-60%	5.4

6.3.3 Non-adjacent open-circuit phase failures

Phase-*a* and -*c* are open-circuit in this experiment. During the test a higher peak-to-peak torque ripple occurs and the generator displays noticeably higher levels of vibration. There is more noise generated by the test rig. Figures 6.29 and 6.30 show the experimental and FEA results of the generator torque and power, and rectifier output dc voltage and load power respectively.

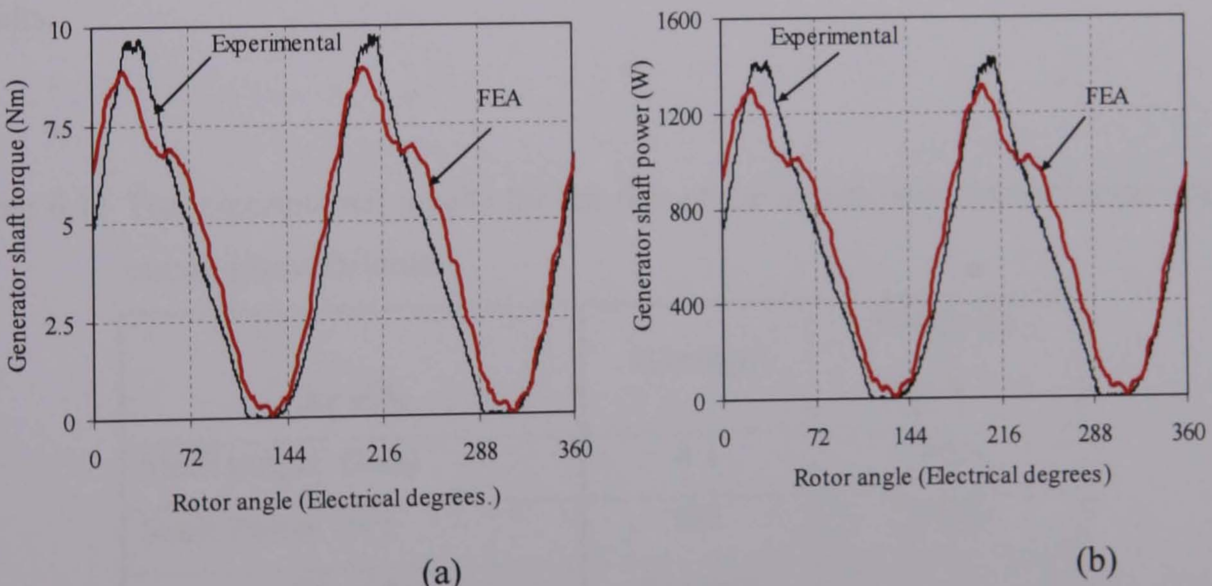

(a) (b)

Figure 6.29. Five-phase (a) estimated shaft torque and (b) shaft power with phase-*a* and -*c* open-circuit at 1400rpm.

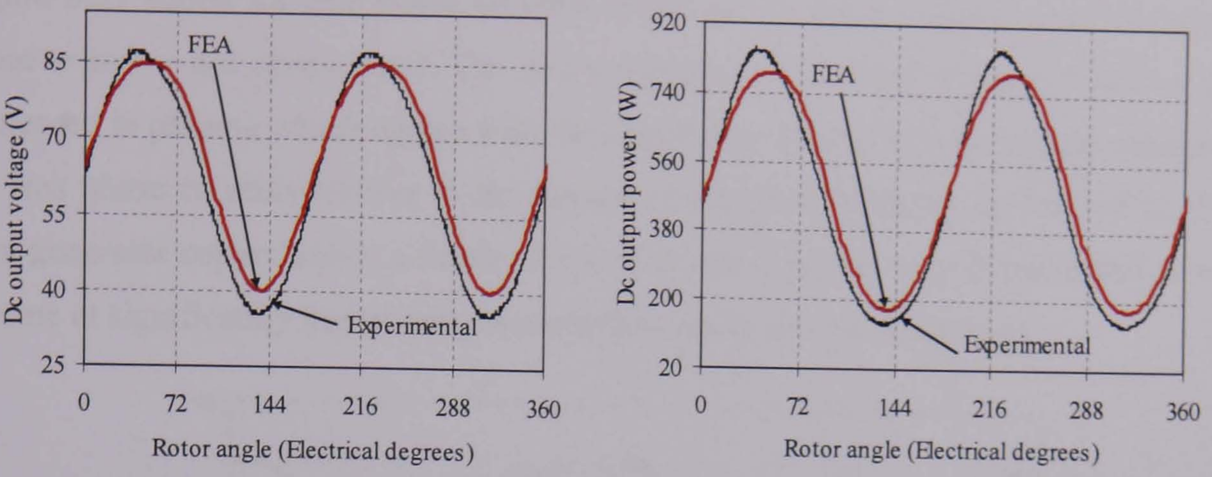

(a) (b)

Figure 6.30. Five-phase (a) measured dc output voltage and (b) load power with phase-*a* and -*c* open-circuit at 1400rpm.

Experimental results for the five-phase system with two non-adjacent open-circuit failures are summarised in Table 6.11. The results show that the resultant efficiency is higher than that when single phase open-circuit, which agrees with the simulation results.

Table 6.11 The experimental results for the five-phase system with non-adjacent open-circuit phase failures.

Ac side	Average	Peak-peak ripple %
Shaft torque (Nm)	4.1	238%
Shaft Power (W)	595	238%
Dc side	Average	
Dc voltage (V)	62.1	83%
Dc power (W)	470	154%
Losses		
Total losses(W)	125	
Efficiency	79%	

Figure 6.31 shows the rms phase currents waveform in the five-phase generator when phase-*a* and -*c* are open-circuit. The rms currents are increased in phase-*b* and -*d* and decreased in phase-*e* which agrees with the simulation results. The percentage change in the rms phase currents relative to the normal rms current is shown in Table 6.12. The total generator copper loss is a factor of 1.3 of the rated copper loss. Phase-*b* and -*d* will operate at significantly higher temperatures than under normal conditions.

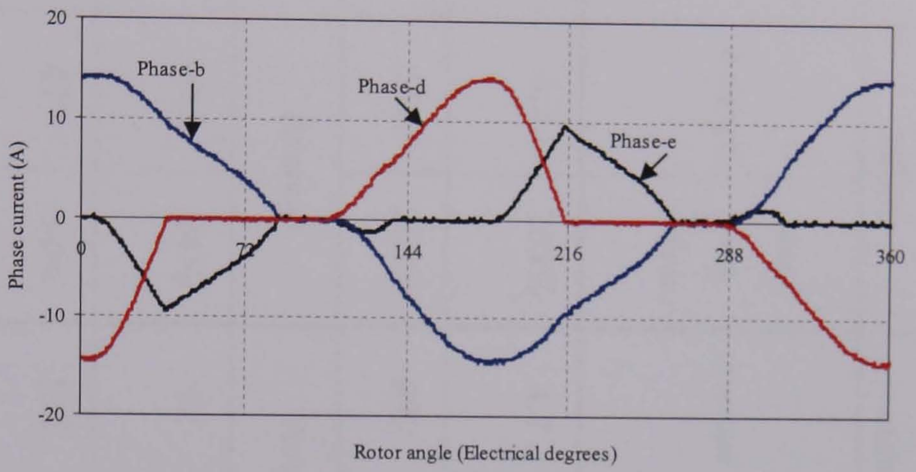

Figure 6.31. Phase currents for the five-phase system with phase-*a* and -*b* open-circuit.

Table 6.12. The percentage increase and decrease of rms phase currents relative to the normal condition in the five-phase system when phase-*a* and-*c* are open-circuit.

	Percentage change	Peak value (A)
Phase-*b*	91% 8.6	14.4
Phase-*d*	62% 7.3	14.4
Phase-*e*	-18% 3.7	9.4

Table 6.13 illustrates the comparison between the five- and three-phase system under normal failure conditions.

Table 6.13. Comparison between experimental results for the five- and three-phase system under normal and failure conditions.

	Three-phase system				Five-phase system							
	Normal condition		Single-phase failure		Normal condition		Single-phase failure		Adjacent phase failures		Non-adjacent phase failures	
Ac side	Average	peak-peak ripple	Average	peak-peak ripple	Average	peak-peak ripple	Average	peak-peak ripple	Average	peak-peak ripple	Average	peak-peak ripple
Shaft torque (Nm)	4.9	31%	3.8	263%	4.7	18%	4.5	183%	3.2	246%	4.1	238%
Shaft Power (W)	719	31%	550	263%	692	18%	660	183%	475	246%	595	238%
Dc side	Average		Average		Average		Average		Average		Average	
Dc voltage (V)	73	3%	60.5	24%	72	1.4%	68.4	53.9%	55.4	88%	62.1	83%
Dc power (w)	606	6%	429	54%	595	2.9%	540	100%	373.3	164%	470	154%
Losses												
Total losses(w)	113		121		97		120		101.7		125	
Efficiency	84%		78%		86%		81.8%		78.6%		79%	

6.4 Summary

In this chapter, the operation of the five-phase and three-phase permanent magnet generator feeding a diode bridge rectifier under single open-circuit phase failures is assessed and discussed. Also the operation of five-phase system with adjacent and non-adjacent open-circuit phase failures is presented.

With a single phase open-circuit failure, the five-phase system has a higher output dc voltage and load power compared to the three-phase system, 7.4% higher. The peak-to-peak torque ripple in the permanent magnet generator for the five-phase is approximately 183% and in the three-phase system is 263%. The five-phase system efficiency is 6% higher than the three-phase system. It is clear from the results that five-phase system has advantages over three-phase system with a single open-circuit phase failure in terms of generator torque ripple, output power, and efficiency.

The five-phase system has adjacent and non-adjacent open-circuit failure modes. With two adjacent phase failures the system has an efficiency of 82.1% and with non-adjacent phase failure the efficiency is 83.8%. In both cases the efficiency is higher than with the three-phase single-phase failure. It observed that non-adjacent failure produces a less extreme operating condition compared to adjacent phase failures particularly in terms of torque ripple and voltage ripple. Under both adjacent and non-adjacent phase failures, the five-phase system still outputs more power than the three-phase system with one failure.

In the three-phase system with an open-circuit phase failure, the remaining two phase currents have the same rms value but the rms value is increased compared to the normal condition. In the five-phase system the rms phase currents are not the same in all phases at failure. Some phases have higher rms value than rated and other phases have a lower rms value. With a single open-circuit phase failure the total copper loss in the three-phase generator is 49% higher than the rated copper loss. In the five-phase generator the copper loss increases by only 14% compared to the normal operating conditions. In the five-phase generator with two open-circuit phase failures the total copper loss is higher than the rated copper loss. With adjacent phase failure the loss is 12% higher than rated loss and with non-adjacent phase failure the total loss is 30% higher than rated loss. The generator may sustain this mode of operation but this will lead to increase the generator temperature if it operates for a long period.

Experimental data for the five- and three-phase permanent magnet generators is used to verify simulation results. There is a slight difference in waveforms due to the back emf distortion in the practical design due to iron saturation around the stator mounting holes. But the results confirm that five-phase system has improved performance under open-circuit failure compared to the three-phase system, these being reduced torque ripple and improved output power.

References

[6.1] P. S. N. De Silva, J. E. Fletcher, and B. W. Williams, "Analysis of Concentrated Winding Multi-phase Machines under Phase Failure using Decoupled Vector Space Theory," IET 3rd International Conference on Power Electronics, Machines and Drives, March 2006, pp. 420-424.

[6.2] H. Xu, H. A. Toliyat, and L. J. Paterson, "Resilient Current Control of Five-Phase Induction Motor under Asymmetrical Fault Conditions," Applied Power Electronics Conference and Exposition, APEC 2002, March 10-14, 2002,Vol. 1, pp. 64-71.

Chapter 7

Analysis of the dc link capacitor current

7.1 Introduction

In this chapter the rms current of the dc link capacitor in the five- and three-phase PM generator systems is investigated using the simulation model, FEA and experimental tests.

Analysis of the dc link capacitor current is presented in section 7.2 and the capacitor rms ripple current and capacitor core temperature are discussed in section 7.3.

Simulation is performed when all phases of the permanent magnet generator are functioning properly (the normal condition), and when single, adjacent and non-adjacent open-circuit failures occur. Simulation results for the five- and three-phase system for both normal cases and failure conditions are discussed in section 7.4. In section 7.5 the capacitor current for the five- and three-phase system is assessed using FEA where the FEA is performed on the practical design.

Experiments under normal and failure conditions are performed for the three- and five-phase systems. The results are presented in section 7.6. These verify the simulation and FEA results. The key outcomes are that under normal operation the five-phase system has advantage of a lower capacitance requirement compared to the three-phase system with the same absolute capacitor core temperature. However, during failure the power delivered from the five-phase system is greater and this imposes a more extreme operating condition on the dc link capacitor. Care must be exercised when specifying the dc link capacitor in a five-phase system that may be expected to operate with one or more phase failures.

7.2 Dc link capacitor current

The capacitor is used to smooth the output voltage thereby generating near constant voltage. The capacitor is connected in parallel with the resistive load as shown in figure 7.1. The diode rectifier current, I_{dc}, equals the sum of the load current, I_L. and capacitor current, I_c.

$$I_{dc} = I_c + I_L \tag{7.1}$$

The capacitor current is

$$I_c = C\frac{dV_{dc\_cap}}{dt} \tag{7.2}$$

where C is the capacitance and V_{dc_cap} is the dc link voltage. The equivalent series resistance of the capacitor is ignored for simplicity. The capacitor current has a frequency equal to six times the source frequency in the three-phase system and ten times the source frequency in the five-phase system under steady-state operation with no fault conditions.

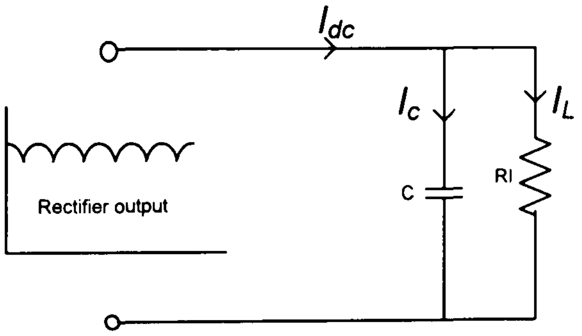

Figure 7.1 The output section showing the load current, I_L, capacitor current, I_c and dc output current, I_{dc}.

7.3 Dc link capacitor rms ripple current and core temperature

Ripple current is a key factor for capacitor lifetime. The lifetime of the capacitor depends on temperature of the capacitor core and periods operation at high core temperatures lead to thermal stress that can have a significant impact on accumulated lifetime. The ripple current in the capacitor is the primary source of heat generation in the core which increases the capacitor core temperature. The capacitor power (or rate of heat generated in the capacitor) is [7.1]

$$P_{cap} = I^2_{c\text{-}rms} R_{ESR} \tag{7.3}$$

where $I_{c\text{-}rms}$ is the rms value (ripple current) of the capacitor current, and R_{ESR} is the equivalent series resistance of the capacitor.

For a given capacitor, R_{ESR} depends on the frequency and core temperature of the capacitor. Characteristic curves are often provided by the manufacturer. The core temperature should not exceed the maximum temperature given by the manufacturer.

The core temperature of the capacitor can be calculated using [7.2]

$$T_c = T_r + T_a \tag{7.4}$$

where T_a is ambient temperature (assumed here to be 45°C worst-case) and T_r is the core temperature rise. T_r is estimated

$$T_r = R_{ha} \times P_{cap} \tag{7.5}$$

where R_{ha} is the thermal resistance.

The thermal resistance, R_{ha}, depends on the capacitor dimensions and the airflow around the capacitor as shown in Table D7 Appendix D. In this thesis the airflow is assumed to be 2ms^{-1}. The dimensions of the 200V 470μF, capacitor used in the five-phase system are $\phi 36 \times 52$mm and for the three-phase system (2200μF, 200V) are $\phi 51 \times 82$mm. From Table D7 the thermal resistance is 8.29°C/W for the five-phase capacitor and 4.7°C/W for the three-phase capacitor. The capacitor type used in this research is the BHC ALS30 Series.

As the R_{ESR} decreases with ripple frequency, the ripple current capability of an electrolytic capacitor increases with ripple frequency. For example, rated rms ripple current for the 470μF capacitor at 100Hz is 2.6A but increases to 4.3A at 10 kHz. Most manufacturers give the rms ripple current for particular frequency. For other frequencies a formula is often provided to correct the rms current ripple [7.3]. For the ALS30 series this formula is

$$I_{rms\_cap} = \sqrt{\frac{F \times A^2 \times B^2}{100 \times \left(B^2 - A^2\right) + \left(F \times A^2\right)}} \tag{7.6}$$

where F is the required frequency, and A and B are the maximum 100Hz ripple current and 10kHz ripple currents respectively and are provided by the manufacturer. The frequency compensation is only made for normal conditions where the fundamental frequency of the current is greater than 100Hz. With failure conditions the fundamental frequency of the capacitor current is 93Hz which is close to 100Hz. Hence frequency compensator for R_{ESR} is only carried out for normal conditions.

7.4 Simulation analysis of dc link capacitor current

The five- and three-phase systems simulated in chapters 4 and 5 are used to investigate the dc link capacitor requirements for the five- and three-phase systems. The simulation is performed for the normal condition, where all phases function, and the failure conditions with a single phase open-circuit, with an adjacent and with a non-adjacent open-circuit failure.

7.4.1 Dc link capacitor current under normal conditions current

Table 7.2 and 7.3 show the simulation results for different values of dc link capacitor. It is clear from the tables that with the same capacitance the five-phase system has a lower rms capacitor current compared to the three-phase system. The capacitor values 470μF and 2200μF produce similar values of output dc voltage ripple for the five- and three-phase systems respectively. These were the chosen for the experimental work in this thesis. The rms capacitor current for the five-phase system is then a factor of 5 lower than the three-phase system. It is observed that the rms capacitor current decreases as the capacitance increases. This is due to relationship between the capacitor current and output dc voltage (7.2). For example, with a small capacitor value the output dc voltage has higher ripple hence the derivative of this voltage has a higher value and the capacitor current, which equals the derivative dc voltage multiplied by the value of capacitor, will be higher. In the five-phase system the capacitance used is lower than the three-phase system, even so the capacitor rms current still lower than that experienced in the three-phase system. This is one advantage of the five-phase system over the three-phase system under normal conditions.

Table 7.1. Simulation results for the five-phase system with different values of dc link capacitor. The average output dc voltage is 78.1V.

Capacitor, μF	Peak-to-peak output ripple, (V)	RMS Capacitor Current, A
220	1	0.23
470	0.6	0.22
680	0.3	0.21
1000	0.2	0.2
2200	0.12	0.2

Table 7.2. Simulation results for the three-phase system with different values of dc link capacitor. The average output dc voltage is 78.0V.

Capacitor, μF	Peak-to-peak output dc ripple, (V)	RMS Capacitor Current, A
220	12.3	1.68
470	4.4	1.32
680	2.8	1.22
1000	1.8	1.2
2200	0.7	1.1

Figure 7.2 and 7.3 show the dc link capacitor current for the five- and three-phase systems respectively. The capacitors in this simulation are the capacitors that give the same output dc voltage ripple for both systems, 2200μF for the three-phase and 470μF for the five-phase system.

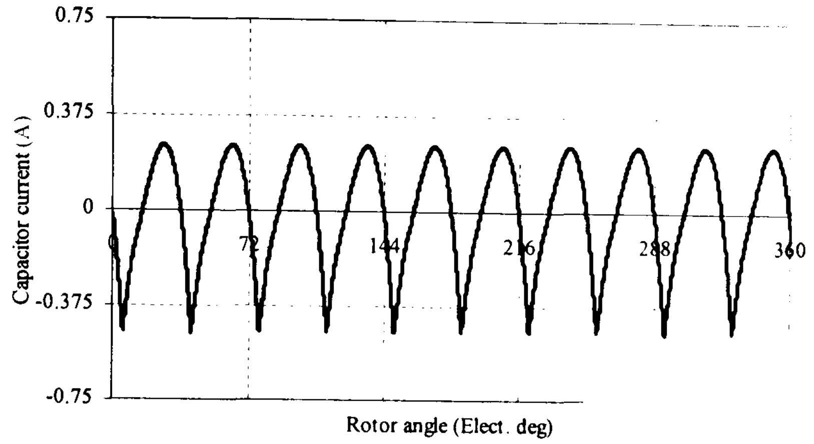

Figure 7.2. Dc link capacitor current from MATLAB simulation for the five-phase system. The dc link capacitor is 470μF.

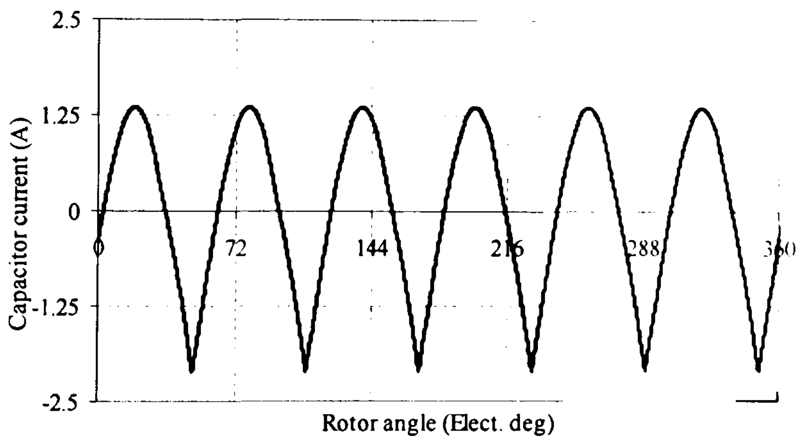

Figure 7.3. Dc link capacitor current from MATLAB simulation for the three-phase system. The dc link capacitor is 2200μF.

From the ALS30 datasheet for the 200V series of capacitors, the rms current ripple for the five-phase system with a 470μF capacitor operated at 466.7Hz (ten times the generator frequency) is 3.9A and for the three-phase system with 2200μF at 280Hz (six times the generator frequency) it is 9.1A. The actual rms capacitor current ripple for the five-phase system is only 6% of the rated rms ripple current. For the three-phase system it is 12% of rated rms current. Even though the 470μF capacitor has a higher R_{ESR}

(286mΩ) compared to the 2200μF capacitor (73mΩ), the five-phase capacitor dissipates 13.8mW internally compared to 88.3mW in the three-phase capacitor. The capacitor core temperature rise in the five-phase system, 0.11°C, is less than the three-phase system, 0.4°C, (Appendix D). Both temperature rises are small. It is clear that the five-phase system has a lower capacitance requirement compared to the three-phase system for the same output ripple and will operate at a lower core temperature.

7.4.2 Dc link capacitor current with a single phase open-circuit failure

In this simulation, phase-*a* is disconnected for both the five- and three-phase systems. The output dc voltage for both systems has higher peak-to-peak ripple as discussed in Chapter 6. Higher output dc voltage ripple will generate higher rms current ripple in the dc link capacitor. Figures 7.4 and 7.5 show the dc link capacitor current waveform for the five- and three-phase systems respectively. The fundamental frequency is twice the generator electrical frequency (93.3Hz) for both systems. The three-phase system capacitor has a peak current (11.5A) equal to 1.6 of the peak value in the five-phase system (7A). The rms current in the five-phase capacitor (3.4A) is lower than the rms current in the three-phase system capacitor (7.0 A). However, in the five-phase system the rms ripple current with a single phase failure has a value which is 110% of the rated rms ripple current of the capacitor. In the three-phase system, the ripple current is 83% of the rated ripple current of the capacitor. As a consequence of the increase in the rms currents in both cases, the capacitor core temperature is increased (Tables D1 and D2, Appendix D). In the five- and three-phase phase systems the capacitor core temperature rise is 27.4°C and 17 °C respectively giving an absolute core temperature of 72.4°C for the five-phase capacitor and 62°C for the three-phase capacitor. As the temperature is below 85°C (maximum operating temperature is 105°C) [7.3] both capacitors are still within specification in the five- and three-phase system, but the lifetime of the three-phase capacitor would be expected to be longer than the five-phase system.

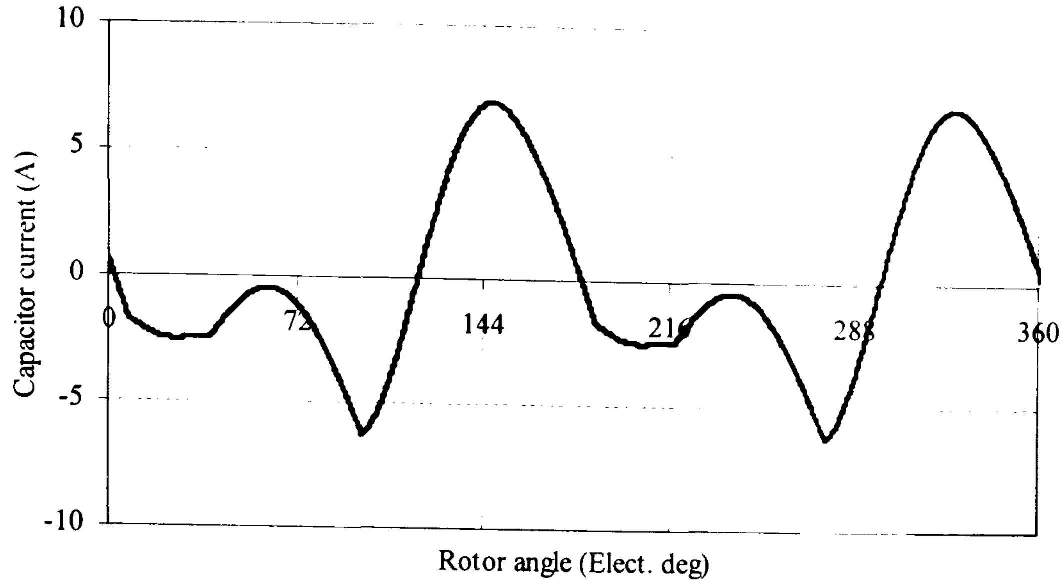

Figure 7.4. Dc link capacitor current from MATLAB simulation for the five-phase system with a single phase open-circuit failure. The dc link capacitor is 470μF.

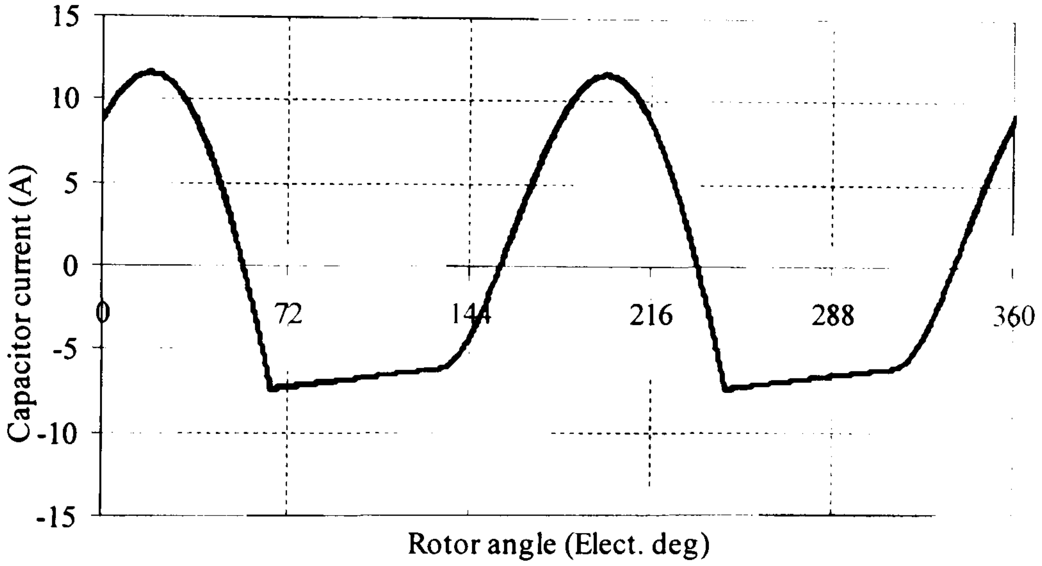

Figure 7.5. Dc link capacitor current from MATLAB simulation for the three-phase system with a single phase open-circuit failure. The dc link capacitor is 2200μF.

7.4.3 Dc link capacitor current with adjacent open-circuit phase failures

In this case, two adjacent phases, phase-*a* and -*b*, are open-circuit in the five-phase system. The capacitor rms current ripple, as expected, is found to be higher than the case of a single phase failure (Section 6.2). Figure 7.6 shows the capacitor current waveform under this condition. The rms current ripple is 4.9A which is a factor of 1.6

higher than rated rms ripple current. The estimated temperature rise of the capacitor core is 55.5°C which would increase the capacitor absolute core temperature to 100.5°C (Table D1). This is a high value and close to the maximum operating temperature of the capacitor, 105°C. Capacitor lifetime would be greatly reduced.

Decreasing the capacitor value reduces the capacitor rms current ripple. For example, by reducing the capacitor from 470uF to 330uF the capacitor rms current reduces to 3.4A. The drawback is that the output dc voltage ripple will increase during normal operation. With the 470uF capacitor, it is possible to increase the load resistance to reduce the rms current in capacitor to rated value. It is found that the load must increase by factor of 3 in order to do this. This will decrease the power captured from the generator by a factor of 3. These simulations show that the five-phase system under adjacent open-circuit failure must either shutdown or control the load in order to avoid damaging the dc link capacitor through excessive rms current. This assumes that the prime mover speed remains the same. In reality, the failure reduces the output power and the turbine blade system would accelerate to a speed where the power from the blade system matched that delivered to the load. In the further work section the system response to a phase failure is identified as an area of future research.

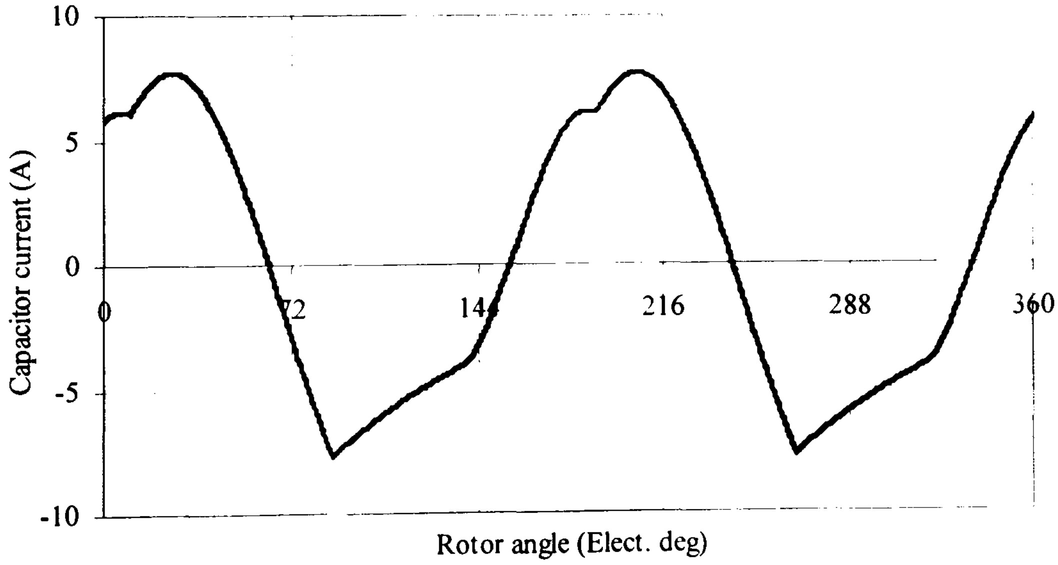

Figure 7.6. Dc link capacitor current with adjacent open-circuit phase failures. The dc link capacitor is 470μF.

7.4.4 Dc link capacitor current with non-adjacent open-circuit phase failures

In this case a pair of non-adjacent phases (phase-*a* and phase-*c*) are open circuit. The dc ripple voltage is 45.5V, which is less than that with an adjacent open-circuit phase failure, therefore the capacitor rms current ripple is expected to be lower compared to the rms current with adjacent failures.

Figure 7.7 shows the capacitor current waveform. It is observed from the figure that the capacitor current has a fundamental frequency equal to twice the generator electrical frequency. The capacitor has an rms current ripple equal to 4.3A which is 142% of the rated ripple current value. In the case of non-adjacent phase open-circuit failure the capacitor core temperature rise is 43.8°C giving an absolute core temperature of 88.5°C (Table D1). This is near to the rated temperature, 85°C, and the expected drawback is a reduction the lifetime of the capacitor. The rated rms ripple can be achieved by increasing the resistive load by 150%. However, reducing the load also reduces the generator shaft power, in this case to 40% of the rated power.

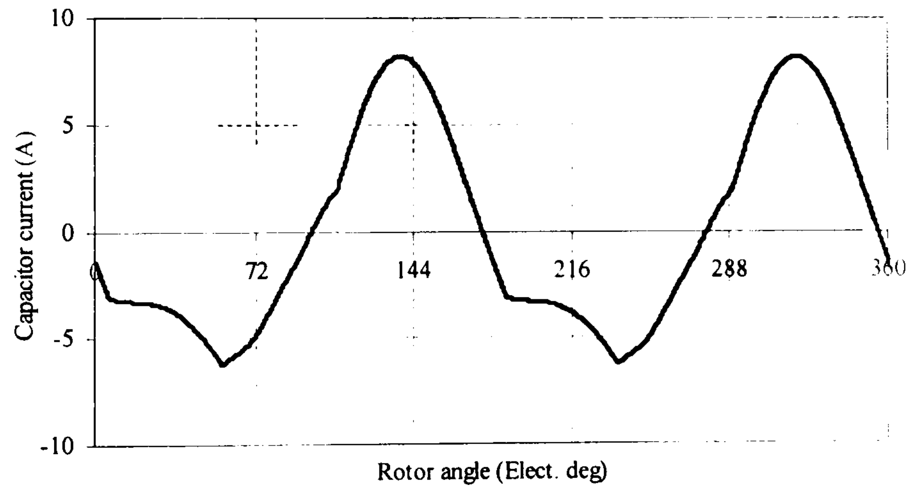

Figure 7.7. Dc link capacitor current with non-adjacent open-circuit failure phase. The dc link capacitor is 470μF.

The simulation results are summarised in Table 7.3 where the capacitor ripple current is also expressed relative to the rating of the capacitor. It is clear from the results that the capacitor in the three-phase system can tolerate a single phase open-circuit failure. In the five-phase system the core temperature calculations suggest that with a single phase failure the absolute core temperature would be tolerable. The increase in rms current in the capacitor is mainly due to the fact that the five-phase system can export more power than the faulted three-phase system. With two adjacent phases failures the five-phase system will be at risk if the system works for a significant time. With two non-adjacent phase failures the capacitor will operate just above the continuous core temperature limit. This would lead to reduced lifetime of the capacitor. In all cases decreasing the load (by increasing the load resistance) leads to a reduction in the capacitor rms current and could be used to satisfy the generator rated current. Ultimately, in the five-phase system, the capacitance could be increased to solve this problem. In the next section simulation results are validated using FEA and the experimental system.

Table 7.3. Simulation results for the dc link capacitor current in the three-and five-phase systems

	Three-phase		Five-phase	
	Capacitor ripple current		Capacitor ripple current	
	rms ripple current (A)	relative to rated rms	rms ripple current(A)	relative to rated rms
Normal condition	1.1	0.12	0.22	0.1
Single phase open-circuit	7.0	0.85	3.4	1.1
Two adjacent open circuit	-	-	4.9	1.6
Two non-adjacent open circuit	-	-	4.3	1.4

7.5 FEA analysis of dc link capacitor

FEA analysis is used to analyse the current in the dc link capacitor of the three- and five-phase systems. FEA is applied to the practical design (with mounting holes). The FEA results are expected to be slightly different from the simulation model results due to the distortion in the phase back emf (Chapter 5). The capacitor current is discussed for both normal and failure conditions.

7.5.1 Dc link capacitor current under normal conditions

In this case, all phases function properly. The mounting holes have a significant effect on the output dc voltage of the five-phase system compared to the three-phase system (Section 5.4). Due to the distortion in the dc output voltage the capacitor current in the five-phase system is different compared to the simulation results. Figure 7.8 and 7.9 show the dc link capacitor current waveform for the five- and three-phase systems respectively. The current in the dc link capacitor in the five-phase system has a fundamental frequency equal to two times the generator electrical frequency instead of ten times. However, the important issue in this chapter is the value of the capacitor rms current ripple. In the three-phase system the capacitor current has a fundamental frequency equal to six times the generator electrical frequency which agrees with the simulation results. The five-phase system's capacitor current has an rms value of 0.44A which is 0.11 of the rated value (3.9A at 467Hz). In the three-phase system, the capacitor current is 1A which is also 0.11 of the capacitor rated ripple current (9.1A at 280Hz). This confirms that when both systems have no failures the capacitor operates within design limits and the five-phase system has the advantage of requiring a lower capacitance compared to the three-phase system.

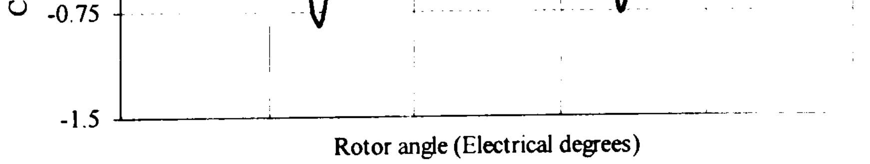

Figure 7.8. FEA simulation of the dc link capacitor current for the five-phase system using the proposed design. The dc link capacitor is 470μF.

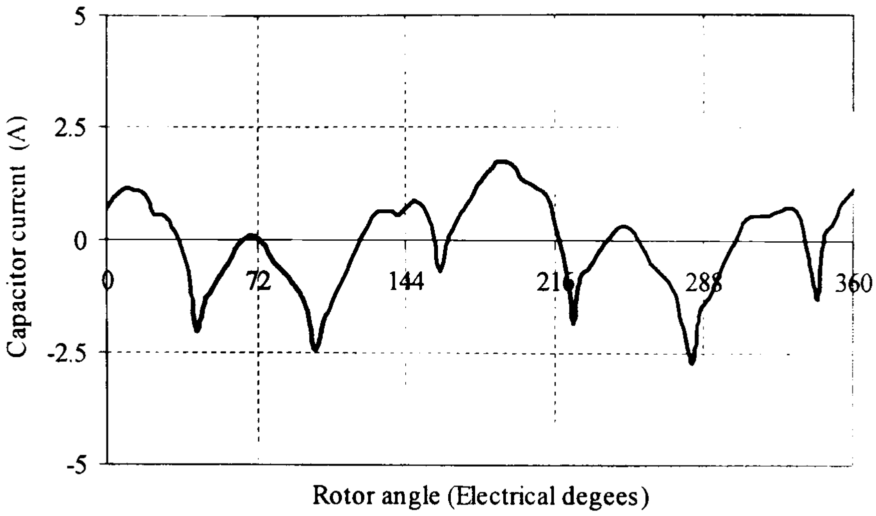

Figure 7.9. FEA simulation of the dc link capacitor current for the three-phase system using the proposed design. The dc link capacitor is 2200μF.

7.5.2 Dc link capacitor current with a single phase open-circuit failure

Figures 7.10 and 7.11 show the capacitor current when phase-*a* is open-circuit for both the five- and three-phase systems. The fundamental frequency for both systems is the same and equal to 93.3Hz. The capacitor rms current ripple in the five-phase system is equal to 3.3A which is 106% of the rated rms ripple current of the capacitor. It is estimated that this current will raise the capacitor core temperature 25.8°C increasing the capacitor's absolute core temperature to 70.8°C which is less than rated temperature (85°C). In the three-phase system the capacitor rms current ripple, 5.8A, is 71% of the rated rms current ripple and the capacitor core temperature rise is estimated at 11.5°C giving an absolute core temperature of 56.5°C. It is clear from the results that the capacitor in the three-phase system has less power dissipation than the capacitor in the five-phase system. These results agree with the results from simulation. However, the five-phase system still captures more power from the wind turbine's blade system and delivers more dc output power.

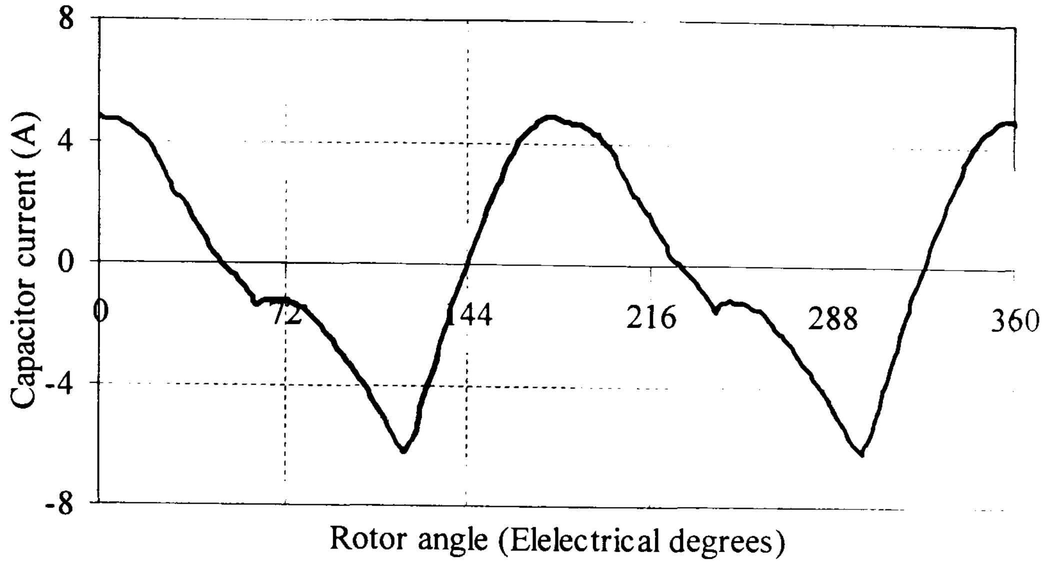

Figure 7.10. FEA simulation of the dc link capacitor current for the five-phase system, with a single phase open-circuit failure. The dc link capacitor is 470μF.

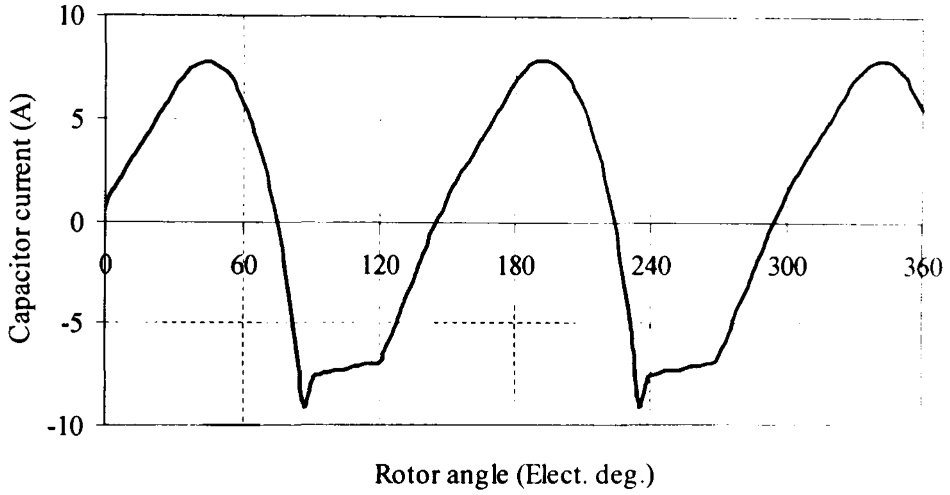

Figure 7.11. FEA simulation of the dc link capacitor current for the three-phase system, with a single phase open-circuit failure. The dc link capacitor is 2200μF.

7.5.3 Dc link capacitor current with adjacent open-circuit phase failures

In this test phase-*a* and -*b* are open open-circuit and the generator speed is 1400rpm. The dc link capacitor is 470μF. Figure 7.12 shows the dc link capacitor current waveform. The fundamental frequency is 93.3Hz which is the same as the simulation result. The dc link capacitor has rms current ripple of 4.8A which is significantly higher than the capacitor rated rms current (3.1A). Under these circumstances, the core temperature rise is estimated at 54°C and increases the absolute core temperature to 99°C. This will reduce lifetime. In this case, it is recommended to shutdown the system or control the load as discussed in section 7.4.3.

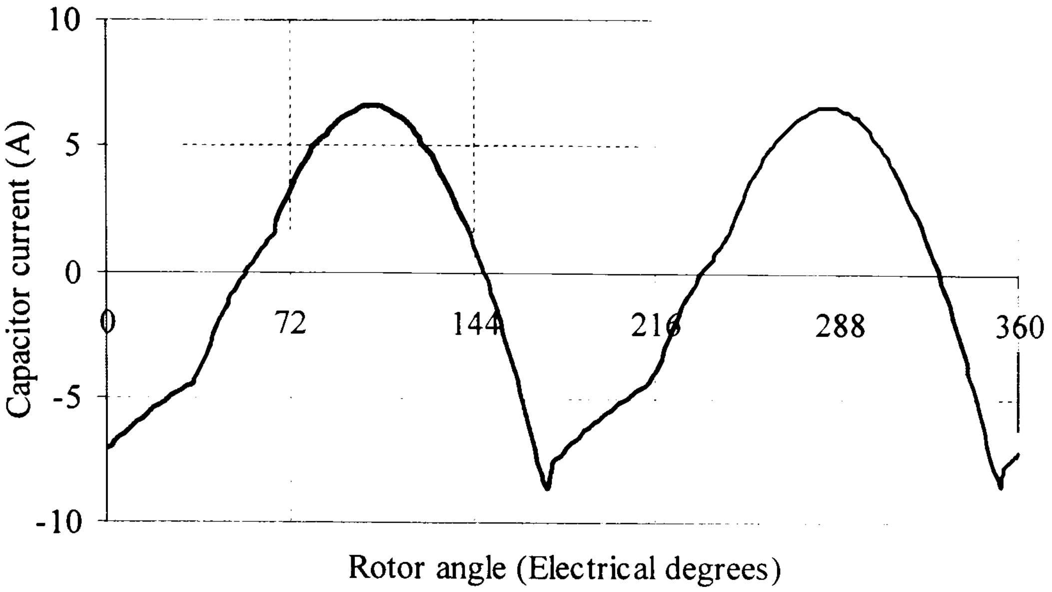

Figure 7.12. FEA simulation of the dc link capacitor current with adjacent open-circuit phase failures. The dc link capacitor is 470μF.

7.5.4 Dc link Capacitor current with non-adjacent open-circuit phase failures

Figure 7.13 shows the dc link capacitor waveform when non-adjacent phases are open-circuit (in this case phase-*a* and-*c*). The speed and dc link capacitor are the same as the normal condition (1400rpm and 470μF). The dc link capacitor rms current ripple (4.3A) agrees with the simulation results. Due to the increase in ripple current the capacitor power dissipation is increased and the capacitor core temperature rise is estimated to be 41°C giving an absolute core temperature of 86°C which is just above the rated operating temperature. The system would operate continuously but the lifetime would be expected to be reduced. The situation is not as severe as the adjacent phase failure condition.

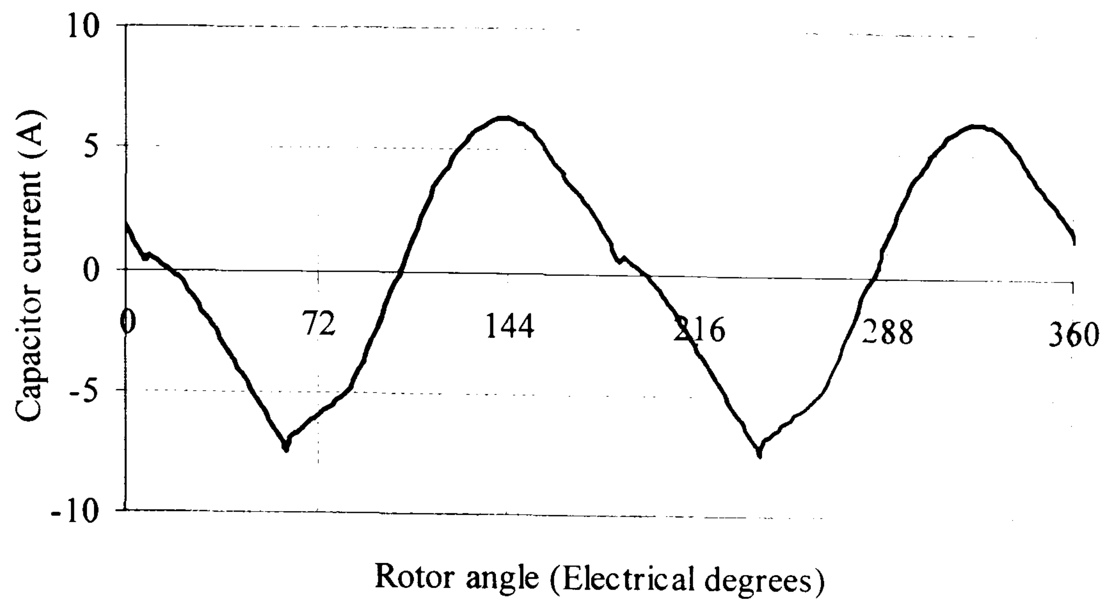

Figure 7.13. FEA simulation of the dc link capacitor current with non-adjacent open-circuit phase failures. The dc link capacitor is 470μF.

7.5.5 Summary of FEA simulation

Table 7.4 summarises the FEA results. It is observed from the results that in the normal condition the dc link capacitor for the two systems works without excessive stress. With a single phase failure, the three-phase capacitor operates without exceeding rated rms current. However, the five-phase capacitor has an rms ripple current that is approximately 106% of the rated current. However, the capacitor core temperature is estimated to be lower than the rated temperature. For adjacent and non-adjacent failures in the five-phase system the rms current is significantly higher than the capacitor rated current. It is clear that in terms of capacitor rms current, the three-phase system operates within manufacturer's ratings. However, this is not the case for the five-phase system with the lower value of capacitance under single phase open circuit and two phase open circuit failures. The results from FEA confirm the results from the simulation. If the load was controlled when failure occurs, the capacitor in the five-phase system could operate within design specification and the system can capture and deliver more power compared to the three-phase system.

Table 7.4. FEA simulation of the dc link capacitor current for the three- and five-phase systems

	Three-phase		Five-phase	
	Capacitor ripple current		Capacitor ripple current	
	rms ripple current (A)	Relative to rated rms	rms ripple current	Relative to rated rms
Normal condition	1	0.11	0.44	0.11
Single phase open-circuit	5.8	0.7	3.3	1.1
Two adjacent open circuit	-	-	4.8	1.5
Two non-adjacent open circuit	-	-	4.2	1.4

7.6 Experimental evaluation

To assess the simulation and FEA results, a set of experimental tests are carried out using the fabricated generator. The generator speed is set to 1400rpm for both systems at full load (10Ω) with 470μF dc link capacitor for the five-phase system and 2200μF for the three-phase system.

7.6.1 Dc link capacitor rms current under normal conditions.

Figures 7.14 and 7.15 show the dc link capacitor current waveforms for the five- and three-phase systems respectively. From figure 7.14 the dc link capacitor current in the five-phase system has an rms current ripple of 0.5A which is 0.16 of the capacitor rated ripple current, 3.1A. The dc link capacitor current in the three-phase system (0.9A) is 0.1 of the rated rms ripple current (8.4A). The results correlate with that from the simulation and FEA.

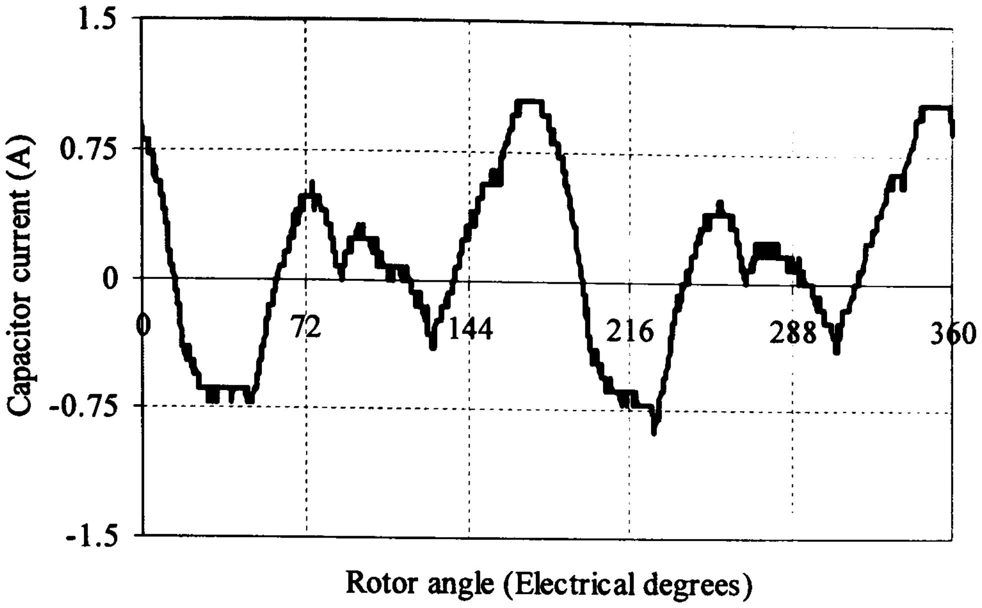

Figure 7.14. Measured dc link capacitor current for the five-phase system. The dc link capacitor is 470μF.

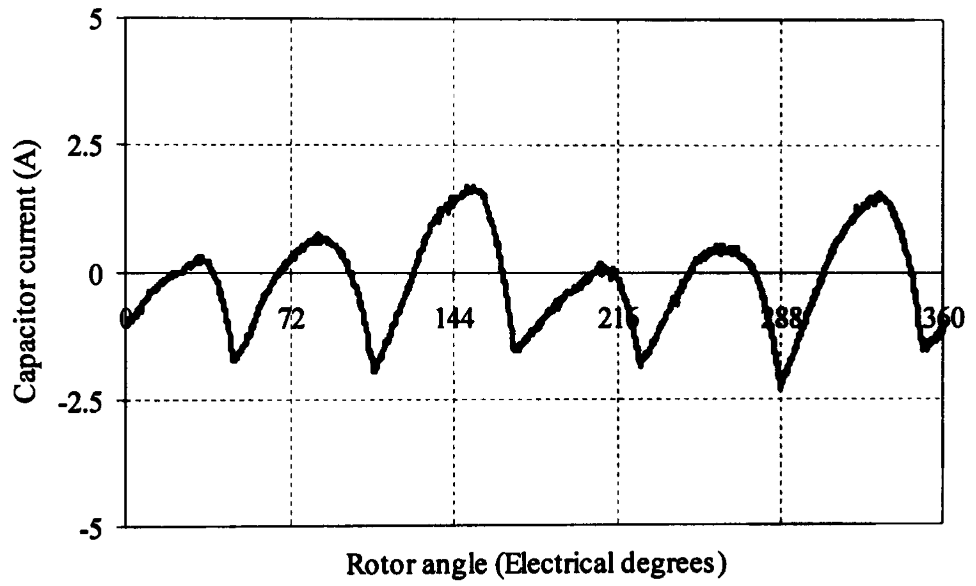

Figure 7.15. Measured dc link capacitor current for the three-phase system. The dc link capacitor is 2200μF.

7.6.2 Dc link capacitor current with a single phase open-circuit failure

This test is carried out for both five- and three-phase systems with phase-*a* open-circuit. Figures 7.16 and 7.17 show the waveforms of the dc link capacitor current for the five- and three-phase systems respectively. The capacitor rms current ripple in the five-phase system is 3.1A which equals the rated rms ripple current of the capacitor. The rms capacitor current in the five-phase system will raise the capacitor core temperature by

22.8°C (Table D5) and with an ambient temperature 45°C the absolute core temperature is 67.8°C which is less than capacitor rated temperature (85°C). The three-phase capacitor is works safely with an rms current ripple (5.7A) which is lower than the rated current of the capacitor (8.2A). The capacitor core temperature rise in the three-phase system is 11.5°C giving an absolute core temperature of 56.5°C which is less than the five-phase system. This leads to an increase the capacitor lifetime in the three-phase system compared to the five-phase system. The results from the five- and three- phase system correlate well with simulation and FEA results.

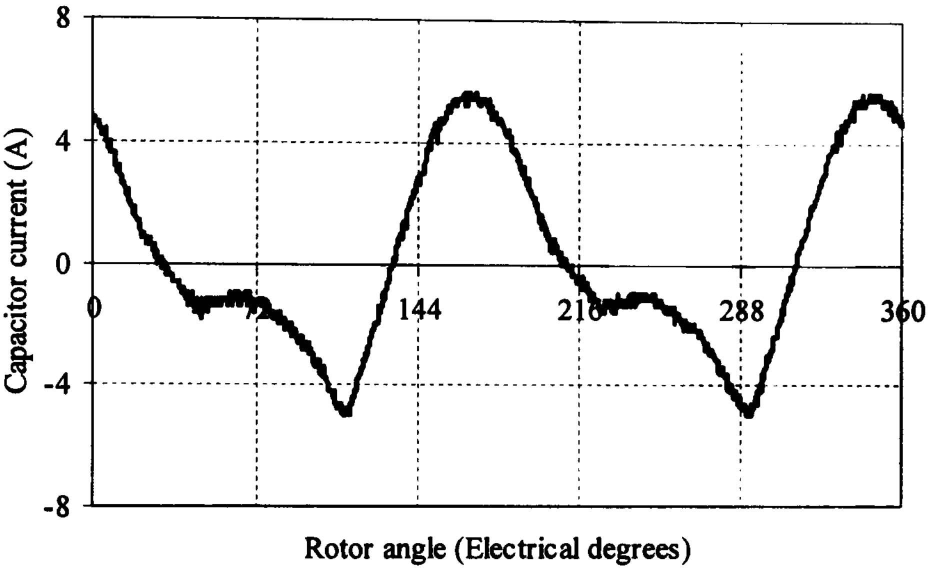

Figure 7.16. Measured dc link capacitor current for the five-phase system with a single phase open-circuit failure. The dc link capacitor is 470μF

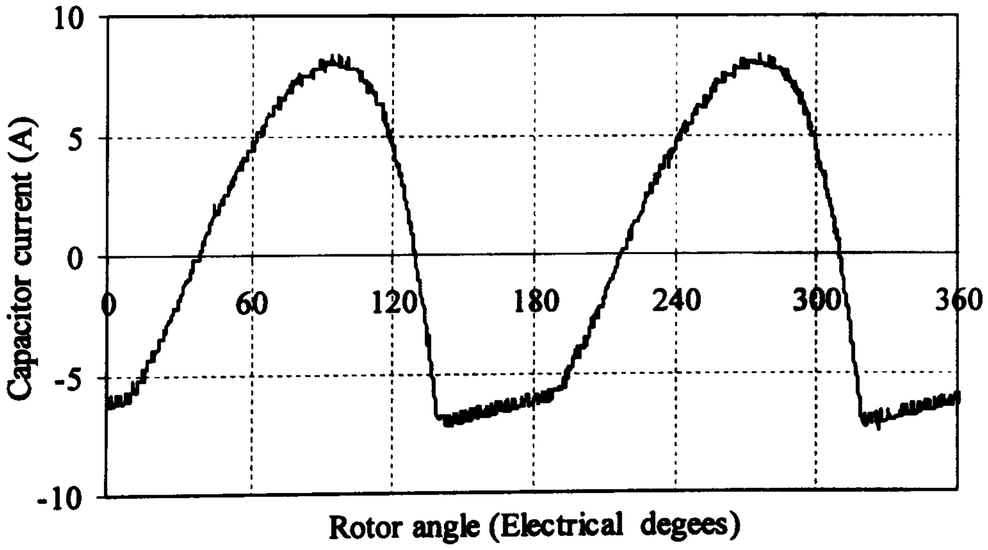

Figure 7.17. Measured dc link capacitor current for the three-phase system with a single phase open-circuit failure. The dc link capacitor is 2200μF.

7.6.3 Dc link capacitor current with adjacent open-circuit phase failures

Adjacent phases, phase-*a* and-*b*, are open-circuit in this test. The capacitor rms current is expected to be more than the capacitor rated current as shown by FEA. The shaft speed in this test is 1400rpm and the capacitor is 470μF. Figure 7.18 shows the capacitor current waveform which agrees with FEA, Figure 7.12. The capacitor has an rms current ripple equal to 4.3A. This value is high enough to raise the capacitor core temperature by estimated 43.8°C giving an absolute core temperature of 88.8°C (Table D5) and as a consequence the lifetime of the capacitor is reduced. With adjacent phase open-circuit failures it is recommended to either increase the capacitor value (extra cost) or control the maximum load power to a value that satisfies the maximum capacitor rms current.

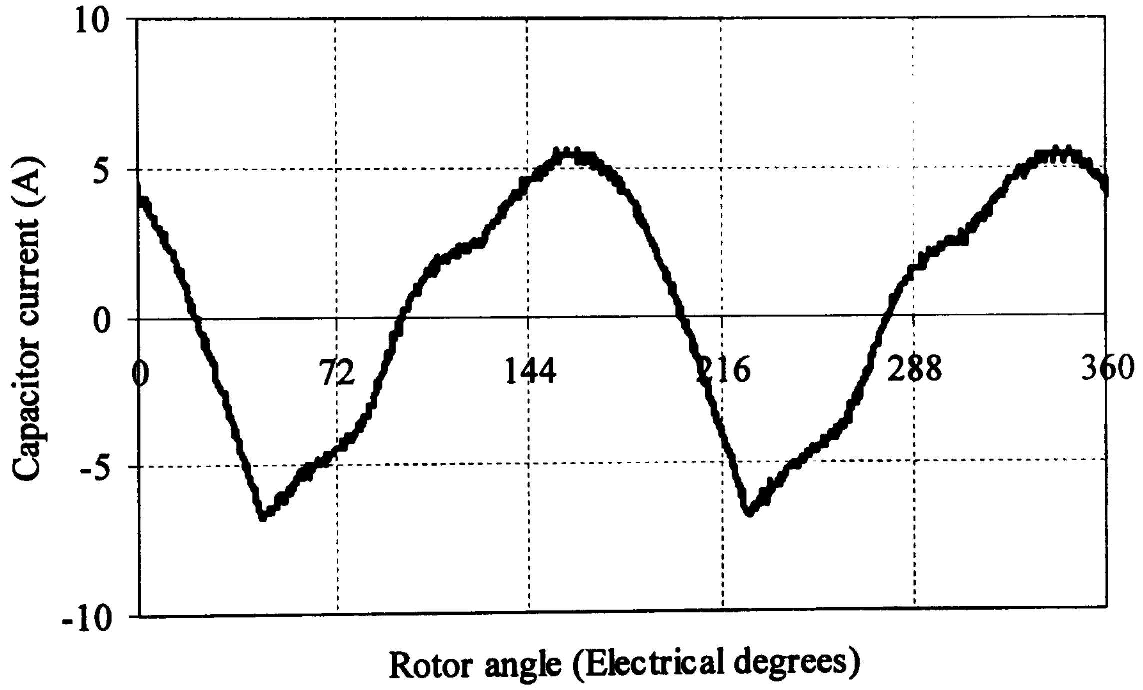

Figure 7.18. Measured dc link capacitor current for five-phase system with adjacent open-circuit phase failures. The dc link capacitor is 470μF.

7.6.4 Dc link capacitor current with non-adjacent open-circuit phase failures

Figure 7.19 shows the waveform of the dc link capacitor current in the five-phase system when two non-adjacent phases are open circuit (phase-*a* and-*c*). The capacitor rms current (3.9A) is a factor of 1.25 of the capacitor's rated rms current. This generates 4.4W of losses in the capacitor which will raise the core capacitor temperature by estimated 36°C giving an absolute core temperature of 81°C. This temperature is less than rated capacitor temperature (85°C). The impact on lifetime is not as great as adjacent phase open-circuit failures but is worse than that for normal conditions or a single phase failure. However, the results from both experimental and FEA show the condition is less extreme than the adjacent phase failure conditions. The impact on capacitor lifetime is not as serious.

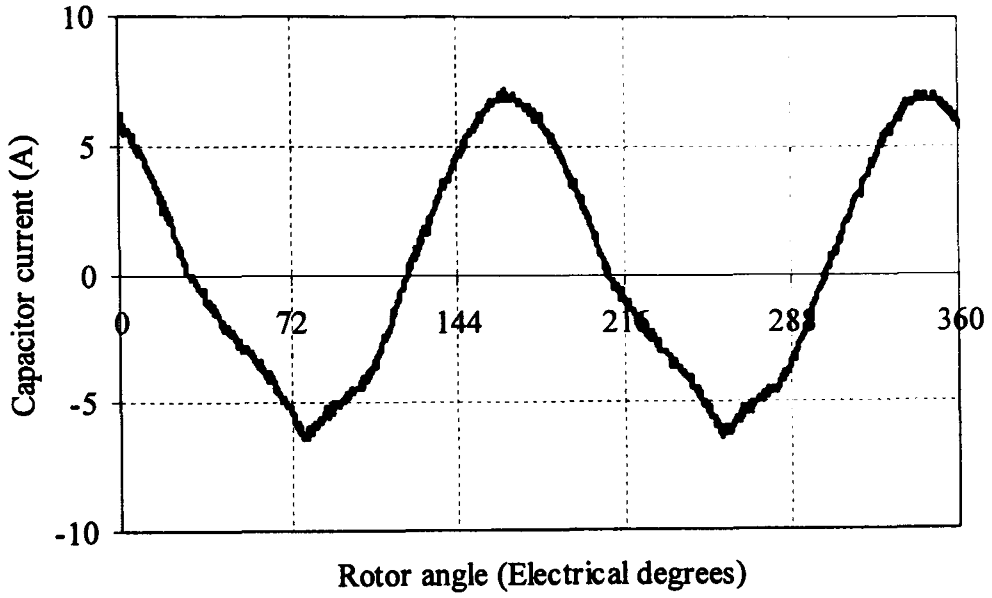

Figure 7.19. Measured dc link capacitor current with non-adjacent open-circuit phase failures. The dc link capacitor is 470μF

7.6.5 Summary of experimental results

Table 7.5 summarises the experimental results. Many remarks can be made from the results:

- The capacitance in the five-phase system is only 0.21 of the three-phase system. Under normal conditions the dc link capacitor for the two systems has the same core temperature.
- With a single phase failure, the capacitor core temperature in the five-phase system is estimated to increase by 22.8°C to 67.8°C which is less than capacitor rated temperature but higher than the absolute core temperature estimated in the three-phase system, 56°C.

- With two adjacent phase failures, the capacitor absolute core temperature, 88.8°C, is higher than rated temperature, 85°C, but less than maximum temperature 105°C. The capacitor will function but with reduced lifetime.
- With two non-adjacent failures, the capacitor absolute core temperature rises to 81°C which is less than rated temperature and also less than that with adjacent phase failure. The capacitor is expected to be able function continuously.
- The FEA simulation is validated by experimental values.

Table 7.5. Summary of measured dc link capacitor current for the three- and five-phase systems

	Three-phase		Five-phase	
	Capacitor ripple current		Capacitor ripple current	
	rms ripple current (A)	relative to rated rms	rms ripple current (A)	relative to rated rms
Normal condition	0.9	0.1	0.5	0.16
Single phase open-circuit	5.7	0.7	3.1	1
Two adjacent open circuit	-	-	4.3	1.4
Two non-adjacent open circuit	-	-	3.9	1.3

7.7 Summary

In this chapter, the rms current in the dc link capacitor is discussed for the five-phase and three-phase permanent magnet generator connected to a diode bridge rectifier. The current is evaluated using simulation, FEA and practical tests. The performance is presented for normal and failure modes.

Under normal conditions the rms current in the five- and three-phase system is much smaller compared to the capacitor rated current (factor of 0.13 and 0.1 for the five- and three-phase system respectively). However, the capacitance in the five-phase system is much less than the three-phase system. It is estimated that the capacitor's absolute core temperature for both systems have similar values (45.6°C and 45.3°C for the five- and three-phase system respectively).

With a single phase open-circuit failure, the capacitor in the five-phase system is estimated to have a higher core temperature compared to the capacitor in the three-phase system. In both systems the capacitor core temperature does not exceed the capacitor's rated temperature.

With adjacent and non-adjacent phase failure in the five-phase system the rated rms current of the capacitor is exceeded. With adjacent phase failures, the increase in rms current causes the estimated to raise the capacitor core temperature above its rated value leading to a reduction in the lifetime of the capacitor. In the case of non-adjacent failure the core temperature is estimated to be lower than the rated temperature.

Experimental tests are carried out to verify the FEA. The results show a good correlation between the FEA and experimental tests in terms of rms values and waveforms.

The key outcome is that whilst a five-phase system has superior tolerance to open-circuit phase failures, the increased power that can be delivered during failure imposes a more extreme operating condition for the dc link capacitor. Care must therefore be exercised when specifying dc link capacitor in five-phase systems that may be expected to operate with one or more phase failures. Specifically, this may require an increase in the link capacitance or the selection of a capacitor with a higher rated ripple current.

References

[7.1] P. John, "Ripple current capabilities", Technical update, KEMET Electronic Group, August 2004.

[7.2] BHC Components, Application notes, "Aluminium Electrolytic Capacitor", from http://www.bhc.co.uk/pdf/AppNotes.pdf

[7.3] BHC components website, ALS30/31 Series, Retrieved 18.0.5.2009, from http://www.bhc.co.uk/als30_tc.htm

Chapter 8

Conclusions

8.1 General conclusion

A three-phase permanent magnet generator connected to a diode bridge rectifier is a popular solution for small wind turbines. The generator shaft torque in the three-phase system displays a high peak-to-peak torque ripple when a dc link capacitor is used and requires mitigating techniques to reduce this ripple. A five-phase permanent magnet generator operated with a diode bridge rectifier is shown to have reduced shaft torque ripple and output dc voltage ripple. Multi-phase generators connected to diode bridge rectifiers have not been the subject of research to ascertain the advantages of multi-phase technology and disadvantages. This research investigates, discusses and compares the performance of a three- and five-phase permanent magnet generator connected to a diode bridge rectifier under normal and failure conditions. The five-phase system shows improved performance compared to the three-phase system under normal conditions and under open-circuit phase failures in terms of generator shaft torque and power delivered to the load. However, the increased power that can be delivered during failure imposes a more extreme operating condition on the dc link capacitor in the five-phase system.

A simulation model using pulse functions for the five- and three-phase PM generator connected to a diode bridge rectifier is developed in chapter 3. The effect of self- and mutual inductance of the generator is discussed. It is shown that the self- and mutual-inductance have a significant effect on the simulated performance of both systems by reducing the generator shaft torque ripple. In the five-phase system, including the self-inductance reduces the generator shaft torque ripple by approximately 4 times compared to without inductance. In the three-phase system the reduction is 2.7 times. With self- and mutual inductance modelled, the reduction in shaft torque ripple in the five-phase system is approximately 12 times compared to without inductance. In the three-phase the reduction is only 3.4 times. Therefore the research demonstrates the importance of including both the self- and mutual inductance during the simulation and analysis of torque ripple.

In chapter 4, the three-phase and five-phase permanent magnet generators are designed. Linear design is performed using the PM magnetisation curve and simple analytical methods. Winding configurations for both generators are proposed to give the same rectified output dc voltage and power. Finite element analysis (FEA) is used to confirm the linear design. Two designs are analysed using FEA; the proposed design (without mounting holes in the stator stack) and the practical design (with the mounting holes in the stator stack). The cogging torque and back emf is assessed using FEA.

In chapter 5, the performance of the prototype five-phase and three-phase permanent magnet generators connected to diode bridge rectifiers are evaluated using FEA and practical tests. Two designs (the proposed design and the practical design) are modelled using FEA to evaluate performance of the proposed design. The proposed design shows that the five-phase generator has lower shaft peak-to-peak torque ripple (0.7Nm) compared to the three-phase generator (1.6Nm). In addition, the five-phase system has output dc voltage ripple 16% lower than the three-phase system. It was shown that the five-phase system can use a lower value of capacitance for the same output voltage ripple. In this case, 470μF compared to 2200μF for the three-phase system. Also it is found that the five-phase system requires diodes with lower current ratings compared to the three-phase system (45% lower). The experimental tests are performed using the practical design. Due to the distorted phase back EMF in the five-phase system, the comparison of the practical design do not compare well with the FEA or simulation results of the proposed design. Hence comparison is made over a restricted period of the electrical cycle where the non-adjacent line voltages are not affected in the five-phase system. This shows that the five-phase system has better performance in terms of shaft torque ripple (0.9Nm) compared to the three-phase system (1.5Nm) for the same output dc voltage and power. The results show that the three-phase system has a total losses (113W) higher than the five-phase system (97W) under normal conditions.

In chapter 6, the operation of the five-phase and the three-phase permanent magnet generator feeding a diode bridge rectifier under open-circuit phase failures in the generator is assessed and discussed. Also, the operation of five-phase system with adjacent and non-adjacent open-circuit phase failures is investigated. The results show that the five-phase system has advantages over three-phase system with a single open-circuit phase failure in terms of generator torque ripple and efficiency. The non-adjacent failure mode produces less extreme operating condition compared to adjacent phase failure mode, particularly in terms of torque ripple and voltage ripple. However, with non-adjacent phase failure the total losses (125W) are higher than the total losses with adjacent phase failure (101.7W). It is also shown that in both modes, the efficiency is higher than with the three-phase single phase failure and the power output is higher.

In chapter 7, the rms current in the dc link capacitor is investigated for the five-phase and three-phase permanent magnet generator connected to a diode bridge rectifier. The current is evaluated using simulation, FEA and practical tests. The performance is presented for normal and failure modes. It is shown that whilst a five-phase system has improved output power during an open-circuit phase failure, the increased power that can be delivered during a failure imposes a more extreme operating condition for the dc link capacitor particularly the adjacent open-circuit failure mode. This imposes a design constraint on the dc link capacitor. The rms ripple current rating of the capacitor now determines the capacitance rather than the dc voltage ripple if operation during open-circuit failures is a requirement of the system.

The five-phase system can be used in small- and medium-scale wind turbines, aerospace applications including unmanned autonomous vehicles, Ground-based vehicles and Micro-CHP applications.

8.2 Main contributions of this thesis

The scientific contribution of this thesis can be summarised as follows:

- A general model for the five-phase permanent magnet with diode rectifier is developed. The developed model includes the generator parameters specifically the self- and mutual-inductance. The developed models are compared with PSpice simulation and show good correlation. The developed model helps describe how the generator performs with a diode bridge rectifier and also shows the importance of modelling generator inductance and the significant effect that mutual inductance has on the performance of the five-phase system.

- The design of a prototype five-phase permanent magnet generator is detailed. The stator is designed with 30 slots such that it can be wound as a three-phase generator or five-phase generator. The rotor has 4 poles for both systems. The winding in both generators is arranged to give the same output dc voltage providing a platform for a fair comparison between the two systems.
- A comparison is provided between the performance of the prototype five- and three-phase permanent magnet generators feeding diode bridge rectifiers with the same dc output power, voltage and volume. The comparison is performed for shaft torque and power and output dc voltage and output power. In addition, a comparison of rms current of the dc link capacitor is made.
- The performance of five-phase permanent magnet generator systems under open-circuit failure (one and two phase failures) is assessed and compared with the three-phase counterpart.
- An assessment of the rms current requirements of the dc link capacitor is made under normal conditions and with single, adjacent and non-adjacent open-circuit phase failures. This is carried out for both three- and five-phase counterparts and a comparison made.

8.3 Further research

The comparison between the three- and five-phase systems is demonstrated for fixed speed and load. But the operation of the generator with an aerodynamic prime-mover and variable speed input requires more investigation, particularly under open-circuit phase failures. Under open-circuit phase failures the reduction in output power from the generator will lead to an increase in the shaft speed as a result of the wind turbine power curve characteristics. Research is required into how the system reacts and what stresses may occur in the system, particularly electrical stresses in the generator and rectifier.

Further, if some form of maximum power point tracker is being used, the system reacts as the tracker attempts to recover the maximum power point (which is determined by the aerodynamic efficiency). The performance of the three- and five-phase system may be significantly different in this respect and requires further investigation.

Other further research includes the performance of the three- and five-phase systems when one or two diodes fail open-circuit. Under such circumstances the performance during such failures will be different to that experienced during phase open-circuit failures. Similar analysis to that in this thesis is required.

It would also be useful to make practical torque measurements on the system to determine true values of shaft torque rather than the estimated values provided in this thesis.

In this thesis the performance of the five-phase permanent magnet generator is investigated under steady-state conditions. However, one key aspect would to study the system under transient operation during the failure. A transient model may need to be developed, including the electromechanical system (permanent magnet generator and diode rectifier) and the aerodynamic system. Also it is important to study the impact that a transient aerodynamic system has on the performance of the electrical system

Appendix A

A1. Possible circuits for 3- and 5-phase system

The circuits represents the twelve periods that generate by the twelve pulses shown in figure 3.15. S1 to S12 represent the twelve pulses.

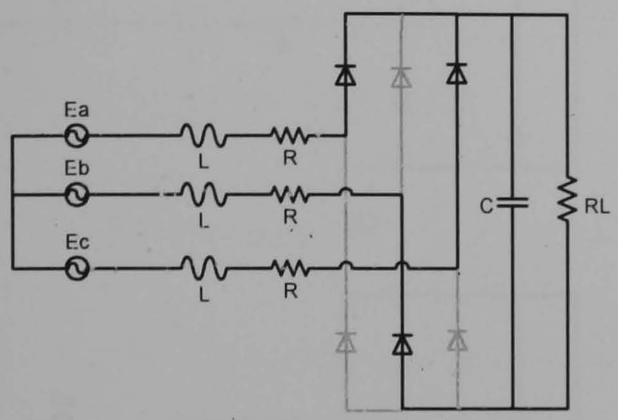

S1

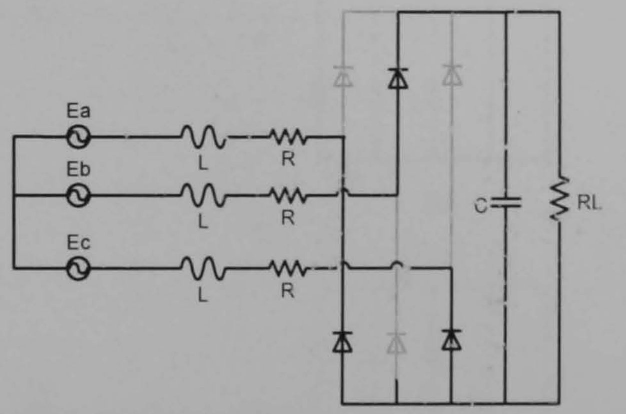

S2

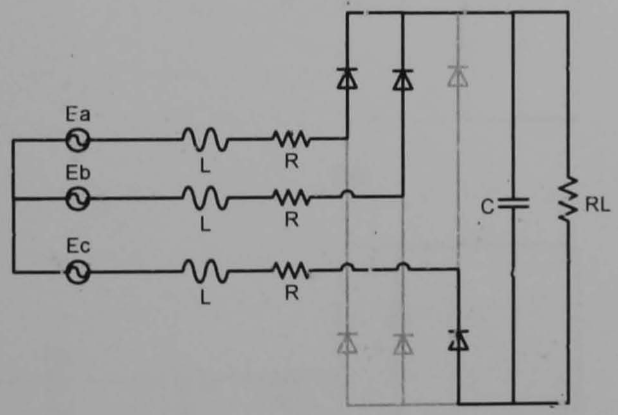

S3

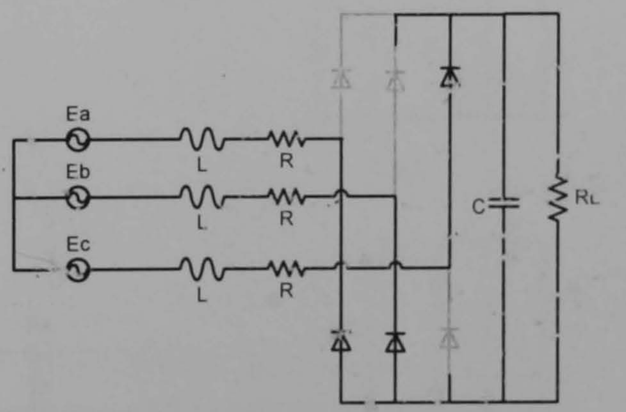

S4

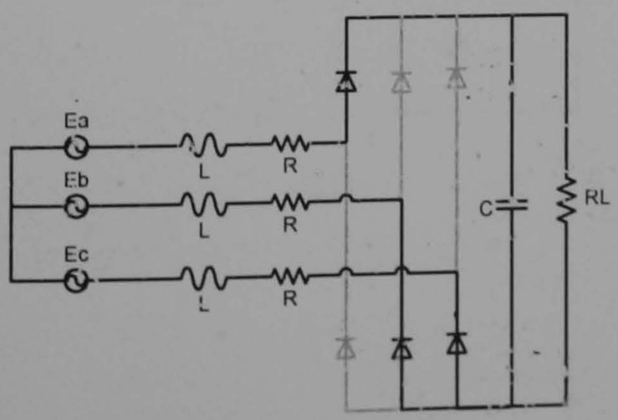

S5

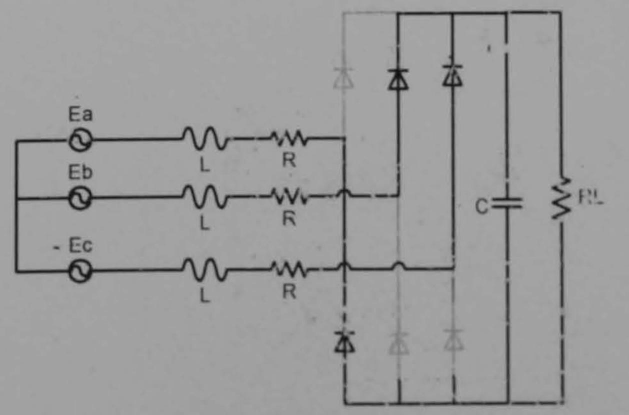

S6

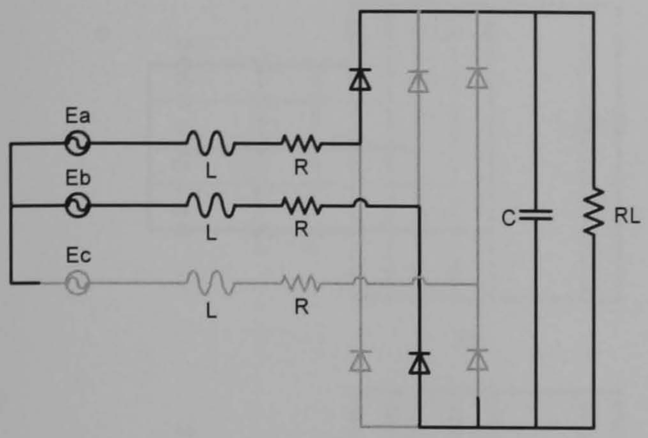

S7

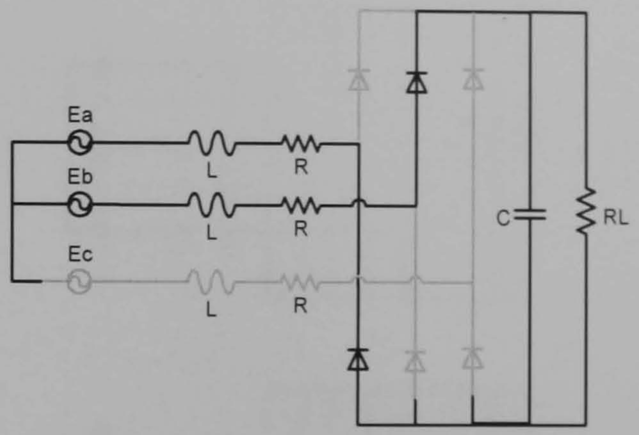

S8

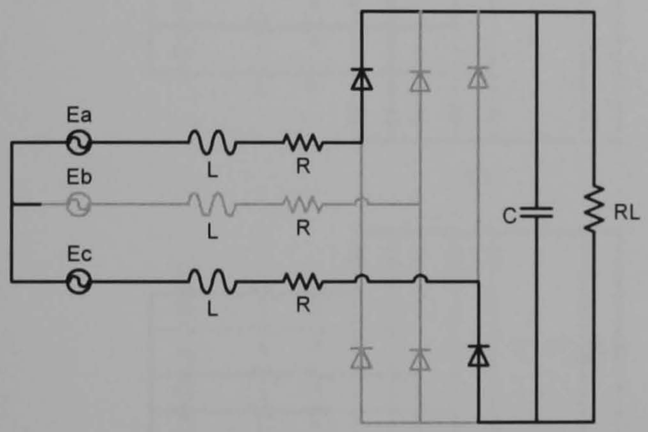

S9

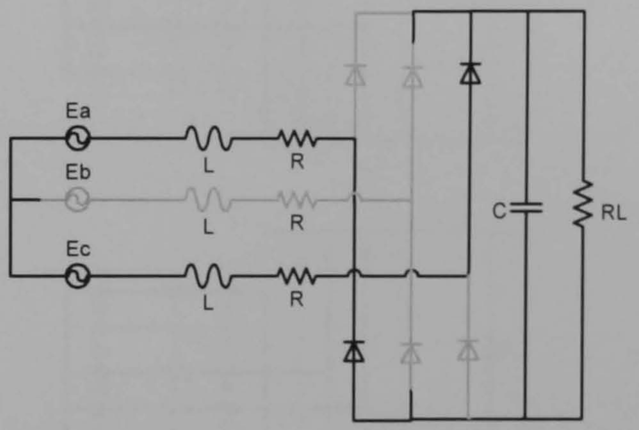

S10

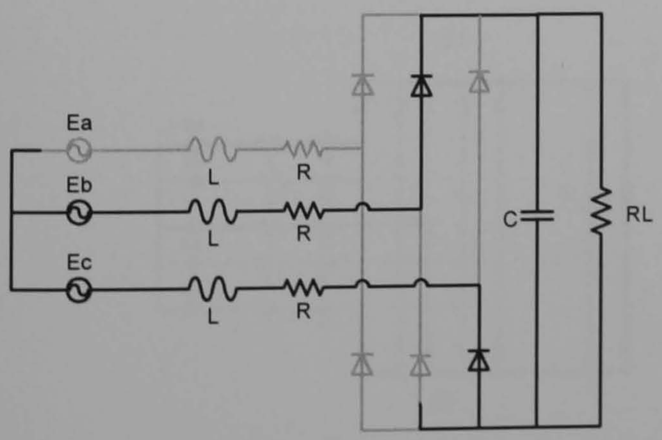

S11

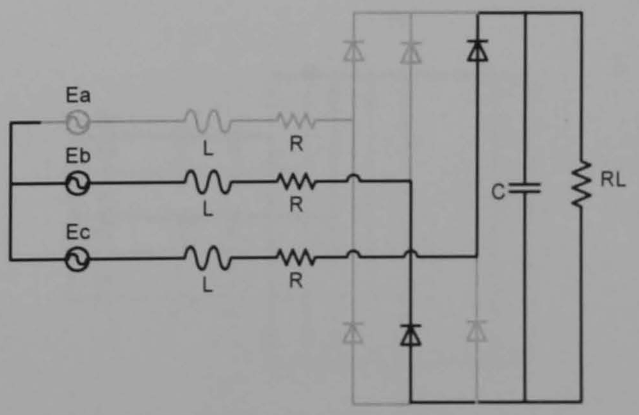

S12

The circuits represents the twenty periods that generate by the twenty pulses shown in figure 3.20. S1 to S20 represent the twelve pulses.

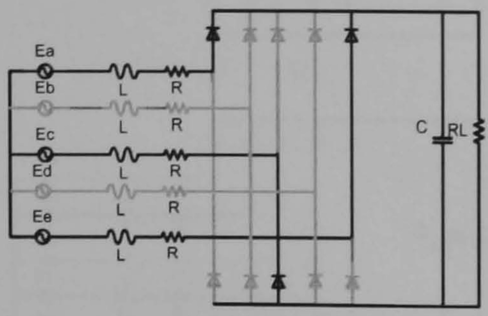

S1

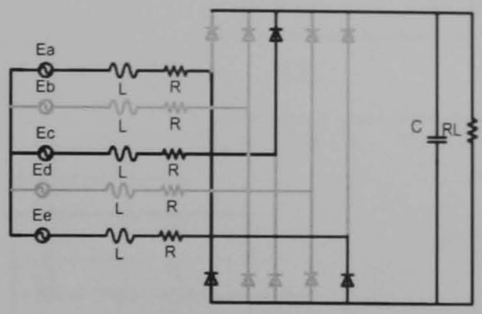

S2

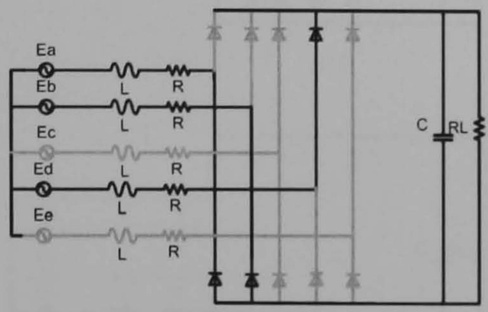

S3

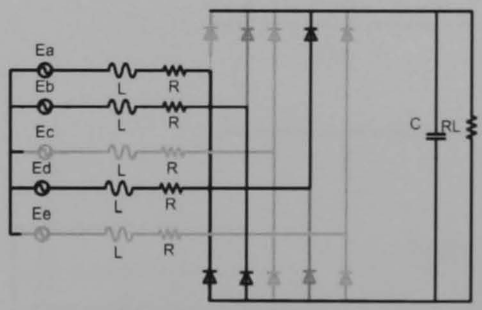

S4

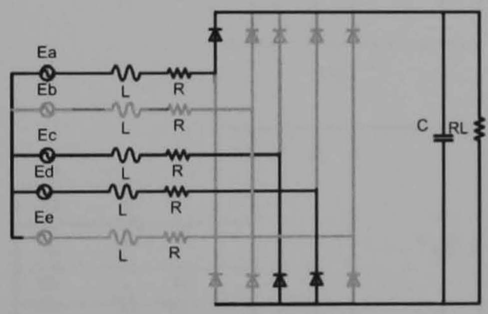

S5

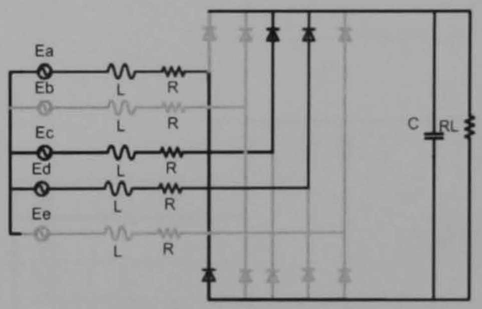

S6

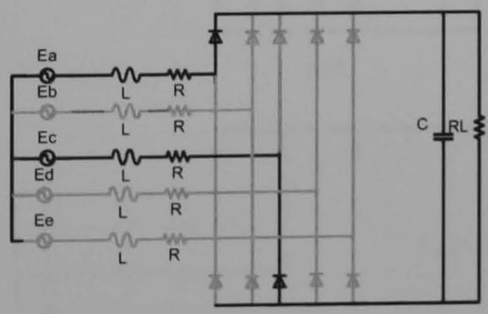

S7

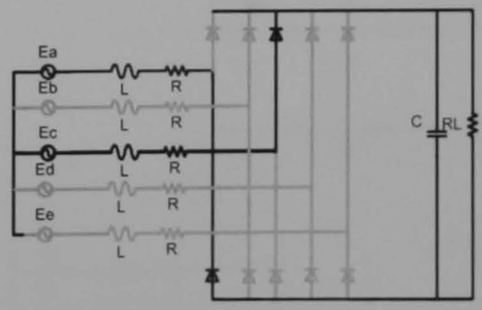

S8

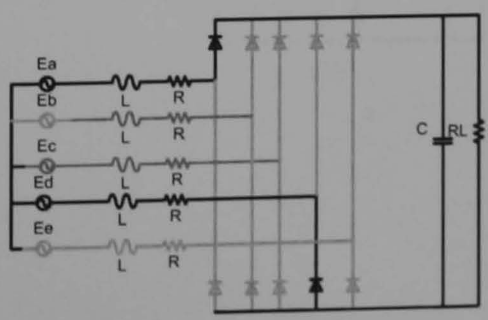

S9

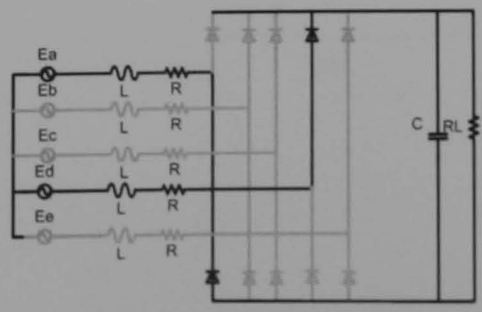

S10

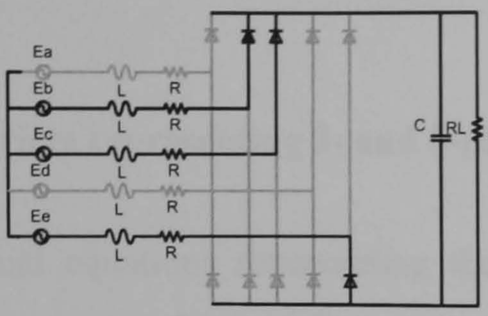

S11

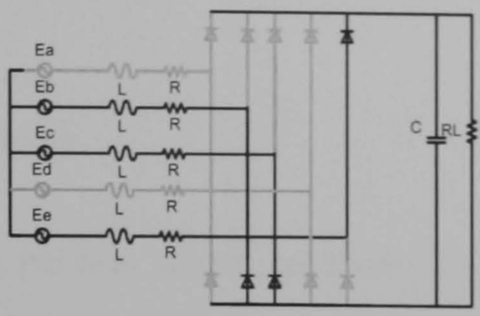

S12

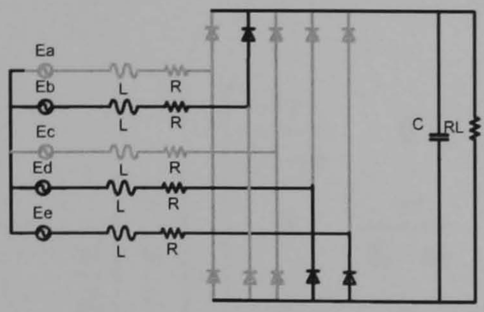

S13

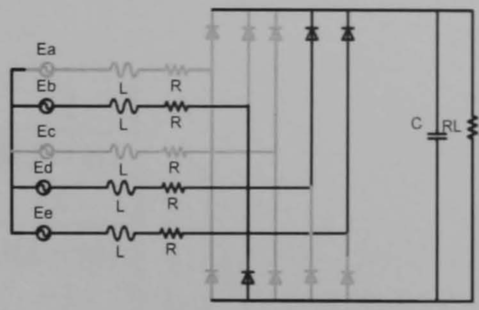

S14

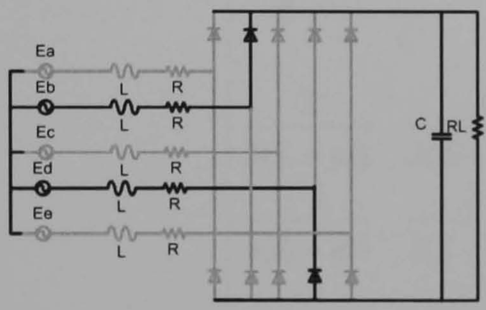

S15

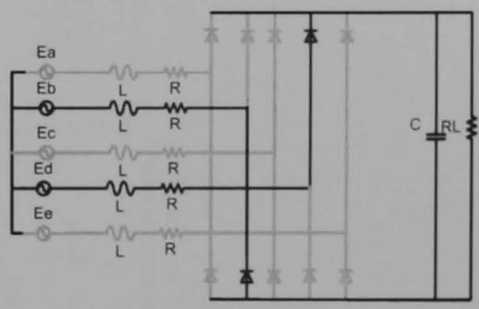

S16

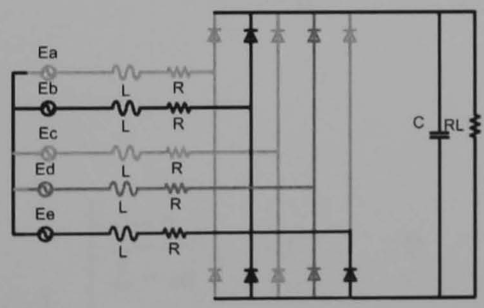

S17

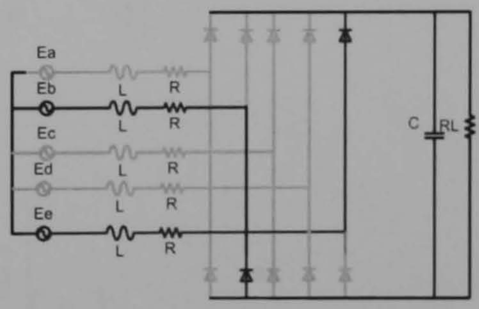

S18

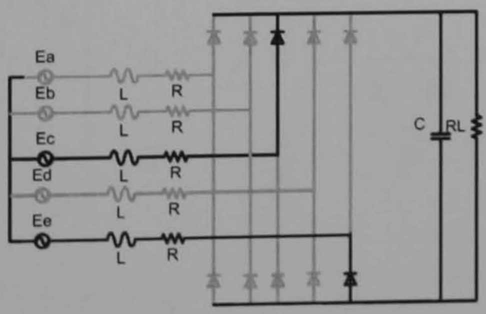

S19

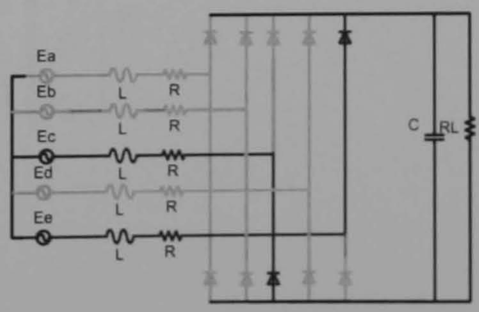

S20

A2. Matrices representing 3- and 5-phase systems

Differential equations representing the twelve periods shown in figure 3.15 for the three-phase system include the output voltage equation.

- S$_1$

$$\frac{d}{dt}\begin{bmatrix} i_a \\ i_b \\ i_c \\ v_{dc} \end{bmatrix} = \begin{bmatrix} \frac{-r}{L-m} & 0 & 0 & \frac{-1}{3(L-m)} \\ 0 & \frac{-r}{L-m} & 0 & \frac{2}{3(L-m)} \\ 0 & 0 & \frac{-r}{L-m} & \frac{-1}{3(L-m)} \\ 0 & \frac{-1}{C} & 0 & \frac{-1}{R_l C} \end{bmatrix} \begin{bmatrix} i_a \\ i_b \\ i_c \\ v_{dc} \end{bmatrix} + \begin{bmatrix} \frac{2}{3(L-m)} & \frac{-1}{3(L-m)} & \frac{-1}{3(L-m)} & 0 \\ \frac{-1}{3(L-m)} & \frac{2}{3(L-m)} & \frac{-1}{3(L-m)} & 0 \\ \frac{-1}{3(L-m)} & \frac{-1}{3(L-m)} & \frac{2}{3(L-m)} & 0 \\ 0 & 0 & 0 & 0 \end{bmatrix} \begin{bmatrix} v_a \\ v_b \\ v_c \\ 0 \end{bmatrix} \tag{A1}$$

- S$_2$

$$\frac{d}{dt}\begin{bmatrix} i_a \\ i_b \\ i_c \\ v_{dc} \end{bmatrix} = \begin{bmatrix} \frac{-r}{L-m} & 0 & 0 & \frac{1}{3(L-m)} \\ 0 & \frac{-r}{L-m} & 0 & \frac{-2}{3(L-m)} \\ 0 & 0 & \frac{-r}{L-m} & \frac{1}{3(L-m)} \\ 0 & \frac{1}{C} & 0 & \frac{-1}{R_l C} \end{bmatrix} \begin{bmatrix} i_a \\ i_b \\ i_c \\ v_{dc} \end{bmatrix} + \begin{bmatrix} \frac{2}{3(L-m)} & \frac{-1}{3(L-m)} & \frac{-1}{3(L-m)} & 0 \\ \frac{-1}{3(L-m)} & \frac{2}{3(L-m)} & \frac{-1}{3(L-m)} & 0 \\ \frac{-1}{3(L-m)} & \frac{-1}{3(L-m)} & \frac{2}{3(L-m)} & 0 \\ 0 & 0 & 0 & 0 \end{bmatrix} \begin{bmatrix} v_a \\ v_b \\ v_c \\ 0 \end{bmatrix} \tag{A2}$$

- S_3

$$\frac{d}{dt}\begin{bmatrix} i_a \\ i_b \\ i_c \\ v_{dc} \end{bmatrix} = \begin{bmatrix} \frac{-r}{L-m} & 0 & 0 & \frac{-1}{3(L-m)} \\ 0 & \frac{-r}{L-m} & 0 & \frac{-1}{3(L-m)} \\ 0 & 0 & \frac{-r}{L-m} & \frac{2}{3(L-m)} \\ 0 & 0 & \frac{-1}{C} & \frac{-1}{R_l C} \end{bmatrix} \begin{bmatrix} i_a \\ i_b \\ i_c \\ v_{dc} \end{bmatrix} +$$

$$\begin{bmatrix} \frac{2}{3(L-m)} & \frac{-1}{3(L-m)} & \frac{-1}{3(L-m)} & 0 \\ \frac{-1}{3(L-m)} & \frac{2}{3(L-m)} & \frac{-1}{3(L-m)} & 0 \\ \frac{-1}{3(L-m)} & \frac{-1}{3(L-m)} & \frac{2}{3(L-m)} & 0 \\ 0 & 0 & 0 & 0 \end{bmatrix} \begin{bmatrix} v_a \\ v_b \\ v_c \\ 0 \end{bmatrix} \tag{A3}$$

- S4

$$\frac{d}{dt}\begin{bmatrix} i_a \\ i_b \\ i_c \\ v_{dc} \end{bmatrix} = \begin{bmatrix} \frac{-r}{L-m} & 0 & 0 & \frac{1}{3(L-m)} \\ 0 & \frac{-r}{L-m} & 0 & \frac{1}{3(L-m)} \\ 0 & 0 & \frac{-r}{L-m} & \frac{-2}{3(L-m)} \\ 0 & 0 & \frac{1}{C} & \frac{-1}{R_l C} \end{bmatrix} \begin{bmatrix} i_a \\ i_b \\ i_c \\ v_{dc} \end{bmatrix} +$$

$$\begin{bmatrix} \frac{2}{3(L-m)} & \frac{-1}{3(L-m)} & \frac{-1}{3(L-m)} & 0 \\ \frac{-1}{3(L-m)} & \frac{2}{3(L-m)} & \frac{-1}{3(L-m)} & 0 \\ \frac{-1}{3(L-m)} & \frac{-1}{3(L-m)} & \frac{2}{3(L-m)} & 0 \\ 0 & 0 & 0 & 0 \end{bmatrix} \begin{bmatrix} v_a \\ v_b \\ v_c \\ 0 \end{bmatrix} \tag{A4}$$

- **S**$_5$

$$\begin{aligned}\frac{d}{dt}\begin{bmatrix} i_a \\ i_b \\ i_c \\ v_{dc} \end{bmatrix} &= \begin{bmatrix} \frac{-r}{L-m} & 0 & 0 & \frac{-2}{3(L-m)} \\ 0 & \frac{-r}{L-m} & 0 & \frac{1}{3(L-m)} \\ 0 & 0 & \frac{-r}{L-m} & \frac{1}{3(L-m)} \\ \frac{1}{C} & 0 & 0 & \frac{-1}{R_l C} \end{bmatrix} \begin{bmatrix} i_a \\ i_b \\ i_c \\ v_{dc} \end{bmatrix} + \\ &\begin{bmatrix} \frac{2}{3(L-m)} & \frac{-1}{3(L-m)} & \frac{-1}{3(L-m)} & 0 \\ \frac{-1}{3(L-m)} & \frac{2}{3(L-m)} & \frac{-1}{3(L-m)} & 0 \\ \frac{-1}{3(L-m)} & \frac{-1}{3(L-m)} & \frac{2}{3(L-m)} & 0 \\ 0 & 0 & 0 & 0 \end{bmatrix} \begin{bmatrix} v_a \\ v_b \\ v_c \\ 0 \end{bmatrix}\end{aligned} \tag{A5}$$

- **S**$_6$

$$\begin{aligned}\frac{d}{dt}\begin{bmatrix} i_a \\ i_b \\ i_c \\ v_{dc} \end{bmatrix} &= \begin{bmatrix} \frac{-r}{L-m} & 0 & 0 & \frac{2}{3(L-m)} \\ 0 & \frac{-r}{L-m} & 0 & \frac{-1}{3(L-m)} \\ 0 & 0 & \frac{-r}{L-m} & \frac{-1}{3(L-m)} \\ \frac{-1}{C} & 0 & 0 & \frac{-1}{R_l C} \end{bmatrix} \begin{bmatrix} i_a \\ i_b \\ i_c \\ v_{dc} \end{bmatrix} + \\ &\begin{bmatrix} \frac{2}{3(L-m)} & \frac{-1}{3(L-m)} & \frac{-1}{3(L-m)} & 0 \\ \frac{-1}{3(L-m)} & \frac{2}{3(L-m)} & \frac{-1}{3(L-m)} & 0 \\ \frac{-1}{3(L-m)} & \frac{-1}{3(L-m)} & \frac{2}{3(L-m)} & 0 \\ 0 & 0 & 0 & 0 \end{bmatrix} \begin{bmatrix} v_a \\ v_b \\ v_c \\ 0 \end{bmatrix}\end{aligned} \tag{A6}$$

- S_7

$$\frac{d}{dt}\begin{bmatrix} i_a \\ i_b \\ v_{dc} \end{bmatrix} = \begin{bmatrix} \frac{-r}{L-m} & 0 & \frac{-1}{2(L-m)} \\ 0 & \frac{-r}{L-m} & \frac{1}{2(L-m)} \\ 0 & \frac{-1}{C} & \frac{-1}{R_l C} \end{bmatrix} \begin{bmatrix} i_a \\ i_b \\ v_{dc} \end{bmatrix} + \begin{bmatrix} \frac{1}{2(L-m)} & \frac{-1}{2(L-m)} & 0 \\ \frac{-1}{2(L-m)} & \frac{1}{2(L-m)} & 0 \\ 0 & 0 & 0 \end{bmatrix} \begin{bmatrix} v_a \\ v_b \\ 0 \end{bmatrix} \tag{A7}$$

- S_8

$$\frac{d}{dt}\begin{bmatrix} i_a \\ i_b \\ v_{dc} \end{bmatrix} = \begin{bmatrix} \frac{-r}{L-m} & 0 & \frac{1}{2(L-m)} \\ 0 & \frac{-r}{L-m} & \frac{-1}{2(L-m)} \\ 0 & \frac{1}{C} & \frac{-1}{R_l C} \end{bmatrix} \begin{bmatrix} i_a \\ i_b \\ v_{dc} \end{bmatrix} + \begin{bmatrix} \frac{1}{2(L-m)} & \frac{-1}{2(L-m)} & 0 \\ \frac{-1}{2(L-m)} & \frac{1}{2(L-m)} & 0 \\ 0 & 0 & 0 \end{bmatrix} \begin{bmatrix} v_a \\ v_b \\ 0 \end{bmatrix} \tag{A8}$$

- S_9

$$\frac{d}{dt}\begin{bmatrix} i_a \\ i_c \\ v_{dc} \end{bmatrix} = \begin{bmatrix} \frac{-r}{L-m} & 0 & \frac{-1}{2(L-m)} \\ 0 & \frac{-r}{L-m} & \frac{1}{2(L-m)} \\ \frac{1}{C} & 0 & \frac{-1}{R_l C} \end{bmatrix} \begin{bmatrix} i_a \\ i_c \\ v_{dc} \end{bmatrix} + \begin{bmatrix} \frac{1}{2(L-m)} & \frac{-1}{2(L-m)} & 0 \\ \frac{-1}{2(L-m)} & \frac{1}{2(L-m)} & 0 \\ 0 & 0 & 0 \end{bmatrix} \begin{bmatrix} v_a \\ v_c \\ 0 \end{bmatrix} \tag{A9}$$

- S_{10}

$$\frac{d}{dt}\begin{bmatrix} i_a \\ i_c \\ v_{dc} \end{bmatrix} = \begin{bmatrix} \frac{-r}{L-m} & 0 & \frac{1}{2(L-m)} \\ 0 & \frac{-r}{L-m} & \frac{-1}{2(L-m)} \\ \frac{-1}{C} & 0 & \frac{-1}{R_l C} \end{bmatrix} \begin{bmatrix} i_a \\ i_c \\ v_{dc} \end{bmatrix} + \begin{bmatrix} \frac{1}{2(L-m)} & \frac{-1}{2(L-m)} & 0 \\ \frac{-1}{2(L-m)} & \frac{1}{2(L-m)} & 0 \\ 0 & 0 & 0 \end{bmatrix} \begin{bmatrix} v_a \\ v_c \\ 0 \end{bmatrix} \tag{A10}$$

- **S_{11}**

$$\frac{d}{dt}\begin{bmatrix} i_b \\ i_c \\ v_{dc} \end{bmatrix} = \begin{bmatrix} \frac{-r}{L-m} & 0 & \frac{-1}{2(L-m)} \\ 0 & \frac{-r}{L-m} & \frac{1}{2(L-m)} \\ 0 & \frac{-1}{C} & \frac{-1}{R_l C} \end{bmatrix} \begin{bmatrix} i_b \\ i_c \\ v_{dc} \end{bmatrix} + \begin{bmatrix} \frac{1}{2(L-m)} & \frac{-1}{2(L-m)} & 0 \\ \frac{-1}{2(L-m)} & \frac{1}{2(L-m)} & 0 \\ 0 & 0 & 0 \end{bmatrix} \begin{bmatrix} v_b \\ v_c \\ 0 \end{bmatrix} \qquad \text{(A11)}$$

- **S_{12}**

$$\frac{d}{dt}\begin{bmatrix} i_b \\ i_c \\ v_{dc} \end{bmatrix} = \begin{bmatrix} \frac{-r}{L-m} & 0 & \frac{1}{2(L-m)} \\ 0 & \frac{-r}{L-m} & \frac{-1}{2(L-m)} \\ 0 & \frac{1}{C} & \frac{-1}{R_l C} \end{bmatrix} \begin{bmatrix} i_b \\ i_c \\ v_{dc} \end{bmatrix} + \begin{bmatrix} \frac{1}{2(L-m)} & \frac{-1}{2(L-m)} & 0 \\ \frac{-1}{2(L-m)} & \frac{1}{2(L-m)} & 0 \\ 0 & 0 & 0 \end{bmatrix} \begin{bmatrix} v_b \\ v_c \\ 0 \end{bmatrix} \qquad \text{(A12)}$$

Differential equations representing the twenty periods shown in figure 3.20 for the five-phase system include the output voltage equation.

- S_1

$$\frac{d}{dt}\begin{bmatrix} ia \\ ic \\ ie \\ vdc \end{bmatrix} = \begin{bmatrix} \frac{-r(3L-2M_2-M_1)}{(L-M_1)(3L-4M_2+M_1)} & 0 & \frac{2r(M1-M2)}{(L-M_1)(3L-4M_2+M_1)} & \frac{-(L-M_1)}{(L-M_1)(3L-4M_2+M_1)} \\ 0 & \frac{-3r}{(3L-4M_2+M_1)} & 0 & \frac{2}{(3L-4M_2+M_1)} \\ 0 & 0 & \frac{-r(3L-2M_2-M_1)}{(L-M_1)(3L-4M_2+M_1)} & \frac{-(L-M_1)}{(L-M_1)(3L-4M_2+M_1)} \\ 0 & \frac{-1}{C} & 0 & \frac{-1}{RC} \end{bmatrix}\begin{bmatrix} ia \\ ic \\ ie \\ vdc \end{bmatrix} + \begin{bmatrix} \frac{2(L-M_2)}{(L-M_1)(3L-4M_2+M_1)} & \frac{-(L-M_1)}{(L-M_1)(3L-4M_2+M_1)} & \frac{-(L-2M_2+M_1)}{(L-M_1)(3L-4M_2+M_1)} & 0 \\ \frac{-1}{(3L-4M_2+M_1)} & \frac{2}{(3L-4M_2+M_1)} & \frac{-1}{(3L-4M_2+M_1)} & 0 \\ \frac{-(L-2M_2+M_1)}{(L-M_1)(3L-4M_2+M_1)} & \frac{-(L-M_1)}{(L-M_1)(3L-4M_2+M_1)} & \frac{2(L-M_2)}{(L-M_1)(3L-4M_2+M_1)} & 0 \\ 0 & 0 & 0 & 0 \end{bmatrix}\begin{bmatrix} va \\ vc \\ ve \\ 0 \end{bmatrix} \quad \text{(A13)}$$

- S_2

$$\frac{d}{dt}\begin{bmatrix} ia \\ ic \\ ie \\ vdc \end{bmatrix} = \begin{bmatrix} \frac{-r(3L-2M_2-M_1)}{(L-M_1)(3L-4M_2+M_1)} & 0 & 0 & \frac{-(L-M_1)}{(L-M_1)(3L-4M_2+M_1)} \\ 0 & \frac{-3r}{(3L-4M_2+M_1)} & 0 & \frac{-2}{(3L-4M_2+M_1)} \\ 0 & 0 & \frac{-r(3L-2M_2-M_1)}{(L-M_1)(3L-4M_2+M_1)} & \frac{-(L-M_1)}{(L-M_1)(3L-4M_2+M_1)} \\ 0 & \frac{1}{C} & 0 & \frac{-1}{RC} \end{bmatrix}\begin{bmatrix} ia \\ ic \\ ie \\ vdc \end{bmatrix} + \begin{bmatrix} \frac{2(L-M_2)}{(L-M_1)(3L-4M_2+M_1)} & \frac{-(L-M_1)}{(L-M_1)(3L-4M_2+M_1)} & \frac{-(L-2M_2+M_1)}{(L-M_1)(3L-4M_2+M_1)} & 0 \\ \frac{-1}{(3L-4M_2+M_1)} & \frac{2}{(3L-4M_2+M_1)} & \frac{-1}{(3L-4M_2+M_1)} & 0 \\ \frac{-(L-2M_2+M_1)}{(L-M_1)(3L-4M_2+M_1)} & \frac{-(L-M_1)}{(L-M_1)(3L-4M_2+M_1)} & \frac{(L-M_2)}{(L-M_1)(3L-4M_2+M_1)} & 0 \\ 0 & 0 & 0 & 0 \end{bmatrix}\begin{bmatrix} va \\ vc \\ ve \\ 0 \end{bmatrix} \quad \text{(A14)}$$

- S_3

$$\frac{d}{dt}\begin{bmatrix} ia \\ ib \\ id \\ vdc \end{bmatrix} = \begin{bmatrix} \frac{-r(3L-2M_2-M_1)}{(L-M_1)(3L-4M_2+M_1)} & 0 & 0 & \frac{-(L-M_1)}{(L-M_1)(3L-4M_2+M_1)} \\ \frac{2r(M1-M2)}{(L-M_1)(3L-4M_2+M_1)} & \frac{-r(3L-2M_2-M_1)}{(L-M_1)(3L-4M_2+M_1)} & 0 & \frac{-(L-M_1)}{(L-M_1)(3L-4M_2+M_1)} \\ 0 & 0 & \frac{-3r}{(3L-4M_2+M_1)} & \frac{2}{(3L-4M_2+M_1)} \\ 0 & 0 & \frac{-1}{C} & \frac{-1}{RC} \end{bmatrix} \begin{bmatrix} ia \\ ib \\ id \\ vdc \end{bmatrix} + \begin{bmatrix} \frac{2(L-M_2)}{(L-M_1)(3L-4M_2+M_1)} & \frac{-(L-2M_1+M_1)}{(L-M_1)(3L-4M_2+M_1)} & \frac{-(L-M_1)}{(L-M_1)(3L-4M_2+M_1)} & 0 \\ \frac{-(L-2M_1+M_1)}{(L-M_1)(3L-4M_2+M_1)} & \frac{2(L-M_2)}{(L-M_1)(3L-4M_2+M_1)} & \frac{-(L-M_1)}{(L-M_1)(3L-4M_2+M_1)} & 0 \\ \frac{-1}{(3L-4M_2+M_1)} & \frac{-1}{(3L-4M_2+M_1)} & \frac{2}{(3L-4M_2+M_1)} & 0 \\ 0 & 0 & 0 & 0 \end{bmatrix} \begin{bmatrix} va \\ vb \\ vd \\ 0 \end{bmatrix} \tag{A15}$$

- S_4

$$\frac{d}{dt}\begin{bmatrix} ia \\ ic \\ id \\ vdc \end{bmatrix} = \begin{bmatrix} \frac{-r(3L-2M_2-M_1)}{(L-M_1)(3L-4M_2+M_1)} & 0 & 0 & \frac{(L-M_1)}{(L-M_1)(3L-4M_2+M_1)} \\ 0 & \frac{-r(3L-2M_2-M_1)}{(L-M_1)(3L-4M_2+M_1)} & 0 & \frac{(L-M_1)}{(L-M_1)(3L-4M_2+M_1)} \\ 0 & 0 & \frac{-3r}{(3L-4M_2+M_1)} & \frac{-2}{(3L-4M_2+M_1)} \\ 0 & 0 & \frac{1}{C} & \frac{-1}{RC} \end{bmatrix} \begin{bmatrix} ia \\ ic \\ id \\ vdc \end{bmatrix} + \begin{bmatrix} \frac{2}{(3L-4M_2+M_1)} & \frac{-1}{(3L-4M_2+M_1)} & \frac{-1}{(3L-4M_2+M_1)} & 0 \\ \frac{-(L-M_1)}{(L-M_1)(3L-4M_2+M_1)} & \frac{2(L-M_2)}{(L-M_1)(3L-4M_2+M_1)} & \frac{-(L-2M_1+M_1)}{(L-M_1)(3L-4M_2+M_1)} & 0 \\ \frac{-(L-M_1)}{(L-M_1)(3L-4M_2+M_1)} & \frac{-(L-2M_1+M_1)}{(L-M_1)(3L-4M_2+M_1)} & \frac{2(L-M_2)}{(L-M_1)(3L-4M_2+M_1)} & 0 \\ 0 & 0 & 0 & 0 \end{bmatrix} \begin{bmatrix} va \\ vc \\ vd \\ 0 \end{bmatrix} \tag{A16}$$

- S_5

$$\frac{d}{dt}\begin{bmatrix} ia \\ ic \\ id \\ vdc \end{bmatrix} = \begin{bmatrix} \dfrac{-3r}{(3L-4M_2+M_1)} & 0 & 0 & \dfrac{-2}{(3L-4M_2+M_1)} \\ 0 & \dfrac{-r(3L-2M_2-M_1)}{(L-M_1)(3L-4M_2+M_1)} & 0 & \dfrac{(L-M_1)}{(L-M_1)(3L-4M_2+M_1)} \\ 0 & 0 & \dfrac{-r(3L-2M_2-M_1)}{(L-M_1)(3L-4M_2+M_1)} & \dfrac{(L-M_1)}{(L-M_1)(3L-4M_2+M_1)} \\ \dfrac{1}{C} & 0 & 0 & \dfrac{-1}{RC} \end{bmatrix} \begin{bmatrix} ia \\ ic \\ id \\ vdc \end{bmatrix} + \begin{bmatrix} \dfrac{2}{(3L-4M_2+M_1)} & \dfrac{-1}{(3L-4M_2+M_1)} & \dfrac{-1}{(3L-4M_2+M_1)} & 0 \\ \dfrac{-(L-M_1)}{(L-M_1)(3L-4M_2+M_1)} & \dfrac{2(L-M_2)}{(L-M_1)(3L-4M_2+M_1)} & \dfrac{-(L-2M_1+M_1)}{(L-M_1)(3L-4M_2+M_1)} & 0 \\ \dfrac{-(L-M_1)}{(L-M_1)(3L-4M_2+M_1)} & \dfrac{-(L-2M_1+M_1)}{(L-M_1)(3L-4M_2+M_1)} & \dfrac{2(L-M_2)}{(L-M_1)(3L-4M_2+M_1)} & 0 \\ 0 & 0 & 0 & 0 \end{bmatrix} \begin{bmatrix} va \\ vc \\ vd \\ 0 \end{bmatrix} \tag{A17}$$

- S_6

$$\frac{d}{dt}\begin{bmatrix} ia \\ ic \\ id \\ vdc \end{bmatrix} = \begin{bmatrix} \dfrac{-3r}{(3L-4M_2+M_1)} & 0 & 0 & \dfrac{-2}{(3L-4M_2+M_1)} \\ 0 & \dfrac{-r(3L-2M_2-M_1)}{(L-M_1)(3L-4M_2+M_1)} & \dfrac{2r(M1-M2)}{(L-M_1)(3L-4M_2+M_1)} & \dfrac{(L-M_1)}{(L-M_1)(3L-4M_2+M_1)} \\ 0 & 0 & \dfrac{-r(3L-2M_2-M_1)}{(L-M_1)(3L-4M_2+M_1)} & \dfrac{(L-M_1)}{(L-M_1)(3L-4M_2+M_1)} \\ \dfrac{-1}{C} & 0 & 0 & \dfrac{-1}{RC} \end{bmatrix} \begin{bmatrix} ia \\ ic \\ id \\ vdc \end{bmatrix} + \begin{bmatrix} \dfrac{2}{(3L-4M_2+M_1)} & \dfrac{-1}{(3L-4M_2+M_1)} & \dfrac{-1}{(3L-4M_2+M_1)} & 0 \\ \dfrac{-(L-M_1)}{(L-M_1)(3L-4M_2+M_1)} & \dfrac{2(L-M_2)}{(L-M_1)(3L-4M_2+M_1)} & \dfrac{-(L-2M_1+M_1)}{(L-M_1)(3L-4M_2+M_1)} & 0 \\ \dfrac{-(L-M_1)}{(L-M_1)(3L-4M_2+M_1)} & \dfrac{-(L-2M_1+M_1)}{(L-M_1)(3L-4M_2+M_1)} & \dfrac{2(L-M_2)}{(L-M_1)(3L-4M_2+M_1)} & 0 \\ 0 & 0 & 0 & 0 \end{bmatrix} \begin{bmatrix} va \\ vc \\ vd \\ 0 \end{bmatrix} \tag{A18}$$

- S_7

$$\frac{d}{dt}\begin{bmatrix} i_a \\ i_c \\ v_{dc} \end{bmatrix} = \begin{bmatrix} \frac{-r}{L-M_2} & 0 & \frac{-1}{2(L-M_2)} \\ 0 & \frac{-r}{L-M_2} & \frac{1}{2(L-M_2)} \\ 0 & \frac{-1}{C} & \frac{-1}{R_l C} \end{bmatrix} \begin{bmatrix} i_a \\ i_b \\ v_{dc} \end{bmatrix} + \begin{bmatrix} \frac{1}{2(L-m)} & \frac{-1}{2(L-m)} & 0 \\ \frac{-1}{2(L-m)} & \frac{1}{2(L-m)} & 0 \\ 0 & 0 & 0 \end{bmatrix} \begin{bmatrix} v_a \\ v_c \\ 0 \end{bmatrix} \quad \text{(A19)}$$

- S_8

$$\frac{d}{dt}\begin{bmatrix} i_a \\ i_c \\ v_{dc} \end{bmatrix} = \begin{bmatrix} \frac{-r}{L-M_2} & 0 & \frac{-1}{2(L-M_2)} \\ 0 & \frac{-r}{L-M_2} & \frac{1}{2(L-M_2)} \\ 0 & \frac{1}{C} & \frac{-1}{R_l C} \end{bmatrix} \begin{bmatrix} i_a \\ i_c \\ v_{dc} \end{bmatrix} + \begin{bmatrix} \frac{1}{2(L-m)} & \frac{-1}{2(L-m)} & 0 \\ \frac{-1}{2(L-m)} & \frac{1}{2(L-m)} & 0 \\ 0 & 0 & 0 \end{bmatrix} \begin{bmatrix} v_c \\ v_e \\ 0 \end{bmatrix} \quad \text{(A20)}$$

- S_9

$$\frac{d}{dt}\begin{bmatrix} i_a \\ i_d \\ v_{dc} \end{bmatrix} = \begin{bmatrix} \frac{-r}{L-M_2} & 0 & \frac{-1}{2(L-M_2)} \\ 0 & \frac{-r}{L-M_2} & \frac{1}{2(L-M_2)} \\ \frac{1}{C} & 0 & \frac{-1}{R_l C} \end{bmatrix} \begin{bmatrix} i_a \\ i_b \\ v_{dc} \end{bmatrix} + \begin{bmatrix} \frac{1}{2(L-m)} & \frac{-1}{2(L-m)} & 0 \\ \frac{-1}{2(L-m)} & \frac{1}{2(L-m)} & 0 \\ 0 & 0 & 0 \end{bmatrix} \begin{bmatrix} v_a \\ v_d \\ 0 \end{bmatrix} \quad \text{(A21)}$$

- S_{10}

$$\frac{d}{dt}\begin{bmatrix} i_a \\ i_d \\ v_{dc} \end{bmatrix} = \begin{bmatrix} \frac{-r}{L-M_2} & 0 & \frac{1}{2(L-M_2)} \\ 0 & \frac{-r}{L-M_2} & \frac{-1}{2(L-M_2)} \\ \frac{-1}{C} & 0 & \frac{-1}{R_l C} \end{bmatrix} \begin{bmatrix} i_a \\ i_d \\ v_{dc} \end{bmatrix} + \begin{bmatrix} \frac{1}{2(L-m)} & \frac{-1}{2(L-m)} & 0 \\ \frac{-1}{2(L-m)} & \frac{1}{2(L-m)} & 0 \\ 0 & 0 & 0 \end{bmatrix} \begin{bmatrix} v_c \\ v_d \\ 0 \end{bmatrix} \quad \text{(A22)}$$

- S_{11}

$$\frac{d}{dt}\begin{bmatrix} ib \\ ic \\ ie \\ vdc \end{bmatrix} = \begin{bmatrix} \frac{-r(3L-2M_2-M_1)}{(L-M_1)(3L-4M_2+M_1)} & \frac{2r(M1-M2)}{(L-M_1)(3L-4M_2+M_1)} & 0 & \frac{-(L-M_1)}{(L-M_1)(3L-4M_2+M_1)} \\ 0 & \frac{-r(3L-2M_2-M_1)}{(L-M_1)(3L-4M_2+M_1)} & 0 & \frac{-(L-M_1)}{(L-M_1)(3L-4M_2+M_1)} \\ 0 & 0 & \frac{-3r}{(3L-4M_2+M_1)} & \frac{2}{(3L-4M_2+M_1)} \\ 0 & 0 & \frac{1}{C} & \frac{-1}{RC} \end{bmatrix} \begin{bmatrix} ib \\ ic \\ ie \\ vdc \end{bmatrix} + \begin{bmatrix} \frac{2(L-M_2)}{(L-M_1)(3L-4M_2+M_1)} & \frac{-(L-2M_2+M_1)}{(L-M_1)(3L-4M_2+M_1)} & \frac{-(L-M_1)}{(L-M_1)(3L-4M_2+M_1)} & 0 \\ \frac{-(L-M_1)}{(L-M_1)(3L-4M_2+M_1)} & \frac{2(L-M_2)}{(L-M_1)(3L-4M_2+M_1)} & \frac{-(L-2M_2+M_1)}{(L-M_1)(3L-4M_2+M_1)} & 0 \\ \frac{-1}{(3L-4M_2+M_1)} & \frac{-1}{(3L-4M_2+M_1)} & \frac{2}{(3L-4M_2+M_1)} & 0 \\ 0 & 0 & 0 & 0 \end{bmatrix} \begin{bmatrix} vb \\ vc \\ ve \\ 0 \end{bmatrix} \tag{A23}$$

- S_{12}

$$\frac{d}{dt}\begin{bmatrix} ib \\ ic \\ ie \\ vdc \end{bmatrix} = \begin{bmatrix} \frac{-r(3L-2M_2-M_1)}{(L-M_1)(3L-4M_2+M_1)} & 0 & 0 & \frac{(L-M_1)}{(L-M_1)(3L-4M_2+M_1)} \\ 0 & \frac{-r(3L-2M_2-M_1)}{(L-M_1)(3L-4M_2+M_1)} & 0 & \frac{(L-M_1)}{(L-M_1)(3L-4M_2+M_1)} \\ 0 & 0 & \frac{-3r}{(3L-4M_2+M_1)} & \frac{-2}{(L-M_1)(3L-4M_2+M_1)} \\ 0 & 0 & \frac{1}{C} & \frac{-1}{RC} \end{bmatrix} \begin{bmatrix} ib \\ ic \\ ie \\ vdc \end{bmatrix} + \begin{bmatrix} \frac{2(L-M_2)}{(L-M_1)(3L-4M_2+M_1)} & \frac{-(L-2M_2+M_1)}{(L-M_1)(3L-4M_2+M_1)} & \frac{-(L-M_1)}{(L-M_1)(3L-4M_2+M_1)} & 0 \\ \frac{-(L-2M_2+M_1)}{(L-M_1)(3L-4M_2+M_1)} & \frac{2(L-M_2)}{(L-M_1)(3L-4M_2+M_1)} & \frac{-(L-M_1)}{(L-M_1)(3L-4M_2+M_1)} & 0 \\ \frac{-1}{(3L-4M_2+M_1)} & \frac{-1}{(3L-4M_2+M_1)} & \frac{2}{(3L-4M_2+M_1)} & 0 \\ 0 & 0 & 0 & 0 \end{bmatrix} \begin{bmatrix} vb \\ vc \\ ve \\ 0 \end{bmatrix} \tag{A24}$$

- S_{13}

$$\frac{d}{dt}\begin{bmatrix} ib \\ id \\ ie \\ vdc \end{bmatrix} = \begin{bmatrix} \frac{-3r}{(3L-4M_2+M_1)} & 0 & 0 & \frac{-2}{(3L-4M_2+M_1)} \\ 0 & \frac{-r(3L-2M_2-M_1)}{(L-M_1)(3L-4M_2+M_1)} & 0 & \frac{1}{(L-M_1)(3L-4M_2+M_1)} \\ 0 & 0 & \frac{-r(3L-2M_2-M_1)}{(L-M_1)(3L-4M_2+M_1)} & \frac{(L-M_1)}{(L-M_1)(3L-4M_2+M_1)} \\ \frac{1}{C} & 0 & 0 & \frac{-1}{RC} \end{bmatrix} \begin{bmatrix} ib \\ id \\ ie \\ vdc \end{bmatrix} + \begin{bmatrix} \frac{2}{(3L-4M_2+M_1)} & \frac{-1}{(3L-4M_2+M_1)} & \frac{-1}{(3L-4M_2+M_1)} & 0 \\ \frac{-(L-M_1)}{(L-M_1)(3L-4M_2+M_1)} & \frac{2(L-M_2)}{(L-M_1)(3L-4M_2+M_1)} & \frac{-(L-2M_2+M_1)}{(L-M_1)(3L-4M_2+M_1)} & 0 \\ \frac{-(L-M_1)}{(L-M_1)(3L-4M_2+M_1)} & \frac{-(L-2M_2+M_1)}{(L-M_1)(3L-4M_2+M_1)} & \frac{2(L-M_2)}{(L-M_1)(3L-4M_2+M_1)} & 0 \\ 0 & 0 & 0 & 0 \end{bmatrix} \begin{bmatrix} vb \\ vd \\ ve \\ 0 \end{bmatrix} \tag{A25}$$

- S_{14}

$$\frac{d}{dt}\begin{bmatrix} ib \\ id \\ ie \\ vdc \end{bmatrix} = \begin{bmatrix} \frac{-3r}{(3L-4M_2+M_1)} & 0 & 0 & \frac{2}{(3L-4M_2+M_1)} \\ 0 & \frac{-r(3L-2M_2-M_1)}{(L-M_1)(3L-4M_2+M_1)} & \frac{2r(M1-M2)}{(L-M_1)(3L-4M_2+M_1)} & \frac{-(L-M_1)}{(L-M_1)(3L-4M_2+M_1)} \\ 0 & 0 & \frac{-r(3L-2M_2-M_1)}{(L-M_1)(3L-4M_2+M_1)} & \frac{-(L-M_1)}{(L-M_1)(3L-4M_2+M_1)} \\ 0 & \frac{1}{C} & 0 & \frac{-1}{RC} \end{bmatrix} \begin{bmatrix} ib \\ id \\ ie \\ vdc \end{bmatrix} + \begin{bmatrix} \frac{2}{(3L-4M_2+M_1)} & \frac{-1}{(3L-4M_2+M_1)} & \frac{-1}{(3L-4M_2+M_1)} & 0 \\ \frac{-(L-M_1)}{(L-M_1)(3L-4M_2+M_1)} & \frac{2(L-M_2)}{(L-M_1)(3L-4M_2+M_1)} & \frac{-(L-2M_2+M_1)}{(L-M_1)(3L-4M_2+M_1)} & 0 \\ \frac{-(L-M_1)}{(L-M_1)(3L-4M_2+M_1)} & \frac{-(L-2M_2+M_1)}{(L-M_1)(3L-4M_2+M_1)} & \frac{2(L-M_2)}{(L-M_1)(3L-4M_2+M_1)} & 0 \\ 0 & 0 & 0 & 0 \end{bmatrix} \begin{bmatrix} vb \\ vd \\ ve \\ 0 \end{bmatrix} \tag{A26}$$

- S_{15}

$$\frac{d}{dt}\begin{bmatrix} i_b \\ i_d \\ v_{dc} \end{bmatrix} = \begin{bmatrix} \frac{-r}{L-M_2} & 0 & \frac{-1}{2(L-M_2)} \\ 0 & \frac{-r}{L-M_2} & \frac{1}{2(L-M_2)} \\ 0 & \frac{-1}{C} & \frac{-1}{R_l C} \end{bmatrix} \begin{bmatrix} i_b \\ i_d \\ v_{dc} \end{bmatrix} + \begin{bmatrix} \frac{1}{2(L-m)} & \frac{-1}{2(L-m)} & 0 \\ \frac{-1}{2(L-m)} & \frac{1}{2(L-m)} & 0 \\ 0 & 0 & 0 \end{bmatrix} \begin{bmatrix} v_b \\ v_d \\ 0 \end{bmatrix} \quad \text{(A27)}$$

- S_{16}

$$\frac{d}{dt}\begin{bmatrix} i_b \\ i_d \\ v_{dc} \end{bmatrix} = \begin{bmatrix} \frac{-r}{L-M_2} & 0 & \frac{1}{2(L-M_2)} \\ 0 & \frac{-r}{L-M_2} & \frac{-1}{2(L-M_2)} \\ 0 & \frac{1}{C} & \frac{-1}{R_l C} \end{bmatrix} \begin{bmatrix} i_b \\ i_d \\ v_{dc} \end{bmatrix} + \begin{bmatrix} \frac{1}{2(L-m)} & \frac{-1}{2(L-m)} & 0 \\ \frac{-1}{2(L-m)} & \frac{1}{2(L-m)} & 0 \\ 0 & 0 & 0 \end{bmatrix} \begin{bmatrix} v_b \\ v_d \\ 0 \end{bmatrix} \quad \text{(A28)}$$

- S_{17}

$$\frac{d}{dt}\begin{bmatrix} i_b \\ i_e \\ v_{dc} \end{bmatrix} = \begin{bmatrix} \frac{-r}{L-M_2} & 0 & \frac{-1}{2(L-M_2)} \\ 0 & \frac{-r}{L-M_2} & \frac{1}{2(L-M_2)} \\ \frac{1}{C} & 0 & \frac{-1}{R_l C} \end{bmatrix} \begin{bmatrix} i_b \\ i_e \\ v_{dc} \end{bmatrix} + \begin{bmatrix} \frac{1}{2(L-m)} & \frac{-1}{2(L-m)} & 0 \\ \frac{-1}{2(L-m)} & \frac{1}{2(L-m)} & 0 \\ 0 & 0 & 0 \end{bmatrix} \begin{bmatrix} v_b \\ v_e \\ 0 \end{bmatrix} \quad \text{(A29)}$$

- S_{18}

$$\frac{d}{dt}\begin{bmatrix} i_b \\ i_e \\ v_{dc} \end{bmatrix} = \begin{bmatrix} \frac{-r}{L-M_2} & 0 & \frac{1}{2(L-M_2)} \\ 0 & \frac{-r}{L-M_2} & \frac{-1}{2(L-M_2)} \\ \frac{-1}{C} & 0 & \frac{-1}{R_l C} \end{bmatrix} \begin{bmatrix} i_b \\ i_e \\ v_{dc} \end{bmatrix} + \begin{bmatrix} \frac{1}{2(L-m)} & \frac{-1}{2(L-m)} & 0 \\ \frac{-1}{2(L-m)} & \frac{1}{2(L-m)} & 0 \\ 0 & 0 & 0 \end{bmatrix} \begin{bmatrix} v_b \\ v_e \\ 0 \end{bmatrix} \quad \text{(A30)}$$

- S_{19}

$$\frac{d}{dt}\begin{bmatrix} i_c \\ i_e \\ v_{dc} \end{bmatrix} = \begin{bmatrix} \frac{-r}{L-M_2} & 0 & \frac{-1}{2(L-M_2)} \\ 0 & \frac{-r}{L-M_2} & \frac{1}{2(L-M_2)} \\ 0 & \frac{-1}{C} & \frac{-1}{R_l C} \end{bmatrix} \begin{bmatrix} i_c \\ i_e \\ v_{dc} \end{bmatrix} + \begin{bmatrix} \frac{1}{2(L-m)} & \frac{-1}{2(L-m)} & 0 \\ \frac{-1}{2(L-m)} & \frac{1}{2(L-m)} & 0 \\ 0 & 0 & 0 \end{bmatrix} \begin{bmatrix} v_c \\ v_e \\ 0 \end{bmatrix} \tag{A31}$$

- S_{20}

$$\frac{d}{dt}\begin{bmatrix} i_c \\ i_e \\ v_{dc} \end{bmatrix} = \begin{bmatrix} \frac{-r}{L-M_2} & 0 & \frac{1}{2(L-M_2)} \\ 0 & \frac{-r}{L-M_2} & \frac{-1}{2(L-M_2)} \\ 0 & \frac{1}{C} & \frac{-1}{R_l C} \end{bmatrix} \begin{bmatrix} i_c \\ i_e \\ v_{dc} \end{bmatrix} + \begin{bmatrix} \frac{1}{2(L-m)} & \frac{-1}{2(L-m)} & 0 \\ \frac{-1}{2(L-m)} & \frac{1}{2(L-m)} & 0 \\ 0 & 0 & 0 \end{bmatrix} \begin{bmatrix} v_c \\ v_e \\ 0 \end{bmatrix} \tag{A32}$$

Appendix B

B1. Possible slot/Pole combinations for 3- and 5- phase machines

Table B.1 Possible Slot/Pole combinations for 3-phase PM machines

Slots	3	6	9	12	15	18	21	24	27	30	33	36	39	42	45	48
Poles	2	2	2	2	2	2	2	2	2	2	2	2	2	2	2	2
	4	4	4	4	4	4	4	4	4	4	4	4	4	4	4	4
			6	8	10	6	8	8	6	8	8	6	8	8	6	8
			8	10		8	14	10	8	10	10	8	10	10	8	10
			12	18		12	16	16	10	20	14	10	14	14	10	14
						14		20	12	22	20	12	16	16	12	16
						16			18	26	22	14	26	26	14	20
									20		26	16	28	28	16	32
									22		28	22	32	32	20	34
									24			24	34	34	28	38
												26			30	40
												28			32	
												30			34	
												32			38	
															40	

Table B.2 Possible Slot/Pole combinations for 5-phase PM machines

Slots	5	10	15	20	25	30	35	40	45
Poles	2	2	2	2	2	2	2	2	2
	4	4	4	4	4	4	4	4	4
		6	6	6	6	6	6	6	6
		8	12	8	8	8	8	8	8
				12	10	12	12	12	12
				14	16	18	14	14	14
				16	18	22	22	16	16
					20	24	24	24	18
					22	26	26	26	28
							28	28	32
								32	34
								34	36

B2. Carter's coefficient

Carter's coefficient is an approximation factor to determine the air gap permeance in the presence of slotting. The permeance can be written as

$$P_g = \mu_o A / g_e \tag{B.1}$$

where g_e is an effective air gap length given by $g_e = K_c g$, where K_c is Carter's coefficient which is described by

$$K_c \approx \left[1 - \frac{w_s}{\tau_s} + \frac{4\left(g + \frac{l_m}{\mu_r}\right)}{\pi \tau_s} \ln\left(1 + \frac{\pi w_s}{4\left(g + \frac{l_m}{\mu_r}\right)} \right) \right]^{-1} \tag{B.2}$$

where w_s slot width τ_s is stator slot pitch, l_m is the machine effective length. μ_r is recoil permeability of the magnet and g is air gap length. In the prototype machine, using the slot dimensions in chapter 4 giving K_c= 1.2

B3. Winding configuration

1. Five phase winding configuration showing the distribution of the phase coils in the stator slots.

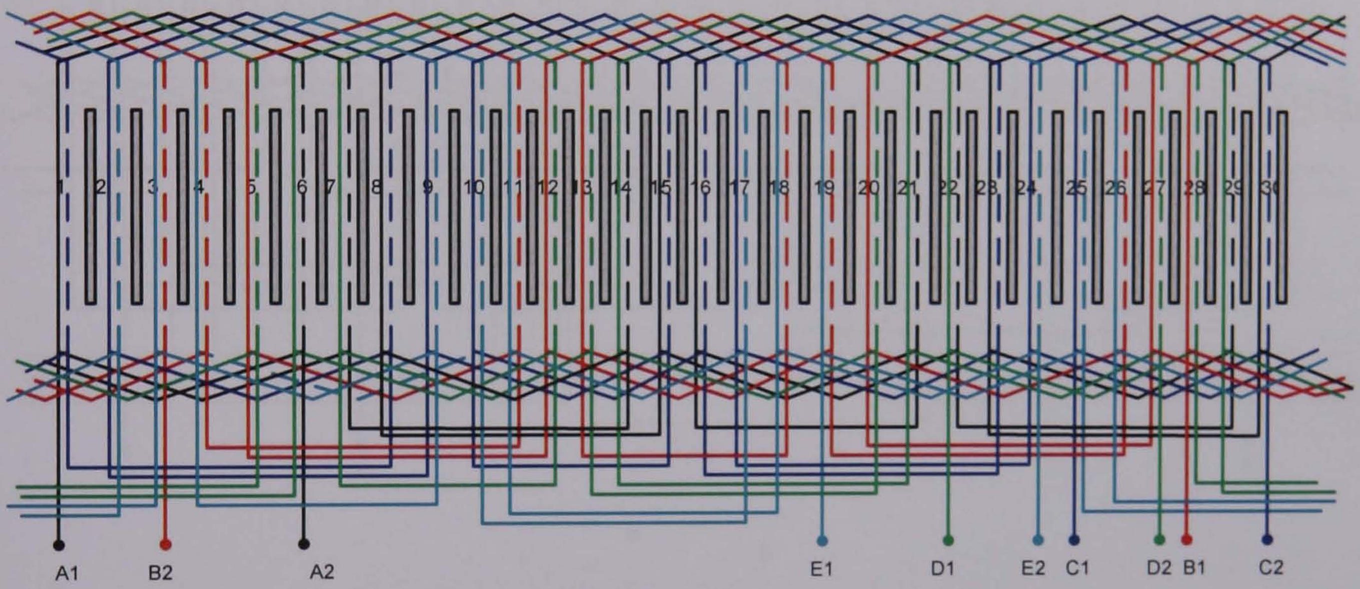

2. Three phase winding configuration showing the distribution of the phase coils in the stator slots.

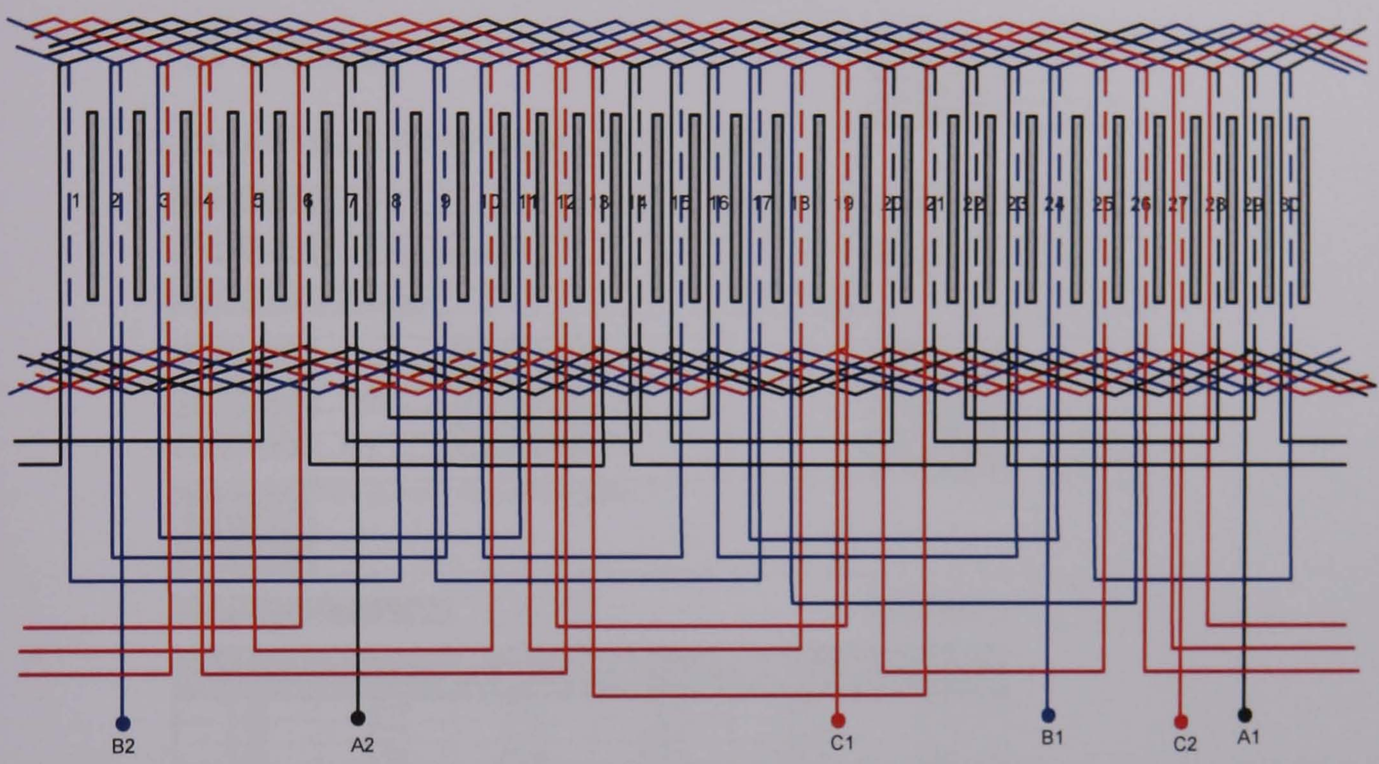

Appendix C

Permanent magnet motor performance

Permanent magnet motor performance produced by LEMAC Company is shown below

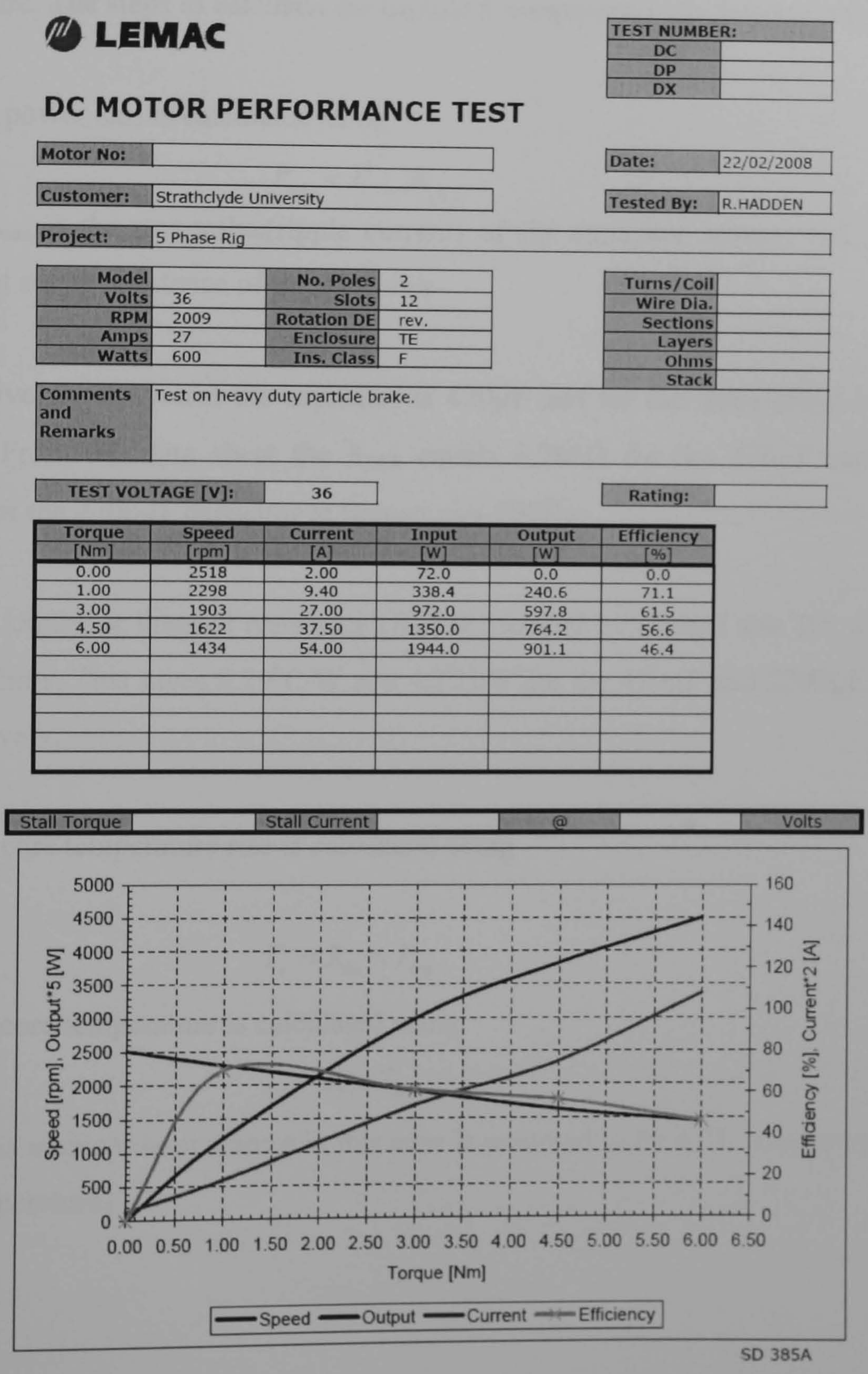

LEMAC

DC MOTOR PERFORMANCE TEST

TEST NUMBER:	
DC	
DP	
DX	

Motor No:	
Customer:	Strathclyde University
Project:	5 Phase Rig
Date:	22/02/2008
Tested By:	R.HADDEN

Model		**No. Poles**	2
Volts	36	**Slots**	12
RPM	2009	**Rotation DE**	rev.
Amps	27	**Enclosure**	TE
Watts	600	**Ins. Class**	F

Turns/Coil	
Wire Dia.	
Sections	
Layers	
Ohms	
Stack	

Comments and Remarks Test on heavy duty particle brake.

TEST VOLTAGE [V]: 36

Rating:

Torque [Nm]	Speed [rpm]	Current [A]	Input [W]	Output [W]	Efficiency [%]
0.00	2518	2.00	72.0	0.0	0.0
1.00	2298	9.40	338.4	240.6	71.1
3.00	1903	27.00	972.0	597.8	61.5
4.50	1622	37.50	1350.0	764.2	56.6
6.00	1434	54.00	1944.0	901.1	46.4

Stall Torque		Stall Current		@		Volts

SD 385A

Appendix D

Capacitor core temperature calculation

Application notes from BHC Components are used to calculate the capacitor core temperature. The steps to calculate the capacitor temperature are detailed below.

[1] The power loss is calculated using

$$P_{cap} = I^2_{c\text{-}rms} R_{ESR} \tag{D1}$$

where $I_{c\text{-}rms}$ is the rms value(ripple current) of the capacitor current and R_{ESR} is the equivalent series resistance of the capacitor

For the five-phase system the capacitor is 470μF and for the three-phase system it is 2200μF. From the data sheet the R_{ESR} equals 0.286Ω for the 470μF capacitor and 0.073Ω for the 2200μF capacitor at frequencies 100Hz.

[2] The capacitor thermal resistance (R_{ha}) is founded by using Table D7 with airflow rate of 2m/s. This gives 8.29°C/W and 4.7°C/W for the 470μF and 2200μF capacitors respectively.

[3] The core temperature rise is calculated using

$$T_r = R_{ha} \times P_{cap} \tag{D2}$$

[4] The core temperature is calculated using

$$T_c = T_r + T_a \tag{D3}$$

where T_a is ambient temperature in this case is assumed to be 45°C (maximum working room temperature)

Calculation

The calculations of the capacitor core temperature for the 470μF and 2200μF capacitors are shown in Tables D1 to D6 for the five- and three- phase system for the normal condition and failure condition. Tables D1and D2 show the estimated from the simulation results, Tables D3 and D4 show the estimated from FEA results and Tables D5 and D6 show the estimated from the experimental results. The capacitors are chosen from BHC Component's ALS30 series with rated dc voltage of 200V. The ambient temperature is chosen to be 45°C. The value of the equivalent series resistance, R_{ESR}, is given by the manufacturer specifications and the power loss is calculated using (7.3).

Table D1. Estimated five-phase dc link capacitor core temperature from the simulation results.

	Five-phase			
	Normal case	Single phase failure	Adjacent phase failure	Non-adjacent phase failure
Capacitor rms current (A)	0.22	3.4	4.9	4.3
Ambient temperature (°C)	45 °C	45 °C	45 °C	45 °C
R_{ESR} (Ω)	0.286	0.286	0.286	0.286
Capacitor thermal resistance (°C/W)	8.29	8.29	8.29	8.29
Power loss (W)	0.014	3.3	6.7	5.2
Core temperature rise (°C)	0.11	27.4	55.5	43.8
Core temperature (°C)	45.1	72.4	100.5	88.8

Table D2. Estimated three-phase dc link capacitor core temperature from the simulation results.

	Three-phase	
	Normal case	Single phase failure
Capacitor rms current (A)	1.1	7
Ambient temperature (°C)	45 °C	45 °C
R_{ESR} (Ω)	0.073	0.073
Capacitor thermal resistance (°C/W)	4.7	4.7
Power loss (W)	0.08	3.6
Core temperature rise (°C)	0.4	17
Core temperature (°C)	45.4	62

Table D3. Estimated five-phase dc link capacitor core temperature using FEA results.

	Five-phase			
	Normal case	Single phase failure	Adjacent phase failure	Non-adjacent phase failure
Capacitor rms current (A)	0.4	3.3	4.8	4.2
Ambient temperature (°C)	45 °C	45 °C	45 °C	45 °C
R_{ESR} (Ω)	0.286	0.286	0.286	0.286
Capacitor thermal resistance (°C/W)	8.29	8.29	8.29	8.29
Power loss (W)	0.05	3.1	6.6	5.0
Core temperature rise (°C)	0.4	25.8	54	41
Core temperature (°C)	45.4	70.8	99	86

Table D4. Estimated three-phase dc link capacitor core temperature using FEA results.

	Three-phase	
	Normal case	Single phase failure
Capacitor rms current (A)	1	5.8
Ambient temperature (°C)	45 °C	45 °C
R_{ESR} (Ω)	0.073	0.073
Capacitor thermal resistance (°C/W)	4.7	4.7
Power loss (W)	0.07	2.5
Core temperature rise (°C)	0.3	11.5
Core temperature (°C)	45.3	56.5

Table D5. Estimated five-phase dc link capacitor core temperature using experimental.

	Five-phase			
	Normal case	Single phase failure	Adjacent phase failure	Non-adjacent phase failure
Capacitor rms current (A)	0.5	3.1	4.3	3.9
Ambient temperature (°C)	45 °C	45 °C	45 °C	45 °C
R_{ESR} (Ω)	0.286	0.286	0.286	0.286
Capacitor thermal resistance (°C/W)	8.29	8.29	8.29	8.29
Power loss (W)	0.07	2.7	5.2	4.4
Core temperature rise (°C)	45.6	22.8	43.8	36
Core temperature (°C)	45.6	67.8	88.8	81

Table D6. Estimated three-phase dc link capacitor core temperature using experimental.

	Three-phase	
	Normal case	Single phase failure
Capacitor rms current (A)	0.9	5.7
Ambient temperature (°C)	45 °C	45 °C
R_{ESR} (Ω)	0.073	0.073
Capacitor thermal resistance (°C/W)	4.7	4.7
Power loss (W)	0.06	2.4
Core temperature rise (°C)	0.3	11
Core temperature (°C)	45.3	56

Table D7. Thermal resistance value for ALS series, from BHC product.

Thermal resistance values for ALS (screw terminal) products, no heat sink.											
Dia	Len	Thermal resistance values Rha °C/W									
mm	mm	<1m/s	1.0 m/s	1.5 m/s	2.0 m/s	2.5 m/s	3.0 m/s	3.5 m/s	4.0 m/s	4.5 m/s	5.0 m/s
36	49	11.2	9.91	9.23	8.68	8.27	7.95	7.69	7.50	7.39	7.34
36	52	10.7	9.47	8.82	8.29	7.90	7.60	7.35	7.17	7.06	7.01
36	62	9.57	8.47	7.89	7.42	7.06	6.79	6.57	6.41	6.32	6.27
36	75	8.53	7.55	7.03	6.61	6.30	6.06	5.86	5.72	5.63	5.59
36	82	8.12	7.19	6.69	6.29	5.99	5.77	5.58	5.44	5.36	5.32
36	105	7.09	6.27	5.84	5.49	5.23	5.03	4.87	4.75	4.68	4.64
36	115	6.77	5.99	5.58	5.25	5.00	4.81	4.65	4.54	4.47	4.43
51	62	7.56	6.69	6.23	5.86	5.58	5.37	5.19	5.07	4.99	4.95
51	75	6.5	5.75	5.36	5.04	4.80	4.62	4.47	4.36	4.29	4.26
51	82	6.06	5.36	4.99	4.70	4.47	4.30	4.16	4.06	4.00	3.97
51	105	5.09	4.50	4.19	3.94	3.76	3.61	3.50	3.41	3.36	3.33
51	115	4.79	4.24	3.95	3.71	3.54	3.40	3.29	3.21	3.16	3.14
51	140	4.3	3.81	3.54	3.33	3.17	3.05	2.95	2.88	2.84	2.82
66	67	5.2	4.60	4.28	4.03	3.84	3.69	3.57	3.48	3.43	3.41
66	75	4.75	4.20	3.91	3.68	3.51	3.37	3.26	3.18	3.14	3.11
66	82	4.4	3.89	3.63	3.41	3.25	3.12	3.02	2.95	2.90	2.88
66	98	3.84	3.40	3.16	2.98	2.83	2.73	2.64	2.57	2.53	2.52
66	105	3.64	3.22	3.00	2.82	2.69	2.58	2.50	2.44	2.40	2.38
66	115	3.4	3.01	2.80	2.64	2.51	2.41	2.34	2.28	2.24	2.23
66	140	3	2.66	2.47	2.33	2.21	2.13	2.06	2.01	1.98	1.97
73	115	2.97	2.63	2.45	2.30	2.19	2.11	2.04	1.99	1.96	1.95
77	67	4.3	3.81	3.54	3.33	3.17	3.05	2.95	2.88	2.84	2.82
77	75	3.94	3.49	3.25	3.05	2.91	2.80	2.71	2.64	2.60	2.58
77	82	3.65	3.23	3.01	2.83	2.69	2.59	2.51	2.45	2.41	2.39
77	98	3.16	2.80	2.60	2.45	2.33	2.24	2.17	2.12	2.09	2.07
77	105	3	2.66	2.47	2.33	2.21	2.13	2.06	2.01	1.98	1.97
77	115	2.79	2.47	2.30	2.16	2.06	1.98	1.92	1.87	1.84	1.83
77	140	2.38	2.11	1.96	1.84	1.76	1.69	1.64	1.59	1.57	1.56
77	146	2.29	2.03	1.89	1.77	1.69	1.63	1.57	1.53	1.51	1.50
77	180	1.9	1.68	1.57	1.47	1.40	1.35	1.31	1.27	1.25	1.24
77	220	1.4	1.24	1.15	1.09	1.03	0.99	0.96	0.94	0.92	0.92
91	67	3.5	3.10	2.88	2.71	2.58	2.49	2.40	2.35	2.31	2.29
91	75	3.2	2.83	2.64	2.48	2.36	2.27	2.20	2.14	2.11	2.10
91	98	2.55	2.26	2.10	1.98	1.88	1.81	1.75	1.71	1.68	1.67
91	146	1.85	1.64	1.52	1.43	1.37	1.31	1.27	1.24	1.22	1.21
91	180	1.55	1.37	1.28	1.20	1.14	1.10	1.06	1.04	1.02	1.02
91	220	1.2	1.06	0.99	0.93	0.89	0.85	0.82	0.80	0.79	0.79

Appendix E

Overall experimental system layout

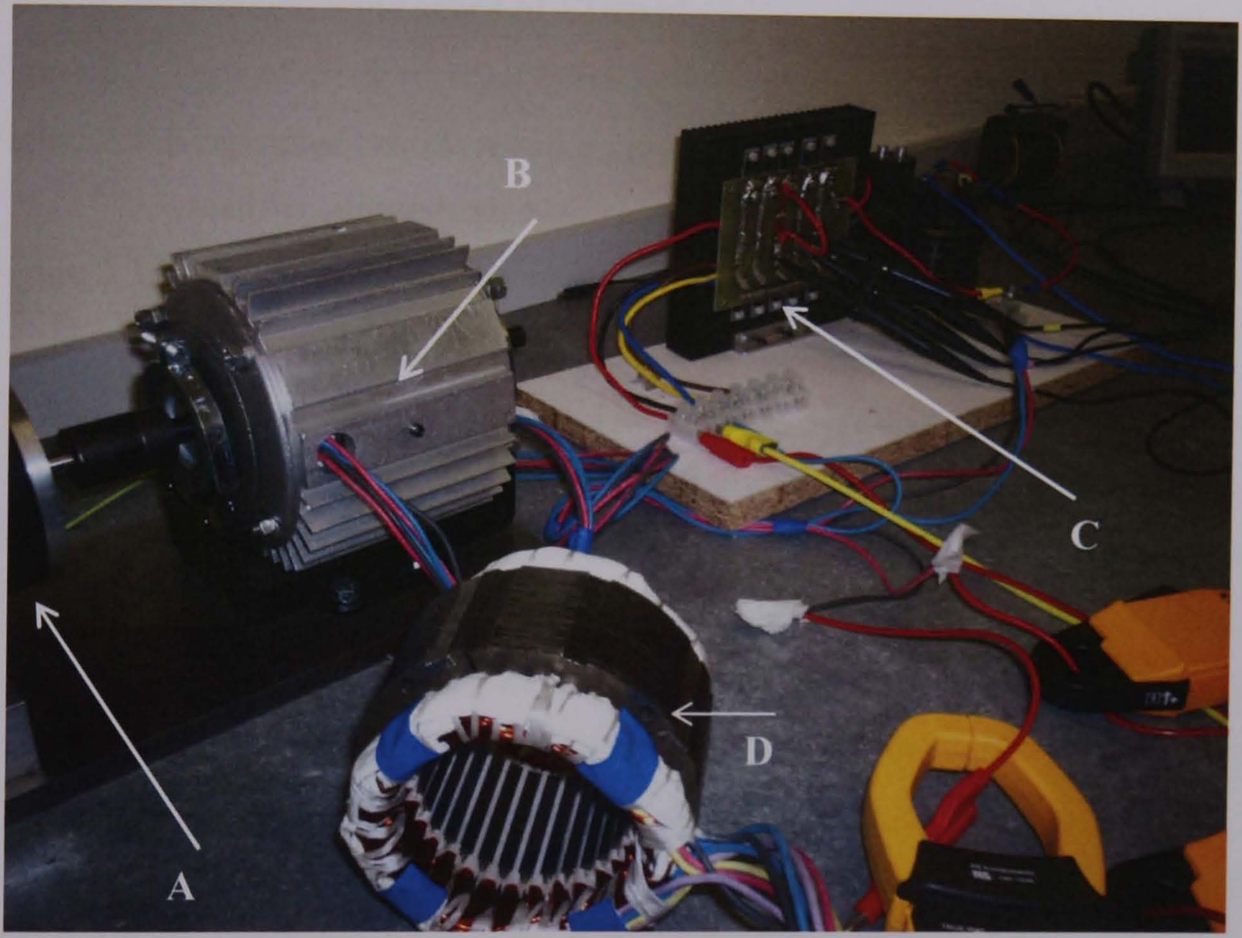

Figure E1. Picture of the experiment showing (A) the dc motor (B) the three-phase prototype generator (C) the diode bridge rectifier, and (D) the stator of the five-phase prototype generator.

Appendix F

List of Figure

Appendix G

List of Tables

Appendix H

List of publications

N. A. M. Hassanain, J. E. Fletcher , "Analysis three- and five-phase permanent magnet machines supplying diode bridge rectifiers for small-scale wind generators," POWERENG 2007 Conference, April 12-14, 2007, Setubal, Portugal, pp. 648-653

Abstract - In this paper, performance of three- and five-phase permanent magnet generators (PMG) feeding rectifier systems are compared analytically for small-scale wind generator systems. The volume and rated speeds of the two generators are kept equal and determined using FEM 2D. No-load induced voltage, self and mutual inductances and resistance are calculated and used to simulate the performance of the 3-phase and 5-phase generators coupled to a dc link through a diode bridge rectifier. Generator mathematical models are developed and simulated. The simulations show that five-phase system has torque ripple that is a factor of 7 lower than the three-phase system with an almost identical efficiency figure.